2 May 2014 | $10

Science



What's Killing the Sea Stars?

AAAS

EDITORIAL

449 The Power of Curiosity
Michael S. Turner

NEWS OF THE WEEK

454 A roundup of the week's top stories

NEWS & ANALYSIS

457 Soaring MERS Cases in Saudi Arabia Raise Alarms
458 Perovskite Solar Cells Keep On Surging
459 Drones Flying High as New Tool for Field Biologists
460 As Pentagon Downsizes, Budgets Shrink for Academic Research
461 Male Scent May Compromise Biomedical Studies
462 Therapeutic Cloning Reaches Milestone
463 Seafloor Mining Plan Advances, Worrying Critics

NEWS FOCUS

464 Death of the Stars
>> Slideshow

LETTERS

469 Shining a Light on Solar Water Splitting
E. A. Chandross
Response
J. A. Turner
Advanced Photon Source Upgrade Benefits All
B. Stephenson
470 CORRECTIONS AND CLARIFICATIONS

BOOKS *ET AL.*

471 Falling Behind?
M. S. Teitelbaum, reviewed by A. B. Jaffe
472 Missing Microbes
M. J. Blaser, reviewed by A. E. Mather

POLICY FORUM

473 Evaluating Flood Resilience Strategies for Coastal Megacities
J. C. J. H. Aerts et al.

PERSPECTIVES

476 Tolerance for Predatory Wildlife
A. Treves and J. Bruskotter
477 Dysfunctional Mechanosensing in Aneurysms
J. D. Humphrey et al.
479 Forming Terrestrial Planets
J. Chambers
480 A New Wrap for Neuronal Activity?
M. E. Bechler and C. ffrench-Constant
>> Research Article p. 487
482 Assembly and Disassembly of Ferrocene-Based Nanotubes
Z. M. Hudson and I. Manners
>> Report p. 499
483 Nonlinear Optics Pushed to the Edge
D. Neshev and Y. Kivshar
>> Report p. 488
484 Limits on Yields in the Corn Belt
D. R. Ort and S. P. Long
>> Report p. 516

REVIEW

486 Multiple Dimensions of Climate Change and Their Implications for Biodiversity
R. A. Garcia et al.
Review Summary; for full text: http://dx.doi.org/10.1126/science.1247579

CONTENTS continued >>



page 459



page 476

ON THE WEB THIS WEEK

>> *Science* Podcast
On this week's show: links between intensive farming and drought sensitivity in corn and a roundup of stories from our daily news site.

>> Find More Online
Check out *Science* Express, the weekly podcast, videos, daily news, our research journals, and *Science* Careers at **www.sciencemag.org.**



COVER

A blood star (*Henricia leviuscula*) near Whidbey Island, Washington state. It is one of 10 species of sea star that appear to be affected by a mysterious wasting syndrome on the west and east coasts of North America. Various levels of mortality have been confirmed in 10 other species, making this the largest documented die-off of echinoderms. See page 464 and http://scim.ag/slide_6183.
Photo: Jan Kocian

DEPARTMENTS

447 This Week in *Science*
450 Editors' Choice
452 *Science* Staff
539 New Products
540 *Science* Careers

RESEARCH ARTICLE

487 Neuronal Activity Promotes Oligodendrogenesis and Adaptive Myelination in the Mammalian Brain
E. M. Gibson et al.
Optogenetic stimulation of the mouse motor cortex incites proliferation of myelin-producing cells and axonal myelination.
Research Article Summary; for full text: http://dx.doi.org/10.1126/science.1252304
>> Perspective p. 480

REPORTS

488 Edge Nonlinear Optics on a MoS_2 Atomic Monolayer
X. Yin et al.
Second-harmonic generation is used to probe and characterize atomically thin layers of molybdenum disulfide.
>> Perspective p. 483

491 Probing Exchange Pathways in One-Dimensional Aggregates with Super-Resolution Microscopy
L. Albertazzi et al.
One-dimensional supramolecular aggregates can swap constituent monomers through a homogeneous exchange mechanism.

495 Interfacial Effects in Iron-Nickel Hydroxide–Platinum Nanoparticles Enhance Catalytic Oxidation
G. Chen et al.
An alloy catalyst for room-temperature CO creates sites for O_2 activation when the CO_2 product is released.

499 Manipulation of Discrete Nanostructures by Selective Modulation of Noncovalent Forces
T. Fukino et al.
Self-assembled, large-diameter ferrocene-based nanotubes can be cleaved into stable rings and then reassembled into tubes.
>> Perspective p. 482

504 Vibrationally Promoted Dissociation of Water on Ni(111)
P. M. Hundt et al.
The barrier to this reaction, a key step in methane steam reforming, is mainly surmounted by vibrational energy.

508 Faster Decomposition Under Increased Atmospheric CO_2 Limits Soil Carbon Storage
K. J. van Groenigen et al.
Soil carbon turnover increases as atmospheric carbon dioxide rises, which limits carbon accumulation in soils.

510 Genomic Signatures of Specialized Metabolism in Plants
L. Chae et al.
A comparative genomic analysis of plant metabolism can distinguish the evolution of specialized versus primary metabolism.

513 Deception by Flexible Alarm Mimicry in an African Bird
T. P. Flower et al.
A clever African bird flexibly mimics the calls of other species to keep fooling them into abandoning their food.

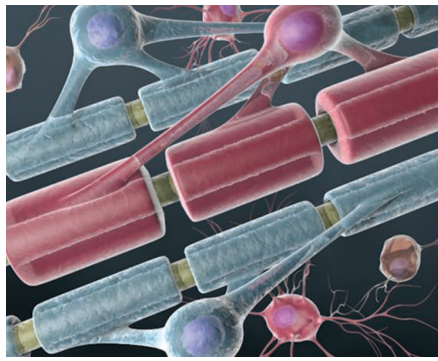
516 Greater Sensitivity to Drought Accompanies Maize Yield Increase in the U.S. Midwest
D. B. Lobell et al.
Selective breeding focused on increasing corn and soybean yields has left a weakness in corn drought tolerance.
>> Perspective p. 484; Science *Podcast*

519 Polarization of the Effects of Autoimmune and Neurodegenerative Risk Alleles in Leukocytes
T. Raj et al.
Genetic variants affecting gene expression show both shared and specific immune cell type effects.

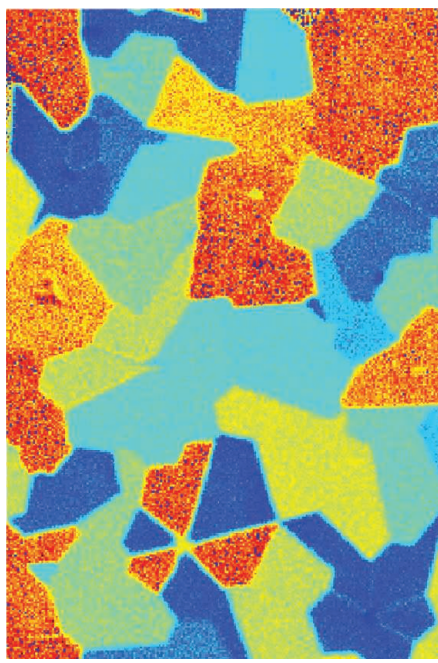
523 Reconstructing the DNA Methylation Maps of the Neandertal and the Denisovan
D. Gokhman et al.
Estimates of differentially methylated nucleotides illuminate differences between modern human and ancient hominid bones.

527 Chemical Inhibition of NAT10 Corrects Defects of Laminopathic Cells
D. Larrieu et al.
The small molecule Remodelin can correct nuclear architecture defects and improve cellular fitness of progeric human cells.

533 Molecular-Level Functional Magnetic Resonance Imaging of Dopaminergic Signaling
T. Lee et al.
Development of a molecular functional magnetic resonance imaging tool to quantify dopamine release simultaneously in different brain regions is shown.



pages 480 & 487



pages 483 & 488

CREDIT: (BOTTOM) XIAOBO YIN

SCIENCE (ISSN 0036-8075) is published weekly on Friday, except the last week in December, by the American Association for the Advancement of Science, 1200 New York Avenue, NW, Washington, DC 20005. Periodicals Mail postage (publication No. 484460) paid at Washington, DC, and additional mailing offices. Copyright © 2014 by the American Association for the Advancement of Science. The title SCIENCE is a registered trademark of the AAAS. Domestic individual membership and subscription (51 issues): $153 ($74 allocated to subscription). Domestic institutional subscription (51 issues): $1282; Foreign postage extra: Mexico, Caribbean (surface mail) $55; other countries (air assist delivery) $85. First class, airmail, student, and emeritus rates on request. Canadian rates with GST available upon request, GST #1254 88122. Publications Mail Agreement Number 1069624. **Printed in the U.S.A.**

Change of address: Allow 4 weeks, giving old and new addresses and 8-digit account number. **Postmaster:** Send change of address to AAAS, P.O. Box 96178, Washington, DC 20090–6178. **Single-copy sales:** $10.00 current issue, $15.00 back issue prepaid includes surface postage; bulk rates on request. **Authorization to photocopy** material for internal or personal use under circumstances not falling within the fair use provisions of the Copyright Act is granted by AAAS to libraries and other users registered with the Copyright Clearance Center (CCC) Transactional Reporting Service, provided that $30.00 per article is paid directly to CCC, 222 Rosewood Drive, Danvers, MA 01923. The identification code for *Science* is 0036-8075. *Science* is indexed in the *Reader's Guide to Periodical Literature* and in several specialized indexes.



<< Trick and Treat

Forked-tailed drongos are a particularly intelligent type of bird found in Africa. Drongos associate with many other bird and mammal species, which can learn to respond to drongo warning calls. Drongos are also exceptional mimics of the other species' alarm calls. Though the increased vigilance across these multispecies associations is a benefit to all, drongos sometimes use these calls as ploys to scare associated species away from food, which the drongos then steal. However, without some approach to maintain the effectiveness of this deception, the drongos' ploy would soon be detected. **Flower *et al.*** (p. 513) now show that drongos are able to fool their target species longer by flexibly varying the type of call they give.

Examining Supramolecular Exchange

Microtubules are a natural example of a one-dimensional (1D) supramolecular structure. Synthetic examples of 1D fibrils often have monomers linked by weak noncovalent interactions that allow monomers to exchange in and out of the fibrils. **Albertazzi *et al.*** (p. 491) used a combination of super-resolution microscopy on individual fibrils and stochastic simulation to study monomer exchange in fibrils formed from stacked 1,3,5-benzenetricarboxamide motifs. Exchange did not require large-scale depolymerization and repolymerization, or reassembly of fragments, but proceeded through individual monomers exchanging homogeneously throughout the fibrils.

Improving Reactions at Interfaces

Alloying precious metals such as platinum with more abundant transition metals, such as iron and nickel, can both improve their catalytic reactivity and lower catalyst cost. **Chen *et al.*** (p. 495) explored using coatings of iron oxide–hydroxide layers on supported platinum nanoparticles for CO oxidation. The presence of this layer allowed the reaction to run rapidly at room temperature by bringing together different reaction sites on the two metals. The addition of nickel improved catalyst lifetime, and an oxidative transformation created a more complex nanoparticle morphology that increased platinum utilization.

CREDIT: THOMAS FLOWER

Nanotube Engineering

In general, the reversible self-assembly of nanotubes through noncovalent bonding either gives fully assembled or fully disassembled products. **Fukino *et al.*** (p. 499, published online 10 April; see the Perspective by **Hudson and Manners**) developed a system with an intermediate possibility. Hollow nanotube structures were assembled from ferrocene-based tetratopic pyridyl ligands mixed with $AgBF_4$. Through oxidation of the ferrocene groups, the tubes could be cut into stable, large rings and then reversibly reassembled into nanotubes by reduction of the ferrocene groups.

Watching Brain Molecules

Functional neuroimaging using magnetic resonance imaging (MRI) molecular sensors would be useful for mechanistic analysis of neural systems. **Lee *et al.*** (p. 533) applied MRI-detectable sensors to measure molecular aspects of brain function in conjunction with noninvasive imaging. The molecular sensor revealed a quantitative spatiotemporal map of dopamine release in the ventral striatum, a brain area involved in processing rewards.

Increasing Turnover

Rising concentrations of CO_2 in the atmosphere are likely to stimulate plant growth, leading to increased biomass and soil carbon stocks, thereby lessening the rate of the rise in atmospheric CO_2 levels. **Van Groenigen *et al.*** (p. 508, published online 24 April) report the results of a meta-analysis and modeling that show that increasing the concentration of atmospheric CO_2 also stimulates microbial decomposition of organic carbon in soils, by roughly the same amount that it increases soil organic carbon, leading to lower equilibrium soil carbon inventories and limiting the accumulation of carbon. Thus, soils may not provide as much carbon storage as hoped.

Predicting Responses to Drought

The U.S. Corn Belt accounts for a sizeable portion of the world's maize growth. Various influences have increased yields over the years. **Lobell *et al.*** (p. 516; see the Perspective by **Ort and Long**) now show that sensitivity to drought has been increasing as well. It seems that as plants have been bred for increased yield under ideal conditions, the plants become more sensitive to non-ideal conditions. A key factor may be the planting density. Although today's maize varieties are more robust to crowding and the farmer can get more plants in per field, this same crowding takes a toll when water resources are limited.

Methylating the Family Tree

DNA sequences show a high level of similarities between humans and ancient hominids but the degree to which there are differences between methylated regions in their genomes that may explain phenotypic differences is unclear. **Gokhman *et al.*** (p. 523, published online 17 April) demonstrate that naturally degraded methylated cytosines in ancient DNA are converted to thymines and can be used to reconstruct ancient methylomes. The results suggest differences in methylation in bone tissues between modern humans and ancient hominids in a set of genes important for limb development.

Remodelin Nuclear Defects

Deregulation of A-type lamin proteins leads to disorganization of chromatin structure and misshapen nuclei, which are believed to underlie the pathologies of various human diseases, including the premature aging disorder Hutchinson Gilford progeria syndrome (HGPS) and various cancers. **Larrieu *et al.*** (p. 527) developed a small molecule, Remodelin, that not only improved nuclear shape defects of human lamin A/C–depleted cells, HGPS cells, and aged normal cells, but also decreased the levels of a DNA damage marker and improved global cellular fitness.

Downloaded from www.sciencemag.org on May 1, 2014

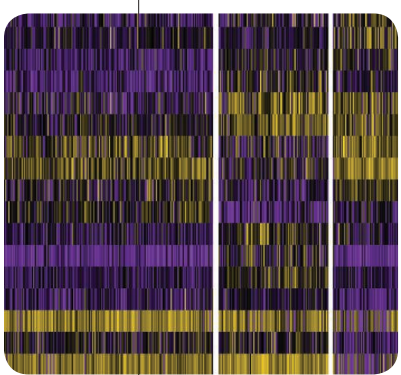
Additional summaries

Interpreting Climate Change Metrics

While forecasts of climate change effects on biodiversity rely mostly on bioclimatic modeling approaches of varying complexity, an alternative to existing models is to use simple metrics to quantify the exposure of regions to climate changes over time and relate them to different threats and opportunities for biodiversity. It remains poorly understood how existing metrics differ in the information they provide, specifically in the context of biodiversity. **Garcia *et al.*** (p. 486) review the variety of metrics commonly used to describe climate change in biodiversity-impact assessments covering local changes in climate averages and extremes, regional changes in the availability and position of climates, and the velocity of climate change. While metrics are often arbitrarily chosen in studies of ecology and evolution, and interchangeably used as synonyms of climate change, they capture different dimensions of change and reveal contrasting spatial patterns across the world. Defining the links between climate change dimensions and the challenges they represent to species leads to a framework for interpreting climate change metrics.

On-Demand Activity

Oligodendroglia ensheath axons in the brain with myelin, which provides the insulation that speeds up transmission of neuronal electrical impulses. The process of myelination in the human brain goes on for decades, concurrent with all manner of brain development and cognitive activity. **Gibson *et al.*** (p. 487, published online 10 April; see the Perspective by **Bechler and ffrench-Constant**) used optogenetics to study myelination in response to neural activity. Electrical activity in the motor cortex of the brain of awake mice led to proliferation and differentiation of oligodendrocytes and consequently increased myelination and alterations in motor response.



CREDIT: RAJ *ET AL.*

Immunogenetic Variation

Many genetic variants have been implicated in disease but their effects in function across tissues and cell-types remain to be resolved. **Raj *et al.*** (p. 519) present an analysis of expression quantative trait loci (eQTL) measuring messenger RNA levels and examined correlations between genotypes and gene expression in purified monocytes and T cells in healthy individuals of European, African, and Asian descent. Most, but not all, of the eQTLs and their effects on expression were shared between the populations, as well as a substantial proportion between the cell types. Links were found with disease-associated variants and loci that previous genome-wide analyses have implicated in neurodegenerative and autoimmune diseases.

Optics On the Edge

The ability to isolate stable materials just one atom thick has provided the impetus for a new generation of thin films technologies. Often, the materials are conceptually imaged in the form of an artist's impression as single continuous layers—a single crystal sheet of atoms. Scanning probe and transmission electron microscopies reveal the reality, however, where the material resembles a patchwork quilt with polycrystals of different orientation and size separated by grain boundaries forming a mosaic. These structures play an influential role in determining the transport and optical properties of the membrane. **Yin *et al.*** (p. 488; see the Perspective by **Neshev and Kivshar**) demonstrate a simple microscopy technique based on the nonlinear optical response of the materials to probe and characterize atomically thin layers of MoS_2. The technique should prove useful during the characterization and optimization of atomically thin membranes.

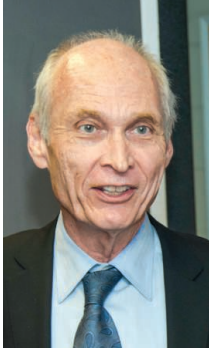
Vibrating Water Apart

The main route for producing hydrogen for industrial chemical synthesis is steam reforming, in which water and methane react at high temperatures on nickel catalysts to produce hydrogen and carbon dioxide. For both water and methane, the initial dissociation step can be promoted by the translational energy of a molecule as well as its internal vibrational energy, and fundamental studies of these reactions try to determine the relative contributions of these pathways. Although the methane reaction has been well studied, only recently have lasers been available to excite the higher stretching vibrations of water. **Hundt *et al.*** (p. 504) now report a joint experimental and theoretical study of D_2O dissociation on the Ni(111) surface. For a given input of energy, vibrational energy was more effective for surmounting the reaction barrier than translational energy.

Specialized Evolution

Many plants make chemical compounds that are potentially of use to humans, but their evolutionary histories are unknown. **Chae *et al.*** (p. 510) examined how algae and land plants have been able to evolve secondary metabolism biochemistry—those compounds produced in response to their environment—in the face of purifying evolutionary pressure to maintain primary and necessary metabolic pathways. Genomic data was used to separate the primary from the secondary metabolism pathway genes and to construct the evolutionary trajectories of secondary metabolism. Secondary metabolic pathways tend to be controlled by clustered, co-regulated sets of newly duplicated and maintained genes.

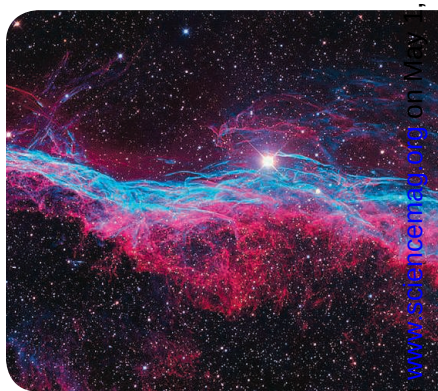
Published by AAAS



Michael S. Turner is the Rauner Distinguished Service Professor and director of the Kavli Institute of Cosmological Physics at the University of Chicago, Chicago, IL. E-mail: mturner@kicp.uchicago.edu

The Power of Curiosity

IN MARCH OF 2014, 47 SCIENTISTS FROM 15 INSTITUTIONS (INCLUDING MY OWN) ANNOUNCED THAT a South Pole–based microwave telescope had taken us back to a time when the universe was 10^{-38} seconds old—when everything that we can see today occupied a space much smaller than that occupied by a proton, and when the energy level of the universe was a trillion times greater than that produced by the world's most powerful accelerator, the Large Hadron Collider in Switzerland. Assuming that this amazing discovery by the Background Imaging of Cosmic Extragalactic Polarization (BICEP2) collaboration is confirmed, this cosmic remnant beats the previous record holder for earliest fossil of our cosmic birth (the helium and deuterium made when the universe was seconds old) by 38 orders of magnitude. Rarely has science advanced by such a giant leap, and it will take us years if not decades to fully comprehend all the implications of this incredible moment in science. Although we are used to cosmology stunning us with beautiful images and mind-stretching discoveries such as dark energy and dark matter, even this cosmologist with almost 40 years of experience was awed and shocked by this big, big find.



According to the standard cosmological model, during its earliest moments, the universe underwent a tremendous growth spurt known as inflation, which created the seeds of galaxies and all other cosmic structures from subatomic quantum fluctuations. Since 1992, measurements of the cosmic microwave background have amassed evidence for this theory, but the BICEP2 telescope may have found the smoking gun: gravitational waves that began as quantum fluctuations in spacetime and left an imprint on the cosmic microwave background in the tiny signal (about 100 nanokelvins) detected by the BICEP2 telescope.

Because of deep and remarkable connections between quarks and the cosmos, this cosmic discovery is related to another big discovery, the Higgs boson. The Higgs, the first of a new class of elementary particles (scalar bosons), accounts for why some elementary particles have mass. The potential instigator of cosmic inflation is a hypothetical scalar boson called the inflaton, and the Higgs discovery boosted its credibility and may even explain how it fits in. Conversely, the BICEP2 discovery has given us a window on the highest energies that particle theorists can imagine, and in doing so, will provide insights into how the fundamental forces and particles are unified.

There are differences between the BICEP2 and Higgs discoveries to be sure, in technique and scale of effort, but both are exemplars of the kind of curiosity-driven science that gets scientists out of bed in the morning and inspires young people to careers in science by asking some of the deepest questions about how the universe began and the events that have shaped our existence. BICEP2 and the Higgs will launch the careers of thousands of new scientists around the world, just as quarks and quasars sparked my career. But we should not forget that great discoveries can have unforeseen practical benefits as well. Some 100 years ago, the discovery of strange new phenomena began the esoteric study of quantum mechanics, with no hint of a practical benefit. The exploitation of these quantum phenomena has enabled the information age that now underpins our economy and way of life.

Whether the fruits of our curiosity are bettering our existence on Earth or our understanding of our place in the cosmos, it all begins with a burning desire to know. The BICEP2 and Higgs discoveries remind us never to underestimate the power of this curiosity, one of humankind's greatest assets.

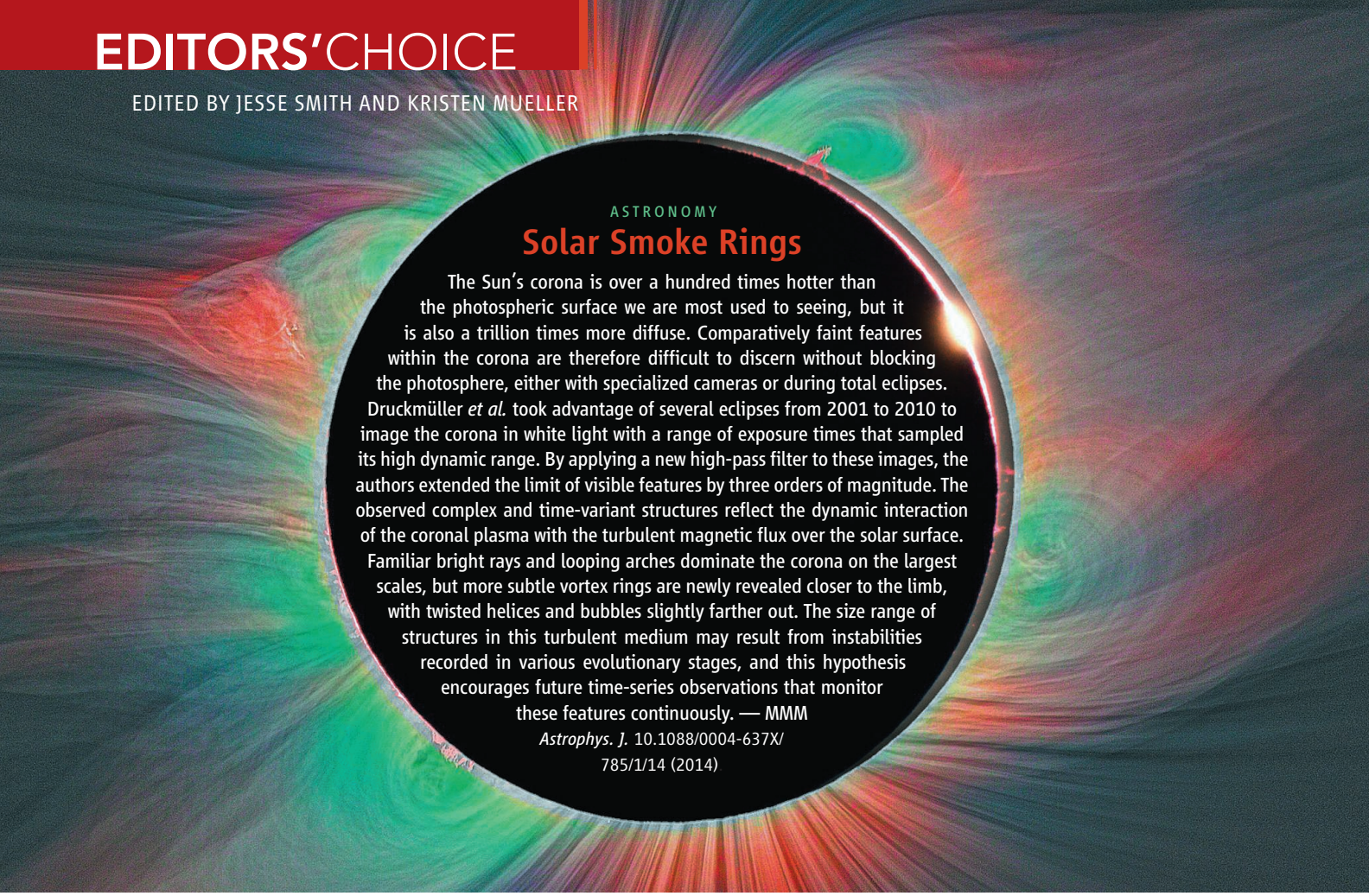
– Michael S. Turner

10.1126/science.1255182

Downloaded from www.sciencemag.org on May 1, 2014

CREDITS: (LEFT) UNIVERSITY OF CHICAGO; (RIGHT) KEN CRAWFORD/WIKIMEDIA COMMONS

Published by AAAS



ASTRONOMY

Solar Smoke Rings

The Sun's corona is over a hundred times hotter than the photospheric surface we are most used to seeing, but it is also a trillion times more diffuse. Comparatively faint features within the corona are therefore difficult to discern without blocking the photosphere, either with specialized cameras or during total eclipses. Druckmüller *et al.* took advantage of several eclipses from 2001 to 2010 to image the corona in white light with a range of exposure times that sampled its high dynamic range. By applying a new high-pass filter to these images, the authors extended the limit of visible features by three orders of magnitude. The observed complex and time-variant structures reflect the dynamic interaction of the coronal plasma with the turbulent magnetic flux over the solar surface. Familiar bright rays and looping arches dominate the corona on the largest scales, but more subtle vortex rings are newly revealed closer to the limb, with twisted helices and bubbles slightly farther out. The size range of structures in this turbulent medium may result from instabilities recorded in various evolutionary stages, and this hypothesis encourages future time-series observations that monitor these features continuously. — MMM

Astrophys. J. 10.1088/0004-637X/785/1/14 (2014)

EDUCATION

Mentoring in All Its Varieties

Mentoring is ubiquitous throughout the academic system, with mentors and mentees representing a diverse set of backgrounds, skill levels, and priorities. As the mentor culture expands to include both formal and informal peer connections between faculty members, as well as between students, the research community struggles to arrive at a single definition of what exactly mentoring is. Rather than add another definition to the mix, Dawson instead develops a framework for mentoring relationships that is capable of absorbing the current variety. Through an ongoing and nonsystematic survey of mentoring literature, an initial mentoring framework of 20 elements was created. Examples of these elements include selection: how mentors and mentees are chosen; matching: how mentoring relationships are created; and time: both length of relationship and the frequency of meetings during the relationship. Over a 5-year period, this framework was continually refined and reduced to 16 elements, on the basis of feedback from presentations of the framework at conferences and mentoring workshops and through consultations with researchers from education and human resources management. This work will be beneficial for anyone looking to institute a mentoring intervention, as this framework identifies important decision points around which proposals can be designed. — MM

Educ. Res. **43**, 137 (2014).

PARASITOLOGY

Sometimes Schistosomiasis

Schistosomiasis-causing blood flukes infect hundreds of millions of people in tropical regions, but the occurrence of pathology is highly variable, with 5 to 10% of infections becoming severe. Likewise, schistosome infections take very different courses in different strains of mice; a phenomenon that relates to their relative ability to generate lymphocytes classified as $CD4^+$ T helper 17 (T_H17) cells. Sick children with blood flukes have also been found to have higher percentages of $CD4^+$ T_H17 cells. Ponichtera *et al.* have now discovered that the antigen-presenting dendritic cells of a mouse strain that develops severe hepatic granulomatous responses to schistosome eggs have a many times greater expression of a C-type lectin receptor called CD209a (a homolog of human ICAM-3–grabbing nonintegrin) on their cell surfaces as compared with a mouse strain that shows little pathology. CD209a is essential for the induction of the cytokines interleukin-1β and interleukin-23 that stimulate $CD4^+$ T_H17 cell development. Possibly the pathology of severe schistosomiasis is caused by elevated CD209a levels in some people sensitizing recognition of the fucose-rich glycans that coat the parasites' egg surface. — CA

J. Immunol. 10.4049/jimmunol.1400121 (2014).

CELL SIGNALING

Finding Folliculin's Function

The tumor-suppressor protein folliculin (FLCN) is turning up as an important component of distinct cell signaling pathways that control cell growth and metabolism. FLCN's structure provides no recognizable clues to its function, but mutations in FLCN cause a cancer syndrome in humans. Exactly how it does so has remained unclear. Recent work showed that FLCN can act as a GAP (guanosine triphosphatase—activating protein) to control the kinase mTORC1, which regulates cell growth. Possik *et al.* report that FLCN binds to and inhibits another key regulatory kinase, AMPK (adenosine monophosphate–activated protein kinase), which helps maintain energy balance in the cell. Loss of FLCN acts through AMPK to help cells resist

CREDIT: S. HABBAL *ET AL.*, *THE ASTROPHYSICAL JOURNAL* **719**, 2 (20 AUGUST 2010) © 2014 IOP PUBLISHING

stresses such as starvation. This effect was mediated, at least in part, by increased autophagy. These results suggest that the loss of FLCN function in cancer cells may make them more tolerant of stress and thus more effective at invading tissues of the host organism. — LBR

PLOS Genet. 10.1371/journal.pgen.1004273 (2014).

APPLIED PHYSICS

Inducing a Single Vibration

Optomechanical systems typically consist of a mechanical oscillator or cantilever that can be driven by the optical radiation pressure of light. The light can either amplify the motion of the cantilever or be used to reduce the amount of vibration and effectively cool it. Recent work has demonstrated cooling to the extent that the number of vibrations, or phonons, in an oscillator can be quantized, even reaching the quantum-mechanical ground. Galland *et al.* introduce a method to introduce a single phonon into their mechanical oscillator. Starting off in the quantum-mechanical ground, they pump the system with a laser pulse that generates an entangled phonon-photon pair. Detection of the photon then heralds that a single-phonon state has been induced into the oscillator. The ability to deterministically control the number of vibrational quanta in such an optomechanical system has important implications for the likes of quantum information processing and quantum enhanced sensing applications. — ISO

Phys. Rev. Lett. **112**, 143602 (2014).

BIOMEDICINE

Breaking Down a Barrier

Ischemic stroke, one of the most common causes of death and disability, occurs when a blood vessel supplying oxygen and nutrients to the brain becomes obstructed. Besides injuring brain cells, a stroke disrupts the function of endothelial cells in the blood-brain barrier (BBB), which exacerbates brain damage. The cellular mechanisms underlying BBB breakdown during a stroke are poorly understood. To study this, Knowland *et al*. created transgenic mice expressing a fluorescent reporter gene in endothelial cells and then, with the help of fluorescent dyes, used two-photon microscopy to image BBB function in the mice after an experimentally induced stroke. In contrast to a prevailing theory emphasizing the primary role played by a diffusion barrier called the tight junction, the imaging study revealed that the initial cause of BBB breakdown (occurring 6 hours after the stroke) was aberrant up-regulation of transcytosis, a process by which molecules are transported across the endothelial cell. It was not until 24 to 48 hours after the stroke that tight junctions showed structural defects. Understanding this sequence of events may lead to therapies that limit the brain damage caused by a stroke. — PAK

Neuron 10.1016/j.neuron.2014.03.003 (2014)

PALEONTOLOGY

Herbivores, After All

After the mass extinctions of the Cretaceous, many terrestrial ecosystems were dominated by large flightless birds. Although the bill anatomy of some of these species suggest a carnivorous diet, the diet of the largest of these, *Gastornis*, has been debated. Angst *et al.* conducted carbon isotope analysis on fossils of *Gastornis* and several contemporaneous herbivorous mammals across several European sites and compared these to isotope profiles from extant birds with known diets. The analysis revealed that *Gastornis* had an herbivorous diet. In fact, in order for a carnivore to have shown similar values it would have needed to prey almost entirely on species that fed on a type of plant that did not evolve until approximately 14 million years after the sampled individuals lived. Isotope evidence was corroborated with morphological comparison of *Gastornis* bill anatomy relative to that of extant birds, which suggested that the large muscle attachment area in *Gastornis* jaws is similar to that found in herbivorous species. This firm placement of *Gastornis* as an herbivore suggests that the community structure of Paleocene Europe was different from that found in North America at the time, and may in fact have been quite similar to the later systems seen on islands, such as Madagascar, where large flightless birds filled many different niches. — SNV

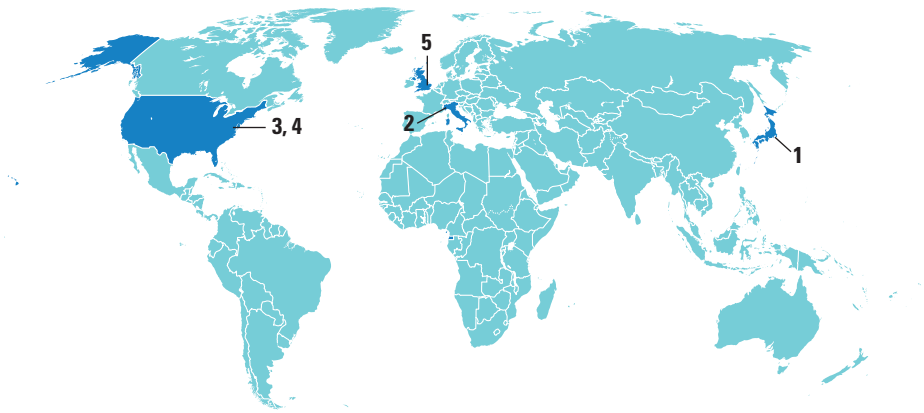


CREDIT: JAIME CHIRINOS/SCIENCE SOURCE

Naturwissenschaften 10.1007/s00114-014-1158-2 (2014).

Published by AAAS

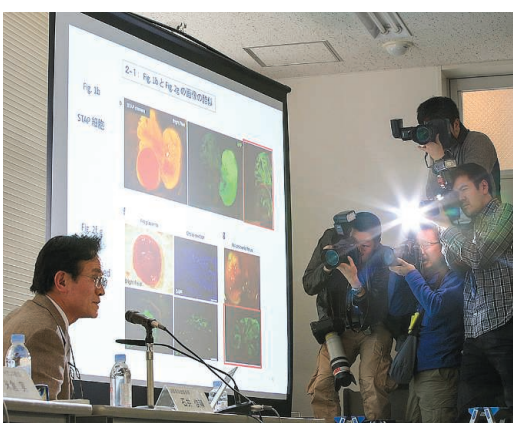
AROUND THE WORLD



Tsukuba, Japan **1**

Investigator Investigated For Misconduct

In a bizarre twist to an already convoluted story, the chair of an investigating committee that found stem cell scientist Haruko Obokata guilty of research misconduct is himself now under investigation for alleged research misconduct. He has submitted a correction for problematic images appearing in one of his 2007 papers and resigned from the investigating committee.



Turnabout. Investigator Shunsuke Ishii, discussing Obokata's work in March, is under investigation.

"Some errors occurred" in arranging images appearing in a paper published in *Oncogene,* writes Shunsuke Ishii, a molecular geneticist at the RIKEN Tsukuba Institute, in a correction posted on his lab's website. "I deeply apologize to everyone for the suspicions that have arisen and for the various troubles these have caused," he adds.

Ishii's committee investigated a research article and a letter authored by Obokata, of the RIKEN Center for Developmental Biology in Kobe, and colleagues that reported finding a new, simple way of creating stem cells, called STAP (stimulus-triggered acquisition of pluripotency). So far, no other groups have been able to reproduce the STAP results. A separate RIKEN team is now trying to replicate every step of the experiments. **http://scim.ag/_Ishii**

Turin, Italy **2**

Report Declares Halted Stem Cell Therapy 'Criminal'

After a 4-year investigation, a public prosecutor in Italy has delivered a withering indictment of stem cell therapy provided by the Stamina Foundation. The report, released on 23 April, describes Stamina President Davide Vannoni as the head of a criminal organization that has defrauded about a thousand patients since 2006 and exposed them to risks including infection, spinal cord injury, and cancer.

The report says that no clinical studies were done, that cells were injected under nonsterile conditions, and that "bovine serum with no specified origin" was used as a culture medium. It also finds that Vannoni tried to bypass laws on stem cell therapies to make the treatment available at public hospitals for patients with neurodegenerative disease.

The Italian Medicines Agency and the National Transplant Center shut down Stamina's activities in 2012, but after public protest, the nation's Parliament ordered a clinical trial of its methods. Italy's health minister, Beatrice Lorenzin, has already said this scientific review needs to proceed as planned. Vannoni could not be reached for comment, but told Italian newspaper *La Repubblica* that the charges were unfounded. **http://scim.ag/_Stamina**



On ice. The U.S. lacks both data and infrastructure to prepare for a major oil spill in its Arctic waters.

Washington, D.C. **3**

U.S. Not Ready for an Arctic Oil Spill

As eagerness to explore the Arctic's oil and gas resources grows, the threat of a major oil spill looms—and the United States has work to do to prepare, a panel convened by the National Research Council declared in a report released on 23 April.

Cleaning up oil in the Arctic is tricky due to extreme weather conditions; the lack of data on bathymetry, ice cover and thickness, and biological populations; and minimal infrastructure. Scientists also lack information about how oil will behave in the region's cold, stratified waters and around sea ice, or how effective chemical dispersants and oil-munching microbes are in that environment. The committee, made up of members of academia and industry, recommended several preparedness strategies, such as beefing up ocean and ice forecasting systems and building infrastructure for cleanup supply chains, as well as conducting field research on oil in the Arctic environment.

Who would coordinate all of this and who would pay for it remain unsettled questions, although the committee recommends a combination of public-private partnerships, interagency coordination, and working with local communities to develop trained local response teams. **http://scim.ag/spillprep**

Washington, D.C. **4**

NSF Oversight Body Joins Critics of FIRST Bill

The presidentially appointed oversight body to the National Science Foundation (NSF) has publicly criticized pending legislation to reauthorize NSF programs.

In a statement released on 24 April, the National Science Board said the Frontiers in Innovation, Research, Science, and Technology (FIRST) Act would "impose significant new burdens on scientists that would

CREDITS (TOP TO BOTTOM): GEORGE STEINMETZ/CORBIS; ATSUSHI TAKETAZU/AP

Published by AAAS

not be offset by gains to the nation … [and] significantly impede NSF's flexibility to deploy its funds." Its comments escalate the yearlong battle between the scientific community and Representative Lamar Smith (R–TX), the chair of the science committee in the U.S. House of Representatives.

The science board objects to what it calls "new, more inflexible, legislated requirements" on how NSF vets grant proposals. But Smith believes such changes are needed to make NSF more accountable. "The NSF wants to be the only federal agency to get a blank check signed by taxpayers, without having to justify how the money is spent," he says.
http://scim.ag/_NSB

London **5**

British Polar Research Ship In the Works

The United Kingdom will invest £200 million in building a new polar research vessel by 2019, Chancellor of the Exchequer George Osborne announced last week. The as-yet-unnamed ship will carry up to 60 researchers deeper into the Arctic and Antarctic than existing U.K. vessels, deploy robotic submarines and underwater gliders, and house extensive onboard laboratories. It



Ship shape. Artist's rendition of the planned ship.

"will be the most advanced oceanographic research vessel in the world," Osborne said during a speech in Cambridge. He added that the new ship will allow scientists to continue their research for more of the year, visit previously inaccessible areas, and "bring back huge amounts of data on the ocean and marine biology."

The United Kingdom's current two polar research ships will be approaching retirement by the end of the decade. The new ship was made possible by a major boost in science capital spending announced by the government last year. Funds for infrastructure will almost double to £1.1 billion for 2015 to 2016 and will rise with inflation.
http://scim.ag/polarship



As the Worm Regrows

Never heard of *Hofstenia miamia*? Well, a few biologists hope the obscure invertebrate (above) will soon worm its way into the hearts of those studying regeneration. Also known as the three-banded panther worm for its striped appearance and voracious appetite, the rice-sized creature can regrow any part of its body. After collecting samples of the worm from a Bermuda pond and confirming anecdotal reports of its regenerative prowess, a team at the Whitehead Institute for Biomedical Research and the Massachusetts Institute of Technology (MIT) in Cambridge spent several years determining the proper conditions to keep it alive in a lab and developing the tools to examine its biology. Many scientists now study flatworms known as planaria that have similar regrowth skills; three-banded panther worms use some of the same molecular pathways to regenerate, even though they are only distantly related, the Whitehead-MIT team reports this week in *Current Biology*. That's evidence, they suggest, that regeneration originated in a common, ancient ancestor of the worms.

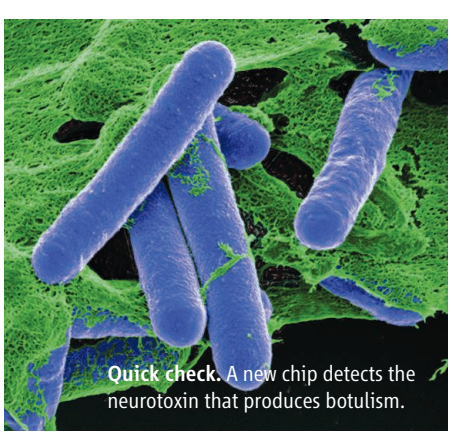
CREDITS (TOP TO BOTTOM): KATHLEEN MAZZA-CURLL AND MANSI SRIVASTAVA/WHITEHEAD INSTITUTE FOR BIOMEDICAL RESEARCH; PETE BUCKTROUT/BRITISH ANTARCTIC SURVEY; GARY GAUGLER/SCIENCE SOURCE

FINDINGS

Botulinum Poison Test Could Save Precious Days

Using a tiny, reactive chip, researchers have developed a quicker and more sensitive test for one of deadliest poisons known to humans. Until now, testing blood samples for botulinum neurotoxin, which causes botulism, has involved injecting a patient's blood into mice, then watching whether they develop symptoms and die.

But a group of French researchers has found a new way to detect the most deadly



Quick check. A new chip detects the neurotoxin that produces botulism.

variant, botulinum neurotoxin A. They knew that the A toxin breaks apart a protein called SNAP-25 that allows nerves and muscles to communicate, so they affixed SNAP-25 to a tiny chip and exposed it to blood containing the toxin. Then they added an antibody that reacts with SNAP-25 only if it has been broken down by neurotoxin A. The chip can detect the toxin in a matter of hours, instead of days, and at much lower concentrations than the mouse test, they report in an upcoming issue of *Biosensors and Bioelectronics*.

Additional labs will need to confirm the test's effectiveness before it will be ready for use in patients. The group is working to expand the test to other botulinum toxin variants. **http://scim.ag/botchip** >>

THEY SAID IT

"I think hell will freeze over before this Congress gives them money."

—UC Davis epidemiologist Garen Wintemute, to ProPublica, on whether the U.S. Centers for Disease Control and Prevention will get new funding to resume gun violence research.

Published by AAAS

>>FINDINGS

Sheep Domestication Caught In the Act

The domestication of plants and animals, beginning about 10,500 years ago in the Middle East, set humans on the road to complex civilization. But archaeologists rarely find evidence of domestication in action. Researchers studying the 11,000-year-old farming site of Aşıklı Höyük in central Turkey, however, traced the settlement's transition from hunting wild animals to herding sheep, thanks to piles of ancient dung.

During the key transition period between hunting wild sheep and herding them, which began about 10,200 years ago and unfolded over several centuries, the sheep were stabled between stone and mudbrick houses, as shown by dung deposits found within the village. The authors, who published their results in the *Proceedings of the National Academy of Sciences* this week, suggest that hunter-gatherers-turned-farmers employed animal herding as a way of resolving the "scheduling conflict" between staying put to tend their fields and roaming afar to hunt wild animals. **http://scim.ag/_sheep**



Housed. Sheep were stabled amid houses.

Random Sample

A World of Plants Comes Into View

Spring is the time to step outside to marvel at local blooms and buds, but an even broader botanical world is just a few taps away. The National Museum of Natural History in Paris has now put online pictures of 6 million plants—almost every species, excluding mosses, lichens, and fungi. "Imaging of a collection this large is unprecedented," says Pamela Soltis, a botanist at the Florida Museum of Natural History in Gainesville.

The Paris herbarium hosts the world's largest natural history plant collection, with 8 million specimens, some dating back to the 17th century. A decade ago, grappling with too little space and about 1 million plants waiting to be sorted and mounted, the curators planned a building overhaul. Given that each plant was going to be handled anyway, they proposed digitizing the collection. The $36 million project included about $15 million for scanning the mounted specimens and for sorting and mounting the unfiled ones, with 200,000 being processed monthly for 30 months in a conveyor belt operation. Though it's been online just over a month, more than 4000 visitors have viewed more than 100,000 images, accessing them by scientific name, geographical region, or barcode.

The botanical project is part of a larger trend. "Digitization—of data and images—is transforming the use of natural history collections," Soltis says. A project called iDigBio has 13 million specimen records, and in the United States, the National Science Foundation has committed $100 million toward digitizing the more than 1 billion specimens in the nation's natural history collections.





MERS Antibodies Identified

Two groups of scientists have identified antibodies against the deadly Middle East respiratory syndrome (MERS) virus, which appears to be exploding in Saudi Arabia (p. 457). The findings could help fight the virus in patients or even prevent new infections with MERS, for which no therapies or vaccines exist.

Wayne Marasco and his team at the Dana-Farber Cancer Institute in Boston screened a library of 27 billion human antibodies and found seven that could block the important spike protein on the viral surface from binding to its receptor on human cells; Linqi Zhang and colleagues at Tsinghua University in Beijing identified two antibodies that do the same. The papers, published in the *Proceedings of the National Academy of Sciences* and *Science Translational Medicine*, respectively, are encouraging, says virologist Bart Haagmans of Erasmus MC in Rotterdam, the Netherlands, but without a good animal model for MERS, testing the antibodies will be challenging. And identifying patients early enough for the treatment to be useful "may be quite difficult logistically."

BY THE NUMBERS

732,000 U.S. deaths prevented since 1994 by the Vaccines for Children program, according to a new estimate from the Centers for Disease Control and Prevention.

4.1% Portion of death row inmates in the U.S. who were falsely convicted, according to an analysis published this week in the *Proceedings of the National Academy of Sciences.* **http://scim.ag/_deathrow**

CREDITS (TOP TO BOTTOM): BY KVAESTAD (OWN WORK) [PUBLIC DOMAIN], VIA WIKIMEDIA COMMONS; (2) © CARLOS MUNOZ YAGUE/LOOK AT SCIENCES

Published by AAAS



Game changer. Worried about MERS, workers wear facemasks at a 22 April soccer match in Riyadh.

CREDITS: (PHOTO) FAYEZ NURELDINE/AFP/GETTY IMAGES/NEWSCOM; (DATA SOURCE) ECDC

EMERGING DISEASES

Soaring MERS Cases in Saudi Arabia Raise Alarms

Scientists are scrambling to make sense of a sharp increase in reported infections with the deadly Middle East respiratory syndrome (MERS) virus. In April alone, Saudi Arabia and the United Arab Emirates have reported over 200 new cases—more than all MERS-affected countries combined in the preceding 2 years. That has sparked fresh fears that the virus may be about to go on a global rampage.

The World Health Organization expressed alarm at the new numbers, and the European Centre for Disease Prevention and Control (ECDC) published an updated risk assessment on 25 April warning European countries to expect more imported cases. Saudi Arabia, meanwhile, replaced its health minister.

The surge has raised concerns that the virus is undergoing genetic changes that might cause it to become pandemic. But none have been identified so far, and several other factors could be to blame, scientists say—from increased testing to sloppy hospital hygiene and a wave of camel births across the region.

Saudi Arabia alone has now reported 345 MERS cases, including 105 deaths, since the start of the epidemic in 2012; most of the new cases are in Jeddah, in the western part of the country. Many worry that mutations in the virus's genome might be making it more adept at spreading between humans—as happened with MERS's distant cousin, severe acute respiratory syndrome (SARS), in 2002 and 2003.

To explore that possibility, virologist Christian Drosten of the University of Bonn in Germany is collaborating with Saudi Deputy Minister of Health Ziad Memish. On 18 April, Drosten's lab received 31 samples taken from Jeddah patients; 29 had tested positive for MERS in two separate PCR tests in a local lab. Drosten's team confirmed the diagnosis for 28 of the samples, suggesting that false positive results—which occur easily with PCR—aren't the problem.

On 26 April, the lab finished sequencing three viral genomes and quickly posted them on the Internet. "These sequences look completely normal," Drosten says. "There is no reason to assume they have acquired changes increasing their pandemic potential."

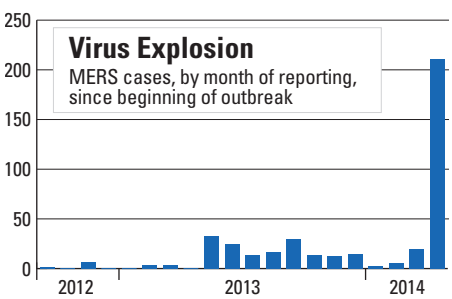
Memish believes the main cause for the surge is increased testing, triggered by growing media attention to MERS. Until recently, only patients with pneumonia who needed intensive care were tested for the virus, he says. "But because of the media hype, people have started coming into emergency rooms and hospitals complaining of mild fever or a cough, demanding to be tested." Doctors have complied, Memish says, leading to more diagnoses, especially of mild cases. Drosten, who was in Riyadh early this week, confirms that the city is on edge: "You see people walking around with facemasks now," he says.

But Denis Coulombier, head of surveillance and response at ECDC, notes that "the proportion of symptomatic to asymptomatic cases is in line with what we have seen previously, so changes in testing do not fully explain the increase we see in April." And Bart Haagmans of Erasmus MC in Rotterdam, the Netherlands, says that it is hard to tell from a sequenced genome whether the virus has undergone adaptive changes. Even in influenza, one of the most studied pathogens in the world, scientists hardly know what mutations to look for, he says.

Drosten believes an additional reason for the spike may be a lack of hygiene in the worst affected hospital in Jeddah, which would help the virus spread between patients and health care workers—although it's unclear exactly what the hospital is doing wrong.

Camels may also play a minor role in the explosive rise. Scientists have shown that many dromedary camels in the Middle East and Africa harbor the virus, and in recent months, camels at breeding facilities have given birth en masse, as they do every winter. The offspring may act as natural virus incubators, increasing the risk that humans become infected.

Drosten's data reinforce the idea that MERS is repeatedly crossing the species barrier between camels and humans, says evolutionary biologist Andrew Rambaut of the University of Edinburgh in the United Kingdom. The three genomes Drosten posted this past weekend are most closely related to one isolated from a Qatari patient who was treated in England in September 2012, Rambaut says. There is no known connection between the cases in Qatar and Jeddah, and given that so many camels are infected, it is much more likely that a virus with this sequence crossed to humans twice—once in Qatar and again at the start of the Jeddah cluster—than that the virus passed through a chain of unknown human patients, he says.



Such jumps from camels to humans "will just continue happening until the exposure to camels is reduced," Rambaut says. The question is how to do that, because it's unclear how the virus crosses from camels

Published by AAAS

to humans. One route could be unpasteurized camel milk, consumed widely in the Middle East; scientists at the U.S. National Institute of Allergy and Infectious Diseases recently showed that the virus is stable for at least 72 hours in raw camel milk. Haagmans hopes to test camel urine and milk from the region for the virus soon. Contaminated meat could also play a role. Another, less likely possibility is that the virus is transmitted through the air. Virus excreted by camels could cling to dust particles, for instance, and infect humans who inhale it.

Some answers may come from Qatar. Researchers there have teamed up with Marion Koopmans and other scientists at Erasmus MC for the biggest study by far of how MERS spreads. The team plans to sample camels and other animals, as well as humans, at about 500 farms to look for the virus and antibodies against it; 80 people have been trained to question farm workers in detail about their behavior, and Koopmans says she has shipped more than 45,000 labels for samples to Qatar. "We really have to step up our efforts to understand what is going on," she says. **–KAI KUPFERSCHMIDT**

ENERGY TECHNOLOGY

Perovskite Solar Cells Keep On Surging

SAN FRANCISCO, CALIFORNIA—The hottest solar cell materials are on the march again. At a meeting here last week, three research groups reported besting the previous efficiency record in cheap, easy-to-make crystalline materials called perovskites. One group's cells turn just shy of 20% of incoming solar energy into electricity. That's up from 16.2% efficiency reported in February and 3.8% just 5 years ago. Few solar technologies have ever improved so much, and none has done it so fast.



Electrifying view. Solar cells called DSSCs already double as windows.

"These are exciting times," says Edward Crossland, a physicist at Oxford Photovoltaics, a United Kingdom–based company working to commercialize perovskite-based solar technology. "There are new ideas coming out all the time." Numerous solar experts say the impressive properties of perovskites could ultimately boost efficiencies as high as 25% in individual devices—as good as today's commercial champions, made of costly single-crystal silicon. Layering perovskite cells on top of conventional solar cells to make "tandem" cells could push the efficiency up to 32%. That could make solar electricity as cheap as electricity produced from coal or natural gas, according to estimates from the U. S. Department of Energy.

Perovskite minerals have been known for nearly 2 centuries. But their ability to convert the energy in sunlight to electricity was discovered only in 2009, when Tsutomu Miyasaka at Toin University of Yokohama in Japan added them as a sunlight-absorbing layer to devices called dye-sensitized solar cells (DSSCs), achieving an efficiency of 3.8%. Researchers quickly realized that perovskites are good not only at capturing sunlight but also at ferrying electric charges.

As scientists began tinkering, efficiencies shot upward (*Science*, 15 November 2013, p. 794), and they haven't stopped since. At the Materials Research Society meeting last week, Yang Yang, a materials scientist at the University of California, Los Angeles, reported that his group has made perovskite solar cells with an efficiency of 19.3%. Yang offered few details about how his group created the cells. But he said the team has focused on growth techniques that limit defects in perovskite crystals and on improving the interfaces between different material layers in the devices. Defects and interfaces commonly trap electrical charges, preventing them from reaching the electrodes, says Nam-Gyu Park, a chemist with Sungkyunkwan University in Suwon, South Korea. Improved crystal growth methods helped Park's own group achieve an efficiency of 17.01% in perovskite solar cells.

Pairing perovskites with mainstream materials has also yielded advances. Michael McGehee, a materials scientist at Stanford University in California, reported that his group made 18.6% efficient tandems in which perovskites sit atop alloys of copper, indium, gallium, and selenium (CIGS). CIGS cells by themselves are 17% efficient, so in this case the perovskites didn't add much. That's probably because the perovskites' electrodes and other non–light-absorbing layers block much of the sunlight from reaching the CIGS cell beneath, McGehee says. That problem should be relatively easy to solve, he says: Because perovskites absorb bluer wavelengths of light than CIGS and crystalline silicon cells do, simply combining both light-absorbing layers between one set of electrodes should improve matters. "There's a straightforward path to go well above 20% efficiency," McGehee says.

The low cost of perovskites could give them an edge even if they don't reach such heights of efficiency. Oxford Photovoltaics, for example, is working to make window-based perovskite photovoltaics (PVs). Window PVs using DSSCs have been on the market for years, and perovskites could improve their efficiencies. Most perovskite cells made so far, however, have a brownish hue—"a tough sell" to architects who design skyscrapers, Crossland says. But at the meeting, Giles Eperon of the University of Oxford reported that by fashioning the perovskite as an array of tiny islands instead of a continuous film, he and colleagues created a neutral-colored semitransparent perovskite cell with 8% efficiency. If 6% efficient window PVs were used to cover a building the size of the Willis Tower in Chicago, the glass alone would generate nearly 5.3 gigawatt-hours of energy per year, Crossland says.

Not for long, however: For now, the materials break down when exposed to moisture. Although several teams reported that they can now get their cells to survive for hundreds of hours, albeit at lower efficiencies, "it's still very early days for this technology," Yang says.

–ROBERT F. SERVICE

CREDIT: © RDR/FERNANDO GUERRA

Published by AAAS



Friendly nudge. Drones are used to drive elephants from inhabited areas.

WILDLIFE CONSERVATION

Drones Flying High as New Tool For Field Biologists

MARA NORTH CONSERVANCY, KENYA—James Ekale Ekiru furrows his brow, straining to hear the rustle of elephants grazing in distant thickets. About 3000 of the animals are scattered across the Maasai Mara, an area of more than 2600 square kilometers north of the Serengeti plains. They aren't easy to spot on this sprawling forested ranch, but conflicts with villagers are all too common—and can end badly for both elephants and people. Once Ekiru, a Turkana tracker, has drawn a bead on the herd, Marc Goss, who leads the Mara Elephant Project, attempts to drive them out of the woods. First he pursues the stampeding elephants by Jeep. Then he deploys a new tool: a four-blade remote-controlled helicopter.

With a smart phone, he sends the quadricopter Parrot AR.Drone zigzagging above our heads. When elephants hear the buzz of a drone, they think bees, which sting the sensitive inner lining of their trunks. This time, the elephants are too far away to be frightened by the drone. Goss will have to try again later in the week to drive the herd back to the relative safety of a wildlife preserve.

Field biologists like Goss are flocking to drones. Also known as unmanned aerial vehicles (UAVs), drones are becoming an essential tool for managing wildlife and fighting poachers. Price tags are no longer the chief consideration: The Parrot drone Goss uses costs $300; more rugged and longer flying drones run up to several thousand dollars. UAVs have recently been used to monitor tigers in Nepal, spot whales off Japan, and count orangutan nests in the Sumatran rainforest. Before long, UAVs "will be as essential as a pair of binoculars," predicts Lian Pin Koh, a conservation ecologist at the University of Adelaide in Australia. In 2012, Koh co-founded a nonprofit called ConservationDrones to build capacity in the tropics for using UAVs for conservation; the outfit, with the Jane Goodall Institute, will run a drone training workshop next month in Washington, D.C.

Already, UAVs are proving far more versatile than binoculars. In South Africa, for example, drones are being deployed in Olifants West conservancy to curtail rampant poaching of rhinos for their horns, which are ground into traditional Asian medicines and can fetch up to $250,000 each. The project is the brainchild of Thomas Snitch, a computer sciences professor at the University of Maryland, College Park, who developed algorithms to help the U.S. military in Iraq predict where insurgents were likely to plant roadside bombs. Snitch realized that the same sort of number crunching, combined with drones, could help rangers intercept poachers.



Modern tracking. Mara project co-founders Iain Douglas-Hamilton, Richard Roberts, and team GPS-collaring an elephant.

Snitch developed computer programs that draw on data including the weather, the phase of the moon, the type of terrain, and the typical behavior of poachers and rhinos to direct UAVs where to fly. Drone surveillance has led to arrests in the conservancy and serves as a powerful deterrent. "Poachers know now that they can be seen at night," Snitch says. "Most have left the area." Drone deployment is slated to expand soon to neighboring Kruger National Park.

For protecting elephants, drones "will give a direct tactical advantage to antipoaching forces," says Kenyan conservationist Iain Douglas-Hamilton, who pioneered the use of GPS collars and satellite imagery to track elephants. Burgeoning demand for ivory in China and Southeast Asia has fueled a spike in poaching; about 35,000 elephants were slaughtered in 2012, according to the Wildlife Conservation Society, and that number is believed to be rising. Poaching outstrips the reproductive rate of elephants in many areas, Douglas-Hamilton says. "When over six of 10 of all elephant mortalities are caused by poaching," he says, "the species is in trouble." While the technology is no panacea, drones should also lead to more accurate censuses and maps of migration corridors that can help managers steer elephants away from conflicts with villagers.

"Farmers and elephants don't mix," Goss says, pointing to a patchwork of beehive huts and newly planted maize fields on the edge of the bush. "The animals can move in here and trample crops. People here have few economic incentives to protect elephants and expose the poachers operating in their midst." Goss plans to equip his drones with thermal imaging cameras to spot poachers at night. But before the poachers can be defeated, he says, he needs to persuade local people that elephants are something more than a menace—and if the buzz of a drone can help, he is more than happy to try.

–RICHARD SCHIFFMAN

Richard Schiffman is a writer based in New York City.

CREDITS: COURTESY OF THE MARA ELEPHANT PROJECT (2)

Published by AAAS

DEFENSE SCIENCE

As Pentagon Downsizes, Budgets Shrink for Academic Research

A planned squeeze on academic science by the U.S. military—part of its long-term efforts to downsize—has triggered concerns in university research offices and in Congress.

"It seems like as we reduce basic research … we're really hurting ourselves," Senator Kay Hagan (D–NC), the head of an armed services subcommittee that oversees military science, told a panel of Pentagon research chiefs at an 8 April hearing.

None of the research chiefs disagreed. The Department of Defense (DOD) has largely shielded basic science budgets from cuts over the past few years, they noted, despite an overall budget that is shrinking as the United States withdraws from wars in the Middle East. But tighter spending limits mean focusing on more immediate needs, the military officials told legislators. It's "not that we don't like university research. We love university research," Alan Shaffer, a top DOD research official, told Hagan. "But given the constraints … we wanted to push more money" into more applied projects that are closer to fruition, he said.

Overall spending on defense science and technology would drop by 5.5% to $11.51 billion under the president's proposed budget for the 2015 fiscal year that begins 1 October. The basic research portion of that total—known as the 6.1 budget line—would take the biggest cut, falling 6.9% to about $2 billion (see table). University researchers receive about one-half of that total in the form of grants, with the rest going to researchers in the military's own labs.

The current cap on domestic spending provides Congress with little flexibility to move money around, and few observers believe it will substantially revise the Pentagon's plan. The cuts will be particularly painful because universities have become more dependent on the Pentagon for research and development dollars. DOD accounted for 12.3%, or about $5 billion, of the $40.1 billion in federal dollars that academia spent on R&D in 2012, up from about 8% a decade ago. The Pentagon now provides about one-half of the research funding in electrical, materials, and aeronautical engineering, about one-third in computer science, and one-fifth in math and physics.

The $150 million reduction in DOD's core basic science budget "will cut about 1500 grants nationwide, give or take," Shaffer told the Senate armed services panel, assuming an average of $100,000 per grant. "That's a lot of university grants that are coming out."

The actual number may be lower if in-house military labs share the pain. But "it is likely that more of the reduction will come out of extramural grants than intramural programs [because] it's easier to reestablish grants than staff," says James Murday, a veteran of the Navy's basic science programs who is now an associate director of the University of Southern California's Washington, D.C., office.

University administrators have begun looking for ways to replace those DOD dollars. But the pickings are slim: The external research budgets at other agencies that fund similar work, such as the Department of Homeland Security and NASA, are also slumping. And industry usually shuns the relatively risky projects that Pentagon program managers often favor. As a result, Murday says, the defense cuts could increase competition for one of the main alternatives—the National Science Foundation's engineering and math programs.

Despite DOD's belt-tightening, Pentagon officials are planning new basic science initiatives in 2015 with money freed up by expiring grants and programs. The Defense Advanced Research Projects Agency (DARPA), whose 2015 budget would remain flat, plans to spend more than $60 million on an array of fresh programs, including efforts to develop materials inspired by biological systems and faster quantum computers.

Such projects reflect DOD's studied effort to balance current needs with the potential for future payoffs, says DARPA Director Arati Prabhakar. A former DARPA program manager who went to Silicon Valley and then returned to lead the agency in the summer of 2012, Prabhakar told the Senate panel that she initially worried that tighter spending would force DARPA to abandon riskier projects in favor of more "incremental" and practical studies. But "in fact I think it's the opposite," she said, because tighter budgets place a premium on making major breakthroughs.

That spirit will be tested in the years ahead. The Obama administration projects a shrinking DOD budget for at least another few years. That pattern means "at best, level funding for basic research, with some loss to inflation," Murday predicts.

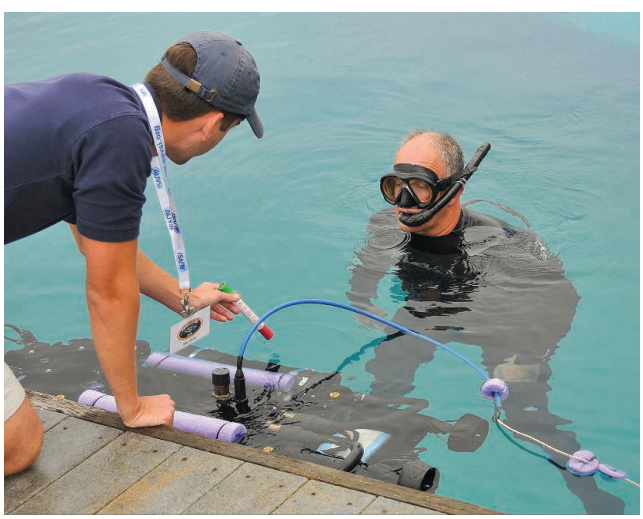
One Pentagon science program likely to see few cuts in 2015 is a special biomedical research account created by Congress in 1992. Lawmakers use the Congressionally Directed Medical Research Programs to steer funding to specific disorders, including cancer and autism. The grants—some $500 million annually in recent years—are awarded through open competitions. Some lawmakers would like the funding to go to the National Institutes of Health, but so far that argument hasn't been persuasive to their colleagues.

–DAVID MALAKOFF

Pentagon Wants to Trim Science Spending

($ billions)

	2014	2015 request	% change
Technology development	$5.375	$5.040	–6.2%
Applied research	$4.643	$4.457	–4.0%
Basic research	$2.167	$2.018	–6.9%
Army basic	$0.436	$0.424	–2.8%
Navy basic	$0.619	$0.576	–6.9%
Air Force basic	$0.525	$0.455	–13.4%
DARPA basic	$0.365	$0.362	–0.8%



Sinking. Academic research programs, such as this 2011 "robosub" competition sponsored by the U.S. Navy, are squeezed in the 2015 budget.

CREDITS: (DATA SOURCE) DEPARTMENT OF DEFENSE; (PHOTO) U.S. NAVY PHOTO BY RICK NAYSTATT/RELEASED

Published by AAAS

ANIMAL RESEARCH

Male Scent May Compromise Biomedical Studies

Jeffrey Mogil's students suspected there was something fishy going on with their experiments. They were injecting an irritant into the feet of mice to test their pain response, but the rodents didn't seem to feel anything. "We thought there was something wrong with the injection," says Mogil, a neuroscientist at McGill University in Montreal, Canada.

The real culprit was far more surprising: The mice that didn't show pain had been handled by *male* students. Mogil's group discovered that this gender distinction alone was enough to throw off their whole experiment—and likely influences the work of other researchers as well.

"This is very important work with wide-ranging implications," says M. Catherine Bushnell, a neuroscientist and the scientific director of the Division of Intramural Research at the National Center for Complementary and Alternative Medicine (NCCAM) in Bethesda, Maryland. "Many people doing research have never thought of this."

Mogil has studied pain for 25 years. He's long suspected that lab animals respond differently to the sensation when researchers are present. In 2007, his lab observed that mice spend less time licking a painful injection—a sign that they're hurting—when a person is nearby, even if that "person" is a cardboard cutout of Paris Hilton. Other scientists began to wonder if their own data were biased by the same effect. "There were whisperings at meetings that this was confounding research results," Mogil says.

So he decided to take a closer look. In the new study, Mogil told the researchers in his lab to inject an inflammatory agent into the foot of a rat or mouse and then take a seat nearby and read a book. A video camera trained on the rodent's face assessed the animal's pain level, based on a 0- to 2-point "grimace scale" developed by the team. The results were mixed. Sometimes the animals showed pain when an experimenter was present, and sometimes they seemed just fine. So, on a hunch, Mogil and colleagues recrunched the data, this time controlling for whether a male or a female experimenter was present. "We were stunned by the results," he says. The rodents showed significantly fewer signs of pain (an average of a 36% lower score on the grimace scale) when a male researcher was in the room than when a female researcher—or no researcher at all—was there.

Thinking back to his Paris Hilton experiment, Mogil wondered whether the rodents were responding to the sight of a woman or man or to something more subtle. So he told the people in his lab to place their worn T-shirts near injected animals and then leave the room. Even when the humans weren't present, the results were the same. Rats and mice showed about a 36% lower score on the grimace scale when exposed to male versus female T-shirts, the team reported online this week in *Nature Methods*. (Female mice were slightly more sensitive to the effect.) Placing a woman's T-shirt next to a man's T-shirt negated the impact. Bedding material from unfamiliar male mice and guinea pigs, as well as pet beds slept in by unsterilized male cats and dogs, produced the same response: Male odors seemed to act like painkillers.



What's that smell? The presence of a male scientist can influence research results.

CREDIT: ALEXANDER H. TUTTLE

Further testing showed that the rodents exposed to male odors were actually feeling less pain, rather than simply hiding the pain they were in. The male aroma ramped up their stress levels, which deadened the hurt. "It's really astounding that such a robust effect could have been missed for so many years," Mogil says.

He suspects the rodents are reacting to scent chemicals that male mammals have produced for eons. "It's a primordial response," he says. "If you smell a solitary male nearby, chances are he's hunting or defending his territory." If you're in pain, you're showing weakness.

Almost every animal behavior studied in the lab, from the effectiveness of experimental drugs to the ability of monkeys to do math, is affected by stress, notes Paul Flecknell, a veterinary anesthesiologist at Newcastle University in the United Kingdom who researches ways to alleviate pain in animals. "This could have an impact on just about everything."

Male odor could even influence human clinical trials. If a male doctor injects you with a new kind of pain medication, do you feel better because of the drug—or because of his gender? "It's not an unreasonable concern," Flecknell says.

The findings may also suggest why some labs have trouble reproducing the results of other groups. "Sometimes pharmaceutical companies can't replicate preclinical work," says Bushnell, who came to NCCAM to develop a pain research program. "This could help explain that."

Still, Mogil doesn't think scientists need to redo decades of animal research. "It's a confounding factor, but not a fatal one," he says. But going forward, he advises, researchers should pay more attention not to just what experiments they're doing, but also to *who's* doing the experiments. "I joke that the solution is to fire all the male researchers," Mogil says. "But at the very least, this is something teams should be noting in the methods sections of their papers. We can change the bath water without throwing out the baby." **–DAVID GRIMM**

Published by AAAS

STEM CELLS

Therapeutic Cloning Reaches Milestone

Last week stem cell researchers finally reached a goal that has eluded them through more than a decade of setbacks and scandal. Two teams have independently derived human embryonic stem cells by cloning adult skin cells. The promise of the technique remains tantalizing: replacement tissues for treating diseases from diabetes to Parkinson's, matched to the patient whose cells gave rise to them. But the practical, ethical, and legal hurdles are as high as ever. The method will also have to prove its worth against a strong competitor: a way to make personalized stem cells that doesn't involve embryos.

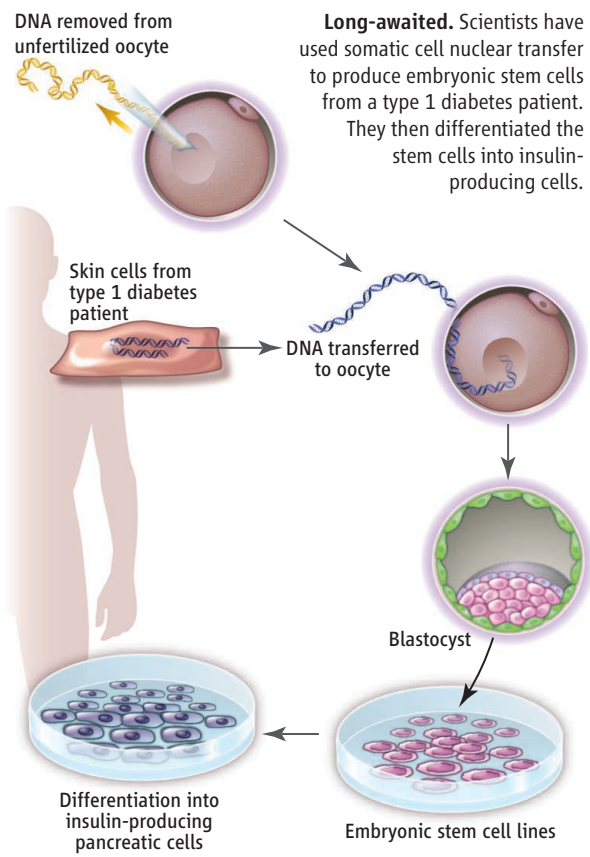
The cloning technique, called somatic cell nuclear transfer (SCNT; see diagram), gained fame with the cloning of Dolly the sheep 18 years ago. Scientists soon learned to use SCNT to clone cattle, mice, dogs, and other animals. Researchers eagerly set out to clone human cells—not to replicate humans, which most scientists strongly oppose, but to generate early human embryos from which stem cells could be harvested. Although a decade ago a South Korean scientist fraudulently claimed success, human cells proved resistant to cloning.

A year ago, Shoukhrat Mitalipov and his colleagues at the Oregon National Primate Research Center in Beaverton finally used SCNT to produce stem cell lines from the DNA of human fetal and infant cells (*Science*, 17 May 2013, p. 795). But it wasn't clear whether the team's tricks would work with cells from human adults.

On 17 April, Dong Ryul Lee and Young Gie Chung of CHA University in Seoul and their colleagues settled that question, reporting in *Cell Stem Cell* the creation of embryonic stem (ES) cell lines from skin cells of two men, one 35 years old and one 75 years old. And on 28 April online in *Nature*, Dieter Egli of the New York Stem Cell Foundation (NYSCF) Research Institute in New York City and his colleagues describe going a step further, making ES cells from a 32-year-old woman who has type 1 diabetes. They then prompted the ES cells to become insulin-producing cells, which are missing in people with the disease.

Egli says that he and his colleagues have put the insulin-producing cells into mice, where they produced the hormone in response to blood glucose levels. (That work is still unpublished.) "We are now one step closer to being able to treat diabetic patients with their own insulin-producing cells," he says.

Whether such personalized replacement cells would help, especially in the long run, remains uncertain, however. They would likely fall prey to the same autoimmune attack that killed a person's original insulin makers, other scientists caution. Obtaining the human oocytes needed to treat the millions with type 1 diabetes via SCNT would also pose a major obstacle. Because extracting eggs from women causes discomfort and poses health risks, both groups paid the standard rate that egg donors for in vitro fertilization procedures receive—in the United States, up to $10,000. Given fair compensation, many women are willing to donate oocytes, Egli maintains. But spurred by ethical worries about undue pressure on women, many organizations and governments prohibit paying egg donors. That includes the California Institute for Regenerative Medicine, a major funder of stem cell research, which put these cells off-limits for its many grantees. Susan Solomon, co-founder and CEO of the privately funded NYSCF that funded Egli's work, predicts that if the technique proves useful to create effective therapies, friends or relatives of someone sick will be willing to donate oocytes.



Long-awaited. Scientists have used somatic cell nuclear transfer to produce embryonic stem cells from a type 1 diabetes patient. They then differentiated the stem cells into insulin-producing cells.



Proof of principle. Human embryonic stem cells derived from a type 1 diabetes patient.

Although early attempts at human SCNT used hundreds of oocytes, Egli says his team's method is now efficient enough to derive a stem cell line from a single egg donation cycle, which usually produces between 15 and 20 oocytes. All three groups found that efficiency seems to depend heavily on the quality of the eggs used, with those from younger donors superior to those from older ones.

Legal issues still constrain SCNT. Many governments forbid or otherwise restrict its use with human cells. In the United States, no federal funding can be used for research that harms or destroys a human embryo, so scientists must set up separate lab space that does not use any National Institutes of Health or other federal grant money. Several U.S. states have banned all human SCNT research.

The political energy needed to overturn those laws might be hard to generate given that there's now an embryo-free alternative to producing patient-specific stem cells. By ramping up the production of a handful of genes, researchers can reprogram mature cells into embryolike ones. These induced pluripotent stem (iPS) cells are already widely used to study disease, and the first clinical trial with them to treat macular degeneration is under way in Japan. But some scientists worry that iPS cells have flaws of their own. Several studies have found that the reprogramming process is often incomplete, leaving iPS cells with molecular traces of

Downloaded from www.sciencemag.org on May 1, 2014

CREDITS: (ILLUSTRATION) K. SUTLIFF/*SCIENCE*; (PHOTO) BJARKI JOHANNESSON, NYSCF

Published by AAAS

the mature cell they came from. (In mouse experiments, SCNT-derived ES cells seem to have fewer traces of their original cells than iPS cells do.) Researchers are not yet sure if the subtle differences are important to the cells' later behavior.

Complicating the comparisons, significant differences exist among iPS cell lines—and perhaps among SCNT-produced ES cells as well. "An open question is, which iPS cells should be the ones to compare to?" says Juan Carlos Izpisua Belmonte of the Salk Institute for Biological Studies in San Diego, California. Careful comparisons could help scientists find more effective ways to make patient-specific cells, whether with oocytes or with other approaches, says Ian Wilmut of the University of Edinburgh in the United Kingdom.

The ability to compare the approaches in human cells is key, says Doug Melton of the Harvard Stem Cell Institute. "The only way to find out is to do these experiments."

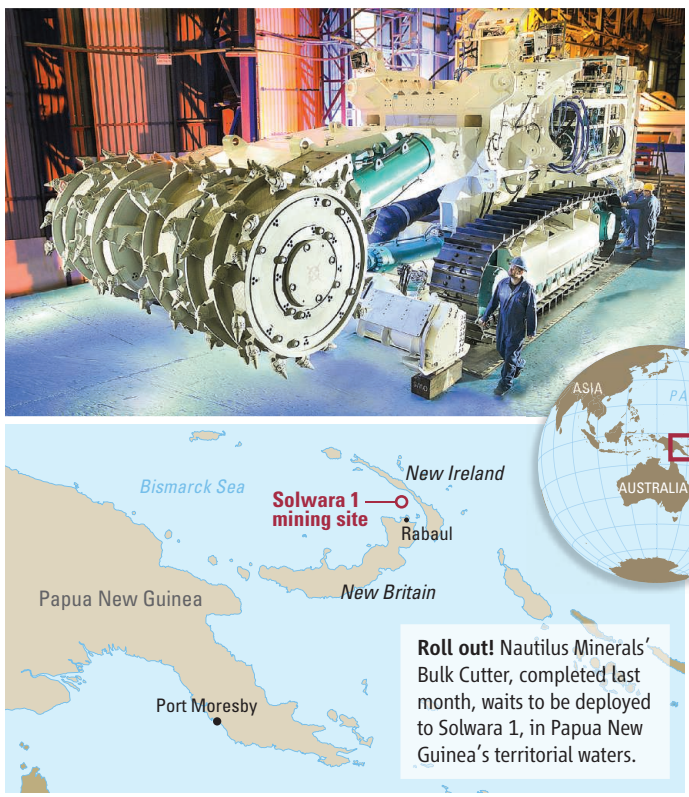
–GRETCHEN VOGEL

ECONOMIC GEOLOGY

Seafloor Mining Plan Advances, Worrying Critics

If all goes as planned, the world's first commercial deep-sea mine will open for business in 2016, with engineers deploying a trio of robots to claw high-grade copper and gold ore from the sea floor 1500 meters down off Papua New Guinea (PNG). Last week, after years of dickering, PNG's government and Canada-based Nautilus Minerals signed an agreement to move forward with the ambitious project. "We were very happy" to get the deal done, says Nautilus CEO Mike Johnston.

Critics aren't so pleased. Some marine biologists worry the mining will start before researchers can assess how it will affect deep-sea ecosystems. Others argue that national and international regulators aren't ready to ensure that underwater miners protect the environment. "The environmental impacts are unknown [and] the mining system is completely untested," said Effrey Dademo of ACT NOW!, a PNG group opposing the mine, in a statement.



Roll out! Nautilus Minerals' Bulk Cutter, completed last month, waits to be deployed to Solwara 1, in Papua New Guinea's territorial waters.

CREDIT: (PHOTO) NAUTILUS MINERALS

For decades, such debates were largely academic, because mining at depths greater than 1000 meters was considered economically unworkable. But as technology advanced, Nautilus and other companies began prospecting. In some locations, the sea floor is littered with polymetallic nodules—hard, round masses of rock slowly precipitated from seawater and bearing iron, manganese, nickel, and other metals—that miners could scoop up with relative ease. In others, mineral-laden water gushing from hydrothermal vents has created rich outcrops. Although the vents are harder to mine, the payoff can be greater, because the deposits can include both precious metals and rare earth elements critical for computers, cellphones, and other modern technologies.

For its project, Nautilus has targeted a vent site known as Solwara 1, located near seafloor cracks created as two tectonic plates pull apart. Superhot fluids spew from deep in the crust, mixing with the cold seawater to form towers of ore-laden sediment known as "black smokers." Company surveyors say the area, covering about 11 hectares, is particularly rich in copper and gold.

It is also home to many kinds of sea creatures, including tubeworms and bivalves, according to environmental impact studies sponsored by Nautilus. But the company says it can mine without doing much long-lasting damage, in part by taking steps to control sediment plumes and relocate animal communities. The "overall effects [will be] reversible and moderate," says a 2008 company study, which predicts that seafloor populations would rebound within a few years after mining ended.

Opponents are skeptical, with some saying they doubt that the PNG government—which has a 15% stake in the project—has the technical expertise to conduct adequate and independent oversight. Oceanographer Cindy Van Dover of Duke University in Durham, North Carolina, who helped Nautilus conduct some of its preliminary studies, concedes that "there's no way to know what the impact" will be. Doing the studies that some scientists would like to see completed before mining begins would be expensive, she notes, with sustained seafloor research costing $80,000 a day or more. There are no concrete plans for major new environmental impact studies. "I don't know how to get to that happy place where the scientific community will let the mining go on and be confident that we will get the right amount of science," she says.

In the meantime, Nautilus says it plans to move ahead with outfitting a vessel to deploy its mining robots, including a 300-ton behemoth that will chew through the sea floor, and another that will pump a slurry of mineral-rich ore to the surface. It hopes to be operating within 30 months, Johnston says.

Nautilus may soon have company. Other nations, including Fiji, are negotiating seafloor mining rights. And the United Nation's little-known International Seabed Authority, based in Kingston, has already issued 19 permits for prospecting in international waters.

–CAROLYN GRAMLING

Published by AAAS

Death of the Stars

The biggest known die-off of sea stars is sweeping North America's coastal waters. Researchers are hurrying to identify the culprit and understand the impacts

THE SEATTLE AQUARIUM SITS ON PIER 59, ABOVE THE COLD, DARK waters of Puget Sound. As children run inside its wood-beamed atrium, Lesanna Lahner peers into the largest display tank. A few salmon swim idly past barren rocks. "This used to be full of sea stars," says Lahner, the aquarium's veterinarian. No more. The five-armed echinoderms, sometimes known as starfish, are victims of a mysterious wasting syndrome that has ravaged the east and west coasts of North America.

Lahner first heard the apocalyptic reports from recreational divers this past October. Sea stars were dying in droves in nearby coastal waters. The deaths were grisly. White lesions appeared, then the bodies sagged, ruptured, and spilled organs. Alarmed, Lahner sent divers to investigate what was happening under the aquarium's pier. About 40% of the sea stars appeared sick, some barely clinging to pilings with drooping arms. By November, all three species that typically live under the aquarium had vanished. "We've seen sea star deaths wax and wane, but never on this scale," Lahner says.

Sea stars in the display tanks, which draw water from the sound, also became ill. Lahner isolated the sick, moving them to quarantine tanks. She monitored their slackening heartbeats with an ultrasonic device. She called the author of the textbook *Invertebrate Medicine*, which has just one paragraph on treating sea stars and other echinoderms, for help. "Sorry," was all he could say. Lahner tried antibiotics, but they were useless. Sea stars collapsed and liquefied in the blue plastic tubs. Others flailed, pulling off their own arms, which eerily crawled around. With growing horror, Lahner began euthanizing any sea stars that showed severe lesions.

Some of those dead stars now rest in Lahner's office, their remains preserved in carefully labeled jars. She has mailed samples to pathologists and geneticists, who are rushing to understand the most widespread disease outbreak ever documented in any echinoderm. There is little time to waste, as the epidemic could burn out—making it harder to identify the pathogen. "A lot of people are scrambling," says ecologist Benjamin Miner of Western Washington University (WWU) in Bellingham, who is surveying the coast and conducting experiments in his lab.

Meanwhile, concern grows. The plague is ravaging perhaps 20 kinds of sea stars along thousands of kilometers of coastline. Some west coast species could even go extinct, biologists fear. "The magnitude of the potential loss to invertebrate biodiversity is so overwhelming," says ecologist Drew Harvell of Cornell University. The loss of sea stars, a top predator in much of the coastal ocean, may also shuffle food webs, testing a classic ecological theory in a long-term, real-world experiment. It could be decades before populations recover, Harvell notes, and sea stars again become the iconic species of the intertidal.

Disaster foretold

When novelist John Steinbeck and biologist Edward Ricketts took a now-famous expedition into the Gulf of California in 1940, the gulf sun star (*Heliaster kubiniji*) was everywhere. Pounded by waves, the black-and-green mottled echinoderms "simply increase their tough-

Lucky star. This leather star has escaped a deadly wasting syndrome—so far.

CREDIT: JAN KOCIAN

Published by AAAS

ness and fight back at the sea with a kind of joyful survival," Steinbeck marveled in *Sea of Cortez: A Leisurely Journal of Travel and Research*.

But the gulf sea star was no match for an enigmatic disease that arrived in the summer of 1978. White lesions spread and populations crashed. The sick and dead animals were coated with bacteria, but researchers weren't sure if they were the culprit or just a secondary infection. The outbreak, researchers suggested, was likely related to strong winds that brought warm water into the gulf (*Science*, 28 May 1982, p. 989). "The thought in the 1980s was that this was a one-time thing," recalls Peter Raimondi, a marine ecologist at the University of California (UC), Santa Cruz.

They were wrong. In 1997, disease struck again. This time, the damage was concentrated off southern California, where an El Niño climate pattern had brought exceptionally warm Pacific waters. At the time, ecologist John Engle of UC Santa Barbara was studying intertidal communities in the Channel Islands, off Santa Barbara. As the stars died, he got a powerful lesson in how their loss can remake marine ecosystems.

Despite their torpid appearance and benign reputation, sea stars are fearsome predators—"the lion of the intertidal," says Bruce Menge of Oregon State University, Corvallis. Even a small star can rip barnacles or limpets from rocks using the hydraulic system that powers its many tube feet. When prying apart mussel shells, some stars evert their stomach, sliding it inside the shell to digest their prey. Unlike other kinds of animals, echinoderms can stiffen their connective tissue for extra power, some in less than a second. And although sea stars aren't known for speed, the sunflower sea star (*Pycnopodia helianthoides*) can hustle along at more than a meter per minute, thanks to the thousands of tube feet beneath its 16 or more arms, and even catch fish. If food is scarce, sea stars easily resist starvation. They just shrink.

When these predators vanish entirely, however, life turns upside down. During the starfish plague of the late 1990s, Engle recalls watching some of *Pycnopodia*'s former prey, sea urchins, run wild around the Channel Islands. The urchins overgrazed the giant kelp forests, in turn distressing fish that liked to settle into the kelp canopy to find food and refuge. For the most part, sea star populations in southern California never rebounded, Engle says. "The whole system really changed."



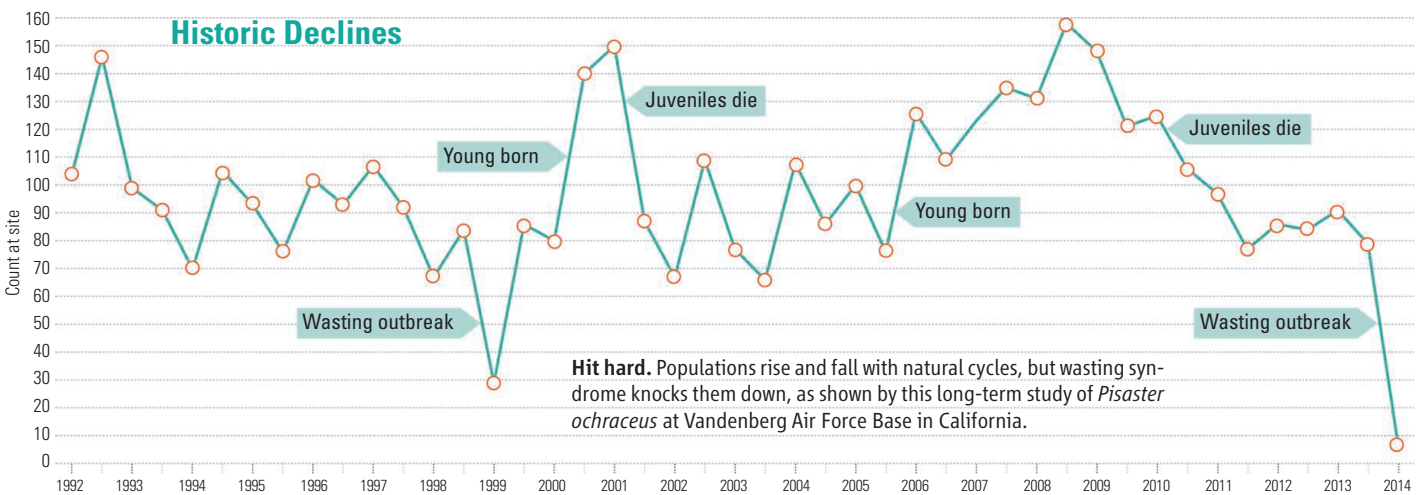
Losing grip. Deeper water species, like this Stimpson's sun star in Washington state, were among the first to succumb, with arms drooping and detaching.

CREDITS (TOP TO BOTTOM): JAN KOCIAN; (DATA SOURCE) PACIFICROCKYINTERTIDAL.ORG

Falling stars

In June 2013, biologists at Olympic National Park in Washington state noticed something odd in the waters off a scenic landmark called Starfish Point. More than a quarter of the point's namesakes were dotted with lesions or other signs of illness. The report might have gone unnoticed except for a scientific consortium—called the Multi-Agency Rocky Intertidal Network (MARINe)—that Engle and other researchers helped cobble together in 1997. With a shoestring budget for database operations, MARINe's mission is to keep tabs on the health of near-shore ecosystems, using standardized methods. After the report from Olympic National Park, MARINe collaborators agreed to quickly check on their roughly 200 sites along the west coast.

By August, the white lesions had been spotted on starfish as far north as Alaska. In British Columbia, divers reported that abundant populations of sea stars had been reduced to ghostly piles of bony white ossicles. "It was hideous," says Jeffrey Marliave, vice president of marine science at the Vancouver Aquarium in Canada. By November, the syndrome was present at more than half of



Hit hard. Populations rise and fall with natural cycles, but wasting syndrome knocks them down, as shown by this long-term study of *Pisaster ochraceus* at Vandenberg Air Force Base in California.

Published by AAAS



Patchy. Wasting syndrome appears concentrated in the north and south, but has started to appear in Oregon as well. Map does not show outbreaks in Alaska or along the east coast.

84 surveyed sites, as far south as San Diego. Citizen scientists checked out more than 300 other locations, with similar results. Mortality ranged up to 100%. Thanks to MARINe, the west coast outbreak has become "the best tracked marine event we've ever had," Raimondi says.

There are many strange things about the outbreak. Past episodes in the west have been associated with warmer coastal waters, but recently those waters have been relatively cool. And this time, a similar sea star disease appears to be spreading along North America's eastern coast as well. Because there is no equivalent monitoring network in the east, the reports have been largely anecdotal. So far, observers have described severe and rapid die-offs in Maine, Connecticut, Massachusetts, and Rhode Island.

Researchers are wondering how the disease has managed to infect so many species, and why they succumb in a particular order—first the sunflower sea stars and giant pink sea stars, then bat stars. Nor do they understand why the western outbreak started in the north and moved south, the opposite of past events. And why have populations in Washington and California suffered intensely, while those in Oregon seem unscathed? "It just pops up willy-nilly," Raimondi says.

Perhaps seabirds, which like to prey on sea stars, are moving it by air. Maybe local currents cause a waterborne pathogen to build up in some areas but not others. Infected prey might explain why even stars in aquaria not directly connected to coastal waters have died; the pathogen may come in with mussels and clams collected to feed the captive animals. Solving the central mystery—the identity of any pathogens—has become a far-flung affair, with labs across the nation joining the hunt.

Contagion

At the University of Rhode Island (URI), Kingston, marine pathologist Marta Gomez-Chiarri and her graduate student Caitlin DelSesto have kept sea stars at a marine lab on Narragansett Bay. They first noticed something disconcerting in 2011: The stars in tanks fed with fresh seawater were wasting away, but those in recirculating tanks with filtered water remained healthy. This past October, the researchers discovered they could kill a seemingly healthy star simply by putting it in a tank that had held sick sea stars. "It was something in the water," Gomez-Chiarri says. Something infectious.

In the following weeks, as snow pelted the Cornell University campus, shipments containing dead sea stars packed in dry ice began arriving at the small laboratory run by microbial oceanographer Ian Hewson. He has studied potential pathogens in a range of invertebrates (water fleas, gorgonian sea fans), and he had recently begun to examine viruses in sea urchins. Not long before the outbreak in sea stars began, "I remarked that I wished there was another mass mortality of echinoderms," he recalls. Unfortunately, he got his wish.

As the volume of sea stars increased last winter to 10 deliveries a week, processing became routine. Opening each cold, clammy plastic bag, Hewson or a student would pull out an arm and slice off a centimeter's worth. It goes into a blender with purified water, and then the researchers amplify the DNA to look for bacteria, which can be identified by their 16S ribosomal genes. The genetic sleuthing, along with other tests, has already ruled out a number of potential killers: fungi, protozoans, larger parasites, and some kinds of bacteria.

Viruses, however, remain a big unknown. Researchers had never described a virus in echinoderms until this past December, when Hewson and a trio of undergraduates identified parvoviruses in three species of sea urchins. Viruses don't have ribosomal markers, however, so Hewson has to identify them using other time-consuming and expensive methods. "This is the biggest study I've done by an order of magnitude," says Hewson, who received a rapid grant from the National Science Foundation in November with Miner of WWU.

Narrowing the list of suspects isn't easy. Hewson has been finding 1200 to 2000 species of bacteria on both healthy and diseased sea stars, in addition to viruses. That's not surprising, because seawater naturally contains a multitude of microbes. And the puzzle is complicated by the rapid death of sea stars, which leaves little time to spot the initial pathogen before secondary infections erupt. Nevertheless, Hewson has tentatively identified about a dozen viral and bacterial candidates, by comparing samples from healthy and diseased animals and looking for microbes that had been replicating.

Eventually, Hewson plans to hunt for pathogens in water and sediment samples that have been collected from aquariums and field sites. "Hopefully they will be useful down the line," says virologist Mya Breitbart of the University of South Florida, St. Petersburg, whose lab is hunting for viral pathogens, primarily in east coast sea stars with the wasting disease. In addition, Hewson is eyeing museum specimens to figure out if the outbreak is being caused by a long-standing or

CREDIT: (DATA SOURCE) PACIFICROCKYINTERTIDAL.ORG

Published by AAAS

newly introduced microbe; he will soon visit the Natural History Museum of Los Angeles County in California to slice samples from stars collected over the past 70 years.

Other detective work is under way in Washington state. At a fish laboratory run by the U.S. Geological Survey (USGS) in Nordland, rows of large plastic tubs contain about 50 sea stars in quarantine. Overhead, a network of gray pipes delivers water that has been double-filtered with sand and purified with ultraviolet light. The tanks are kept at 8°C, a comfortable temperature for echinoderms. Pumps whir, pipes gurgle.

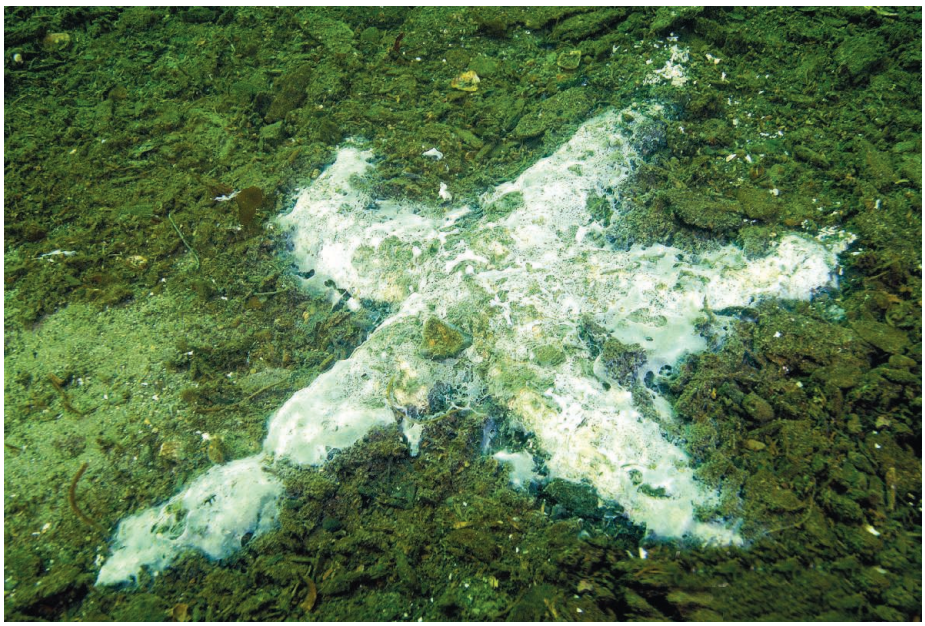
Colleen Burge, a former student of Harvell's and now a postdoc at the University of Washington (UW), Seattle, has looked at the possibility of infected prey. She fed healthy stars with mussels collected from stricken tide pools, for example. In other tanks, Burge added diseased arms. After 3 months, only one star had died. "Obviously, we've had a lot of success keeping them healthy," she said with frustration in late March. Since then, they have infected more sea stars by heating the tanks. Even though the outbreak seems not to have been influenced by warming waters so far, heat makes individual animals more susceptible.

Dismal experiment

Outside the labs, researchers continue to survey tide pools and near shore waters. At the Port Hadlock Marina in Washington state, about 14 kilometers from the USGS lab, Harvell, Burge, and Cornell graduate student Morgan Eisenlord recently examined a dock at low tide. They were concerned that the shift to daytime low tides would expose sea stars to more heat. The pylons were covered with delicate, white sea anemones, tentacles floating gently. Burge spotted a large red *Pycnopodia* clasped to one of the wooden posts with its 18 arms. Harvell walked over. "I wouldn't mind taking a look at him," she said. "His arms look a little weird."

One arm bore a white lesion. Another had apparently pulled itself off. The crippled starfish had crawled a little distance away, beige gonads hanging out (see photo, right). Eisenlord dropped the arm into a plastic bag to take back to the lab. As the rigging of sailboats clinked in the wind, Harvell's yellow Labrador retriever trotted along the sun-warmed dock. But Harvell was gloomy. The Pacific Northwest is a hot spot of sea star diversity, she says, and it's become imperiled.

On a grand scale, the epidemic is replicating a classic experiment performed a half-century ago. Robert Paine, then a young ecologist at UW, wondered about the role of sea stars in the intertidal zone. On a rocky coast not far from Port Hadlock, he systematically plucked the common sea star *Pisaster ochraceus* from certain tide pools and watched what happened. One species of mussel, no longer eaten by sea stars, outcompeted all the others. Diversity plummeted. In a now-classic 1966 paper in *The American Naturalist*, Paine coined the term "keystone predator" to describe the apex influence of sea stars.





Ghost. Some sea stars leave only ossicles and bacteria behind (*top*), while researchers find others while they are still sick, such as this sunflower star (*bottom*) collected in Washington state.

Now, human hands aren't needed to repeat Paine's experiment all along the coast. What's more, baseline data on intertidal populations extends back 2 decades or more in many places, making it possible to draw statistically meaningful insights into how communities change as a result of the die-off.

For better or worse, the natural experiment continues to expand. There's an early report that previously untouched sea stars in Oregon might be afflicted. And a worrisome development from New England: URI's Gomez-Chiarri has found that sick sea stars can infect not only their own kind, but sea urchins and sea cucumbers, too.

Watching nervously from San Juan Island off the coast of Washington, Harvell fears the kills could worsen as water continues to warm. And there's a good chance that an intense El Niño will reach the west coast in August, Raimondi says. "We could be at the beginning, middle, or end of the outbreak," he says. "We don't know. And that's very disconcerting."

–ERIK STOKSTAD

CREDITS (TOP TO BOTTOM): NEIL MCDANIEL; ERIK STOKSTAD

Published by AAAS

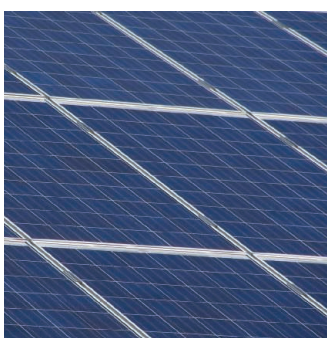
LETTERS

edited by Jennifer Sills

Shining a Light on Solar Water Splitting

DIRECT PHOTOCATALYTIC SPLITTING WATER TO HYDROGEN AND OXYGEN HAS BEEN THE SUBject of thousands of papers over the past four decades, with many optimistic promises. In his Perspective "A nickel finish protects silicon photoanodes for water splitting" (15 November 2013, p. 811), J. A. Turner highlights progress in finding a stable electrode. It's fascinating science, but could this actually be a successful technology?

Although cells with vertical electrodes are usually used for laboratory work, large-scale deployment will require solar cells angled according to latitude. Let's set aside the gas separation and membrane issues required and focus on some simple but critically important questions that must be addressed if direct solar water splitting is to be an important contender. Quantum efficiency is not the only issue.



How large could individual cells be? Would they be in interconnected modules making up panels, as solid-state photovoltaics are now assembled? The need for a transparent cell cover means that low gas pressure is unavoidable. How would cells generating low-pressure hydrogen be connected in modules and then by extensive piping to a hydrogen collection point? Could any leaky cells in the array be sealed off? Installations would have to be in locations where the temperature is never low enough to freeze water and risk fracturing the cells. Eventually, the gas has to be compressed and stored for use.

A second network to replenish the water (and electrolyte?) is less problematic but necessary. A typical large solar cell field can span 1 to 2 km^2, as shown in the photo on the National Renewable Energy Laboratory (NREL) Web site (www.nrel.gov/ncpv/). Try to imagine the pipe network needed to bring the gas from hundreds of modules to a collection point. Hydrogen is notoriously difficult to contain, and the cost and maintenance of the extensive pipe network are unattractive. Moreover, the electrode surfaces would often be in hot water for years, likely resulting in degradation, and replacement is not economically feasible. Obviously, implementing photocatalytic water splitting presents a remarkably difficult engineering problem. Sun Catalytix, a startup funded by the Advanced Research Projects—Energy (ARPA-E), abandoned it shortly after beginning work (*1*, *2*).

NREL has extensively studied alternative paths to solar hydrogen production (*3*), but such alternatives are rarely mentioned in discussions of direct solar hydrogen generation. The simplest possibility is an array of commercial silicon cells (efficiency >16%) coupled to a commercial electrolyzer with about 70% efficient hydrogen generation. These components will produce hydrogen at about 10% efficiency and last a long time. There is also a recent extensive discussion of key components for photosplitting systems (*4*). The advantages of hydrogen generation in a central facility are obvious.

Can direct solar water splitting be competitive with already established solar electricity technology and electrolysis? Serious discussion is long overdue.

EDWIN A. CHANDROSS

Murray Hill, NJ 07974, USA. E-mail: eac@materialschemistry.com

References

1. R. V. Noorden, *Nat. News* 10.1038/nature.2012.10703 (2012).
2. E. Waltz, "Sun Catalytix Won't be Raking It in with Artificial Leaf," *IEEE Spectrum* (24 May 2012).
3. NREL, Photoelectrochemical Water Splitting (www.nrel.gov/hydrogen/proj_production_delivery.html#split).
4. J. McKone, H. Gray, N. S. Lewis, *Chem. Mater.* **26**, 407 (2014).

Response

A NUMBER OF CHANDROSS'S QUESTIONS are addressed in References 5 and 6 of the Perspective (*1*, *2*). Reference 2 provides a detailed engineering analysis for four different photoelectrochemical (PEC) water-splitting system designs, including tilted panels. Designs 1 and 2 have been discussed in the literature and have been found to be unfeasible, but designs 3 and 4, a tilted flat-plate and tracking concentrator design, respectively, are representative of two deployable approaches.

The figure in the Perspective was for illustrative purposes only, and the need for tilted working panels has been recognized for decades. An early commercial example of a solar-to-fuel producing system was the 1977 Texas Instruments panels that split HBr (*3*). Although not a true PEC cell (the silicon cells were coated with a thin film of metal), the system was designed to collect hydrogen while tilted outdoors. In 2008, I gave another example of a tilted panel concept with light concentration (*4*).

Concerning the size of the actual cells, that will be determined by the semiconductor technology and the panel design. Therefore, the size could range from continuous plastic-like sheets to small centimeter-sized cells. Reference 2 discusses some possibilities for cells and manufacturing, as well as pressurization and the use of PVC tubing for hydrogen collection and transport.

As for hydrogen being "notoriously difficult to contain," industry has many decades of practice for its safe containment, distribution, and delivery (*5*, *6*). Hydrogen is a commodity chemical that is moved though pipelines (*7*–*9*), as a compressed gas in tube trailers and gas cylinders, and as a liquid in tanker trucks (*10*, *11*). As a commodity chemical, any loss of hydrogen represents lost revenue. On a smaller scale, many research buildings and commercial facilities around the world are plumbed for hydrogen. Hydrogen filling stations are being built around the world, and fuel cell vehicles using compressed

CREDIT: WIKIMEDIA COMMONS

hydrogen are set to be introduced commercially in selected areas starting next year. The current fleet of demonstration fuel cell vehicles and filling stations has had an exemplary safety and reliability record (*12*).

Concerning freeze issues, while specific electrolytes will depend on the semiconducting materials, the canonical solutions for PEC are 1 M sulfuric acid and 1 M potassium hydroxide, which freeze at –6° and –4°C, respectively; 3 M sulfuric acid has been used previously (*13*), which freezes at –17°C. Under operation in the sun, solution temperatures could reach 60° to 70°C, which may be sufficient heat to last through a few hours of freezing temperatures. One engineering solution may be to drain the panels into underground tanks during extreme cold spells and bury all the water lines.

Although a large-area PEC field for hydrogen production has yet to be built, the issues associated with a hydrogen collection system are probably no more difficult than those with a natural gas distribution system. Until now, there has been no material system that warranted a scale-up and full engineering design and build.

Efficiency is certainly important, but it is not the correct metric for comparing technologies; the cost of the produced hydrogen is the correct metric. State-of-the-art solar cells have efficiencies of more than 40%, but they would not be used in a photovoltaic/electrolysis system because of their high capital costs. The technoeconomic analysis shows that if certain material properties of the PEC device can be met, then hydrogen from PEC could be cost-competitive (*2*). However, there are many assumptions in that technoeconomic analysis that can only be addressed by actually building a water-splitting panel and system. Several major efforts around the world are focused on accomplishing just that. The most well known is the U.S. Department of Energy's Solar Fuels Hub, the Joint Center for Artificial Photosynthesis, currently in the process of designing and building prototypes and doing detailed engineering analysis of cell design and operation (*14*). A video ("NREL Photoelectrolysis") of one of our water-splitting systems in an outdoor test is available (*15*)

The lack of progress in the 40 years since the first PEC water-splitting report is the unfortunate result of the field taking the easy route—looking at common metal oxides with poor solar conversion properties, and thinking that even an inefficient cell would be so inexpensive that it would be economically viable. Now, the field is recognizing that semiconductors with excellent electronic properties are necessary, which is why I was pleased to be able to comment on the Stanford result.

JOHN A. TURNER

National Renewable Energy Laboratory, Golden, CO 80401–3393, USA. E-mail: John.Turner@nrel.gov

References

1. B. A. Pinaud *et al.*, *Energy Environ. Sci.* **6**, 1983 (2013).
2. D. James, G. N. Baum, J. Perez, K. N. Baum, "Technoeconomic analysis of photoelectrochemical (PEC) hydrogen production" (Directed Technologies Inc., Arlington, VA, 2009); www1.eere.energy.gov/hydrogenandfuelcells/pdfs/pec_technoeconomic_analysis.pdf.
3. J. S. Kilby, J. W. Lanthrop, W. A. Porter, U.S. Patent 4,021,323 (1977); U.S. Patent 4,100,051 (1978); U.S. Patent 4,136,436 (1979).
4. J. Turner, *Nat. Mater.* **7**, 770 (2008).
5. U.S. Department of Energy, Hydrogen and Fuel Cells Program, Safety (www.hydrogen.energy.gov/safety.html).
6. Air Products, Hydrogen Energy Research Center (www.airproducts.com/industries/Energy/Hydrogen-Energy/resource-center.aspx).
7. Praxair, Pipeline (www.praxair.com/services/industrial-gas-supply-and-management/gas-pipelines).
8. Air Products, World's Largest Hydrogen Pipeline Supply Network (www.airproducts.com/microsite/h2-pipeline/index.asp).
9. U.S. Department of Transportation, Pipeline and Hazardous Materials Safety Administration, Hydrogen (http://primis.phmsa.dot.gov/comm/hydrogen.htm).
10. Praxair, Hydrogen (www.praxair.com/gases/buy-compressed-hydrogen-gas-or-liquid-hydrogen).
11. Air Products, Hydrogen Energy (www.airproducts.com/h2energy).
12. NREL, Presentations Containing All CDPs (www.nrel.gov/hydrogen/proj_fc_market_demo.html#allcdp).
13. O. Khasalev, J. A. Turner, *Science* **280**, 425 (1998).
14. Joint Center for Artificial Photosynthesis (solarfuelshub.org).
15. NREL Photoelectrolysis (www.youtube.com/watch?v=6GT4Oiig1-8).

Advanced Photon Source Upgrade Benefits All

IN THE NEWS & ANALYSIS STORY "LEADING U.S. x-ray source goes after bigger upgrade" (3 January, p. 12), A. Cho suggests that the Advanced Photon Source (APS) upgrade will only benefit a fraction of those who use the facility. I disagree.

A remarkable scientific opportunity has emerged to boost the brightness of the x-ray sources at APS by amazing factors of 100 or more by incorporating a multi-bend achromat (MBA) lattice technology into the storage ring (*1*). This will provide a new generation of capabilities such as x-ray analysis with nanometer-scale resolution and sensitivities approaching individual atoms. The higher brightness will benefit researchers across the full range of science. Biological researchers will benefit from microfocus crystallography, which will allow them to obtain protein structures not possible now, and from sensitive imaging of the molecular mechanisms inside cells.

The greatly enhanced brightness is primarily due to much higher x-ray coherence, with only moderate increase in x-ray intensity. The x-ray sources are thus much more useful for research without introducing deleterious effects such as damage to samples or heat load problems for optics. All of the APS's existing beamlines will be able to benefit from the enhanced brightness. Of course, we fully expect improvements to beamline capabilities to continue to be proposed as user needs evolve.

The MBA technology has been developing for several years and recently reached maturity. The new APS storage ring would be the best way to enable new science and strengthen the nation's complementary suite of light sources to keep them providing world-leading capabilities for many decades to come. We at Argonne will continue to work with the Department of Energy Office of Science to deliver the upgrade that maintains the U.S. leadership in light sources and serves the broad user community.

BRIAN STEPHENSON

Director, Advanced Photon Source, Associate Laboratory Director for Photon Sciences, Argonne National Laboratory, Argonne, IL 60439, USA. E-mail: aps-director@aps.an.gov

Reference

1. "A MBA lattice at the APS: A new generation: A preliminary report on the October 2013 workshop on new science opportunities provided by a multi-bend achromat lattice at the APS" (www.aps.anl.gov/Upgrade/Workshops/2013/MBA-Technology/includes/aps%20workshop%20report.pdf).

CORRECTIONS AND CLARIFICATIONS

Reports: "CRL4 complex regulates mammalian oocyte survival and reprogramming by activation of TET proteins" by C. Yu *et al.* (20 December 2013, p. 1518). The authors wish to acknowledge contributions of Tadashi Nakagawa and Yue Xiong (University of North Carolina—Chapel Hill). Nakagawa and Xiong initiated the VprBP-Tet project and made substantial contributions to the published study. Xiong's lab generated and provided us the VprBP conditional mutant mice on the basis of direct collaboration in summer 2012. Nakagawa, a postdoctoral fellow in Xiong's lab, discovered the VprBP-Tet interaction by immunoprecipitation and mass spectrometry analysis of the VprBP immunocomplex in early 2012. Nakagawa also discovered in 2012, through knocking down and knockout VprBP in cultured human cells and in mouse embryo fibroblasts, that the function of VprBP is critically important for the activity of Tet. Xiong has communicated these and other unpublished results to us in multiple communications between August 2012 and April 2013. The HTML version online has been corrected.

Letters to the Editor

Letters (~300 words) discuss material published in *Science* in the past 3 months or matters of general interest. Letters are not acknowledged upon receipt. Whether published in full or in part, Letters are subject to editing for clarity and space. Letters submitted, published, or posted elsewhere, in print or online, will be disqualified. To submit a Letter, go to www.submit2science.org.

Published by AAAS

SCIENCE POLICY

Category 5 or Tempest in a Teapot?

Adam B. Jaffe

Scientists are like hogs. Not in the sense that they feed at some metaphorical trough, but in the sense that the scientific labor market behaves according to what economists have long described as the "hog cycle." That is, if some shock to demand or supply causes a shortage of pork, the price rises. In response, hog farmers increase the size of their herds. But it takes time for the hogs to fatten up; in the interim, the price stays high or rises further. When these new fat hogs come to market, the price falls. In response, farmers cut back on their herds. After more time, this reduction in supply causes a new shortage and resulting price rise, and the cycle begins again. Because of the lag between the price signal and the supply response, the system is inherently unstable in the short run and generates boom and bust [e.g., (*1*)].

Falling Behind?
Boom, Bust and the Global Race for Scientific Talent

by Michael S. Teitelbaum
Princeton University Press, Princeton, NJ, 2014. 277 pp. $29.95. ISBN 9780691154664.

In *Falling Behind?*, Michael Teitelbaum describes how this phenomenon played out in the U.S. science and engineering workforce from the end of World War II through the 1998–2005 doubling of the National Institutes of Health (NIH) budget and subsequent leveling off of funding (*2*). As he richly documents, the inherent instability of this kind of system was repeatedly exacerbated by purple-prosed calls for action to deal with asserted or projected shortages of scientists and engineers that did not exist or did not materialize. Exemplifying these calls are the 2005 National Research Council Report *Rising Above the Gathering Storm* (*3*) and its 2010 update (*4*), which concluded "The Gathering Storm increasingly appears to be a Category 5." Teitelbaum (Harvard Law School) analyzes in detail the development of these reports, including the apparent balance between public interest and self-interest of the participants. Crucially, he untangles the multiple distinct perceived "threats," primarily three: The average scores of American K-12 students on internationally compared math-science tests are mediocre to poor. The United States does, or will soon, not have enough scientists and engineers to meet the needs of industry and government. The United States is losing its preeminence in international science.

Teitelbaum shows that the difference in average scores is real and due primarily to the poor performance of the lower tail of the distribution—and that it is bad for those students and for overall U.S. productivity and income. However, as he notes, it has almost nothing to do with the supply of scientists and engineers, who come overwhelmingly from the upper tail of the distribution.

Teitelbaum demonstrates that claims of actual or impending shortage were almost always based on poor data and proved over time to be overblown or false. Nonetheless, they had political impact and sometimes exacerbated subsequent extended periods of oversupply of scientists.

Teitelbaum characterizes the U.S. position in the global science picture as a "glass half-full." Although its preeminent position in the decades after World War II has slipped somewhat, that change stems from other countries having rapidly expanded their science investments and training of scientists. The U.S. science enterprise has continued to grow, albeit unevenly over time and across scientific fields. By my calculation based on Organization for Economic Cooperation and Development (OECD) data (*5*), the United States finances almost half of all of the government-funded research of the OECD nations collectively. Relative to the size of the economy, its public investment of about 1% of gross domestic product is higher than that of any other large country. Whereas particular needs (e.g., the reduction of dependence on fossil fuels to counter climate change) may call for increased research in specific areas, the current U.S. rate of investment is simply not low in absolute terms or relative to the investments of others.

Having rejected simplistic crisis diagnoses, Teitelbaum turns to more nuanced discussion of what ails U.S. science. While not new, his discussion usefully pulls together previous work by him and others that shows that the existing funding model and practices of universities have uncoupled the supply of new scientists from the need for new scientists, particularly in the life sciences [e.g., (*6*–*9*)]. When additional funding does become available (e.g., the NIH doubling beginning in 1998), expansion occurs in a way that is unsustainable once growth levels off. The result is the seeming paradox that grant acceptance rates and job prospects for new scientists are poor despite the level of public funding being well above where it was as recently as 2000. Teitelbaum makes some reasonable suggestions for reform, such as changing indirect cost recovery and faculty salary coverage rules that encourage overexpansion and overdependence on federal funding; improving career information for prospective graduate students; rethinking visa and funding policies for foreign graduate students; and increasing the use of long-term funded staff scientists in university research labs. But he also notes sensibly that we should be aware of the law of unintended consequences and proceed carefully and incrementally, so as to allow the system to adapt and to adjust the policies as outcomes emerge.



Photograph from Alejandro Guijarro's Momentum Series (2010–2013).

Falling Behind? also illuminates a bigger picture: Scientists must recognize that the solution to low grant acceptance rates and poor job prospects for new scientists is not increased public funding for research. At present, increased funding is not only politically impractical, it is actually unreasonable—given the competing demands for public resources and the fact that U.S. science investment is already large relative to historical norms and the investment levels of other countries. More fundamentally, increasing funding will not solve the problems, which are structural. As long as those remain, an increase in funding will, at best, provide temporary reprieve—much as building new

The reviewer is at the Department of Economics, Brandeis University and Motu Economic and Public Policy Research, Post Office Box 24390, Wellington 6142, New Zealand. E-mail: adam.joffe@motu.org.nz

CREDIT: © ALEJANDRO GUIJARRO/WWW.ALEJANDROGUIJARRO.COM/

Downloaded from www.sciencemag.org on May 1, 2014

Published by AAAS

highways to relieve traffic congestion eases things for a while but induces additional driving until the roads are again clogged. Funding agencies and research organizations should make the changes that would gradually adjust the current excess supply of new scientists to match demand and prevent new funding from simply inducing expansion that recreates excess supply. Only then could we have a productive discussion about the benefits of additional public funding.

References and Notes

1. S. Rosen, K. Murphy, J. Scheinkman, *J. Polit. Econ.* **102**, 468 (1994).
2. Teitelbaum identifies five cycles. Denoted by what triggered the initial boom, these are: the start of the Cold War in the 1950s, Sputnik, the "War on Cancer" and Reagan defense budget, the 1990s high-tech boom and Y2K panic, and the Clinton-Bush doubling of the NIH budget.
3. www.nap.edu/openbook.php?record_id=11463.
4. www.nap.edu/openbook.php?record_id=12999.
5. http://dx.doi.org/10.1787/888932486659.
6. M. S. Teitelbaum, *Science* **321**, 644–645 (2008).
7. P. Stephan, *How Economics Shapes Science* (Harvard Univ. Press, Cambridge, MA, 2012); reviewed in (*10*).
8. NIH, "Biomedical research work-force working group report" (NIH, Bethesda, MD, 2012); http://acd.od.nih.gov/biomedical_research_wgreport.pdf.
9. P. Stephan, "The Endless Frontier: Reaping what Bush sowed?," National Bureau of Economic Research Working Paper No. 19687 (2013).
10. M. Feldman, *Science* **335**, 1171 (2012).

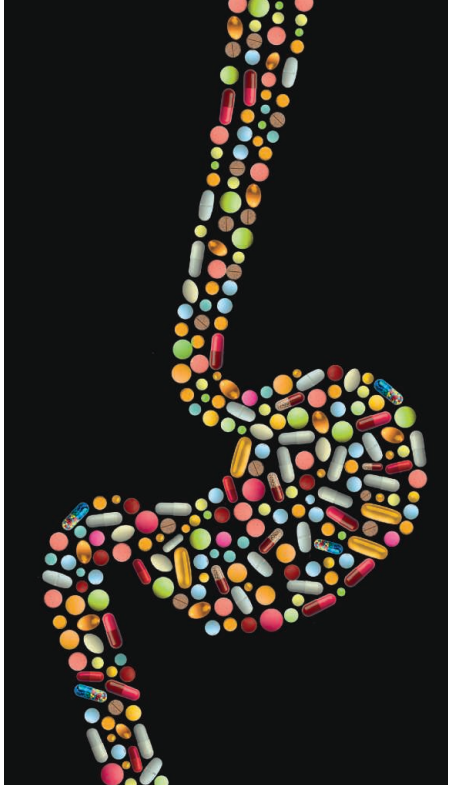
10.1126/science.1252696

PUBLIC HEALTH

Antibiotics and Collateral Damage

Alison E. Mather

Most people recognize that antimicrobial drugs are becoming increasingly ineffective, due to the rise of antimicrobial resistance (AMR). The incredible adaptability of microbes and the strong and varied selection pressures to which they are exposed compromise our ability to fight infections, and many common procedures (from hip replacements to cancer therapies) carry greater risks. This has been highlighted in recent government reports such as the *UK Five Year Antimicrobial Resistance Strategy 2013 to 2018* (*1*) and the U.S. Centers for Disease Control and Prevention's *Antibiotic Resistance Threats in the United States, 2013* (*2*). With very few new drugs in the pipeline, there is no doubt that the increasing resistance to antimicrobials poses a serious threat to human and animal health.



While AMR can be observed and measured on relatively short time scales, there are other consequences to the use of antimicrobials and the less frequently considered sanitizers and disinfectants. Their long-term effects, at both individual and population levels, have rarely been addressed and are the central themes in Martin Blaser's *Missing Microbes*. Blaser (an infectious disease specialist at New York University) has dedicated decades to investigating how our use of antimicrobials over the past 70 years or so relates to the phenomena of obesity, food allergies, asthma, and heartburn, epidemics he refers to as our "modern plagues." He argues that changes to our microbiota—the collection of microbes in our bodies, which helps us digest our food, clot our blood, and protect us from invading pathogens—are responsible for many human ills of the 21st century.

Blaser sets the scene by portraying the complexity and diversity of microbial populations and their interactions within human bodies. He has a particular and personal interest in *Helicobacter pylori*, a bacterium that for years has been associated with gastritis and ulcers. Whereas the organism is often portrayed as a villain, Blaser instead promotes its dual nature, arguing that its absence is associated with different disorders, an example being gastroesophageal reflux disease. Illustrating his points with a combination of data and personal anecdote, he walks readers through the processes by which the use of antimicrobials changes the nature and composition of the resident microbial populations that have evolved with us and notes how certain bacteria, such as *H. pylori*, are disappearing. In doing so, Blaser argues that we are interfering with our immune systems and other key biological processes and thus predisposing ourselves to these modern epidemics. In another example, he draws an analogy between the frequent prescription of antimicrobials in children (often for viral infections on which they have no impact) and the provision of antimicrobials for growth promotion in food animals, "inadvertently fattening [our children] up."

As the author, to his credit, recognizes, the strength of evidence for the association between changing microbiota and these diseases is, without doubt, variable. The diseases are complex and multifactorial, and, interesting though Blaser's observations are, for most of these illnesses a full understanding of causal relationships lies some way off. Importantly, he makes clear the critical distinction between association and causation, and his explanations of ecological and epidemiological concepts are among the book's strong points. So too are his descriptions of necessary but not sufficient factors and the importance of seeking other vantage points from which to view one's data.

There can be little disagreement with Blaser's concern that we are now facing the doomsday scenario of an "antibiotic winter." In discussing that, he shifts from the long-term, unintended consequences of antimicrobial use and focuses instead on the more immediate prospects of untreatable resistant infections and human populations, with their disrupted microbiota, becoming more susceptible to pathogens. Expressed in a style ranging from moderate to strongly assertive, many of Blaser's views are contentious. However, new ideas and fresh approaches are best generated from intellectual sandpits and the tails of the distribution of opinions. Readable and challenging, *Missing Microbes* provides a stimulus with which to probe existing dogma.

Missing Microbes
How the Overuse of Antibiotics Is Fueling Our Modern Plagues

by Martin J. Blaser
Holt, New York, 2014. 288 pp. $28. ISBN 9780805098105.

References

1. www.gov.uk/government/uploads/system/uploads/attachment_data/file/244058/20130902_UK_5_year_AMR_strategy.pdf.
2. www.cdc.gov/drugresistance/threat-report-2013/.

10.1126/science.1252914

The reviewer is at the Wellcome Trust Sanger Institute, Wellcome Trust Genome Campus, Hinxton CB10 1SA, UK. E-mail: am24@sanger.ac.uk

CREDIT: DAVID SHOEMAKER/COURTESY HENRY HOLT AND COMPANY

Published by AAAS

CLIMATE ADAPTATION

Evaluating Flood Resilience Strategies for Coastal Megacities

Integration of models for storms and floods, damages and protections, should aid resilience planning and investments.

Jeroen C. J. H. Aerts,[1]* W. J. Wouter Botzen,[1] Kerry Emanuel,[2] Ning Lin,[3] Hans de Moel,[1] Erwann O. Michel-Kerjan[4]*



Recent flood disasters in the United States (2005, 2008, 2012); the Philippines (2012, 2013); and Britain (2014) illustrate how vulnerable coastal cities are to storm surge flooding (*1*). Floods caused the largest portion of insured losses among all catastrophes around the world in 2013 (*2*). Population density in flood-prone coastal zones and megacities is expected to grow by 25% by 2050; projected climate change and sea level rise may further increase the frequency and/or severity of large-scale floods (*3*–*7*).

Despite trillions of dollars of assets located in coastal flood-prone areas, investments in protection have often been inadequate (*8*), postponed for short-term economic reasons, for lack of consensus on how to properly evaluate the return on investment, or from the fear of making irreversible choices that become suboptimal over time. To help inform policy decisions, we have developed a multidisciplinary scientific approach to evaluate flood management strategies. It combines probabilistic risk assessment of hurricanes and storm surge with vulnerability determination of exposed assets at a census level, accounting for sources of uncertainty and the timing of investments in storm-surge flood-risk protection. We applied this methodology to New York City (NYC)—one of the most exposed coastal megacities—working with local policy-makers.

Barriers and Building Codes

A wealth of ideas about protecting NYC from floods has been proposed (*9*, *10*), including barriers, levees, wetland restoration and beach strengthening that are effective in reducing flood occurrence in large parts of the city. However, as in other cities, some of these large-scale engineering options have been criticized because they are costly or may harm the environment. Other measures, such as reducing exposure and vulnerability (e.g., by enacting zoning regulations and enhancing building codes), may considerably reduce flood damage and entail lower investment costs, but they do not prevent flood waters from entering the city.

We present three main classes of strategies that focus on reducing vulnerability or avoiding flooding or a combination of both [see the figure and supplementary material (SM)]. The Resilient Open City strategy (S1) is a cluster of measures to enhance building-code strategies in NYC (*11*) by elevating, or dry or wet flood-proofing, both existing and new buildings. Storm surge barrier strategies (S2, a, b, and c) aim to lower flood probabilities in NYC and parts of New Jersey (NJ), with barriers, levees, and beach nourishments. "Environmental dynamics" (S2a) consists of three barriers to close off parts of NYC and NJ that preserve wetland dynamics of Jamaica Bay. "Bay closed" (S2b) expands on S2a by adding a fourth barrier that closes off Jamaica Bay. "NJ-NY connect" (S2c) replaces three barriers from S2b with one large barrier in the outer harbor to protect a larger area (see the figure). The barrier systems are designed to withstand an extreme surge of 8 to 10 m (25 to 30 feet).

The "hybrid solution" (S3) (see the figure), reflecting many measures in (*9*), combines building code measures of S1 that turned out to be cost-effective according to our analysis (SM) only in high-risk 100-year return flood zones (defined by the U.S. Federal Emergency Management Agency), with protection of critical infrastructure to reduce economic loss due to business interruption. S3 includes moderate local flood protection measures, such as levees and beach nourishment that are also part of S2c. The local protection measures and building codes for new structures are adjustable to future climate change, as they can be upgraded if flood risk increases in the coming decades.

Modeling Flood Risks, Estimating Costs

The heart of the method is a probabilistic flood-risk model developed for the city (*12*–*14*) (SM §1). We simulated 549 storm-surge simulations, varying from extremely low probability events to more frequent storms, using a new coupled hurricane–hydrodynamic–inundation model (*15*) (SM). Then we applied flood depth–damage curves to calculate potential damage to buildings and vehicles at the census block level. In addition to flood risk to buildings, the risk to other categories (like infrastructure), the risk to parts of NJ, and indirect economic effects were added, based on observed consequences of Hurricane Sandy in 2012 (*13*).

We estimate the average annual expected flood loss for NYC alone at $174 million/year, if no flood management measures are implemented. Flood losses with a 100- and 1000-year return period are $2.2 billion and $25.4 billion, respectively. Our loss estimates for an extreme event of return period similar to Sandy are very close to the actual damages it triggered (SM §1.11).

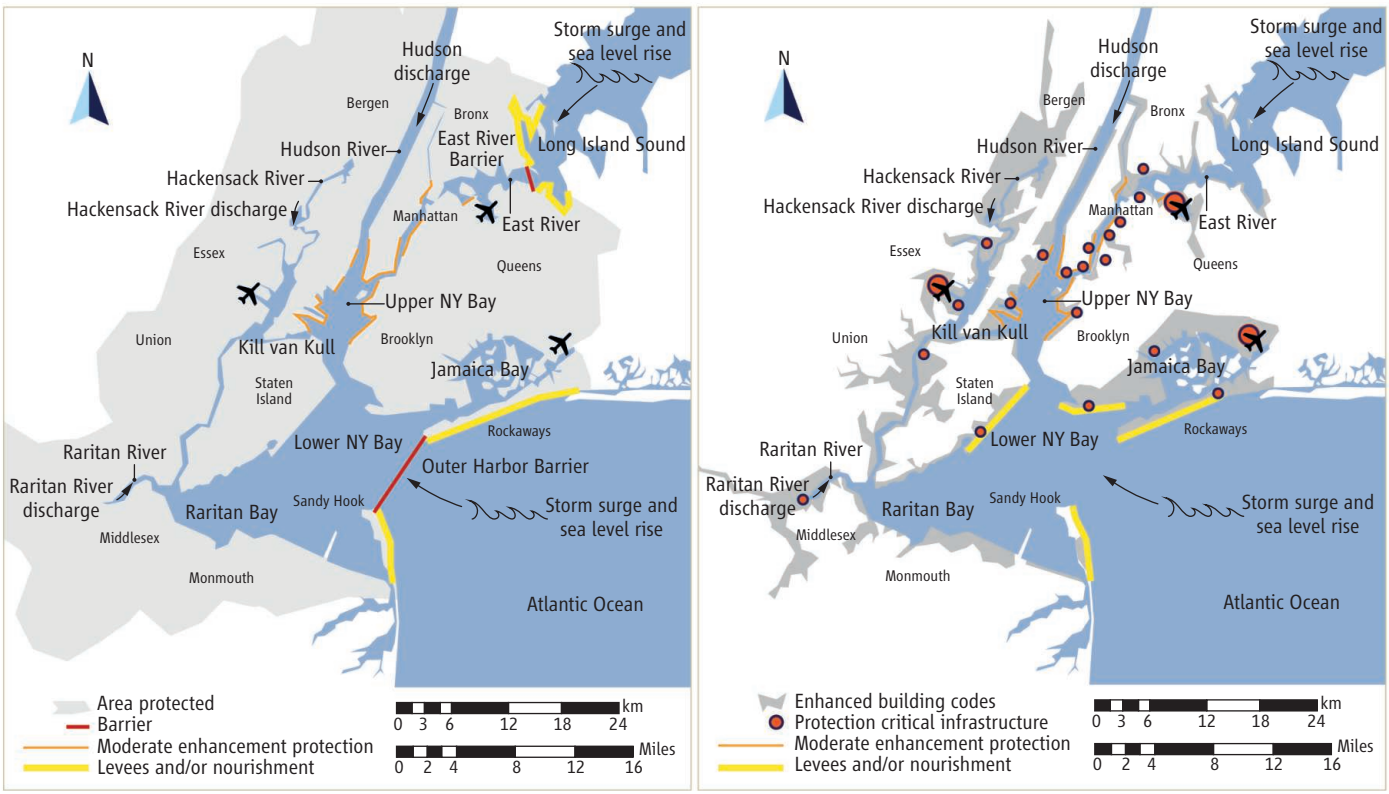
The future risk in 2040 and 2080 is also calculated, accounting for estimated changes in surge probabilities (*15*) and projected sea-level rise under future climate change scenarios, as well as the increase in urban exposure due to new construction in flood zones (SM §1.3). Flood defenses in the storm surge barrier strategies (S2, a, b, and c) are assumed not to fail. A benefit-cost analysis (BCA) of flood risk–management strategies was conducted for NYC over a 100-year period to evaluate the benefit (avoided risk) of each strategy and its cost (*13*), under future scenarios (SM §2). We tested the robustness of the

[1]Institute for Environmental Studies, VU University, 1081HV, Amsterdam, Netherlands. [2]Department of Earth, Atmospheric, and Planetary Sciences, Massachusetts Institute of Technology, Cambridge, MA 02139, USA. [3]Department of Civil and Environmental Engineering, Princeton University, Princeton, NJ 08544, USA. [4]Center for Risk Management and Operations and Information Managment Department, The Wharton School of the University of Pennsylvania, Philadelphia, PA 19104, USA. *Corresponding authors. E-mail: jeroen.aerts@vu.nl (J.C.J.H.A.) and erwannmk@wharton.upenn.edu (E.M.-K.).

CREDIT: NEONJELLYFISH/ISTOCKPHOTO

Downloaded from www.sciencemag.org on May 1, 2014

Published by AAAS



Strategies for protection vs. reducing vulnerability. (**Left**) Strategy S2c reduces the length of the coastline of the NYC-NJ area as much as possible, to minimize flood protection costs. Two storm-surge barriers are developed: one large barrier that connects Sandy Hook in NJ and the tip of the Rockaways in Queens, NY, and a barrier in the East River. Some lower spots (bulkheads, levees, or landfill) on the inside of the protection system will be elevated to accommodate rising water levels caused by Hudson River peak discharges during a storm event. (**Right**) Strategy S3 combines cost-effective flood-proofing measures with local protection measures of critical infrastructure. Such a "hybrid solution" aims at keeping options open: either (a) building codes can be enhanced in the future with additional local protection measures or (b) storm-surge barriers can be developed. See SM for details.

BCA by considering various scenarios of climate change and different assumptions about the discount rate (SM §2) and by propagating uncertainty in water depth and damage estimation (SM §1.9) into the final risk assessment. For the barrier strategies, often seen as an irreversible choice, we also tested different investment timings.

Combined investment costs for NYC and NJ are a maximum of $14.7 to $23.8 billion for S2, a, b, and c, and $11.6 billion for S3 (see the table) (*11*). Yearly maintenance costs are much higher for the barrier strategies than for S3. BCA results of different building-code strategies (S1) are given in the SM. Cost-effective strategies from S1 are incorporated into S3: elevation of new houses (4 feet or 6 feet, depending on flood zone) and wet flood-proofing (2 feet) of existing buildings.

None of the flood protection–barrier strategies is economically attractive [their benefit-cost ratios (BCRs) are less than 1] under current climate conditions or a low climate change scenario. S2c and S3 have a BCR higher than 1 in a middle climate change scenario. All barrier strategies and the hybrid strategy are, however, economically attractive if flood risk develops according to a high climate change scenario (rapid ice melt and significant increase in storm activity), with the highest net present value of $64 billion for S2c and $50 billion for S3 (SM §3.2). Investment strategies are slightly more economically attractive if a 150-year lifetime is used (SM §3.2).

For a given discount rate and climate scenario, there is inherent uncertainty in the models, which influences the BCA results (see the table). But, the impact of this within-scenario uncertainty on the results is smaller than the impact of selecting a different discount rate and/or climate scenario. The latter is particularly challenging for policy-makers because trends in climate change–caused flood risks are still highly uncertain (*16*, *17*).

Making Policies, Making Payments

Our study provides economic rationale for some measures proposed by the City of New York in (*9*). Implementing improved cost-effective building codes (parts of S3)—such as elevating new buildings and protecting critical infrastructure by including adaptation measures into maintenance works—is the most cost-effective strategy. Given the large existing building stock in NYC, this might only have marginal impacts if another hurricane occurs in the next few years though. A challenge with flood-proofing buildings is to incentivize those at risk to make such investments and to monitor compliance with building code regulations, which has been shown to be an important behavioral issue internationally.

BCA results of delaying investment in barriers by 25 years show that independent of the discount rate, it is economically effective to invest in a storm surge barrier system in 2040 if climate change develops according to the middle scenario; still this strategy needs to be studied now (SM §3.3).

Now comes the big policy question: Who should pay to make NYC (or any city) more resilient to future flood disasters? A small part of the investment costs of S3 will have to be paid directly by homeowners for flood-proofing their houses, whereas the largest costs of flood defenses are supposed to be paid by the city (through new taxes, increased debt or reallocation of the current budget). If estimated benefits to the rest of the United

Published by AAAS

States and the international economy of preventing future flooding of NYC are effectively captured though (positive externalities), costs could arguably be shared by city, state, and federal government and the private sector, which would mean that protection costs are distributed more widely. For instance, with more than 50 million tourists visiting the city every year, a simple $10 resilience fee—equivalent to the maximum September 11 airline security fee anyone traveling in the United States is now paying for a roundtrip ticket—could help. If the financial burden on the NYC budget is offset by such complementary funding and spread over time (for instance, by issuing a dedicated resilience bond paid back over 15 years), protecting the city becomes more financially appealing to local policy-makers.

Additional policies are needed to support the involvement and commitment of stakeholders to flood resilience. Enhancing financial protection is critical, too. That 80% of households and 95% of small businesses in the area inundated by Sandy did not have flood insurance is disturbing, as it is available from the federal government at a subsidized rate for many. Recent legislation passed by the U.S. Congress phases out some of these subsidies over time, which is likely to make investment in risk-reduction measures even more appealing in order to lower the cost of more expensive flood insurance (*3*, *9*, *18*).

Physical and financial protection can also be linked creatively. For example, the U.S. federal government provides premium reduction for residents in a community that actively participates in the Community Rating System program, which requires specific flood resilience activities. About 1300 communities participate today; NYC does not as yet.

Transferability to Other Coastal Cities

Elements of our methodology are applicable for coastal megacities around the world, where flood resilience plans are currently debated (*19*). Many strategies that were implemented have thus far been the result of long learning-by-doing processes, such as elements of large-scale flood protection that have been employed with substantial economic and environmental benefits in the Netherlands (*20*). International examples can serve as an inspiration for designing effective flood resilience policies elsewhere (*21*), but flood risks and management approaches require location-specific analysis.

Climate and hydrological models for creating flooding scenarios are available at research institutes and meteorological services, but often need to be tailor-made for application at the regional or city level. In estimating risks from flooding scenarios, cities play an important role as they have access to (spatial) data on the assets—such as buildings, infrastructure, and environmentally protected areas—and socio-demographics of flood zones. Catastrophic modeling expertise from the insurance industry can be useful for cities, and new knowledge partnerships are needed between city agencies, research institutes and private sector specialists (*22*). The "100 Resilient Cities" challenge of the Rockefeller Foundation, the Zurich Insurance's "Flood Resilience Alliance" initiative and the European "Enhance program" on managing natural hazards are excellent examples of the initiation of such new partnerships (*23*–*25*).

In order to better inform decision-makers about the robustness of their investment choices, scientists have to accompany BCAs with a broad range of (future) scenarios, different discount rates, and an interval of model outputs representing model uncertainty and sensitivity results. It is also important to maintain the flexibility to change policies when new information on future scenarios becomes available (*26*). Most BCAs address one of these issues in isolation, and we recommend that all should be included in an integrated analysis. Uncertainty is inherent to such estimations, but it should not be used to justify not doing anything.

	Where/ how much	Environ.dyn. S2a	Bay closed S2b	NJ-JY connect S2c	Hybrid solution S3
Costs					
Total investment	NYC	$16.9–21.1 billion	$15.9–21.8 billion	$11.0–14.7 billion	$6.4–7.6 billion
Total investment	NJ	$2 billion	$2 billion	n/a	$4 billion
Total investment	NYC+NJ	$18.9–23.1 billion	$17.9–23.8 billion	$11.0–14.7 billion	$10.4–11.6 billion
Maintenance	NYC+NJ	$98.5 million	$126 million	$117.5 million	$13.5 million
BCR for current climate					
BCR	4% discount	0.21 (0.11; 0.35)	0.21 (0.11; 0.34)	0.36 (0.18; 0.59)	0.45 (0.23; 0.73)
	7% discount	0.13 (0.07; 0.21)	0.12 (0.07; 0.20)	0.23 (0.12; 0.37)	0.26 (0.13; 0.43)
BCR for middle climate change scenario					
BCR	4% discount	1.32 (0.67; 2.16)	1.29 (0.65; 2.11)	2.24 (1.14; 3.67)	2.45 (1.24; 4.00)
	7% discount	0.60 (0.30; 0.98)	0.60 (0.30; 0.97)	1.06 (0.54; 1.74)	1.09 (0.55; 1.78)

Costs and main BCA results of flood management strategies. (**Top**) Total costs. Environ. dyn., environmental dynamics; inv., total investment as billions of U.S. dollars; maintenance, maintenance costs as millions of U.S. dollars per year; n.a., not applicable. (**Bottom**) BCA results with modeling uncertainty as 95% confidence intervals (in parentheses). If BCR > 1, then the measure is cost effective. For S3, BCA results are shown for the scenario of high effectiveness of wet flood-proofing. See SM for details.

References and Notes

1. R. J. Nicholls, A. Cazenave, *Science* **328**, 1517 (2010).
2. SwissRe, Natural catastrophes and man-made disasters in 2013; www.SwissRe.com/sigma/.
3. E. Michel-Kerjan, H. Kunreuther, *New York Times Sunday Review*, 24 November 2012, p. SR7.
4. S. Hanson *et al.*, *Clim. Change* **104**, 89 (2011).
5. S. Hallegatte *et al.*, *Nat. Clim. Change* **3**, 802 (2013).
6. B. Jongman *et al.*, *Glob. Environ. Change* **22**, 823 (2012).
7. Intergovernmental Panel on Climate Change, *Managing the Risks of Extreme Events and Disasters to Advance Climate Change Adaptation* (Cambridge Univ. Press, Cambridge, 2012).
8. R. J. Nicholls *et al.*, "Ranking port cities with high exposure and vulnerability to climate extremes: Exposure estimates" (Working paper, Organization for Economic Cooperation and Development, Paris, 2008).
9. NYC Special Initiative on Rebuilding and Resiliency, A Stronger, More Resilient New York (New York City Mayor's Office, New York, 2013); www.nyc.gov/html/sirr/html/home/home.shtml.
10. J. Tollefson, *Nature* **491**, 167 (2012).
11. J. C. J. H. Aerts, W. J. Botzen, H. de Moel, M. Bowman, *Ann. N. Y. Acad. Sci.* **1294**, 1 (2013).
12. J. C. J. H. Aerts, W. J. W. Botzen, *Ann. N. Y. Acad. Sci.* **1227**, 1 (2011).
13. J. C. J. H. Aerts, N. Lin, W. Botzen, K. Emanuel, H. de Moel, *Risk Anal.* **33**, 772 (2013).
14. Federal Emergency Management Agency, "Hazus MH MR4 Technical Manual" (FEMA, Washington DC, 2009).
15. N. Lin, K. Emanuel, M. Oppenheimer, E. Vanmarcke, *Nat. Clim. Change* **2**, 462 (2012).
16. S. Hallegatte, "Investment decision making under deep uncertainty: Application to climate change" (World Bank, Washington, DC, 2012).
17. H. Kunreuther *et al.*, *Nat. Clim. Change* **3**, 447 (2013).
18. E. Michel-Kerjan, H. Kunreuther, *Science* **333**, 408 (2011).
19. World Bank, "Climate risks and adaptation in Asian coastal megacities: A synthesis report" (World Bank, Washington, DC, 2010).
20. P. Kabat, W. van Vierssen, J. Veraart, P. Vellinga, J. Aerts, *Nature* **438**, 283 (2005).
21. C. Rosenzweig, W. Solecki, S. A. Hammer, S. Mehrotra, *Nature* **467**, 909 (2010).
22. E. Michel-Kerjan, *Nature* **491**, 497 (2012).
23. 100 Resilient Cities, http://100resilientcities.rockefellerfoundation.org.
24. Enhancing Community Flood Resilience, www.zurich.com/aboutus/corporateresponsibility/flood-resilience/flood-resilience.htm.
25. Enhance Partnership for Risk Reduction, http://enhanceproject.eu/.
26. R. J. Dawson *et al.*, *Glob. Environ. Change* **21**, 628 (2011).

Acknowledgments: See the supplementary materials for funding sources.

Supplementary Materials

www.sciencemag.org/content/344/6183/473/suppl/DC1

10.1126/science.1248222

Published by AAAS

ECOLOGY

Tolerance for Predatory Wildlife

Can individual tolerance toward predators affect the success of predator conservation?

Adrian Treves[1] and Jeremy Bruskotter[2]

Around the world, populations of many large, predatory animals are declining, with wide-ranging consequences for other species and ecosystem services (*1*). The declines have a variety of causes, but for mammalian carnivores and sharks, direct human causes of mortality predominate (*2*). Scientists and policy-makers have concluded that promoting human tolerance is critical to the success of predator conservation efforts (*1*, *3*–*5*). Yet the factors that affect people's tolerance of wildlife are not well understood.

The terms tolerance and intolerance are widely used to capture both individual-level judgments of predators (such as attitudes and perceptions), as well as individual behaviors (such as poaching) that directly or indirectly influence outcomes for predators (*5*). It is widely assumed that intolerant behavior toward predators—whether in the form of eradication policies (such as bounties) or illegal killing—is motivated by retaliation for real and perceived losses of livelihood (*5*, *6*). Under this assumption, governments and private organizations aiming to protect predators have implemented economic incentives to reduce the perceived costs of predator conservation and raise tolerance for predators.

Sweden's pioneering program that pays Sami reindeer herders to tolerate predators elucidates the limits and potential benefits of economic incentives for predator conservation. The Swedish government appears to be succeeding in protecting wolverines, brown bears, and lynxes by paying Sami villagers for each successful predator reproduction on communal grazing areas (*6*). However, the Sami have thus far refused to accept incentives for protecting gray wolves because these predators are perceived to scare and scatter reindeer widely. As a result, wolves have only recolonized south of the reindeer areas.

Since the early 1990s, livestock producers have been offered subsidies for predator-proof electric fencing and its installation in south-central Sweden. A correlational study of 445 Swedes living in wolf territories found that those who received subsidies tolerated wolves better than those who had not, regardless of the number of verified wolf attacks on sheep or dogs (*7*). However, the study could not rule out that tolerant farmers were more likely to accept government subsidies, or that intolerant farmers rejected subsidies because they took care of predator problems independently and illicitly.



Friend or foe? Human tolerance toward predators such as jaguars depends on social factors and can be influenced by information on the risks and benefits from the predators.

CREDIT: EDSON GRANDISOLI

These studies suggest that economic incentives can be used to increase tolerance for some predators and protect some from poaching. However, Liberg *et al.* concluded that between 1998 and 2009, an estimated 51% of Sweden's wolves died of poaching; 69% of the latter were concealed by the perpetrators (*8*). Thus, incentives may change poaching behavior in some people but are not a panacea. The delivery of benefits may need to be supplemented by social change. Support for this idea comes from a correlational study of Kenyan Maasai livestock herders, which shows that lion killing diminished when compensation was paid for livestock losses and diminished further when trusted community members were paid to protect livestock, warn villagers of the presence of lions, and monitor lion movements (*9*).

The influence of peers and social norms on poaching intentions is revealed by research on Brazilian ranchers living near jaguar territories. On the basis of interviews with 268 Brazilian cattle ranchers about their intentions to kill jaguars illegally, Marchini and Macdonald concluded that social factors were more influential than retaliation for jaguar predation on cattle or perceived threats to humans (*10*). The ranchers' intentions to kill jaguars positively correlated with the size of their land holdings and were best explained by social norms; ranchers who thought that others kill jaguars or expected such poaching were more intent to kill jaguars themselves. The social facilitation that results in areas where poaching is common and accepted can create predator-free zones as neighbors and associates coordinate their actions explicitly or tacitly (*10*).

Because some hunters in North America and Europe historically helped to conserve populations of valued game (such as deer and ducks), policy-makers in these regions often assume that hunters will also help to conserve predators designated as legal game. For example, a program that allowed up to 43 endangered wolves to be killed in Wisconsin had the explicit purpose of fostering greater social tolerance for wolves (*11*). Yet a study of 656 residents of Wisconsin's wolf population range showed a decline in tolerance and an increase in intention to poach wolves between 2001 and 2009, after the implementation of government culling of wolves implicated in livestock attacks (*12*). Tolerance continued to

[1]Nelson Institute for Environmental Studies, University of Wisconsin, Madison, WI 53706, USA. [2]School of Environment and Natural Resources, Ohio State University, Columbus, OH 43210, USA. E-mail: atreves@wisc.edu

Published by AAAS

decline following the first-ever regulated wolf harvest in Wisconsin (*13*). These results are not consistent with the expectation that legalizing predator killing will reverse intolerance or intention to poach.

Before-and-after comparisons cannot disentangle the effects of coincidental changes in policy and public debate; for that, one needs controlled experiments. A study of individual acceptance of American black bears measured changes in tolerance in four treatment groups that received different information about black bears. Information about the benefits people gain from bears, in combination with information about how to reduce risks posed by bears, increased subjects' acceptance of bears in their region (*14*). Information about how to reduce risks alone (without accompanying information about benefits) decreased subjects' acceptance of bears, possibly by increasing the salience of risks. A correlational study of attitudes among residents around a Nepalese national park came to a similar conclusion, reporting that the strongest predictors of acceptance of tigers were the perceived benefits, none of which involved killing tigers (*15*).

The above studies of jaguars, wolves, lions, and bears challenge the conventional view that intolerance for predators and intention to kill predators result primarily from perceived threats to livelihoods. Although monetary incentives for predator tolerance appear to have been successful in several cases, there is evidence that predator-poaching is influenced more strongly by social factors, with peer group norms and government-sanctioned predator-killing affecting people's intentions to poach predators. We therefore recommend caution in legalizing the killing of predators. Experimentally manipulating monetary and social incentives would help conservationists to determine which factors influence poaching, both among individuals and across cultures that have different histories with various predators. These insights could be highly valuable for future recovery and restoration efforts.

References

1. W. J. Ripple *et al.*, *Science* **343**, 151 (2014).
2. R. A. Myers *et al.*, *Science* **315**, 1846 (2007).
3. *Fed. Reg.* **78**, pp.35664–35719 (13 June 2013), see www.gpo.gov/fdsys/pkg/FR-2013-06-13/pdf/2013-13982.pdf.
4. C. Packer *et al.*, *PLOS ONE* **4**, e5941 (2009).
5. J. T. Bruskotter, J. A. Vucetich, S. Enzler, A. Treves, M. P. Nelson, *Conserv. Lett.* 10.1111/conl.12081 (2013).
6. A. Zabel, K. Holm-Müller, *Conserv. Biol.* **22**, 247 (2008).
7. J. Karlsson, M. Sjostrom, *Ecol. Soc.* **16**, 16 (2011).
8. O. Liberg *et al.*, *Proc. Biol. Sci.* **270**, 91 (2011).
9. L. Hazzah *et al.*, *Conserv. Biol.* 10.1111/cobi.12244 (2014).
10. S. Marchini, D. W. Macdonald, *Biol. Conserv.* **147**, 213 (2012).
11. *Humane Society of the United States et al.* v. *U.S. Department of the Interior, District Court DC*, 06-1279 (2006).
12. A. Treves, L. Naughton-Treves, V. Shelley, *Conserv. Biol.* **27**, 315 (2013).
13. J. Hogberg, Thesis, University of Wisconsin (2014).
14. K. Slagle, R. Zajac, J. Bruskotter, R. Wilson, S. Prange, *J. Wildl. Manage.* **77**, 863 (2013).
15. N. H. Carter, S. J. Riley, J. Liu, *Oryx* **46**, 525 (2012).

10.1126/science.1252690

CELL BIOLOGY

Dysfunctional Mechanosensing in Aneurysms

Cellular sensing of a compliant extracellular matrix may be critical in maintaining structural integrity of the aorta.

Jay D. Humphrey,[1] Dianna M. Milewicz,[2] George Tellides,[3] Martin A. Schwartz[4]

The aorta is the body's main conduit for blood flow, passing through the chest and abdomen. When this artery's wall—thick as a garden hose—weakens, the aorta can dilate abnormally, rupture, and cause life-threatening bleeding. Abdominal aortic aneurysms occur most commonly in individuals between 65 and 75 years old. By contrast, thoracic aortic aneurysms and dissections (TAADs) afflict the young as well and arise primarily from noninflammatory mechanisms that often involve underlying genetic mutations (*1*, *2*). Rupture results from mechanical failure, but what renders the aortic wall vulnerable? It may be that TAADs arise from a failure of cellular mechanosensing.

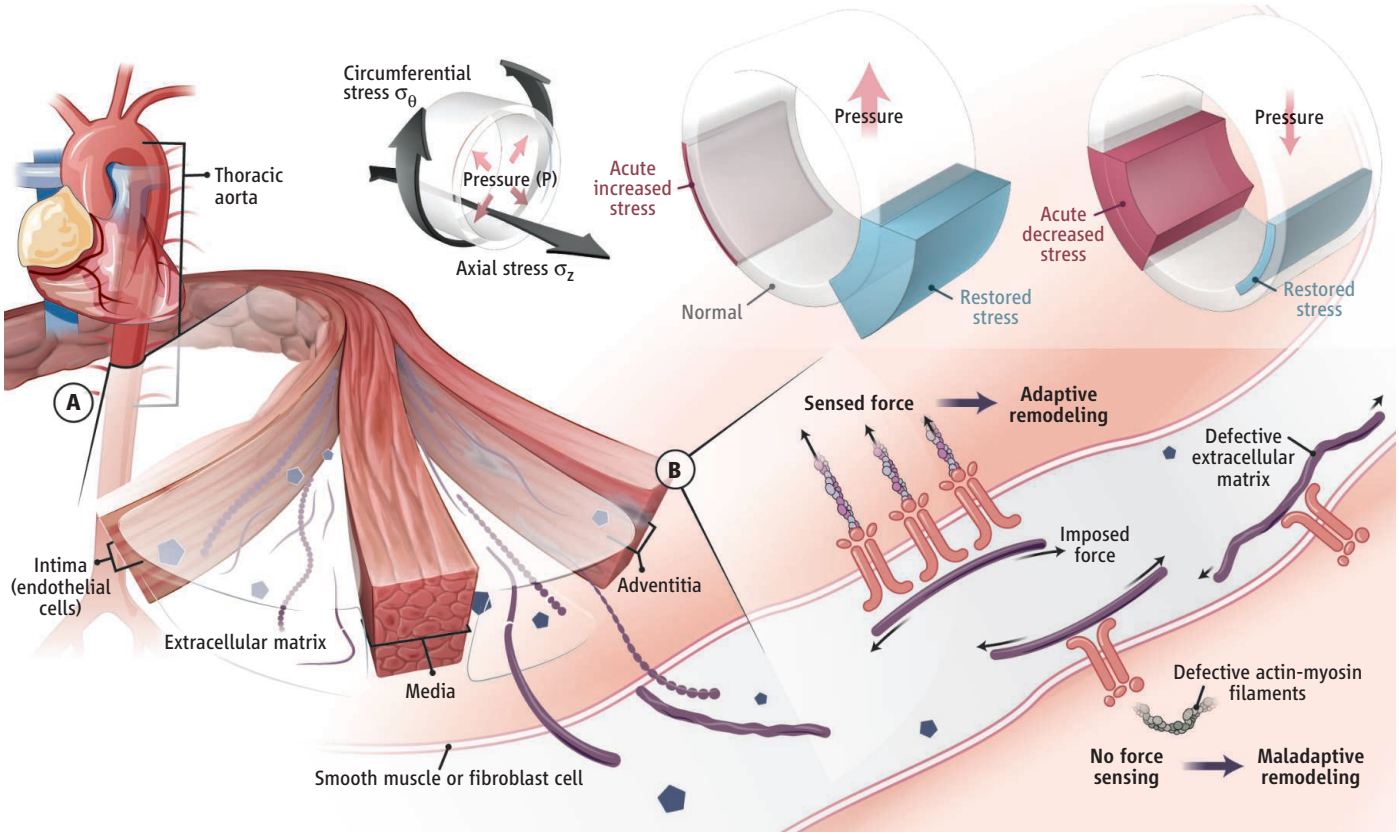
All large arteries grow and remodel to establish and preserve mechanical homeostasis in response to changing hemodynamic conditions (*3*, *4*). The thoracic aorta (see the figure) is subjected to the largest cyclic circumferential stretch from the distending blood pressure, and axial stretch from gross motions of the heart. Like other large arteries, it responds to sustained changes in blood pressure, but its extreme compliance and elastic recoil allow it to accommodate large changes in pressure-driven blood flow without changing the contraction of the smooth muscle cells within the wall.

Cells of the aortic wall are embedded in an extracellular matrix that bears most of the stress from blood pressure. Whereas wall stresses are typically 100 to 200 kPa, stresses supported or exerted by cells of the wall are about 3 to 5 kPa (*4*). This implies that the matrix shields these cells from high stresses. Yet, cells still must sense altered stresses to initiate appropriate remodeling (*5*, *6*). Matrix proteins must also be prestressed when incorporated within existing stressed matrix to promote mechanical homeostasis (*4*). That is, smooth muscle cells and fibroblasts do not merely secrete collagen fibers; rather, they assemble organized collagen fibrils through force-dependent processes that involve cell adhesion proteins (integrins) and the cytoskeleton (actin and myosin) (*7*). Hence, cell sensing and regulation of a compliant extracellular matrix are fundamental to maintaining proper thoracic aortic function and structural integrity.

The aortic extracellular matrix consists of myriad proteins, glycoproteins, and glycosaminoglycans, but elastin and collagen play particularly important roles in compliance and recoil, and stiffness and strength, respectively. Smooth muscle cells and fibroblasts sense (*5*, *6*) the mechanical state of this matrix through integrins and the cytoskeleton. Transduction of this information to intracellular signaling pathways allows them to control the synthesis of matrix components and alter their cytoskeleton in response to cycles of increased mechanical load (see the figure) (*5*, *6*). This force-regulated matrix remodeling involves factors that are secreted by cells within the aortic wall. Smooth muscle cells and fibroblasts release transforming growth factor–β (TGF-β), a cytokine that binds to the matrix in latent form and is activated by proteases or integrins through force-dependent

[1]Department of Biomedical Engineering, Yale University, New Haven, CT, USA. [2]Department of Internal Medicine, University of Texas Health Science Center, Houston, TX, USA. [3]Department of Surgery, Yale School of Medicine, New Haven, CT, USA. [4]Cardiovascular Research Center, Yale School of Medicine, New Haven, CT, USA. E-mail: martin.schwartz@yale.edu

Published by AAAS



Aortic mechanobiology. (**A**) Cells of the thoracic aortic wall remodel an extracellular matrix. Endothelial cells sense and respond to changes in wall shear stress resulting from blood flow; smooth muscle cells and fibroblasts sense and respond to changes in intramural circumferential (σ_θ) and axial (σ_z) stresses resulting from blood pressure (P) and motion of the heart. Increases in P increase wall stress but adaptive thickening restores stress to normal values; decreases in P decrease stress but adaptive thinning restores stress. (**B**) Cells sense and regulate the extracellular matrix via integrins and intracellular contractile structures (actin-myosin filaments). Sensing low versus high stress results in different cell signaling. Misperception of high stress as low stress can result in maladaptive remodeling.

processes. Platelet-derived growth factor (PDGF) is also secreted into the matrix and can be released by matrix metalloproteinases (MMPs), which themselves can be influenced by the mechanical state of the matrix. Once released from the matrix, TGF-β and PDGF modulate the expression of matrix and cytoskeletal proteins, thereby controlling structural integrity. Another key factor is the peptide hormone angiotensin II, which is released from smooth muscle cells in response to cyclic loading (*8*).

A critical aspect of this system is that mechanotransduction depends on cell-generated forces and prestressed cytoskeletal structures (*9*, *10*). This is because the entire aortic wall structure, from the matrix across the cell membrane to the cytoskeleton, is physically interconnected and bears force, with multiple components within this linkage contributing to mechanotransduction. Thus, loss of force anywhere within this chain can inhibit mechanosensing.

Genetic mutations that predispose patients to TAADs (*1*, *2*) affect structural components of the aortic wall (e.g., collagen type III and fibrillin-1–containing microfibrils), cellular force generation (e.g., α-actin, myosin heavy chain, and myosin light chain kinase), and transmembrane structures that transduce mechanical stimuli (e.g., polycystins). Animal models have also revealed additional genes that encode either structural components of the matrix (e.g., fibulin-4 and biglycan) or mechanosensing signaling molecules (e.g., integrin-linked kinase) whose mutation leads to TAADs. This list thus includes genes that affect both structure and the ability to modify structure in response to changes in mechanical loads. These two aspects are interwoven—mechanosensing requires intact load-bearing structures and assembly of load-bearing structures requires intact mechanosensing. Compromising either component will give rise to similar deficiencies in mechanical homeostasis.

Physiological adaptation of the aortic wall to elevated wall stress includes smooth muscle proliferation (e.g., via PDGF), synthesis of collagen and other matrix components (e.g., via TGF-β), and increased cell signaling through angiotensin II receptors. Together, these pathways promote thickening and reinforcement of the vessel wall (*4*–*6*, *11*, *12*). By contrast, adaptation to reduced wall stress includes smooth muscle cell death, elaboration of proteolytic enzymes, and thinning of the wall. Thus, defects in either force transmission or mechanosensing could lead to the misperception of high stress as low stress, which would trigger the activation of catabolic low-force pathways that reduce load-bearing capability. Mutations that lead to loss of mechanosensing might include those in the actomyosin–focal adhesion kinase signaling pathway that senses loads, in the TGF-β or angiotensin pathways that contribute to force-dependent matrix remodeling, in other mechanosensors such as polycystins, and in the matrix itself (e.g., defective fibrillin-1). Such mutations might diminish force-dependent responses so that they fail to keep up with changing mechanical conditions, or alter the homeostatic "set point" such that remodeling is inappropriate for the actual mechanics. Hence, defective structural proteins will give rise to dysfunctional mechanosensing,

CREDIT: V. ALTOUNIAN/*SCIENCE*

which will lead to the formation of defective structures. This may explain why so many distinct mutations generate similar outcomes and account for the elaboration of MMPs in the face of high stresses. Cells that mistake high stress for low stress would likely activate the degradative pathways observed in TAADs.

Seen this way, regulatory pathways that govern mechanotransduction and matrix remodeling are potential targets for treating TAADs. For example, inhibiting a kinase that signals low stress could block maladaptive signaling that contributes to weakening of the aortic wall, whereas activating a pathway that signals high stress might increase wall strength. Understanding the mechanobiology of the thoracic aorta in molecular detail is thus essential to future progress in tackling this disorder.

References

1. D. M. Milewicz *et al.*, *Annu. Rev. Genomics Hum. Genet.* **9**, 283 (2008).
2. M. E. Lindsay, H. C. Dietz, *Nature* **473**, 308 (2011).
3. D. Dajnowiec, B. L. Langille, *Clin. Sci.* **113**, 15 (2007).
4. J. D. Humphrey, *Cell Biochem. Biophys.* **50**, 53 (2008).
5. P. Lacolley, V. Regnault, A. Nicoletti, Z. Li, J.-B. Michel, *Cardiovasc. Res.* **95**, 194 (2012).
6. A. Forte, A. Della Corte, M. De Feo, F. Cerasuolo, M. Cipollaro, *Cardiovasc. Res.* **88**, 395 (2010).
7. S. Li, C. Van Den Diepstraten, S. J. D'Souza, B. M. C. Chan, J. G. Pickering, *Am. J. Pathol.* **163**, 1045 (2003).
8. M. A. Schwartz, *Cold Spring Harb. Perspect. Biol.* **2**, a005066 (2010).
9. Q. Li, Y. Muragaki, I. Hatamura, H. Ueno, A. Ooshima, *J. Vasc. Res.* **35**, 93 (1998).
10. C. C. DuFort, M. J. Paszek, V. M. Weaver, *Nat. Rev. Mol. Cell Biol.* **12**, 308 (2011).
11. S.-Q. Kuang *et al.*, *Arterioscler. Thromb. Vasc. Biol.* **33**, 2172 (2013).
12. W. Li *et al.*, *J. Clin. Invest.* **124**, 755 (2014).

10.1126/science.1253026

PLANETARY SCIENCE

Forming Terrestrial Planets

Recent numerical models may provide a clearer understanding of the forces that shape planetary systems.

John Chambers

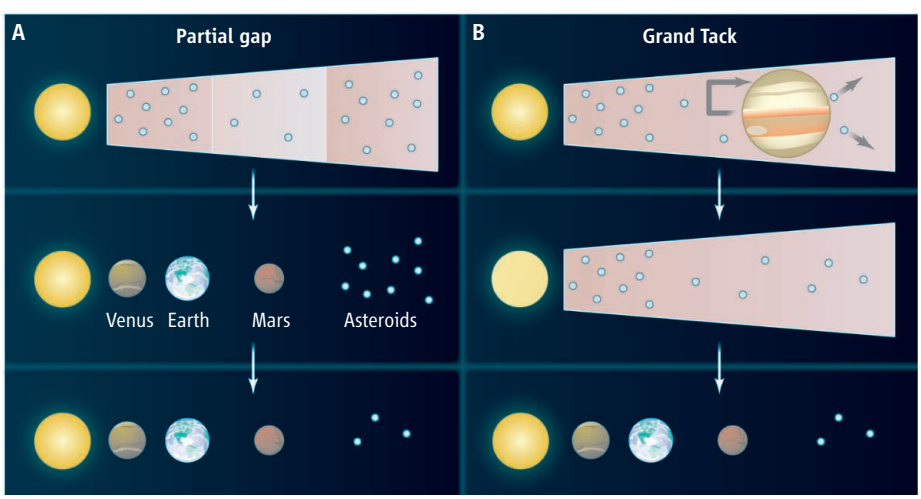
The Sun's rocky planets come in a range of sizes. Mercury weighs in at barely 5% of Earth's mass, perhaps because it formed under harsh conditions close to the Sun. Venus is similar in size to our own planet. However, the modest mass of Mars is perplexing. Current theories for planet formation can explain the gross features of the solar system, such as the dichotomy between its rocky and gas-rich planets, but there is no consensus on why Mars is almost a tenth the mass of Earth and Venus. Now, simulations by Izidoro *et al*. (*1*) show that Mars' small size may date back to a partial gap in the solar nebula, the cloud of gas surrounding the young Sun.

The Sun's planets grew in several steps, beginning with microscopic grains of dust embedded in the solar nebula. These grains clumped together owing to electrostatic forces and gravity to form asteroid-sized planetesimals, which then coalesced into a few dozen planetary embryos. In the outer solar system, where the effect of the Sun's gravity is weak, each embryo held sway over a large region, sweeping up a lot of material as a result. A few objects grew massive enough to pull in gas from the nebula, becoming gas giant planets within a few million years. Closer to the Sun, embryos were smaller, probably similar in size to Mars. The final growth of Venus and Earth involved occasional mergers between these embryos over a time scale of tens of millions of years (*2*).

Department of Terrestrial Magnetism, Carnegie Institution for Science, 5241 Broad Branch Road, NW, Washington, DC 20015, USA. E-mail: jchambers@carnegiescience.edu

The mystery is why Mars failed to grow larger in the same way. Most simulations of planet formation in the solar system produce Mars analogs that are similar in size to Earth (*3*). These simulations usually begin with a solar nebula that varies smoothly with distance from the Sun apart from a jump in the asteroid belt where temperatures became cold enough for water ice to condense. That leaves a lot of material for Mars to sweep up. The masses of the terrestrial planets would be easier to understand if the solar nebula were nonuniform with a depleted region extending outward from Earth's orbit at 1 astronomical unit (AU) (*4*, *5*).

Why would the solar nebula have had such a gap? To date, the most plausible explanation is the Grand Tack model (*6*). In this scenario, the orbits of Jupiter and Saturn migrated inward through the asteroid belt owing to gravitational interactions with the solar nebula, changed tack, and then retreated back to the outer solar system (see the figure, panel B). Most planetesimals and planetary embryos encountered en route were swept up or scattered elsewhere by the giants' gravity. This behavior is consistent with detailed simulations of planetary migration, but the timing of the tack cannot be predicted from first principles, and yet it is critical to the outcome. Provided that Jupiter changed direction close to 1.5 AU, the growth of Mars would be successfully stunted while leaving enough material closer to the Sun to form Earth and Venus (*6*).



Stunted growth. Two ways to stop Mars growing larger. (**A**) If the solar nebula (shown in pink) had a partial gap near Mars' orbit, the growth of solid bodies would have been less effective, reducing the final mass of Mars while allowing Earth and Venus to grow larger. Separate events then depleted the asteroid belt. (**B**) In the Grand Tack model, Jupiter's orbit crossed the asteroid belt twice, removing most planetary building blocks from the region beyond Earth's orbit and reducing the mass of Mars and the asteroid belt.

CREDIT: P. HUEY/*SCIENCE*

Published by AAAS

An added bonus is that the wandering giant planets would have caused mayhem in the asteroid belt. In the Grand Tack model, most planetesimals and planetary embryos were ejected from the belt, and the survivors are a mixture of objects that formed interior and exterior to Jupiter's original orbit. This may explain the paltry mass of the belt today and the diverse characteristics of asteroids' spectra (*7*). However, this diversity may also be a weakness of the model because the wide range of implied formation locations may be hard to reconcile with the isotopic abundances seen in meteorites (*8*).

Izidoro *et al*. propose a less traumatic alternative. They point to simulations of gas flow within the solar nebula (*9*) that suggest that material flowed toward the Sun, moving at different speeds at different distances from the star (see the figure, panel A). As a result, the nebula probably thinned out somewhere between 1 and 3 AU. If this partial gap survived long enough, it could have been preserved in the distribution of planetesimals and planetary embryos that formed subsequently. The simulations performed by Izidoro *et al*. show that reducing the number of planetary building blocks near Mars' current orbit by 50 to 75% favors the formation of a puny red planet.

In both of these models, a Mars-like planet typically forms near 1 AU and is gravitationally scattered into the depleted region of the solar nebula at an early stage. Here the planet is starved of building material and stops growing. This suggests that Mars should be appreciably older than Earth, which is supported by radiometric dating (*10*), and that Earth and Mars should be made of similar stuff. It remains to be seen whether known differences in the two planets' compositions (*11*) are small enough to be consistent with this prediction.

The two models differ when it comes to the asteroid belt. The scenario described by Izidoro *et al*. predicts that the asteroids formed more or less where they are today, and the asteroid belt was depleted gradually over several hundred million years by long-range gravitational perturbations from the giant planets. In the Grand Tack model, the asteroid belt was purged at a very early stage, and the surviving members sample a much larger region of the solar nebula. These differences may help us distinguish between the models in future.

Some caveats are in order. Like all current theories for planet formation, the models described here are incomplete. In particular, we lack a clear understanding of how and where planetesimals formed in the solar nebula, which obviously has a bearing on subsequent events. The final stage of growth is also notoriously chaotic—a tiny change in initial conditions can completely change the final outcome. So, luck played a big role in shaping the solar system. Conventional planet-formation simulations (*12*) generate respectable Mars analogs in a few percent of cases without requiring any special measures. This leaves the slim possibility that Mars represents a bizarre statistical outlier, and its small size contains no deeper truths about our solar system.

References

1. A. Izidoro, N. Haghighipour, O. C. Winter, M. Tsuchida, *Astrophys. J.* **782**, 31 (2014).
2. C. J. Allegre, G. Manhes, C. Gopel, *Earth Planet. Sci. Lett.* **267**, 386 (2008).
3. S. N. Raymond, D. P. O'Brien, A. Morbidelli, N. A. Kaib, *Icarus* **203**, 644 (2009).
4. G. W. Wetherill, in *Protostars and Planets*, T. Gehrels, Ed. (Univ. of Arizona, Tucson, 1977), pp. 565–598.
5. B. M. S. Hansen, *Astrophys. J.* **703**, 1131 (2009).
6. K. J. Walsh, A. Morbidelli, S. N. Raymond, D. P. O'Brien, A. M. Mandell, *Nature* **475**, 206 (2011).
7. J. Gradie, E. Tedesco, *Science* **216**, 1405 (1982).
8. C. M. O'D. Alexander *et al*., *Science* **337**, 721 (2012).
9. L. Jin, W. D. Arnett, N. Sui, X. Wang, *Astrophys. J.* **674**, L105 (2008).
10. N. Dauphas, A. Pourmand, *Nature* **473**, 489 (2011).
11. I. A. Franchi, I. P. Wright, A. S. Sexton, C. T. Pillinger, *Meteorit. Planet. Sci.* **34**, 657 (1999).
12. R. A. Fischer, F. J. Ciesla, *Earth Planet. Sci. Lett.* **392**, 28 (2014).

10.1126/science.1252257

NEUROSCIENCE

A New Wrap for Neuronal Activity?

Neuron activity alters the state of white matter in the mammalian brain.

Marie E. Bechler and Charles ffrench-Constant

As we learn and experience the world around us, our brains are remodeling neuronal pathways. Is this remodeling only a property of neurons, or are other brain cell types also adapting and contributing to learning? A substantial proportion of cells in the mammalian brain are oligodendrocytes and their precursors (collectively called oligodendroglia). Oligodendrocytes generate multiple myelin sheaths, lipid-rich extensions of specialized plasma membrane that spirally coat condensed layers around neurons. This insulation facilitates rapid nerve conduction, increasing velocities of neuron signals 10-fold (*1*) by restricting current flow to the small gaps between sheaths—the nodes of Ranvier. More than half of the human brain is composed of myelinated nerves ("white matter"). With such extensive myelinated neural networks, it raises the questions: Do the myelin-producing oligodendrocytes in the brain also adapt as neural circuits are modified in response to activity, and does adaptation of oligodendrocytes then affect the underlying neural circuits? On page 487 of this issue, Gibson *et al*. (*2*) provide new evidence to address how neuron activity may promote oligodendroglia changes.

Brain magnetic resonance imaging studies of individuals engaging in long-term learning tasks, such as practicing piano, show white matter changes in brain regions associated with these experiences (*3*). Adults learning new skills, such as juggling, also have shown potential changes in myelin (*4*). However, this imaging technique cannot definitively pinpoint changes specific to myelin sheaths, as the measurements may also reflect changes in axon diameter, density, and organization (*3*). Therefore, direct analysis of oligodendrocyte morphology is required. Such analysis in mice has shown a correlation between social isolation and the appearance of fewer and thinner myelin sheaths in brain regions associated with social behavior (*5*, *6*).

Previous studies have linked neuron activity to changes in oligodendrocyte precursor proliferation, differentiation, and myelination. Gibson *et al*. extend these findings using optogenetics, a technique that allows specific neurons expressing a light-sensitive ion channel to be excited by light. Surprisingly, short periods (2.5 min/day for 7 days) of selective stimulation of premotor cortex neurons in juvenile and adult mice, sufficient to induce turning behavior, led to precursor proliferation and increased oligodendrocyte numbers (see the figure). The authors also noted an increase in myelin thickness and improvements in motor function, neither of which was seen

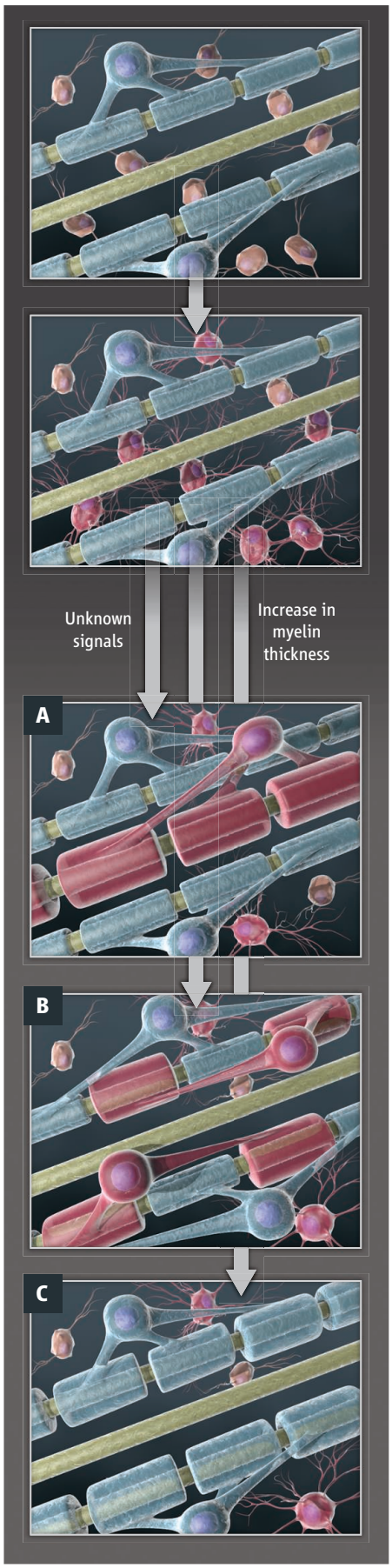
MRC Centre for Regenerative Medicine, University of Edinburgh, Edinburgh EH16 4UU, UK. E-mail: cffc@ed.ac.uk; mbechler@staffmail.ed.ac.uk

Published by AAAS

if stimulation was combined with an inhibitor of epigenetic changes required for cell differentiation. Gibson *et al*. infer that the effects on myelin and motor function are due to adaptive changes in oligodendroglia in response to activity, a conclusion with important implications for understanding brain plasticity.

Verification of this interpretation should address some key questions. How does neuronal firing drive local increases in oligodendroglia proliferation and differentiation? Several secreted molecules from active neurons or responding glia have been reported to increase proliferation and/or differentiation, including platelet-derived growth factor, brain-derived neurotrophic factor, adenosine 5′-triphosphate, and glutamate. Oligodendroglia also have ion channels that may respond to neurotransmitters or local ion concentrations (*7*, *8*). Further work should establish what neuronal firing frequencies and duration are sufficient to elicit physiological changes in these and other potential regulatory signals, and whether the responding oligodendroglia require direct contact with the axon in which activity is increased.

Are the newly formed oligodendrocytes responsible for thicker myelin? Newer oligodendrocytes are normally generated throughout life, and these new cells can incorporate shorter sheaths into already myelinated neuron tracts, perhaps accounting for shorter myelin in older animals (*9*). It will be important to establish the fate of the additional new oligodendrocytes generated in response to neuronal activity. Do they generate the thicker myelin, or do existing oligodendrocytes increase the thickness of the already-formed sheaths? We know that existing sheaths may be dynamic, as they can increase thickness and be retracted once formed (*10*, *11*). Equally, it will be important to consider whether the increased number of precursors (that may have homeostatic roles in their own right), rather than changes in myelination, may be contributing to any behavioral effects observed.



Adaptive oligodendroglia. Activation of neurons (green) in the mouse premotor cortex increases the proliferation of oligodendrocyte precursors (orange), which differentiate into oligodendrocytes (red). The increased myelin thickness observed could have several possible explanations (not mutually exclusive): (**A**) myelination of unmyelinated axons by the new oligodendrocytes (red); (**B**) intercalation of new sheaths on myelinated axons; (**C**) thickening of existing sheaths (blue). The (unknown) signals responsible may be released by the active axons, leading to thicker myelin on neighboring axons even if their activity levels are not altered.

CREDIT: C. BICKEL/*SCIENCE*

Does an increase in myelin thickness affect axonal conduction? Changes in myelin affect conduction velocity and could thereby influence the timing of signals throughout the nervous system—coordination required for synchronization or staggering to permit meaningful interpretation of sensory input and orchestration of fine movements (*12*). However, conduction velocity is also controlled by myelin sheath length, and the response of length to activity needs to be quantified. It cannot be assumed that any changes will speed conduction; although increasing myelin sheath length and thickness up to a limit will increase conduction velocities, there is a maximum beyond which these properties no longer increase velocity (*1*, *13*). Whether thinning, shortening, or loss of myelin occurs, and whether this results from reduced activity, is also important to determine.

The concept of myelin as an adaptable structure that changes to modulate the conduction of neurons, rather than a static structure with set properties, has many implications for understanding how neuronal circuits work in the adult, aged, healthy, and diseased brain. The use of optogenetics to probe adaptive myelination is an important technological advance and may be valuable for further experiments to explore this hypothesis. Further work should explore the dynamics of these changes, whether diminished activity causes reduction or retraction of existing sheaths, and whether myelin can be adapted in brain regions that, unlike the corpus callosum examined by Gibson *et al*., have very few unmyelinated axons. Determining mechanisms for modifying specific myelin sheath properties also will deepen our understanding of how glia contribute to learning and adapting from experience.

References

1. W. A. H. Rushton, *J. Physiol.* **115**, 101 (1951).
2. E. M. Gibson *et al*., *Science* **344**, 1252304 (2014); 10.1126/science.1252304.
3. R. J. Zatorre, R. D. Fields, H. Johansen-Berg, *Nat. Neurosci.* **15**, 528 (2012).
4. C. Sampaio-Baptista *et al*., *J. Neurosci.* **33**, 19499 (2013).
5. J. Liu *et al*., *Nat. Neurosci.* **15**, 1621 (2012).
6. M. Makinodan, K. M. Rosen, S. Ito, G. Corfas, *Science* **337**, 1357 (2012).
7. R. Káradóttir, N. B. Hamilton, Y. Bakiri, D. Attwell, *Nat. Neurosci.* **11**, 450 (2008).
8. P. P. Maldonado, M. Vélez-Fort, F. Levavasseur, M. C. Angulo, *J. Neurosci.* **33**, 2432 (2013).
9. K. M. Young *et al*., *Neuron* **77**, 873 (2013).
10. S. Goebbels *et al*., *J. Neurosci.* **30**, 8953 (2010).
11. T. Czopka, C. ffrench-Constant, D. A. Lyons, *Dev. Cell* **25**, 599 (2013).
12. A. H. Seidl, *Neuroscience* 10.1016/j.neuroscience.2013.06.047 (2013).
13. L. M. N. Wu, A. Williams, A. Delaney, D. L. Sherman, P. J. Brophy, *Curr. Biol.* **22**, 1957 (2012).

10.1126/science.1254446

Published by AAAS

CHEMISTRY

Assembly and Disassembly of Ferrocene-Based Nanotubes

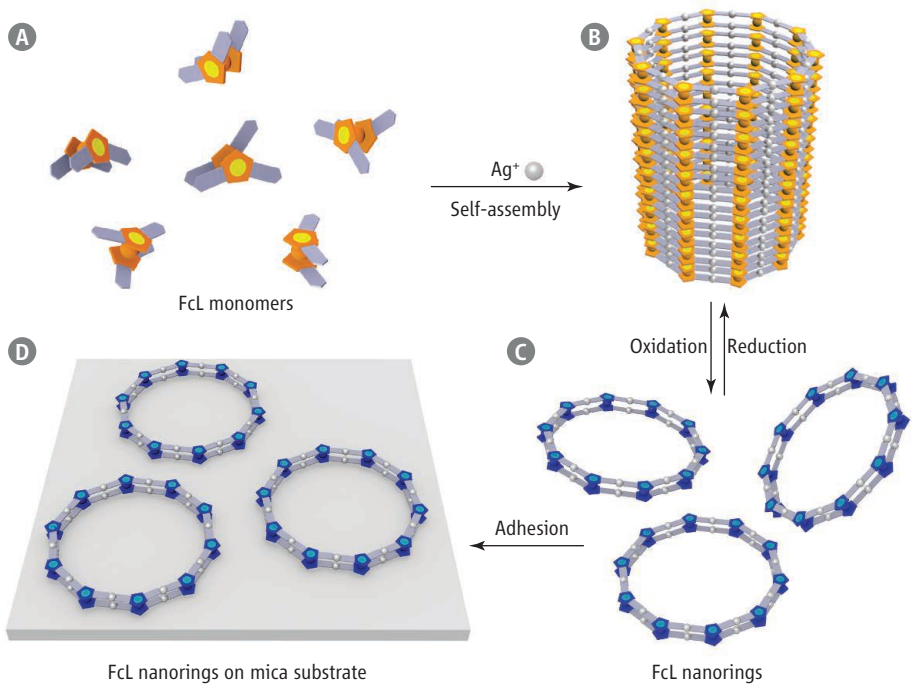
The stacked rings of a nanotube can be dissociated and reassembled through oxidation and reduction of its constituent metal complexes.

Zachary M. Hudson and Ian Manners

Harnessing noncovalent interactions to create controlled routes to functional materials with nanoscopic dimensions is a key challenge in contemporary chemical science. The use of molecular species, polymers, and nanoparticles as building blocks combined with self-assembly approaches that involve hydrogen-bonding, π-stacking, coordination or metallophilic interactions (*1*–*5*), immiscibility and solvophobicity (*6*–*8*), or crystallization (*9*) has led to a range of important recent advances. The introduction of further complexity through multistep processing and the manipulation of the resulting nanostructures through attenuation and enhancement of noncovalent forces represent examples of important further goals, but much remains to be achieved with respect to these objectives. On page 499 of this issue, Fukino *et al*. (*10*) provide an elegant demonstration of how π-stacking and metallophilic interactions can be used to control the assembly of ferrocene-based molecular building blocks into ordered and complex nanoscale objects. They report the selective assembly of ferrocene-based units into large-diameter nanotubes that can then be reversibly cleaved into nanorings.

Metal-containing species represent attractive components of self-assembled materials (*5*). For example, ferrocene, the prototypical "metal sandwich" species, is both inexpensive and stable, and also exhibits versatile derivatization chemistry and remarkable properties. Thus, the cyclopentadienyl group freely rotates about its bond to the iron atom, which has been likened to a ball-bearing (*11*), and ferrocene can undergo reversible electron loss to generate the stable blue ferrocenium ion under mild conditions. The latter feature has been exploited in polymeric ferrocene–containing materials to generate redox-switchable gels and capsules with uses as actuators in photonic crystal displays and as containers with walls of tunable permeability (*5*, *12*).

Fukino *et al*. assemble ferrocene-based building blocks bearing pyridyl ligands (see the figure). Upon the addition of silver cations (Ag^+), these complexes readily assemble into nanotubes with diameters of 7.2 nm or 13.3 nm, depending on the particular size of the building block. The selectivity of this process is made possible by the dynamic nature of the ferrocene units, which exhibit free rotation in solution. The presence of π-π stacking between the ferrocene centers, as well as Ag-Ag metallophilic interactions, appears essential to the hierarchical self-assembly process and nanotube stability. Fukino *et al*. characterized these structures through modeling studies and also through detailed x-ray diffraction measurements on thin films of nanotubes that had been oriented in a magnetic field. The resulting structures of the nanotube walls were consistent with the presence of giant 200- or 360-membered nanoring subcomponents, each constructed from 10 bent ferrocene-based units together with 20 Ag^+ cations. The periphery of the nanotubes was proposed to contain oligoethylene glycol chains derived from the molecular building blocks, together with counteranions from the Ag^+ salt.



The ring-assembly cycle. Fukino *et al*. prepared ferrocene-based building blocks bearing pyridyl ligands (FcL) (**A**) that readily self-assemble in the presence of Ag^+ to give nanotubes (**B**) containing discrete 200- and 360-membered nanorings. This process is driven by noncovalent π-π stacking and metallophilic interactions between the Ag(I) centers. Oxidation of the ferrocene units leads to disassembly of the nanotubes into giant polycationic nanorings (**C**) in a process driven by electrostatic repulsion. Reassembly into nanotubes can then be induced by chemical reduction back to neutral nanorings. In the oxidized state, the giant cationic nanorings can be "pasted" onto anionic substrates such as mica (**D**).

The authors go on to demonstrate that assembly to form nanotubes can be reversed by taking advantage of the redox chemistry of ferrocene. Oxidation of the ferrocene units causes the stacking interactions to be weakened because of electrostatic repulsion and disassembles the nanotubes. The giant polycationic nanorings are released and then can be readily "pasted" onto anionic mica substrates. The surfaces are decorated with uniform toroidal nano-objects. Reduction of the oxidized nanorings causes them to reassemble into uniform nanotubes. However, this process is rather slow, presumably as a result of the high entropic barrier.

The mechanism of the initial Ag(I)-mediated formation for the nanotubes represents a particularly intriguing feature of

School of Chemistry, University of Bristol BS8 1TS, UK. E-mail: ian.manners@bristol.ac.uk

CREDIT: ZACHARY M. HUDSON/SCHOOL OF CHEMISTRY, UNIVERSITY OF BRISTOL

Published by AAAS

this work. As noncovalent interactions tend to be weaker than covalent bonds, the steps in a self-assembly process are often reversible—such that errors made are readily "corrected" as the assemblies funnel toward the thermodynamically most favorable arrangement. The reversibility of this type of assembly process lends itself well to the construction of large, intricate structures that would be difficult to access by traditional covalent synthesis. Fukino *et al*. speculate that the initial nanotube formation from their ferrocene-based building blocks is a stochastic process that does not involve the initial formation of nanorings for entropic reasons but rather doubly-bridged oligomeric units. With respect to the formation of the latter units, the added Ag^+ cations are believed to induce an eclipsed geometry and a bent shape to the molecular building blocks because of metallophilic interactions. The oligomers are then proposed to stack into curved sheets that ultimately form the observed nanotubes.

The results reported by Fukino *et al*. open the door to many fascinating new possibilities. The generation of other shaped molecular precursors and their subsequent dynamic self-assembly is expected to be a fertile field for future discovery. Moreover, the manipulation of noncovalent stacking interactions in the resulting nanostructures and the ability to paste to substrates offer interesting opportunities in nanoscience for both synthesis and patterning.

References

1. T. F. De Greef *et al*., *Chem. Rev.* **109**, 5687 (2009).
2. M. Yoshizawa, J. K. Klosterman, M. Fujita, *Angew. Chem. Int. Ed.* **48**, 3418 (2009).
3. R. Chakrabarty, P. S. Mukherjee, P. J. Stang, *Chem. Rev.* **111**, 6810 (2011).
4. M. Kastler, W. Pisula, D. Wasserfallen, T. Pakula, K. Müllen, *J. Am. Chem. Soc.* **127**, 4286 (2005).
5. G. R. Whittell, M. D. Hager, U. S. Schubert, I. Manners, *Nat. Mater.* **10**, 176 (2011).
6. J. Zhu *et al*., *Nat. Commun.* **4**, 2297 (2013).
7. A. H. Gröschel *et al*., *Nat. Commun.* **3**, 710 (2012).
8. L. A. Fielding *et al*., *Chem. Sci.* **4**, 2081 (2013).
9. P. A. Rupar, L. Chabanne, M. A. Winnik, I. Manners, *Science* **337**, 559 (2012).
10. T. Fukino *et al*., *Science* **344**, 499 (2014).; 10.1126/science.1252120.
11. C. Li *et al*., *J. Am. Chem. Soc.* **119**, 1609 (1997).
12. Y. Ma, W. -F. Dong, M. A. Hempenius, H. Möhwald, G. J. Vancso, *Nat. Mater.* **5**, 724 (2006).

10.1126/science.1254140

PHYSICS

Nonlinear Optics Pushed to the Edge

The edges of small flakes of atomically thin crystals become directly visible at optical wavelengths by doubling the frequency of input infrared light.

Dragomir Neshev and Yuri Kivshar

Nonlinear optics describes processes in which coherent photons change their properties, such as their frequency, when they pass through a medium. This field traces back to the demonstration of frequency doubling (*1*)—generating photons with twice the frequency of the input laser light—via second-harmonic generation [(SHG); see the figure, panel A]. Because SHG is a second-order parametric process, the symmetry of the medium must lack inversion symmetry (*2*). Interfaces between bulk (or three-dimensional) materials can meet this criterion, which has made SHG microscopy an indispensable tool for their study (*3*). On page 488 of this issue, Yin *et al*. (*4*) open a new dimension in second-harmonic microscopy with the optical visualization of the edge modes in two-dimensional (2D), atomically thick materials (*5*).

These 2D materials are composed of single or a few layers of atoms or molecules and include graphene, boron nitride, and transition metal dichalcogenides such as molybdenum disulfide (MoS_2). However, when the lateral dimensions of these materials are reduced to create small flakes, structural discontinuities appear at the edges and boundaries between different flakes that break in-plane translational symmetry. These regions support strongly localized electron states that are expected to enhance SHG.

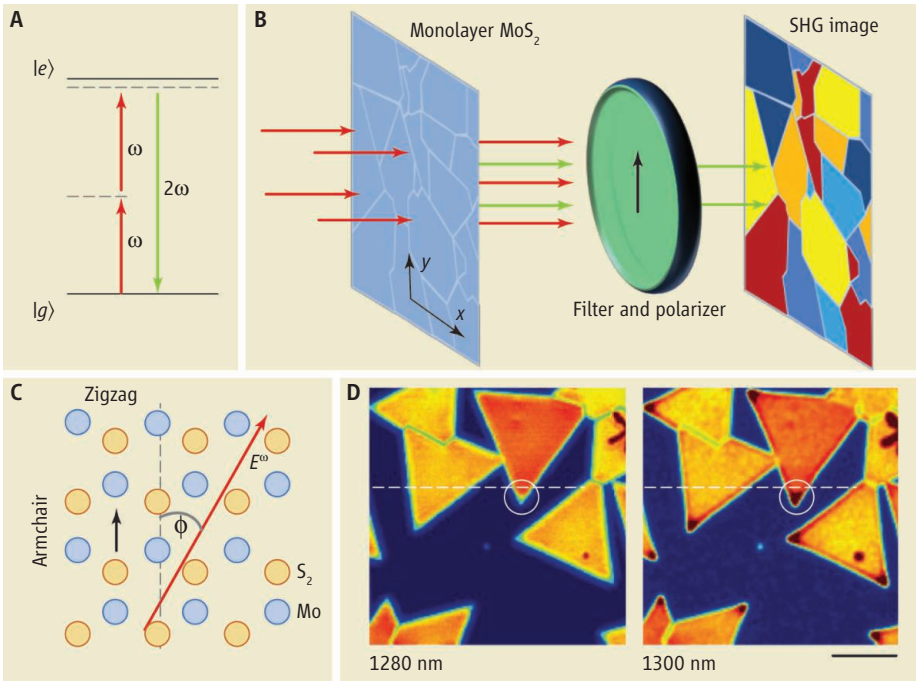
Yin *et al*. used second-order nonlinear optics to study the edges and boundaries of the hexagonal lattice of MoS_2 atomic membranes, grown by large-scale chemical vapor deposition techniques. Previous studies have applied SHG spectroscopy to few-layer MoS_2 and other 2D materials (*6*–*9*). Notably, MoS_2 with an odd number of layers lacks inversion symmetry, while for an even number of layers the transverse inversion symmetry is restored. As such, the SHG signal from MoS_2 with odd numbers of layers was orders of magnitude more intense than that for even numbers of layers (*6*–*9*). This method provides strong contrast between single and bilayer samples. For MoS_2 structures with odd numbers of layers, the exact number of layers can also be determined from the strong variation of SHG intensity.

For a monolayer of MoS_2, the longitudinal phase matching (longitudinal here is in the z direction, and transverse is across the 2D plane, x and y; see the figure, panel B) is not important, and the SHG emission is emitted equally in both the forward and backward directions. However, the strength of emission strongly depends on the transverse symmetry and phase matching (*10*). The SHG signal also depends strongly on the orientation of the crystal. For example, for x-polarized pump beams (see the figure, panel B), the SHG signal can have x or y polarization with powers $P_x^{2\omega} \approx \cos 3\phi$ and $P_y^{2\omega} \approx \sin 3\phi$, respectively, where ϕ is the angle between the incident polarization and the crystal orientation (see the figure, panel C). The measurement of $P_x^{2\omega}$ and $P_y^{2\omega}$ allows the orientation of the crystallographic axes to be determined. Yin *et al*. performed such a nonlinear optical imaging technique that allows rapid determination of the crystal orientations at a large scale (see the figure, panel B). The presence of constructive or destructive interference of the SHG signal at the boundary between two flakes could even discriminate between two MoS_2 flakes with opposite crystal orientations.

This purely optical method for characterizing MoS_2 requires minimal sample preparation, is noninvasive, and imposes no special environmental requirements. However, the most exciting results arise from the second-order nonlinear susceptibility being highly sensitive to extremely small changes in materials' electronic properties. If the small MoS_2 flakes possess internal energy levels resonant with either the input or SHG radiation (*2*), these internal resonances will show up in the SHG signal. Such small flakes can be obtained in the chemical vapor deposition process for short growth time and appear as small triangles (see the figure, panel D).

Nonlinear Physics Center, Australian National University, Canberra, ACT 0200, Australia. E-mail: ysk@internode.on.net; dnn124@physics.anu.edu.au

Published by AAAS



Edges do a frequency-doubled take. (**A**) In a second-harmonic generation (SHG) process, two photons of frequency ω (red arrows) absorbed by the ground state $|g\rangle$ combine to form a high-frequency (2ω) photon (green arrow). The proximity of atomic states (or edge states $|e\rangle$) to the energy 2ω of the output beam strongly enhances the generation of harmonics. (**B**) The SHG signal depends on the orientation of the MoS_2 flakes and the incident polarization of the excitation laser. The SHG image shows flakes of different brightness (encoded with different colors) for different crystal orientations. (**C**) Two-dimensional crystal orientation and incident field polarization. (**D**) Yin *et al*. show that when the energy of the two pump photons is near the SHG frequency, the harmonic is strongly enhanced, as seen in the edge modes on the right circled in white; scale bar, 20 μm.

Although rough at the atomic scale, the edges of these monolayer islands are the more energetically favorable termination of MoS_2 zigzag edges, and they appear straight and sharp under the optical microscope. These zigzag edges have localized electronic states because they break translational symmetry. As Yin *et al*. show in proof-of-concept calculations, these edge modes have energies just below the band gap of an infinite MoS_2 monolayer. The localized electronic states enhanced in-plane nonlinear polarizability, and the resulting SHG enhancement allowed the direct optical imaging of the atomic edges.

Why were Yin *et al*. the first to optically observe such edge states? Other groups (*6*–*9*) used pump wavelengths of ~800 nm, but Yin *et al*. tuned their laser precisely at a two-photon resonance with the energy of the edge states, namely at ~1300 nm. They measured a well-pronounced maximum for the SHG from the edge states. Comparing the left and right images in panel D of the figure, even a detuning of 20 nm from the resonant input wavelength causes the signature of the edge states to completely disappear.

Edge states play an important role in electron dynamics for the quantum Hall effect and topological insulators, and the understanding of their physics is an important goal in realizing robust topological states in both solids and optics. Optical monitoring of the dynamics of such edge states could further clarify the mechanism of electrocatalytic hydrogen evolution (*11*). The direct mapping of edge states by optical methods developed by Yin *et al*. is an important step toward these goals. The nonlinear response reveals the structural and symmetry properties of 2D atomic monolayers, and it would allow the exploration of other types of 2D crystalline structures.

References

1. P. A. Franken, A. Hill, C. Peters, G. Weinreich, *Phys. Rev. Lett.* **7**, 118 (1961).
2. R. W. Boyd, *Nonlinear Optics* (Academic Press, San Diego, CA, ed. 3, 2008).
3. Y. R. Shen, *Nature* **337**, 519 (1989).
4. X. Yin *et al*., *Science* **344**, 488 (2014).
5. K. S. Novoselov *et al*., *Science* **306**, 666 (2004).
6. H. Zeng *et al*., *Sci. Rep.* **3**, 1608 (2013).
7. N. Kumar *et al*., *Phys. Rev. B* **87**, 161403 (2013).
8. L. M. Malard, T. V. Alencar, A. P. M. Barboza, K. F. Mak, A. M. de Paula, *Phys. Rev. B* **87**, 201401 (2013).
9. Y. Li *et al*., *Nano Lett.* **13**, 3329 (2013).
10. S. M. Saltiel *et al*., *Phys. Rev. Lett.* **100**, 103902 (2008).
11. T. F. Jaramillo *et al*., *Science* **317**, 100 (2007).

10.1126/science.1253531

BOTANY

Limits on Yields in the Corn Belt

Increasing vapor pressure deficit and drought sensitivity will limit future corn yields in the U.S. Midwest.

Donald R. Ort[1,2] and Stephen P. Long[2]

In total global production, corn (maize, *Zea mays* L.) is the most important food and feed crop. Of the 967 million metric tons produced in 2013, 36.5% were produced in the United States, mostly in the Midwest Corn Belt. The United States is by far the world's largest corn exporter, accounting for 50% of corn exports globally (*1*, *2*).

[1]Global Change and Photosynthesis Research Unit, USDA/ARS, University of Illinois, Urbana, IL 61801, USA. [2]Departments of Plant Biology & Crop Sciences, University of Illinois, Urbana, IL 61801, USA. E-mail: d-ort@igb.illinois.edu

Until recently, breeding and management have allowed farmers to increase the number of plants per acre without loss of yield per plant. On page 516 of this issue, Lobell *et al*. (*3*) use a detailed data set for farms across the Corn Belt, to show that increasing yields have been accompanied by rising drought sensitivity, with important implications for future crop yields.

The data set contains yields, environmental variables, and management variables for Midwest corn fields in each year from 1995 to 2012. Lobell *et al*.'s analysis reveals that while corn yield has increased, drought sensitivity has also increased. This may be explained by the fact that with more plants per acre, less soil water is available to each plant. Yield was most sensitive to water vapor pressure deficit (VPD), a factor that has rarely been included in past analyses but that has major implications for yields as climate change progresses in the Corn Belt.

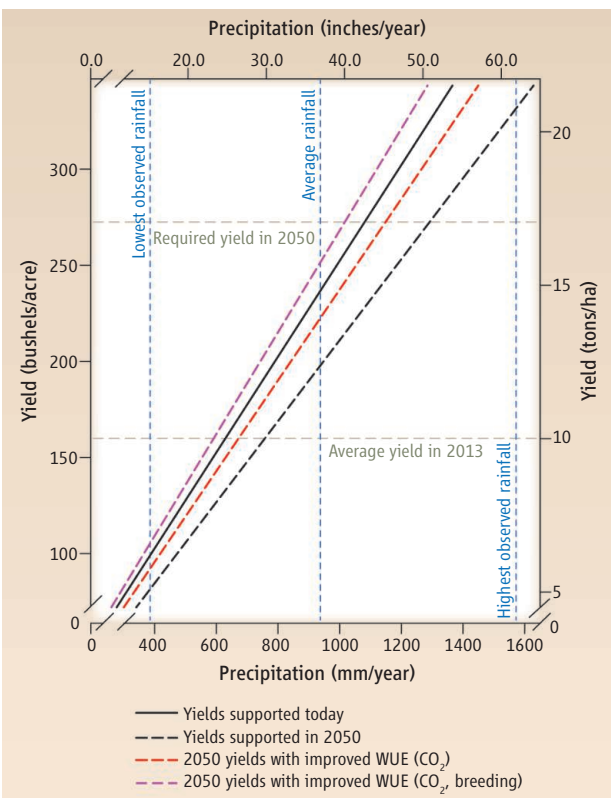
So what is the VPD, and why is it so important to crop production? To assimilate CO_2

Published by AAAS

from the atmosphere, crop leaves must expose wet surfaces on the photosynthetic cells inside the leaf to the atmosphere. Pores (stomata) in the leaf surface open to allow CO_2 to diffuse to these wet surfaces; the same pores simultaneously allow water vapor to escape. This evaporation of water from the leaf, called transpiration, is an inescapable consequence of carbon assimilation by a crop. Through this process, 99% of the water absorbed by crop roots is lost to the atmosphere. The amount of carbon assimilated per unit of water lost is termed the water use efficiency of a crop (WUE). However, the rate of transpiration is proportional to the humidity gradient between the water vapor–saturated leaf interior and the drier bulk air; this gradient is the VPD. VPD can increase with rising temperature even if relative humidity (RH) rises. Although RH is most commonly reported, it is VPD and not RH that is directly proportional to water loss from crop leaves.

Lobell *et al*. show that VPD is expected to increase across their study area from 2.2 kPa today to 2.65 kPa by 2050. To understand the effect of this increase, consider that today, average precipitation across the study area is 37 inches (940 mm) per year. If we assume that 70% of this water is available to the crop, with the remaining 30% lost in drainage and runoff, then a VPD of 2.2 kPa would support a yield of 214 bushels per acre (see table S1). This is more than enough water to support the 2013 average yield of ~170 bushels per acre but would limit yield in areas receiving less than 25 inches of precipitation. If VPD rises to 2.65 kPa, an average rainfall of 37 inches would only support 192 bushels per acre (see the figure), making production far more vulnerable even to moderate droughts. However, if improved genetics and agronomy can achieve the 70% yield increase to 272 bushels per acre projected to be needed by 2050 (*4*, *5*), this would require 50 inches of precipitation per year (see the figure). Today, production across the study region is largely rainfed, but meeting these targets would require irrigation. Such a productivity increase is unlikely to be sustainable with respect to water resources. Are there any prospects that this demand could be mitigated?

A direct effect of rising atmospheric CO_2 concentrations is to increase WUE at the leaf level. This is because at higher atmospheric CO_2 concentrations, leaves can gain the CO_2 needed for photosynthesis with their stomata less open. Thus, less water is lost per CO_2 molecule assimilated. However, few studies have attempted to quantify this assumed benefit in a farm field. A study with soybean found that elevation of CO_2 to the anticipated 2050 level increased WUE by 12.5% on average across 4 years (*6*). A similar increase in WUE for corn would lower 2050 water demand to 44 inches, still well above current average regional precipitation.



Balancing corn yield and water needs. Across the three major Corn Belt states covered by Lobell *et al*.'s study, a given amount of precipitation will support average corn yields given by the black line. Lower yields would be supported under the higher VPD conditions projected for 2050 (dashed black line). If the anticipated rise in atmospheric CO_2 concentrations over this period leads to improved water use efficiency, this would raise yields somewhat (dashed red line). Breeding to optimize crop water use efficiency could lead to further improvements (dashed purple line). The central vertical blue line represents the mean rainfall for this area (calculated over a 36 year period to 2010), the left-hand vertical line the lowest annual rainfall during this period, and the right-hand vertical line the highest. The lower horizontal line gives the mean yield for 2013, and the upper horizontal line the yield projected to be needed to meet the growth in global demand for corn by 2050. Even in the most optimistic case, on average, there will only be sufficient rain to support about half of the increase in yield needed by 2050.

An opportunity to further increase WUE was shown by a recent computational analysis that considered where within the crop canopy photosynthesis occurs (*7*). Normally, most photosynthesis occurs near the top of the canopy, where the humidity is closest to that of the bulk atmosphere and WUE is lowest. By making leaves more vertical or leaves at the top of the canopy less pigmented, light and thus photosynthesis could be distributed to deeper layers. This approach could increase WUE because humidity increases with depth into a crop canopy, allowing photosynthesis to occur at a lower VPD. A canopy bred to take full advantage of this principle could increase WUE by 13%, further lowering the 2050 water demand to 40 inches, but would still have substantial drought vulnerability.

These projections assume that the effect of VPD is mainly through photosynthetic productivity, as indicated by Lobell *et al*.'s study. However, the study raises a potentially grave concern beyond 2050, when yields are projected to decline at an accelerating rate with increasing VPD, perhaps because of other VPD-sensitive factors such as pollination. Beyond a VPD of about 2.8 kPa, yield decline with VPD becomes much sharper, with possible average yield losses of 40% as early as 2060. Thus, although rising CO_2 and crop redesign could provide some mitigation, the only real solution will be to avoid the CO_2 emissions that will otherwise cause rises in temperature (*8*) and, in turn, VPD.

References

1. Food and Agriculture Organization of the United Nations (FAO), (FAO Statistical Databases, Rome, 2013); http://faostat.fao.org.
2. The 2012 Statistical Abstract, Agriculture: Agricultural Exports and Imports 849—Agricultural Exports and Imports—Value (United States Census Bureau, Department of Commerce, 2012); www.census.gov/compendia/statab/cats/agriculture.html.
3. D. B. Lobell *et al*., *Science* **344**, 516 (2014).
4. N. Alexandratos, J. Bruinsma, *World Agriculture Towards 2030/2050: The 2012 Revision No. 12-03* (UN FAO, Rome, 2012).
5. D. Tilman, C. Balzer, J. Hill, B. L. Befort, *Proc. Natl. Acad. Sci. U.S.A.* **108**, 20260 (2011).
6. C. J. Bernacchi, B. A. Kimball, D. R. Quarles, S. P. Long, D. R. Ort, *Plant Physiol.* **143**, 134 (2007).
7. D. T. Drewry, P. Kumar, S. P. Long, *Glob. Change Biol.* **20**, 10.1111/gcb.12567 (2014).
8. IPCC, *Climate Change 2014: Impacts, Adaptation, and Vulnerability. Contribution of Working Group II to the Fifth Assessment Report of the Intergovernmental Panel on Climate Change.* C. B. Field, V. Barros, K. Mach, M. Mastrandrea, Eds. (Cambridge Univ. Press, Cambridge/New York, 2014).

Supplementary Materials

www.sciencemag.org/content/344/6183/484/suppl/DC1
Table S1

10.1126/science.1253884

Published by AAAS

READ THE FULL ARTICLE ONLINE
http://dx.doi.org/10.1126/science.1247579

A framework is proposed to guide the selection and integration of different climate-change metrics in biodiversity impact assessments.

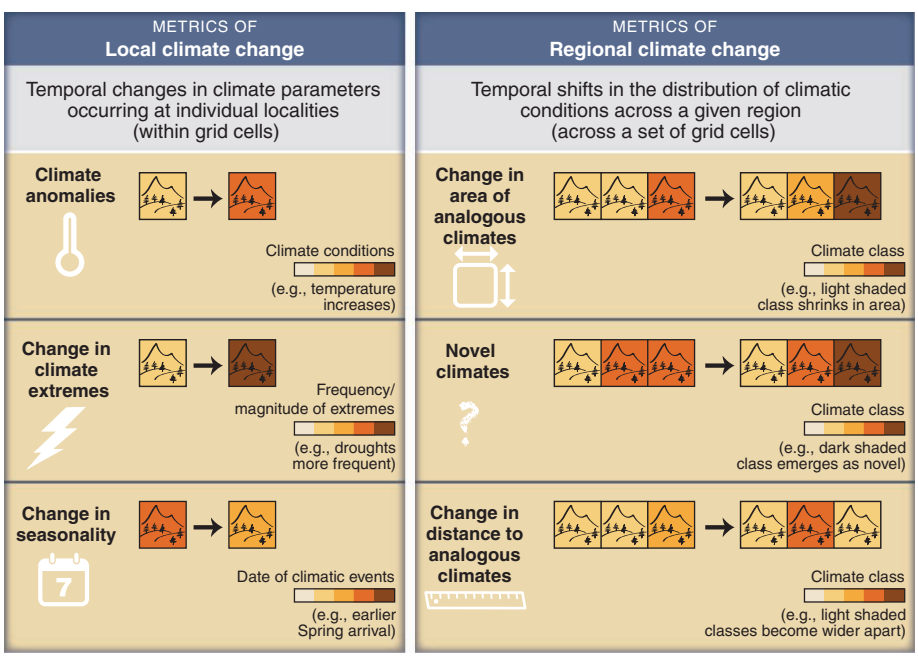
Multiple Dimensions of Climate Change and Their Implications for Biodiversity

Raquel A. Garcia,* Mar Cabeza, Carsten Rahbek, Miguel B. Araújo*

Background: Changes in Earth's climate over time can be measured in many ways. The different metrics available represent alternative dimensions of climate change, each with distinct implications for biodiversity conservation and other sectors. However, this diversity is rarely recognized. At any given locality, average temperature or precipitation can increase or decrease, extreme values can become more intense or frequent, and the timing of specific climatic events can shift. At the same time, climatic conditions are redistributed at broader spatial extents. Across sets of localities, particular climatic conditions can become more or less available and can shift closer or farther in position at different velocities. Metrics quantifying these and other dimensions of change are commonly used in basic and applied sciences. In ecological contexts, individual metrics have helped to explain the role of past climate changes in driving species diversity or extinctions and to forecast the exposure of biodiversity to future climate changes. Yet, a comparison of the many alternative metrics in use is lacking to gain understanding of their properties and guide their use in biodiversity assessments.

Advances: Our review demonstrates that six commonly used metrics of climate change show contrasting patterns under 21st-century climate forecasts across the world. For example, whereas polar climates are projected to warm and shrink in area, the tropics see the emergence of novel climatic conditions and undergo local changes in average climates beyond past variability. To help interpret metrics of climate change, our review critically assesses the ecological implications of different metrics. Supported by examples of empirical links between observed changes in biological systems and different dimensions of climate change, we outline a conceptual framework for classification of climate change metrics according to the types of threat and opportunity they are likely to impose on biodiversity. Climate changes at the locality level are often associated with demographic threats and opportunities at the population level, whereas changes across localities can have positive or negative implications for the size and the position of species' ranges.

Outlook: Forecasting the long-term impacts of future climate changes on biodiversity is challenging, not least because the responses of organisms are contingent on demographic, physiological, and evolutionary mechanisms, as well as on the interaction with other human-induced stressors such as habitat fragmentation. Lack of data for the majority of species on Earth further hampers the use of available bioclimatic modeling methods. By contrast, the use of simple metrics of climate change is more easily scalable to wholesale biodiversity. When appropriately implemented, such examination can provide a first-order assessment of the challenges that species are potentially exposed to, and in many circumstances, it might be the only option available.



The diversity of metrics of climate change. Climate parameters, such as temperature or precipitation, can change at individual localities over time (left), whereas shifts in the distribution of climatic conditions across sets of localities can also occur (right). Local metrics can quantify changes in the magnitude of average or extreme values, as well as shifts in the timing of climatic events. Regional metrics describe how specific climatic conditions may increase or decrease in area, become more dissimilar to past climatic conditions, or move in space. These and other commonly used metrics of climate change describe different dimensions of change and are expected to relate to distinct challenges for biodiversity. Different metrics thus provide complementary information when describing future climates and their potential effects. Examining metrics in combination can show how they interact to exacerbate or lessen species' exposure to climate change.

The list of author affiliations is available in the full article online.
*Corresponding author. E-mail: raquel.ag@gmail.com (R.A.G.); miguel.araujo@imperial.ac.uk (M.B.A.)
Cite this article as R. A. Garcia *et al.*, *Science* **344**, 1247579 (2014). DOI: 10.1126/science.1247579

Multiple Dimensions of Climate Change and Their Implications for Biodiversity

Raquel A. Garcia,[1,2,3,4]* Mar Cabeza,[4] Carsten Rahbek,[2,5] Miguel B. Araújo[1,2,3,5]*

The 21st century is projected to witness unprecedented climatic changes, with greater warming often reported for high latitudes. Yet, climate change can be measured in a variety of ways, reflecting distinct dimensions of change with unequal spatial patterns across the world. Polar climates are projected to not only warm, but also to shrink in area. By contrast, today's hot and arid climates are expected to expand worldwide and to reach climate states with no current analog. Although rarely appreciated in combination, these multiple dimensions of change convey complementary information. We review existing climate change metrics and discuss how they relate to threats and opportunities for biodiversity. Interpreting climate change metrics is particularly useful for unknown or poorly described species, which represent most of Earth's biodiversity.

The interaction between the climatic changes projected for the 21st century and other ongoing human-induced threats, such as habitat loss, presents a major challenge to biodiversity (*1*, *2*). Accurate forecasts of climate change effects on biodiversity are thus required to address broader societal commitments toward natural resource management and conservation (*3*, *4*). To address this problem, researchers have developed a range of bioclimatic models. Statistical models (*5*) measure species' exposure to climate change by relating species' distributions to aspects of climate. By contrast, mechanistic models explicitly consider demographic (*6*) and physiological (*7*) processes to predict species' responses to climate change exposure. Given the limited availability of demographic and physiological data, most assessments of climate change effects on biodiversity use statistical rather than process-based models. Yet, for most species on Earth, distributional data are also lacking so that even the simplest statistical model cannot be fitted. An alternative is to use simple metrics of climate change to quantify the exposure of areas to different dimensions of change and relate these dimensions to different threats and opportunities for biodiversity [e.g., (*8*–*11*)].

The anomalies in climate parameters at any given locality over time are a commonly used metric, but a vast array of alternative metrics exists. They include temporal differences in extreme events, such as droughts; decreases or increases in total area with given climatic conditions; and the velocity at which climate moves across space and time. Such climate change metrics have been applied to a variety of questions. For example, when coupled with climate hindcasts, they have been used to examine the role of historical climatic changes in species richness gradients (*12*–*15*), the geographical distribution of centers of diversity (*16*) or past climatic refugia (*17*, *18*), the pace of distributional shifts of species over past decades (*19*) or millennia (*20*), the risk of species extinctions (*21*), and the degree of biotic network specialization across latitude (*22*). When coupled with climate change forecasts, they have supported risk assessments for biodiversity (*8*, *10*, *11*, *23*–*27*) and conservation areas (*9*, *28*–*30*), while also enabling the identification of potential regional pools of species (*31*).

Despite the increased use of climate change metrics in basic and applied sciences, the variety of existing metrics and their ecological implications have hitherto not been fully appreciated. Studies spanning different geographical areas have used single metrics (*11*, *16*, *26*, *29*) more frequently than multiple metrics in combination (*21*, *23*, *24*). A comprehensive comparison of metrics, including the analysis of their global patterns and implications for biodiversity, is thus needed to gain understanding of their properties and guide their use. Here, we review the climate change metrics commonly used in biodiversity assessments. We first describe the different types of metrics and illustrate their differences by implementing six of the most commonly used metrics with global 21st-century climate projections. We then explore how the different metrics capture distinct dimensions of climate change and carry complementary information that is vital for understanding the potential impacts of ongoing climate changes on biodiversity. Finally, we outline a conceptual framework for linking the different metrics to assessments of threat and opportunity for species and discuss its advantages and limitations.

Climate Change Metrics

Metrics of climate change describe temporal changes in single or multiple climate parameters, such as temperature or precipitation. Existing metrics fall into one of two categories (Box 1 and table S1). They measure either temporal changes in climate parameters at individual localities (hereafter termed "local metrics"), or shifts in the distribution of climatic conditions over space and time (hereafter termed "regional metrics"). Beyond the geographical context of the measurements, metrics can also characterize different dimensions of climate change. For example, local metrics can characterize the magnitude of changes by quantifying how average (*23*, *32*) or extreme (*10*, *26*) values of climate are altered in a given locality (cell) over time. Shifts in the timing of climatic events can also be measured at the locality level (*13*, *33*). In turn, regional metrics begin with the characterization of climatic conditions across a given region and then measure temporal changes in the availability of analogous climatic conditions across that region (*23*, *34*, *35*), as well as changes in the direction to, or distance between, the positions of analogous climatic conditions (*34*). Within the region neighboring any given locality, the velocity at which climate shifts its position can also be quantified (*9*, *16*).

Mapping Multiple Dimensions of Climate Change

Although several metrics of climate change exist, they have typically been applied in isolation. Implementation of six common climate change metrics worldwide reveals that each characterizes different, sometimes opposing, patterns (Fig. 1). Local climate anomalies are projected to affect the tropics, subtropics, and northern high latitudes. More than half the global area currently covered by tropical climates faces large changes in average climate in relation to historical interannual variability (Fig. 2; for more details, see fig. S3). Large anomalies are also projected for more than 30% of the area of polar climates. The extreme drying and warming events explored here are projected to affect mainly the tropics. However, changes in other local extreme events may produce different patterns, with metrics describing extreme seasonal or annual precipitation and extreme daily maximum temperatures, for example, highlighting the high latitudes (*36*, *37*).

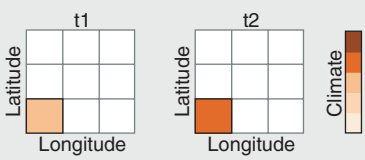
In turn, regional metrics describing changes in the area covered by different climate types reveal a trend toward expansion of the hot arid climates of the Sahara, southern Africa, and Australia, accompanied by reductions in the area of polar and mountain climates. The climatic

[1]Department of Biogeography and Global Change, National Museum of Natural Sciences, Consejo Superior de Investigaciones Científicas, Calle José Gutierrez Abascal 2, 28006 Madrid, Spain. [2]Center for Macroecology, Evolution and Climate, Natural History Museum of Denmark, University of Copenhagen, DK-2100 Copenhagen, Denmark. [3]Research Network in Biodiversity and Evolutionary Biology (InBIO)–Research Center in Biodiversity and Genetic Resources (CIBIO), University of Évora, Largo dos Colegiais, 7000 Évora, Portugal. [4]Metapopulation Research Group, Department of Biosciences, University of Helsinki, FIN-00014 Helsinki, Finland. [5]Imperial College London, Silwood Park, Buckhurst Road, Ascot, Berkshire SL5 7PY, UK.

*Corresponding author. E-mail: raquel.ag@gmail.com (R.A.G.); miguel.araujo@imperial.ac.uk (M.B.A.)

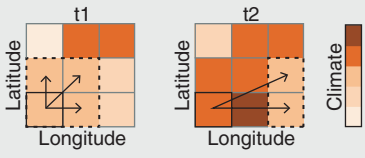
Box 1: Metrics of climate change.

Panel 1. Metrics of climate change within a grid cell. From period *t*1 to *t*2, the climate within a given cell (lower left corner) is altered on a scale that can represent average or extreme climates, or the timing of climatic events.



Examples of metrics	MAGNITUDE	Examples of ecological applications
Anomalies: the difference in climate parameters at a given locality over time.		Examining the influence of Quaternary climate changes on European dung beetle (*14*) and amphibian and reptile (*12*) diversity patterns, and of future climate changes across global mountain systems (*116*).
Standardized anomalies:* the Euclidean distance between baseline and future climate at a given locality, standardized by historical interannual climate variability (*23*).		Examining the exposure of different localities (cells) worldwide to future climate changes in relation to existing biodiversity (*23*, *24*).
Change in the probability of extremes:* the difference over time, at a given locality, in the magnitude of extreme climatic events, or in the probability of occurrence of the most extreme historical climatic event (*117*).		Examining the influence of extreme climates on invasion susceptibility of plant communities in north-central Chile over the past decades (*26*).
	TIMING	
Change in seasonality: the difference over time in the timing of climatic events.		Assessing the role of delayed snowmelt on the hibernation emergence date of ground squirrels in Canada (*33*).

Panel 2. Metrics of change across grid cells. Between periods *t*1 and *t*2, the climate of a given cell (lower left corner) becomes less available across the entire region (from four to two cells), and more distant (longer arrows). The lightest shade in *t*1 corresponds to disappearing climates, whereas the darkest shade in *t*2 emerges as a novel climate.



Examples of metrics	AVAILABILITY	Examples of ecological applications
Change in area of analogous climates:* the change over time in area experiencing similar climates [defined with reference to the difference between climates (*23*, *34*), classification rules (*118*), histograms (*35*), or clustering analysis (*119*)].		Exploring climate determinants of centers of rarity for Northern Hemisphere plant, bird, and butterfly species (*8*), and assessing the role of changes in Late Quaternary climate availability on mammal extinctions (*21*).
Novel climates:* emergence of future climatic conditions not found at present [future conditions that are most dissimilar to baseline climates (*23*), that do not overlap with present conditions in environmental space (*29*), or that lack baseline-analogs as defined above]. Conversely, disappearing climates refer to the disappearance of extant climates.		Examining plant associations in eastern North America over the past 18,000 years, and testing whether the associations most dissimilar to today's associations occur in areas where past climates were also most dissimilar to today's climates (*76*, *77*).
	POSITION	
Change in distance to analogous climates:* the change over time in the distance to similar climates (as defined above for the change in area of analogous climates).		Assessing the role of Late Quaternary climate movements on mammal extinctions (*21*).
Climate change velocity:* the ratio of the temporal climatic gradient at a given locality to the spatial climatic gradient across neighboring cells (*9*).		Predicting climate residence time in global protected areas (*9*), and comparing past climate velocities to Australian bird distribution shifts (*19*) and to global vertebrate endemism (*16*).

*Climate change metric implemented in our global comparison of climate change patterns.

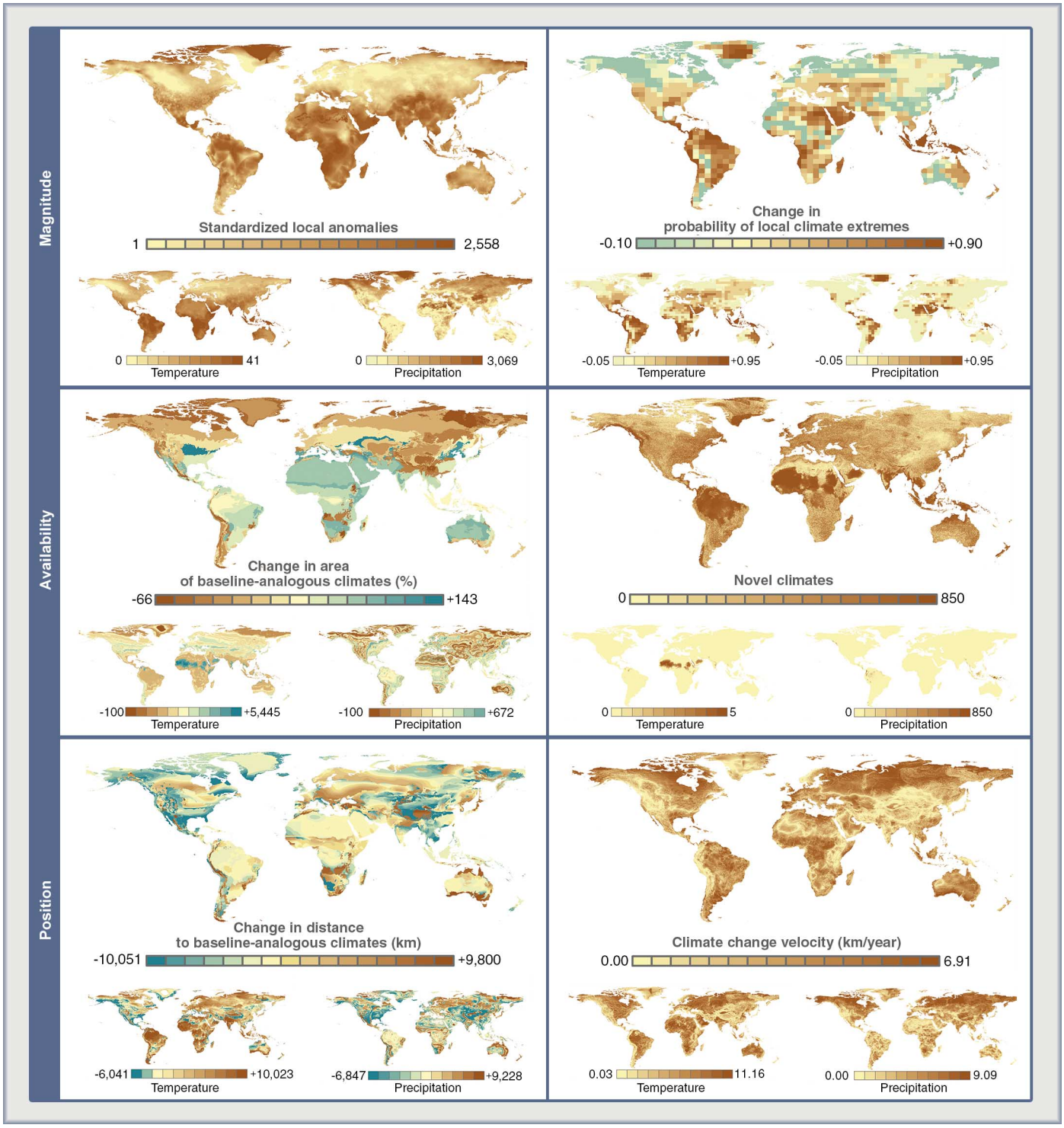


Fig. 1. Projected global climate change according to six metrics. The maps show projections of change in mean annual temperature and total annual precipitation between the baseline and an end-of-century multimodel ensemble under the A1B emissions scenario (*120*). The metrics illustrated characterize three dimensions of climate change: the magnitude of local changes in average or extreme climates [standardized climate anomalies (*23*) and change in the probability of extreme climates (*117*)], changes in the regional availability of climatic conditions [change in area of analogous climates (*34*, *118*), and novel climates (*23*)], and regional shifts in the position of climatic conditions [change in distance to analogous climates (*34*, *118*), and climate change velocity (*9*, *16*)]. Among the several methodologies available to compute these metrics (table S1), we selected methodologies that are commonly used. Pairwise spatial correlation between these metrics was significant but generally low (table S2). In each panel, the main maps show changes for temperature and precipitation combined, and the smaller maps show changes for each climate parameter individually. The scales were defined using quantiles and reflect a gradient from small changes (light brown shades) to large changes (dark brown shades), or from favorable changes (blue shades) to adverse changes (brown shades). Local anomalies, novel climates, and climate change velocity values were converted to logarithmic scale for visualization. See figs. S1 and S2 for analysis of sensitivity to alternative climate models.

conditions over the polar region and major mountains across the world are projected to shrink by up to 66%. By contrast, novel climates are more likely to emerge in the tropics and subtropics, owing to warmer temperatures: End-of-century temperatures for 62% of the world's tropical areas are projected to be the most dissimilar from today's temperatures. In about a third of the temperate and polar regions, distances to similar climatic conditions will increase more than anywhere else on the globe. The velocity of changes in temperature and precipitation is forecast to be high in such latitudes, but also in the tropical regions of central Africa, the western Amazon, and southern Australia.

Examining metrics in combination shows that different areas are exposed to different dimensions of climate change. The global patterns are far more complex than the often reported disproportionate warming for land areas at higher northern latitudes (*38*). In the polar regions, reductions in the global availability of similar climatic conditions are by far the greatest threat among all three dimensions examined (Fig. 2). The tropics and, to a lesser extent, hot arid regions are exposed to the emergence of climatic conditions lacking current analogs, and to changes of great magnitude in average climates and in extreme drying and warming events. Temperate regions are exposed almost equally to all dimensions of change, whereas cold regions are particularly exposed to large-distance or high-velocity shifts in the position of prevailing climates.

Linking Metrics to Threats and Opportunities for Biodiversity

Our global implementation of metrics shows that different climate change metrics have different spatial patterns around the world, but the question remains as to what the implications of each are for biodiversity. We outline a conceptual framework that describes the links between metrics of climate change and the potential extrinsic threats and opportunities that such changes represent for biodiversity (Fig. 3). The framework assumes that suitable climates for species exist where species presently occur, and it is based on two principles. First, under changing climates, and all else being equal, persistence of local populations is more likely where climatic conditions remain suitable (*39*, *40*). Second, the survival of species requires, among other factors, the continued availability of suitable climatic conditions either within or outside the present ranges of species (*41*). Under these general principles, local changes can be seen as a proxy for demographic threats and opportunities acting at the population level, whereas regional changes in climate can have negative or positive implications for the size and position of entire species' ranges. Support for the suggested links between climate change metrics and threats or opportunities for biodiversity (Fig. 3) can be found in studies covering a variety of taxonomic groups across regions.

Threats and Opportunities from Local Climate Change

All else being equal, large changes in climate at the local (cell) level are more likely to result in large changes in local suitability for populations than small changes, particularly when climate changes exceed past local variability (*23*). Decreased local climatic suitability can have effects on the physiology, morphology, or behavior of the organisms in a population (*42*), potentially leading to changes in population dynamics. Two examples are the reported local extinctions of lizards in Mexico, attributed to reduced activity of individuals during warmer reproductive seasons (*43*), and the mortality and population declines at the retracting margin of *Aloe* trees in the Namib desert, owing to desiccation stress (*44*). Nested within gradual trends (*45*), changes in extreme climates may pose even greater threats to populations (*46*). For instance, increased tree mortality across the globe over the last decades has been attributed to drought- and heat-induced stress (*47*). Positive changes in local suitability for populations under warming or altered rainfall patterns are less frequently documented, but include reports of higher fitness in common lizards in southern France resulting from an increase in body size (*48*),

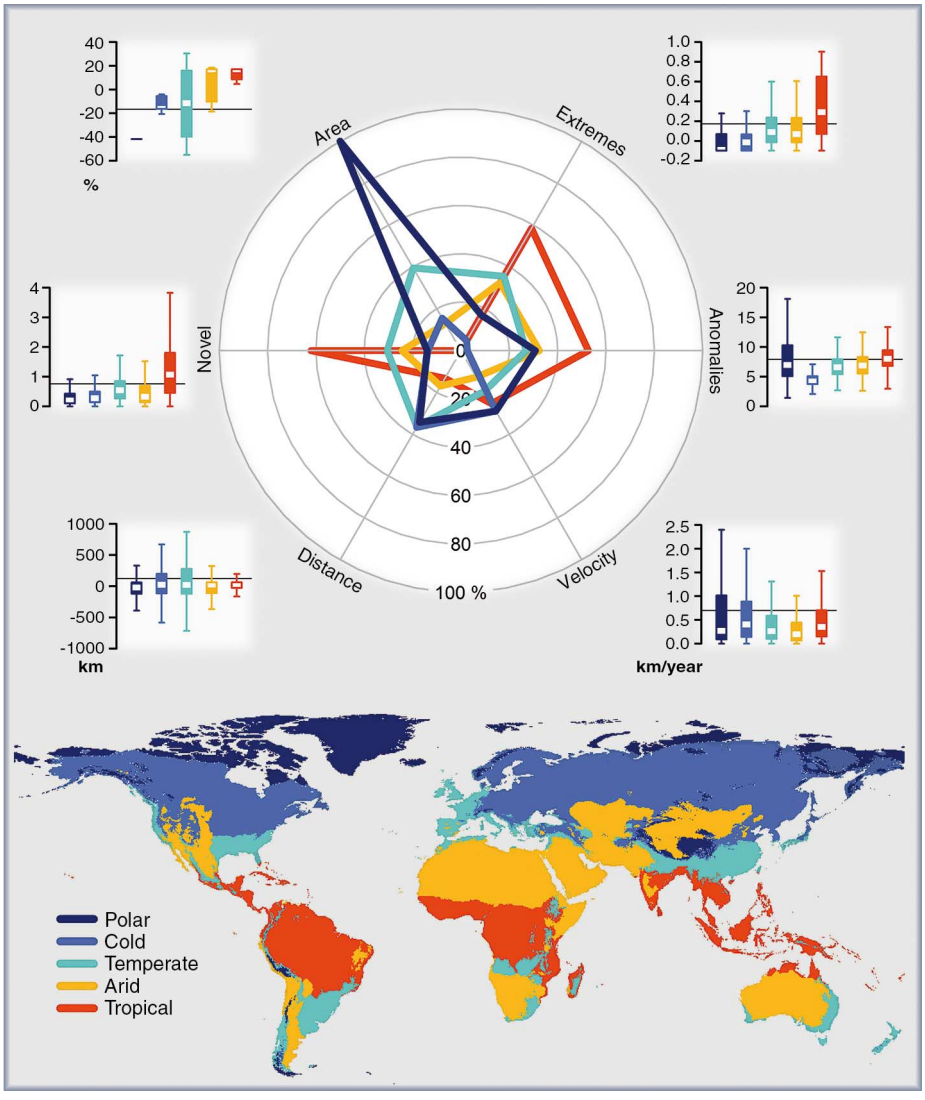


Fig. 2. Exposure of the world's climatic regions to different climate change dimensions. The star plot (upper panel) shows the percentage of area of different climatic regions of the world that are exposed to large changes in six climate change metrics (values above the 75th percentile of the worldwide distribution of values) capturing the magnitude of local changes in average or extreme climates, and regional changes in the availability and position of climatic conditions (*120*). For each metric, the distribution of values across climatic regions is shown in boxplots, with the horizontal lines indicating the 75th percentile. The colors on the star plot and boxplots correspond to the Köppen-Geiger broad climatic regions represented on the map (bottom panel; see fig. S4). See fig. S5 for analysis of sensitivity to alternative climate models.

increased growth and population numbers of plants in high-latitude ecosystems (*49*, *50*), and increased abundance of Svalbard reindeer during phases of population growth (*51*).

In turn, shifts in the timing of climatic events can lead to populations altering the timing of seasonal activities such as migration, flowering, or breeding, with potential consequences for the demography and population dynamics of species and communities (*52*, *53*). Such phenological shifts are commonly observed in response to climate change (*54*) and have been linked to the seasonality of climate (*33*), but also to trends in climatic averages (*55*) and extremes (*56*). Delays of snowmelt date, for example, have led to delays in the hibernation emergence date of ground squirrels in Canada (*33*).

Threats and Opportunities from Regional Climate Change

Shifts in the regional distribution of climates can affect the availability and distribution of climatically suitable areas for species across time and space (*41*). Increases or decreases in the area of climatic conditions that are suitable for species can lead to range expansions or contractions. Long-term ecological data reveal that species' distributions and abundances in both Northern and Southern Hemispheres often match, with time lag, warming and cooling cycles (*57*–*60*). Alpine trees (*61*) and other cold-adapted species of birds and butterflies (*8*), and small mammals like the mountain beaver and the western pocket gopher (*62*), for example, became confined to small and isolated pockets of cool conditions as the end of the last glacial period brought warmer temperatures. Climatic changes have also helped to explain range reductions of large mammals toward the end of the Late Quaternary (*63*). Indeed, continents losing more area representative of cold and dry conditions owing to climate changes during that period witnessed more extinctions of megafauna (*21*). By contrast, the extensive fossil record in North America and Eurasia provides evidence of increases in the distribution or abundance of plant species like elm and pine (*64*) and expansion of oaks out of glacial refugia (*65*) during the warming period of the last glacial. Contemporary changes have also been observed in high-latitude terrestrial ecosystems, where reduced ice-field extent has exposed new terrain for colonization and range expansion (*66*).

In turn, shifts in the position of climatic conditions affect the ability with which species track climatic conditions (*67*), and modulate the risk of range fragmentation. The magnitude of the Late Quaternary megafaunal extinctions discussed above was also greater in continents where suitable cold and dry conditions retreated farther (*21*). Over more recent decades, average range shifts observed for various taxonomic groups, mostly in the Northern Hemisphere, generally matched expectations from the poleward displacement of isotherms, despite variation in responses among species (*54*, *68*). Differences and delays in responses (*69*) can partly result from barriers to dispersal imposed by habitat fragmentation (*70*) or unsuitable climate across time or space (*71*, *72*), and can be stronger in lowland areas (*73*). Analyzing the direction to analogous climates can help to identify dispersal challenges as well as buffers, whereas the velocity of climate change provides an indication of the dispersal rates required to track suitable climates across the surrounding topography (*74*). In eastern North America, for example, the rate of northward shifts in the distribution of woody taxa populations over the last 16,000 years was paced by the velocity of temperature changes (*20*). The coincidence of global diversity patterns for amphibians, mammals and birds, and areas of low-velocity temperature change since the Last Glacial Maximum, 21,000 years ago, further illustrates the potential role of climate tracking for in situ persistence of species, particularly less vagile ones (*16*).

Predicting the effects of climate change on whole assemblages of species remains challenging.

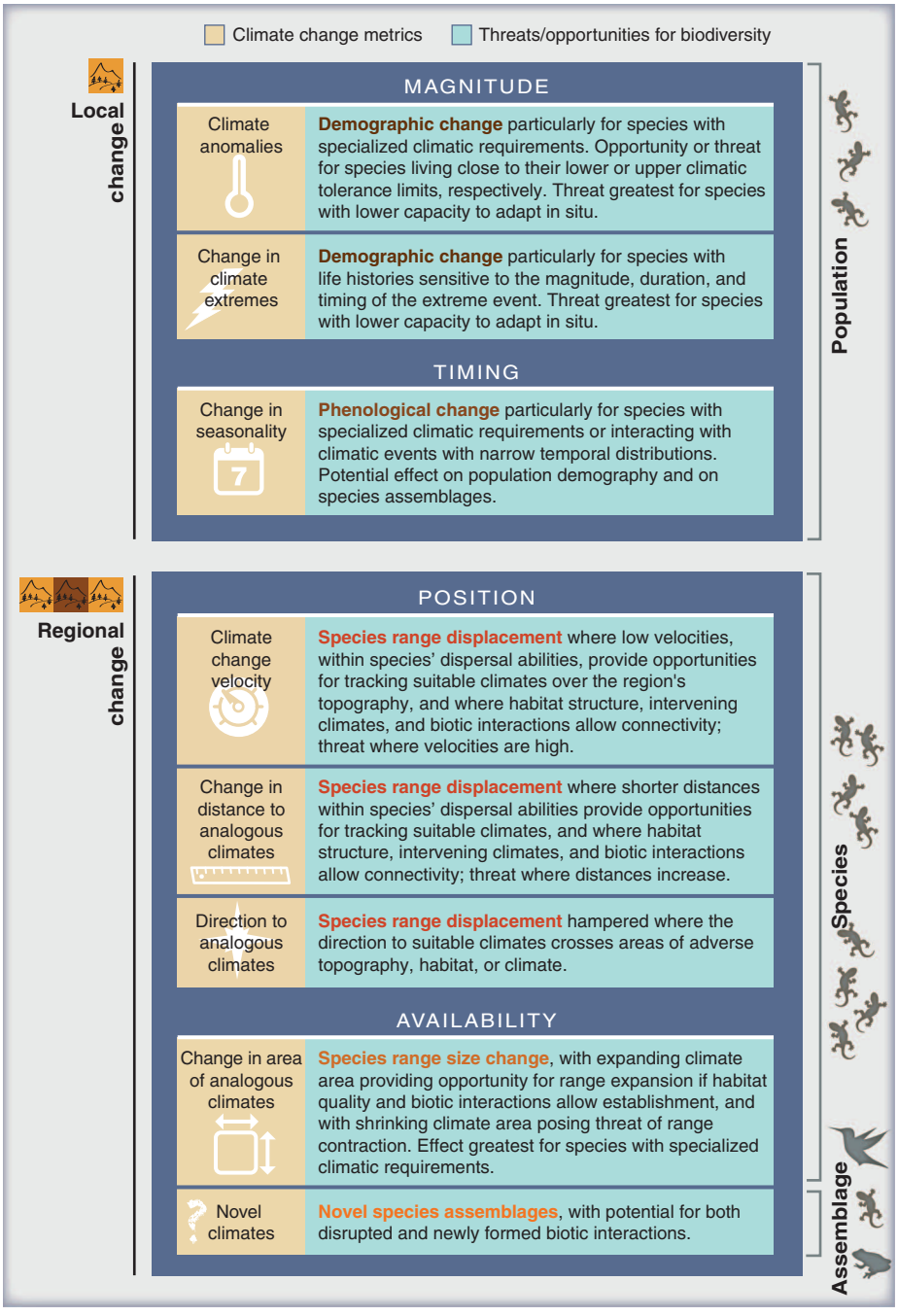


Fig. 3. Metrics of climate change and associated threats and opportunities for species. Metrics of climate change are grouped into four dimensions of change, and they either quantify changes at local (locality) level or at regional (set of localities) level (see Box 1). Links are established between metrics and potential threats and opportunities for population dynamics, species occurrence, and species assemblages.

Novel climates have been suggested to be associated with species assemblages also lacking modern analogs (*75*). One documented example is that of nonanalog vegetation assemblages in late-glacial eastern North America, which coincided with climatic conditions different from those occurring today (*76*, *77*). In turn, disappearing climates can lead to the disaggregation of extant assemblages (*23*). In general, spatiotemporal shifts in the distribution of climate can result in the rearrangement of assemblages, with potential implications for species interactions and community reshuffling. Nonanalog communities (*23*, *78*) can arise under changing climates either when species' individualistic responses lead to the disruption of existing interactions, or when species with nonoverlapping ranges come into contact and interact with one another (*53*, *79*, *80*). Examples include the climate-induced spread of pathogens (*81*, *82*) or invasive species (*83*), decline of prey species (*84*), and disruption of synchronization between different trophic levels (*85*). When exposed to extreme climates, communities can also switch into alternative ecological states (*46*, *86*). Despite the complexity of community dynamics under climate change, measuring the multiple dimensions of climate change and their likely consequences for individual species (Fig. 3) is a first step toward a better understanding of the potential threats and opportunities for biodiversity.

The Limits of Climate Change Metrics

Linking multiple dimensions of climate change to threats and opportunities for species is only a first step toward understanding the effects of climate change on biodiversity. Ultimately, the effects of climate change on organisms are also dependent on their intrinsic abilities to cope with, or adapt to, the different challenges they face (*87*). Although climate change metrics can be used as proxies for the threats and opportunities facing biodiversity, a number of considerations relating to the properties of individual species and the environment in which they live are important when interpreting metric outputs (see also Fig. 3). A first consideration is that climatic threats and opportunities do not act in isolation, but rather interact with other human-induced, ongoing threats (*2*). Notably, human-dominated landscapes (*88*) are an obstacle to species' dispersal and establishment, hampering opportunities to track suitable climates.

A second consideration when using metrics of climate change in biodiversity assessments is that the vulnerability of species to a given threat, or the capacity to seize a given opportunity, will vary across species. For example, individuals with higher genetic diversity, or higher capacity to change key morphological, physiological, or behavioral traits in response to adverse local

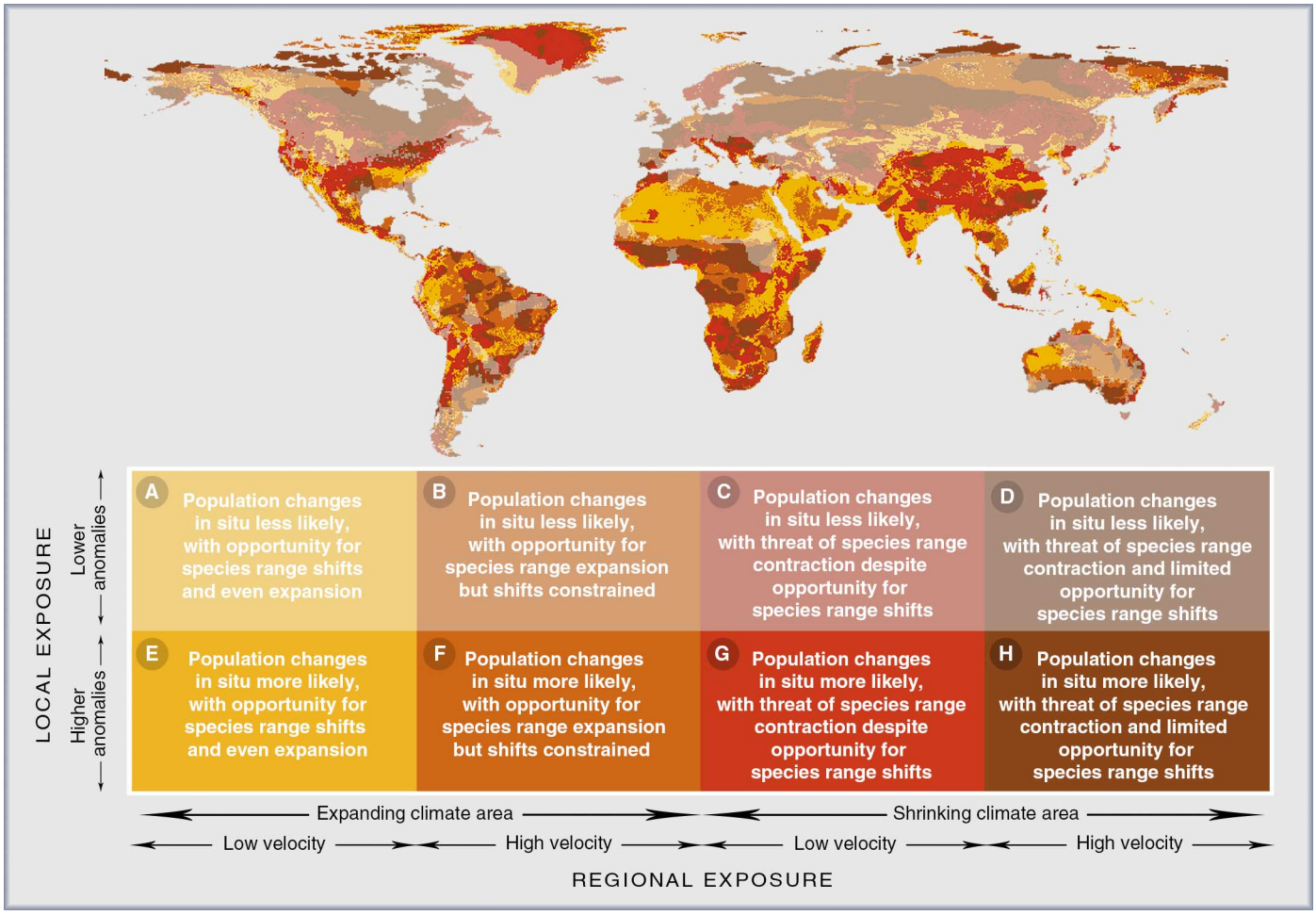


Fig. 4. Spatial overlap of climate change metrics. The three metrics selected as illustration—standardized local anomalies, change in area of baseline-analogous climates, and climate change velocity (*120*)—relate to different climate-induced threats and opportunities for biodiversity (Fig. 3). To account for species' potential dispersal limitations, changes in area of baseline-analogous climates were calculated by restricting the pool of climatic analogs to cells within 500 km from each cell (*23*). For each metric, two classes of values were defined. For anomalies, the two classes of values above and below the median denote higher and lower chances of demographic changes, respectively. For changes in area, the two classes of positive and negative values correspond to opportunity for species range expansion and threat of range contraction, respectively. For velocity, the two classes of values above and below the median denote difficulty and opportunity for range displacement, respectively. The different shades on the map reflect the interaction between the three metrics overlaid in space, with the inferences about potential threats and opportunities for biodiversity dependent on species' and landscape characteristics (see Fig. 3). See fig. S6 for analysis of sensitivity to alternative climate models and fig. S7 for alternative combinations of climate change metrics.

climate changes, are better equipped to persist in situ under local climate change (*87*). Faced with extreme climate events, individuals with life histories more sensitive to the duration and magnitude of such events also face greater threat (*45*). Likewise, changes in the regional distribution of climates can disproportionately affect species with more specialized climatic requirements, as such species need to follow suitable climatic conditions more closely (*8*, *23*). Where suitable climates are displaced, dispersal challenges will be greater for poor-dispersing and slow-reproducing species (*89*, *90*).

Species also respond to different climate parameters (*91*), and such variability should be considered when interpreting climate change metrics. As the spatial patterns arising from a given metric vary between temperature and precipitation, for example [(*19*, *92*) and this review], the threats and opportunities inferred from metrics may affect individual species differently depending on which parameter is measured. Finally, the temporal and spatial scales at which climate changes are measured are also important (*93*, *94*). Climatic thresholds for the survival or reproduction of individuals, often mediating population demographic changes, vary across seasons and life-history stages (*93*). Likewise, the effect of extreme events of a given magnitude and duration is best assessed relative to the life cycles of organisms (*45*). Changes measured over long time frames can also conceal finer-scale climatic variability that drives pulses of expansion or contraction in species' ranges, as has been shown for North American trees during the Holocene (*95*). Likewise, climatic changes quantified at coarse spatial resolutions can overlook microrefugia and thereby overestimate risks. Evidence exists that such refugia have enabled species to persist through periods of climate change, especially those with small home ranges (*96*). The relevant spatial extent for calculating regional metrics may also vary across species with different dispersal abilities (*23*). For example, broad regional pools of climates may be accessible to vagile species, but not to poor dispersers.

A Combined View of Threats and Opportunities

Given that alternative metrics reveal contrasting spatial patterns (Fig. 1) and represent different threats and opportunities for species (Fig. 3), how should they be used in assessments of climate change impacts on biodiversity? Single metrics of climate change have been used to predict the degree to which global biodiversity will be exposed to extreme climates at the locality level (*10*), to reduced availability of similar climates worldwide (*23*) or within ecoregions (*11*), or to high velocities of climate displacement across the surrounding topography (*9*). Although individual dimensions of change may be critical for particular species, they each provide only one facet of the many climatic challenges facing biodiversity. For example, mapping climate anomalies reveals where populations may potentially be most threatened with demographic changes, but not where opportunities may arise for organisms to track moving climates. Likewise, a map of the future availability of climatic conditions contains no information about how accessible such conditions are to species.

In principle, threats or opportunities for biodiversity should increase where species are simultaneously exposed to several dimensions of climate change (*2*, *97*). Examining multiple metrics in combination can show how dimensions of climate change interact among themselves to exacerbate or lessen species' exposure to climate change. The selection of metrics is contingent on the question, but should cover all dimensions of change deemed relevant. For illustration, we considered three metrics quantifying alternative dimensions of climate change: standardized anomalies, change in area of neighboring analogous climates (*23*), and climate change velocity. These metrics are expected to relate to local demographic changes, species' range contractions or expansions, and species' range displacements, respectively (Fig. 3). Spatially overlaying the selected metrics worldwide (Fig. 4) highlights the interactions among dimensions of climate change across broad geographical areas. However, how such changes will translate into threats and opportunities for biodiversity is likely perceived differently across species (Fig. 3).

Nearly 11% of the global land surface is exposed to large changes in the three metrics examined, mostly in the Nordic tundra and tropical areas [shade (H) in Fig. 4]. Both positive and negative effects of local warming have been reported on population dynamics in high-latitude areas (*50*, *51*, *98*). Species with wide tolerance to the environmental variability that is typical of such areas (*99*), or with access to microrefugia, are better equipped to cope with adverse changes. Yet, at the spatial scale used here, the high velocities required to track polar climates in the future compound the regional shrinkage of these climates, placing polar species under the threat of range contraction.

Mountain areas offer more opportunities for species to track slow-moving climates over the complex mosaic of microclimates provided by the local topography (*94*). However, range contraction still appears as a threat at the regional level [shade (G) in Fig. 4]. Where suitable climates disappear altogether within the species' reach, threat of extinction from habitat and ecosystem loss will be greater for species endemic to those climates (*8*, *23*). Small-ranged species of tropical mountain areas with high levels of endemism, and species lacking the genetic variability to survive in remnant isolated populations (*100*), thus appear particularly threatened. Species in cold climate areas of the Northern Hemisphere face similar decreases in availability of suitable climates [shades (C) and (D) in Fig. 4]. In such areas, local anomalies pose smaller threats relative to the historical interannual variability, but at the regional level, species that are specialized on these cold climates might face the threat of range contraction. Where the velocity of climate displacement is high [shade (D) in Fig. 4], or where landscapes are highly modified, dispersal challenges will also be greater.

By contrast, most of the remaining tropical and subtropical regions are exposed to climates that are expanding regionally as well as changing locally [shades (E) and (F) in Fig. 4]. If tropical species require specialized climatic conditions, or live closer to their upper tolerance limits, as seems often to be the case (*101*, *102*), then they are likely threatened by local changes because phenotypic plasticity (*103*) and physiological adaptation (*104*) are reduced in such circumstances. Faced with local changes, species in areas of low climate velocities have greater opportunities for adaptation through dispersal [shade (E) in Fig. 4], particularly if such species are poor dispersers. By contrast, the shallower latitudinal gradients of temperature (*105*) of the lowlands of the Amazon and Congo Basin, for example, may prevent dispersal and expansion into newly suitable areas [shade (F) in Fig. 4].

Challenges for Impact Assessment and Conservation

No single unifying metric of climate change exists. The conceptual framework proposed here can help interpreting the outputs of different metrics by classifying them into common currencies of threat and opportunity. Although the framework can be applied to a range of sectors, including agriculture, forestry and health, our focus is on impacts of climate change on biodiversity.

Projecting the level of exposure of biodiversity to climatic changes is an integral part of any framework to assess risks and select appropriate conservation strategies. Some of the existing frameworks for conservation under changing climates rely on single metrics of climate change as proxies for exposure, including the velocity of climate change (*106*), local anomalies (*107*), and the availability of climatic conditions (*11*). Whereas each of these frameworks addresses conservation needs in the face of specific threats and opportunities for biodiversity, integrating multiple metrics into a single framework would allow for the identification of complementary conservation strategies. For example, mitigating local impacts through abatement of habitat loss and enhancement of habitat quality or heterogeneity (*108*) can be vital in areas where shrinking climates reduce opportunities for species survival outside present ranges, particularly for climatically specialized species. By contrast, promoting landscape connectivity (*109*) and restoring new target habitat will be warranted wherever local changes threaten in situ persistence but low velocities of climate change enable species to track suitable climates.

The actual effects of climate change on biodiversity are extremely difficult to predict owing to the complexity of species and community dynamics, in addition to the interaction with other stressors. Climate change metrics do not account for intrinsic responses of species to climatic and other changes and are affected by the uncertainty

of the underlying climate data. Yet, metrics are likely to remain an important assessment tool for at least three reasons. First, models assessing the effects of climate change on biodiversity are typically calibrated to average climates, and little attention has been paid to alternative dimensions of local change such as climatic extremes or the timing of climatic events. Teasing apart alternative dimensions of change to complement model-based assessments, or integrating them into models (*110*, *111*), can bring valuable additional information.

Second, metrics can be used for assessing climate change exposure when insufficient data are available on the distributions of species. Such is the case for the majority of known species across taxa (*112*), and particularly for the species-rich and highly impacted tropical areas (*113*). Research on climate change impacts for biodiversity has to date been geographically and taxonomically biased (*114*), often excluding cryptic species and those that are currently most threatened owing to lack of sufficient data points for modeling. Hence, it is not a trivial feature of metric-based assessments that they can be applied when and where limited knowledge of biodiversity exists.

Third, the sheer number of underdescribed and undiscovered species (*115*) means that assessments relying on available data represent a very small proportion of the total existing biodiversity. For example, global inventories are estimated to cover only 20% of all existing insects (*115*), a group with considerable influence on ecosystem functioning and services. When carefully implemented and linked to threats and opportunities, simple metrics of climate change can provide a first-order assessment of the potential effects on the biota as a whole.

References and Notes

1. G.-R. Walther *et al.*, Ecological responses to recent climate change. *Nature* **416**, 389–395 (2002). doi: 10.1038/416389a; pmid: 11919621
2. B. W. Brook, N. S. Sodhi, C. J. A. Bradshaw, Synergies among extinction drivers under global change. *Trends Ecol. Evol.* **23**, 453–460 (2008). doi: 10.1016/j.tree.2008.03.011; pmid: 18582986
3. H. M. Pereira *et al.*, Scenarios for global biodiversity in the 21st century. *Science* **330**, 1496–1501 (2010). doi: 10.1126/science.1196624; pmid: 20978282
4. S. M. McMahon *et al.*, Improving assessment and modelling of climate change impacts on global terrestrial biodiversity. *Trends Ecol. Evol.* **26**, 249–259 (2011). doi: 10.1016/j.tree.2011.02.012; pmid: 21474198
5. A. T. Peterson *et al.*, *Ecological Niches and Geographic Distributions* (Monographs in Population Biology, Princeton Univ. Press, Princeton, NJ, 2011).
6. D. A. Keith *et al.*, Predicting extinction risks under climate change: Coupling stochastic population models with dynamic bioclimatic habitat models. *Biol. Lett.* **4**, 560–563 (2008). doi: 10.1098/rsbl.2008.0049;pmid: 18664424
7. M. Kearney, W. Porter, Mechanistic niche modelling: Combining physiological and spatial data to predict species' ranges. *Ecol. Lett.* **12**, 334–350 (2009). doi: 10.1111/j.1461-0248.2008.01277.x; pmid: 19292794
8. R. Ohlemüller *et al.*, The coincidence of climatic and species rarity: High risk to small-range species from climate change. *Biol. Lett.* **4**, 568–572 (2008). doi: 10.1098/rsbl.2008.0097; pmid: 18664421
9. S. R. Loarie *et al.*, The velocity of climate change. *Nature* **462**, 1052–1055 (2009). doi: 10.1038/nature08649; pmid: 20033047
10. L. J. Beaumont *et al.*, Impacts of climate change on the world's most exceptional ecoregions. *Proc. Natl. Acad. Sci. U.S.A.* **108**, 2306–2311 (2011). doi: 10.1073/pnas.1007217108; pmid: 21262825
11. J. E. M. Watson, T. Iwamura, N. Butt, Mapping vulnerability and conservation adaptation strategies under climate change. *Nat. Clim. Change* **3**, 989–994 (2013). doi: 10.1038/nclimate2007
12. M. B. Araújo *et al.*, Quaternary climate changes explain diversity among reptiles and amphibians. *Ecography* **31**, 8–15 (2008). doi: 10.1111/j.2007.0906-7590.05318.x
13. M. T. Burrows *et al.*, The pace of shifting climate in marine and terrestrial ecosystems. *Science* **334**, 652–655 (2011). doi: 10.1126/science.1210288; pmid: 22053045
14. J. Hortal *et al.*, Ice age climate, evolutionary constraints and diversity patterns of European dung beetles. *Ecol. Lett.* **14**, 741–748 (2011). doi: 10.1111/j.1461-0248.2011.01634.x; pmid: 21645193
15. S. F. Gouveia, J. Hortal, F. S. Cassemiro, T. F. Rangel, J. A. F. Diniz-Filho, Nonstationary effects of productivity, seasonality, and historical climate changes on global amphibian diversity. *Ecography* **36**, 104–113 (2013). doi: 10.1111/j.1600-0587.2012.07553.x
16. B. Sandel *et al.*, The influence of Late Quaternary climate-change velocity on species endemism. *Science* **334**, 660–664 (2011). doi: 10.1126/science.1210173; pmid: 21979937
17. M. B. Ashcroft, J. R. Gollan, D. I. Warton, D. Ramp, A novel approach to quantify and locate potential microrefugia using topoclimate, climate stability, and isolation from the matrix. *Glob. Change Biol.* **18**, 1866–1879 (2012). doi: 10.1111/j.1365-2486.2012.02661.x
18. F. P. Werneck, C. Nogueira, G. R. Colli, J. W. Sites Jr., G. C. Costa, Climatic stability in the Brazilian Cerrado: Implications for biogeographical connections of South American savannas, species richness and conservation in a biodiversity hotspot. *J. Biogeogr.* **39**, 1695–1706 (2012). doi: 10.1111/j.1365-2699.2012.02715.x
19. J. VanDerWal *et al.*, Focus on poleward shifts in species' distribution underestimates the fingerprint of climate change. *Nat. Clim. Change* **3**, 239–243 (2013). doi: 10.1038/nclimate1688
20. A. Ordonez, J. W. Williams, Climatic and biotic velocities for woody taxa distributions over the last 16 000 years in eastern North America. *Ecol. Lett.* **16**, 773–781 (2013). doi: 10.1111/ele.12110; pmid: 23574198
21. D. Nogués-Bravo, R. Ohlemüller, P. Batra, M. B. Araújo, Climate predictors of late quaternary extinctions. *Evolution* **64**, 2442–2449 (2010). pmid: 20707809
22. B. Dalsgaard *et al.*, Specialization in plant-hummingbird networks is associated with species richness, contemporary precipitation and quaternary climate-change velocity. *PLOS ONE* **6**, e25891 (2011). doi: 10.1371/journal.pone.0025891; pmid: 21998716
23. J. W. Williams, S. T. Jackson, J. E. Kutzbach, Projected distributions of novel and disappearing climates by 2100 AD. *Proc. Natl. Acad. Sci. U.S.A.* **104**, 5738–5742 (2007). doi: 10.1073/pnas.0606292104; pmid: 17389402
24. C. D. Thomas *et al.*, Exporting the ecological effects of climate change. Developed and developing countries will suffer the consequences of climate change, but differ in both their responsibility and how badly it will affect their ecosystems. *EMBO Rep.* **9** (suppl. 1), S28–S33 (2008). doi: 10.1038/embor.2008.42; pmid: 18578020
25. S. J. Wright, H. C. Muller-Landau, J. Schipper, The future of tropical species on a warmer planet. *Conserv. Biol.* **23**, 1418–1426 (2009). doi: 10.1111/j.1523-1739.2009.01337.x; pmid: 20078642
26. M. A. Jiménez *et al.*, Extreme climatic events change the dynamics and invasibility of semi-arid annual plant communities. *Ecol. Lett.* **14**, 1227–1235 (2011). doi: 10.1111/j.1461-0248.2011.01693.x; pmid: 21988736
27. J. Li *et al.*, Global priority conservation areas in the face of 21st century climate change. *PLOS ONE* **8**, e54839 (2013). doi: 10.1371/journal.pone.0054839; pmid: 23359638
28. T. Iwamura, K. A. Wilson, O. Venter, H. P. Possingham, A climatic stability approach to prioritizing global conservation investments. *PLOS ONE* **5**, e15103 (2010). doi: 10.1371/journal.pone.0015103; pmid: 21152095
29. J. A. Wiens, N. E. Seavy, D. Jongsomjit, Protected areas in climate space: What will the future bring? *Biol. Conserv.* **144**, 2119–2125 (2011). doi: 10.1016/j.biocon.2011.05.002
30. T. Iwamura, A. Guisan, K. A. Wilson, H. P. Possingham, How robust are global conservation priorities to climate change? *Glob. Environ. Change* **23**, 1277–1284 (2013). doi: 10.1016/j.gloenvcha.2013.07.016
31. J. Bergmann *et al.*, The Iberian Peninsula as a potential source for the plant species pool in Germany under projected climate change. *Plant Ecol.* **207**, 191–201 (2010). doi: 10.1007/s11258-009-9664-6
32. F. Giorgi, Climate change hot-spots. *Geophys. Res. Lett.* **33**, L08707 (2006). doi: 10.1029/2006GL025734
33. J. E. Lane, L. E. B. Kruuk, A. Charmantier, J. O. Murie, F. S. Dobson, Delayed phenology and reduced fitness associated with climate change in a wild hibernator. *Nature* **489**, 554–557 (2012). doi: 10.1038/nature11335; pmid: 22878721
34. R. Ohlemüller, E. S. Gritti, M. T. Sykes, C. D. Thomas, Towards European climate risk surfaces: The extent and distribution of analogous and non-analogous climates 1931–2100. *Glob. Ecol. Biogeogr.* **15**, 395–405 (2006). doi: 10.1111/j.1466-822X.2006.00245.x
35. D. D. Ackerly *et al.*, The geography of climate change: Implications for conservation biogeography. *Divers. Distrib.* **16**, 476–487 (2010). doi: 10.1111/j.1472-4642.2010.00654.x
36. C. Tebaldi, K. Hayhoe, J. M. Arblaster, G. A. Meehl, Going to the Extremes. *Clim. Change* **79**, 185–211 (2006). doi: 10.1007/s10584-006-9051-4
37. B. Orlowsky, S. Seneviratne, Global changes in extreme events: Regional and seasonal dimension. *Clim. Change* **110**, 669–696 (2012). doi: 10.1007/s10584-011-0122-9
38. G. A. Meehl *et al.*, in *Climate Change 2007: The Physical Science Basis. Contribution of Working Group I to the Fourth Assessment Report of the Intergovernmental Panel on Climate Change*, S. Solomon *et al.*, Eds. (Cambridge Univ. Press, Cambridge, UK, and New York, 2007), chap. 10.
39. L. R. Holdridge, Determination of world plant formations from simple climatic data. *Science* **105**, 367–368 (1947). doi: 10.1126/science.105.2727.367; pmid: 17800882
40. R. H. Whittaker, *Communities and ecosystems* (Macmillan, New York, ed. 2, 1975).
41. S. T. Jackson, J. T. Overpeck, Responses of Plant Populations and Communities to Environmental Changes of the Late Quaternary. *Paleobiology* **26** (sp4), 194–220 (2000). doi: 10.1666/0094-8373(2000)26[194:ROPPAC]2.0.CO;2
42. J. Peñuelas *et al.*, Evidence of current impact of climate change on life: A walk from genes to the biosphere. *Glob. Change Biol.* **19**, 2303–2338 (2013). doi: 10.1111/gcb.12143; pmid: 23505157
43. B. Sinervo *et al.*, Erosion of lizard diversity by climate change and altered thermal niches. *Science* **328**, 894–899 (2010). doi: 10.1126/science.1184695; pmid: 20466932
44. W. Foden *et al.*, A changing climate is eroding the geographical range of the Namib Desert tree Aloe through population declines and dispersal lags. *Divers. Distrib.* **13**, 645–653 (2007). doi: 10.1111/j.1472-4642.2007.00391.x
45. A. Jentsch, J. Kreyling, C. Beierkuhnlein, A new generation of climate-change experiments: Events, not trends. *Front. Ecol. Environ* **5**, 365–374 (2007). doi: 10.1890/1540-9295(2007)5[365:ANGOCE]2.0.CO;2
46. A. Jentsch, C. Beierkuhnlein, Research frontiers in climate change: Effects of extreme meteorological events on ecosystems. *C. R. Geosci.* **340**, 621–628 (2008). doi: 10.1016/j.crte.2008.07.002
47. C. D. Allen *et al.*, A global overview of drought and heat-induced tree mortality reveals emerging climate change risks for forests. *For. Ecol. Manage.* **259**, 660–684 (2010). doi: 10.1016/j.foreco.2009.09.001
48. S. Chamaillé-Jammes, M. Massot, P. Aragón, J. Clobert, Global warming and positive fitness response in mountain populations of common lizards Lacerta

vivipara. *Glob. Change Biol.* **12**, 392–402 (2006). doi: 10.1111/j.1365-2486.2005.01088.x

49. J. A. Fowbert, R. I. L. Smith, Rapid Population Increases in Native Vascular Plants in the Argentine Islands, Antarctic Peninsula. *Arct. Alp. Res.* **26**, 290–296 (1994). doi: 10.2307/1551941
50. G. B. Hill, G. H. R. Henry, Responses of High Arctic wet sedge tundra to climate warming since 1980. *Glob. Change Biol.* **17**, 276–287 (2011). doi: 10.1111/j.1365-2486.2010.02244.x
51. N. J. C. Tyler, M. C. Forchhammer, N. A. Øritsland, Nonlinear effects of climate and density in the dynamics of a fluctuating population of reindeer. *Ecology* **89**, 1675–1686 (2008). doi: 10.1890/07-0416.1; pmid: 18589531
52. A. J. Miller-Rushing, T. T. Høye, D. W. Inouye, E. Post, The effects of phenological mismatches on demography. *Philos. Trans. R. Soc. Lond. B Biol. Sci.* **365**, 3177–3186 (2010). doi: 10.1098/rstb.2010.0148; pmid: 20819811
53. E. Post, *Ecology of Climate Change. The Importance of Biotic Interactions* (Princeton Univ. Press, Princeton, NJ, 2013).
54. C. Parmesan, G. Yohe, A globally coherent fingerprint of climate change impacts across natural systems. *Nature* **421**, 37–42 (2003). doi: 10.1038/nature01286; pmid: 12511946
55. T. L. Root *et al.*, Fingerprints of global warming on wild animals and plants. *Nature* **421**, 57–60 (2003). doi: 10.1038/nature01333; pmid: 12511952
56. A. Jentsch, J. Kreyling, J. Boettcher-Treschkow, C. Beierkuhnlein, Beyond gradual warming: Extreme weather events alter flower phenology of European grassland and heath species. *Glob. Change Biol.* **15**, 837–849 (2009). doi: 10.1111/j.1365-2486.2008.01690.x
57. L. R. Flenley, Tropical forests under the climates of the last 30,000 Years. *Clim. Change* **39**, 177–197 (1998). doi: 10.1023/A:1005367822750
58. R. J. Morley, M. Bush, J. Flenley, W. Gosling, in *Tropical Rainforest Responses to Clim. Change*, M. B. Bush, J. R. Flenley, W. D. Gosling, Eds. (Springer, Berlin and Heidelberg, Germany, 2011), pp. 1–34.
59. K. J. Willis, G. M. MacDonald, Long-term ecological records and their relevance to climate change predictions for a warmer world. *Annu. Rev. Ecol. Evol. Syst.* **42**, 267–287 (2011). doi: 10.1146/annurev-ecolsys-102209-144704
60. K. J. Willis, K. D. Bennett, S. L. Burrough, M. Macias-Fauria, C. Tovar, Determining the response of African biota to climate change: Using the past to model the future. *Philos. Trans. R. Soc. Lond. B Biol. Sci.* **368**, 20120491 (2013). doi: 10.1098/rstb.2012.0491; pmid: 23878343
61. H. J. B. Birks, K. J. Willis, Alpines, trees, and refugia in Europe. *Plant Ecol. Divers.* **1**, 147–160 (2008). doi: 10.1080/17550870802349146
62. J. L. Blois, J. L. McGuire, E. A. Hadly, Small mammal diversity loss in response to late-Pleistocene climatic change. *Nature* **465**, 771–774 (2010). doi: 10.1038/nature09077; pmid: 20495547
63. E. D. Lorenzen *et al.*, Species-specific responses of Late Quaternary megafauna to climate and humans. *Nature* **479**, 359–364 (2011). doi: 10.1038/nature10574; pmid: 22048313
64. J. W. Williams, B. N. Shuman, T. Webb III, P. J. Bartlein, P. L. Leduc, Late-Quaternary vegetation dynamics in North America: Scaling from taxa to biomes. *Ecol. Monogr.* **74**, 309–334 (2004). doi: 10.1890/02-4045
65. M. B. Davis, R. G. Shaw, Range shifts and adaptive responses to Quaternary climate change. *Science* **292**, 673–679 (2001). doi: 10.1126/science.292.5517.673; pmid: 11326089
66. P. Convey, R. I. Smith, Responses of terrestrial Antarctic ecosystems to climate change. *Plant Ecol.* **182**, 1–10 (2006).
67. L. F. Pitelka *et al.*, Plant migration and climate change. *Am. Sci.* **85**, 464–474 (1997).
68. I.-C. Chen, J. K. Hill, R. Ohlemüller, D. B. Roy, C. D. Thomas, Rapid range shifts of species associated with high levels of climate warming. *Science* **333**, 1024–1026 (2011). doi: 10.1126/science.1206432; pmid: 21852500
69. M. B. Davis, in *Community Ecology*, J. Diamond, T. J. Case, Eds. (Harper and Row, 1986), pp. 269–284.
70. J. K. Hill *et al.*, Impacts of landscape structure on butterfly range expansion. *Ecol. Lett.* **4**, 313–321 (2001). doi: 10.1046/j.1461-0248.2001.00222.x
71. R. Early, D. F. Sax, Analysis of climate paths reveals potential limitations on species range shifts. *Ecol. Lett.* **14**, 1125–1133 (2011). doi: 10.1111/j.1461-0248.2011.01681.x; pmid: 21955643
72. J. Bennie *et al.*, Range expansion through fragmented landscapes under a variable climate. *Ecol. Lett.* **16**, 921–929 (2013). doi: 10.1111/ele.12129; pmid: 23701124
73. R. Bertrand *et al.*, Changes in plant community composition lag behind climate warming in lowland forests. *Nature* **479**, 517–520 (2011). doi: 10.1038/nature10548; pmid: 22012261
74. D. L. Peterson, E. G. Schreiner, N. M. Buckingham, Gradients, vegetation and climate: Spatial and temporal dynamics in the Olympic Mountains, U.S.A. *Global Ecol. Biogeogr. Lett.* **6**, 7–17 (1997). doi: 10.2307/2997523
75. J. W. Williams, S. T. Jackson, Novel climates, no-analog communities, and ecological surprises. *Front. Ecol. Environ* **5**, 475–482 (2007). doi: 10.1890/070037
76. J. W. Williams, B. N. Shuman, I. I. I. T. Webb, Dissimilarity analyses of late-Quaternary vegetation and climate in eastern North America. *Ecology* **82**, 3346–3362 (2001).
77. J. T. Overpeck, R. S. Webb, T. Webb III, Mapping eastern North American vegetation change of the past 18 ka: No-analogs and the future. *Geology* **20**, 1071–1074 (1992). doi: 10.1130/0091-7613(1992)020<1071:MENAVC>2.3.CO;2
78. R. W. Graham *et al.*, Spatial response of mammals to late Quaternary environmental fluctuations. *Science* **272**, 1601–1606 (1996). doi: 10.1126/science.272.5268.1601; pmid: 8662471
79. E. Post *et al.*, Ecological dynamics across the Arctic associated with recent climate change. *Science* **325**, 1355–1358 (2009). doi: 10.1126/science.1173113; pmid: 19745143
80. G.-R. Walther, Community and ecosystem responses to recent climate change. *Philos. Trans. R. Soc. Lond. B Biol. Sci.* **365**, 2019–2024 (2010). doi: 10.1098/rstb.2010.0021; pmid: 20513710
81. J. A. Pounds *et al.*, Widespread amphibian extinctions from epidemic disease driven by global warming. *Nature* **439**, 161–167 (2006). doi: 10.1038/nature04246; pmid: 16407945
82. J. R. Rohr, T. R. Raffel, Linking global climate and temperature variability to widespread amphibian declines putatively caused by disease. *Proc. Natl. Acad. Sci. U.S.A.* **107**, 8269–8274 (2010). doi: 10.1073/pnas.0912883107; pmid: 20404180
83. J. M. Diez *et al.*, Will extreme climatic events facilitate biological invasions? *Front. Ecol. Environ* **10**, 249–257 (2012). doi: 10.1890/110137
84. I. Durance, S. J. Ormerod, Evidence for the role of climate in the local extinction of a cool-water triclad. *J. N. Am. Benthol. Soc.* **29**, 1367–1378 (2010). doi: 10.1899/09-159.1
85. M. E. Visser, L. J. M. Holleman, Warmer springs disrupt the synchrony of oak and winter moth phenology. *Proc. R. Soc. Lond. B Biol. Sci.* **268**, 289–294 (2001). doi: 10.1098/rspb.2000.1363; pmid: 11217900
86. M. Scheffer, S. Carpenter, J. A. Foley, C. Folke, B. Walker, Catastrophic shifts in ecosystems. *Nature* **413**, 591–596 (2001). doi: 10.1038/35098000; pmid: 11595939
87. L.-M. Chevin, R. Lande, G. M. Mace, Adaptation, plasticity, and extinction in a changing environment: Towards a predictive theory. *PLOS Biol.* **8**, e1000357 (2010). doi: 10.1371/journal.pbio.1000357; pmid: 20463950
88. E. C. Ellis, N. Ramankutty, Putting people in the map: Anthropogenic biomes of the world. *Front. Ecol. Environ* **6**, 439–447 (2008). doi: 10.1890/070062
89. A. L. Angert *et al.*, Do species' traits predict recent shifts at expanding range edges? *Ecol. Lett.* **14**, 677–689 (2011). doi: 10.1111/j.1461-0248.2011.01620.x; pmid: 21535340
90. C. A. Schloss, T. A. Nuñez, J. J. Lawler, Dispersal will limit ability of mammals to track climate change in the Western Hemisphere. *Proc. Natl. Acad. Sci. U.S.A.* **109**, 8606–8611 (2012). doi: 10.1073/pnas.1116791109; pmid: 22586104
91. M. W. Tingley, W. B. Monahan, S. R. Beissinger, C. Moritz, Birds track their Grinnellian niche through a century of climate change. *Proc. Natl. Acad. Sci. U.S.A.* **106** (suppl. 2), 19637–19643 (2009). doi: 10.1073/pnas.0901562106; pmid: 19805037
92. A. Ordonez, J. W. Williams, Projected climate reshuffling based on multivariate climate-availability, climate-analog, and climate-velocity analyses: Implications for community disaggregation. *Clim. Change* **119**, 659–675 (2013). doi: 10.1007/s10584-013-0752-1
93. S. T. Jackson, J. L. Betancourt, R. K. Booth, S. T. Gray, Ecology and the ratchet of events: Climate variability, niche dimensions, and species distributions. *Proc. Natl. Acad. Sci. U.S.A.* **106** (suppl. 2), 19685–19692 (2009). doi: 10.1073/pnas.0901644106; pmid: 19805104
94. S. Z. Dobrowski, A climatic basis for microrefugia: The influence of terrain on climate. *Glob. Change Biol.* **17**, 1022–1035 (2011). doi: 10.1111/j.1365-2486.2010.02263.x
95. S. T. Gray, J. L. Betancourt, S. T. Jackson, R. G. Eddy, Role of multidecadal climate variability in a range extension of pinyon pine. *Ecology* **87**, 1124–1130 (2006). doi: 10.1890/0012-9658(2006)87[1124:ROMCVI]2.0.CO;2; pmid: 16761590
96. K. J. Willis, T. H. van Andel, Trees or no trees? The environments of central and eastern Europe during the Last Glaciation. *Quat. Sci. Rev.* **23**, 2369–2387 (2004). doi: 10.1016/j.quascirev.2004.06.002
97. C. Hof, M. B. Araújo, W. Jetz, C. Rahbek, Additive threats from pathogens, climate and land-use change for global amphibian diversity. *Nature* **480**, 516–519 (2011). pmid: 22089134
98. K. L. Laidre *et al.*, Quantifying the sensitivity of Arctic marine mammals to climate-induced habitat change. *Ecol. Appl.* **18** (suppl.), S97–S125 (2008). doi: 10.1890/06-0546.1; pmid: 18494365
99. P. Convey, in *Antarctic Peninsula Climate Variability: Historical and Paleoenvironmental Perspectives*, E. Domack *et al.*, Eds. (American Geophysical Union, Washington, DC, 2003), pp. 145–158.
100. J. Overpeck, C. Whitlock, B. Huntley, in *Paleoclimate, Global Change and the Future*, K. D. Alverson, R. S. Bradley, T. F. Pedersen, Eds. (Springer, Berlin, 2003), pp. 81–103.
101. R. B. Huey *et al.*, Why tropical forest lizards are vulnerable to climate warming. *Proc. R. Soc. Lond. B Biol. Sci.* **276**, 1939–1948 (2009). doi: 10.1098/rspb.2008.1957; pmid: 19324762
102. J. M. Sunday, A. E. Bates, N. K. Dulvy, Global analysis of thermal tolerance and latitude in ectotherms. *Proc. R. Soc. Lond. B Biol. Sci.* **278**, 1823–1830 (2011). doi: 10.1098/rspb.2010.1295; pmid: 21106582
103. A. A. Hoffmann, S. L. Chown, S. Clusella-Trullas, Upper thermal limits in terrestrial ectotherms: How constrained are they? *Funct. Ecol.* **27**, 934–949 (2013). doi: 10.1111/j.1365-2435.2012.02036.x
104. M. B. Araújo *et al.*, Heat freezes niche evolution. *Ecol. Lett.* **16**, 1206–1219 (2013). doi: 10.1111/ele.12155; pmid: 23869696
105. R. K. Colwell, G. Brehm, C. L. Cardelús, A. C. Gilman, J. T. Longino, Global warming, elevational range shifts, and lowland biotic attrition in the wet tropics. *Science* **322**, 258–261 (2008). doi: 10.1126/science.1162547; pmid: 18845754
106. L. Gillson, T. P. Dawson, S. Jack, M. A. McGeoch, Accommodating climate change contingencies in conservation strategy. *Trends Ecol. Evol.* **28**, 135–142 (2013). doi: 10.1016/j.tree.2012.10.008; pmid: 23146578
107. W. B. Foden *et al.*, Identifying the world's most climate change vulnerable species: A systematic trait-based assessment of all birds, amphibians and corals. *PLOS ONE* **8**, e65427 (2013). doi: 10.1371/journal.pone.0065427; pmid: 23950785
108. L. P. Shoo *et al.*, Engineering a future for amphibians under climate change. *J. Appl. Ecol.* **48**, 487–492 (2011). doi: 10.1111/j.1365-2664.2010.01942.x
109. P. Williams *et al.*, Planning for climate change: Identifying minimum-dispersal corridors for the Cape

Proteaceae. *Conserv. Biol.* **19**, 1063–1074 (2005). doi: 10.1111/j.1523-1739.2005.00080.x
110. R. Altwegg *et al.*, Novel methods reveal shifts in migration phenology of barn swallows in South Africa. *Proc. R. Soc. Lond. B Biol. Sci.* **279**, 1485–1490 (2012). doi: 10.1098/rspb.2011.1897; pmid: 22072608
111. N. E. Zimmermann *et al.*, Climatic extremes improve predictions of spatial patterns of tree species. *Proc. Natl. Acad. Sci. U.S.A.* **106** (suppl. 2), 19723–19728 (2009). doi: 10.1073/pnas.0901643106; pmid: 19897732
112. M. V. Lomolino, in *Frontiers of Biogeography: New directions in the geography of nature*, M. V. Lomolino, L. R. Heaney, Eds. (Sinauer, Sunderland, MA, 2004), pp. 293–296.
113. K. J. Feeley, M. R. Silman, The data void in modeling current and future distributions of tropical species. *Glob. Change Biol.* **17**, 626–630 (2011). doi: 10.1111/j.1365-2486.2010.02239.x
114. A. Felton *et al.*, Climate change, conservation and management: An assessment of the peer-reviewed scientific journal literature. *Biodivers. Conserv.* **18**, 2243–2253 (2009). doi: 10.1007/s10531-009-9652-0
115. B. R. Scheffers, L. N. Joppa, S. L. Pimm, W. F. Laurance, What we know and don't know about Earth's missing biodiversity. *Trends Ecol. Evol.* **27**, 501–510 (2012). doi: 10.1016/j.tree.2012.05.008; pmid: 22784409
116. D. Nogués-Bravo, M. B. Araújo, M. P. Errea, J. P. Martinez-Rica, Exposure of global mountain systems to climate warming during the 21st Century. *Glob. Environ. Change* **17**, 420–428 (2007). doi: 10.1016/j.gloenvcha.2006.11.007
117. R. W. Katz, G. S. Brush, M. B. Parlange, Statistics of extremes: Modeling ecological disturbances. *Ecology* **86**, 1124–1134 (2005). doi: 10.1890/04-0606
118. K. Fraedrich, F. W. Gerstengarbe, P. C. Werner, Climate shifts during the last century. *Clim. Change* **50**, 405–417 (2001). doi: 10.1023/A:1010699428863
119. W. W. Hargrove, F. M. Hoffman, Potential of multivariate quantitative methods for delineation and visualization of ecoregions. *Environ. Manage.* **34** (suppl. 1), S39–S60 (2004). doi: 10.1007/s00267-003-1084-0;pmid: 15883870
120. Materials and Methods are available as supplementary materials on *Science* Online.

Acknowledgments: We thank H. Prasad for assisting with baseline climate data handling and B. Sandel for sharing the R script for the spatial gradient of climate change. We are grateful to three anonymous reviewers for constructive comments on our manuscript. R.A.G. is funded through a Foundation for Science and Technology (FCT) Ph.D. studentship (SFRH/BD/65615/2009), M.B.A. through the FCT PTDC/AAC-AMB/98163/2008 project and the Integrated Program of IC&DT Call Nº 1/SAESCTN/ALENT-07-0224-FEDER-00175, and M.C. through the Academy of Finland (grant 257686). C.R., R.A.G., and M.B.A. thank the Danish National Research Foundation for support to the Center for Macroecology, Evolution and Climate, and C.R. and M.B.A. also thank the Imperial College London's Grand Challenges in Ecosystems and Environment initiative for support of their research.

Supplementary Materials

www.sciencemag.org/content/344/6183/1247579/suppl/DC1
Materials and Methods
Figs. S1 to S7
Tables S1 and S2
References (*121*–*165*)

10.1126/science.1247579

READ THE FULL ARTICLE ONLINE
http://dx.doi.org/10.1126/science.1252304

Optogenetic stimulation of the mouse motor cortex incites proliferation of myelin-producing cells and axonal myelination.

Neuronal Activity Promotes Oligodendrogenesis and Adaptive Myelination in the Mammalian Brain

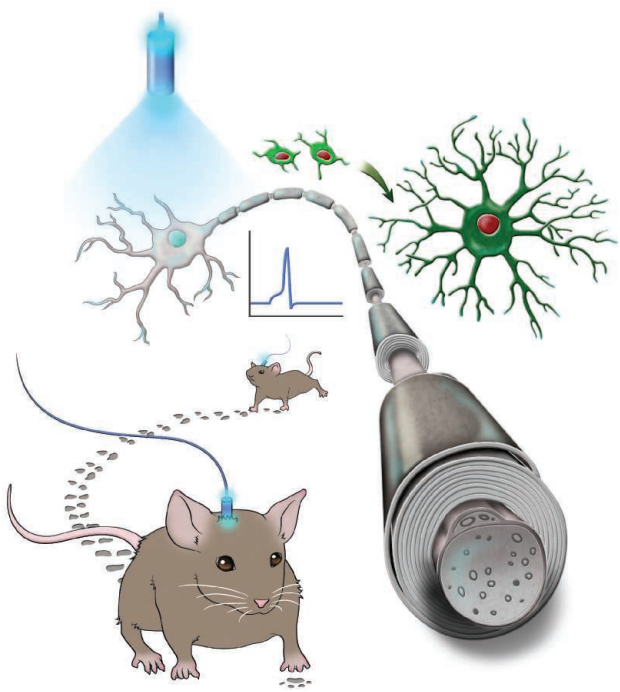
Erin M. Gibson, David Purger, Christopher W. Mount, Andrea K. Goldstein, Grant L. Lin, Lauren S. Wood, Ingrid Inema, Sarah E. Miller, Gregor Bieri, J. Bradley Zuchero, Ben A. Barres, Pamelyn J. Woo, Hannes Vogel, Michelle Monje*

RELATED ITEMS IN *SCIENCE*

M. E. Bechler, C. ffrench-Constant, A new wrap for neuronal activity? *Science* **344**, 480–481 (2014). DOI: 10.1126/science.1254446

Introduction: Myelin is formed by mature oligodendrocytes to facilitate fast propagation of action potentials in axons. Small changes in myelin thickness can confer substantial changes in conduction speed and may thus alter neural circuit function. The idea that active neurons may modulate myelination is supported by in vitro studies and correlations between experience and myelin microstructure, but direct in vivo evidence demonstrating that neuronal activity regulates oligodendrocyte precursor cell (OPC) proliferation, differentiation, or changes in myelin microstructure has been lacking. We use in vivo optogenetic techniques in awake, behaving mice to provide direct evidence that neuronal activity regulates changes in myelin-forming cells within an active circuit.

Rationale: Demonstrating the direct effects of behaviorally relevant neuronal activity on oligodendroglial lineage cells in vivo has been a challenge because traditional methods of directly promoting neuronal activity involve placement of an electrode, and the resultant tissue injury and subsequent inflammation affects OPC dynamics. Optogenetic technology allows for in vivo control of neuronal firing with millisecond precision using light delivered at a distance from the target and, thus, avoids extensive electrode-related tissue damage. We used an optogenetic (Thy1::ChR2) mouse model in which 470-nm light delivered near the brain surface stimulates the excitatory opsin channelrhodopsin expressed by cortical layer V projection neurons. Wild-type littermate controls lacking channelrhodopsin were identically manipulated to control for effects of surgery, optical fiber placement, and light exposure. In Thy1::ChR2 mice, light stimulation delivered unilaterally to the premotor cortex elicits complex motor behavior (unidirectional ambulation). The thymidine analog 5-ethynyl-2′-deoxyuridine (EdU) was administered at the time of optogenetic stimulation to mark actively dividing cells. Animals were evaluated at various time points to examine the effects of neuronal activity on myelin-forming cells and myelin microstructure, as well as the functional consequences of neuronal activity–regulated myelin changes.



Neuronal activity promotes OPC proliferation, oligodendrogenesis, and myelin remodeling. Optogenetic stimulation of unilateral premotor cortex layer V projection neurons in awake, behaving Thy1::ChR2 mice promotes OPC proliferation (light green cells, red EdU$^+$ nuclei), oligodendrogenesis (newly generated, EdU-marked oligodendrocyte; dark green cell), and an increase in myelin sheath thickness (viewed in cross section, gray). Together with these adaptive myelin changes, motor performance of the correlate limb is improved during normal gait 4 weeks after premotor cortex stimulation.

Results: Optogenetic stimulation of cortical layer V projection neurons resulted in robust proliferation of OPCs within the premotor circuit, from the deep layers of the premotor cortex to the subcortical projections through the corpus callosum. Four weeks later, an increase in newly generated oligodendrocytes and increased myelin sheath thickness were found within the stimulated premotor circuit. Behavioral testing revealed increased swing speed of the correlate forelimb. Pharmacological blockade of OPC differentiation prevented activity-regulated oligodendrogenesis and myelin changes, as well as the associated behavioral change.

Conclusion: Neuronal activity regulates OPC proliferation, differentiation, and myelin remodeling in the murine brain with accompanying changes in behavioral function. Taken together, these findings suggest that adaptive changes in myelin-forming cells represent a type of behaviorally relevant neural plasticity, raising numerous conceptual and mechanistic questions. Mechanisms regulating myelin plasticity may be important for adaptive neural function and could be leveraged for interventions in diseases of myelin. Conversely, dysregulated myelin plasticity could conceivably contribute to disease.

The list of author affiliations is available in the full article online.
*Corresponding author. E-mail: mmonje@stanford.edu
Cite this article as E. M. Gibson *et al.*, *Science* **344**, 1252304 (2014). DOI: 10.1126/science.1252304

Neuronal Activity Promotes Oligodendrogenesis and Adaptive Myelination in the Mammalian Brain

Erin M. Gibson,[1]* David Purger,[1,2]* Christopher W. Mount,[1,3] Andrea K. Goldstein,[1] Grant L. Lin,[1,3] Lauren S. Wood,[1] Ingrid Inema,[1] Sarah E. Miller,[1] Gregor Bieri,[3] J. Bradley Zuchero,[4] Ben A. Barres,[4] Pamelyn J. Woo,[1] Hannes Vogel,[5] Michelle Monje[1]†

Myelination of the central nervous system requires the generation of functionally mature oligodendrocytes from oligodendrocyte precursor cells (OPCs). Electrically active neurons may influence OPC function and selectively instruct myelination of an active neural circuit. In this work, we use optogenetic stimulation of the premotor cortex in awake, behaving mice to demonstrate that neuronal activity elicits a mitogenic response of neural progenitor cells and OPCs, promotes oligodendrogenesis, and increases myelination within the deep layers of the premotor cortex and subcortical white matter. We further show that this neuronal activity–regulated oligodendrogenesis and myelination is associated with improved motor function of the corresponding limb. Oligodendrogenesis and myelination appear necessary for the observed functional improvement, as epigenetic blockade of oligodendrocyte differentiation and myelin changes prevents the activity-regulated behavioral improvement.

Development of the myelinated fiber infrastructure of the brain occurs throughout childhood and young adulthood and is classically thought to complete when the frontal lobes finish myelin formation in the fourth decade of human life (*1*, *2*). Maturation of the complex neural circuitry necessary for high-level cognitive and motor functions depends on myelination, the process by which oligodendrocytes ensheathe and insulate axons to facilitate fast, saltatory conduction of electrical impulses. Whereas the protracted nature of neocortical myelination is well recognized, the mechanisms governing myelination after infancy remain largely unknown (*1*, *3*, *4*).

An intriguing but unproven possibility is that postnatal myelination may be modulated by mature neurons to augment an active circuit. The idea that excitatory neuronal activity instructs myelination, including oligodendrocyte precursor cell (OPC) proliferation, differentiation, and myelin biosynthesis, is supported by multiple lines of evidence. Blockade of activity in the developing optic nerve by axotomy or tetrodotoxin decreases OPC proliferation (*5*); myelination in vitro is activity-dependent (*6*–*9*); and some data suggest that OPC proliferation, differentiation, or the rate of myelin development in vivo is enhanced by nonphysiological (333 Hz) or pathological perturbations of electrical activity (*10*, *11*). Further supporting the idea that excitatory neuronal activity may influence OPC behavior, neurons form glutamatergic synaptic connections onto OPCs (*12*–*17*). However, an elegant study conditionally ablating a necessary subunit of the *N*-methyl-D-aspartate (NMDA) receptor in oligodendroglial lineage cells during development did not demonstrate deficits in oligodendrogenesis or myelination, arguing against a role for direct NMDA receptor-mediated axoglial synaptic neurotransmission as a mechanism regulating myelination in vivo (*18*). The potential role of neuronal activity in the regulation of myelin-forming cells remains unclear in vivo; if established, this would constitute a previously underappreciated mechanism by which experience directs adaptive behavioral change.

Results

Description of the Optogenetic Model and Experimental Paradigm

In this work, we used optogenetic stimulation of the premotor cortex in awake, behaving Thy1::channelrhodopsin 2 (ChR2) mice (*19*, *20*) to test the effects of neuronal activity on oligodendroglial cells in vivo. In this well-characterized model, the excitatory opsin is expressed in a subset of neurons under the control of the Thy1 promoter. In the cortex, the Thy1 promoter and, thus, the excitatory opsin are expressed chiefly in cortical layer V projection neurons and are not expressed in glial cell types (*19*, *20*). ChR2-expressing neurons respond to pulses of blue (470-nm) light with millisecond precision such that the frequency of light pulses elicits neuronal spiking of the same frequency (*19*, *20*). Expression of ChR2 does not alter the electrical properties of neurons in the absence of blue light and does not affect neuronal survival under basal conditions or with blue light stimulation using standard experimental parameters (*21*). When the optical fiber is placed just below the pial surface, ~10% of the blue light penetrates 0.5 mm, or about halfway through the cortex, and ~1% reaches 1 mm (to cortical layer VI) (*22*). This stimulates the apical dendrites of layer V neurons and, to a lesser extent as the light is attenuated by layer V, the neuronal somata, resulting in neuronal firing of layer V projection neurons (*22*). Heat generated by this system is negligible under these conditions and localized to the optical fiber (*22*). Stimulating from just below the pial surface limits hardware-related injury to the skull and cortical layer I, in contrast to alternative strategies such as intracortical microstimulation that involve more extensive electrode-related tissue damage.

We placed the optical-neural interface just below the pial surface in cortical layer I of area M2 (premotor area) (Fig. 1A) in juvenile [postnatal day 35 (P35)] mice and stimulated unilaterally with blue light for 30-s intervals every 2 min over a 30-min period at 20 Hz, a frequency consistent with the 10- to 40-Hz physiological firing rates of layer V projection neurons in the motor cortex (*19*). Unilateral stimulation of right-sided M2, a high-level cortical region involved in motor planning and the generation of complex and goal-directed motor behavior (*23*), caused mice to ambulate consistently in the contralateral (left) direction when the blue light was on (movie S1). This behavioral measure confirms proper placement of the light-stimulation fiber and demonstrates the expected behavioral consequences of optogenetic premotor cortex stimulation.

The placement of the fiber requires breaching the skull and dura, and the optical fiber penetrates the most superficial layer of the cortex (layer I). Because injury (*24*) and the associated microglial inflammation (*25*) can influence OPC behavior, wild-type [(WT), no opsin present] littermate control animals were identically manipulated to control for effects of surgery, fiber placement, and light. In WT mice, blue light stimulation causes no observable change in behavior. We used manipulated WT littermate controls in all analyses described below to account for effects of injury and inflammation.

Neuronal Activity–Regulated Precursor Cell Proliferation

To test the acute effects of neuronal activity on cell proliferation, we administered the thymidine analog 5-ethynyl-2′-deoxyuridine (EdU) at the beginning of the 30-min stimulation period to label dividing cells and sacrificed mice 3 hours later. Following this period of activity, we observed a proliferative response in the premotor

[1]Departments of Neurology, Neurosurgery, and Pediatrics, Institute for Stem Cell Biology and Regenerative Medicine, Stanford University School of Medicine, Stanford, CA 94305, USA. [2]Graduate Program in Stem Cell Biology and Regenerative Medicine, Stanford University School of Medicine, Stanford, CA 94305, USA. [3]Graduate Program in Neuroscience, Stanford University School of Medicine, Stanford, CA 94305, USA. [4]Departments of Neurobiology and Developmental Biology, Stanford University School of Medicine, Stanford, CA 94305, USA. [5]Department of Pathology, Stanford University School of Medicine, Stanford, CA 94305, USA.

*These authors contributed equally to this work.
†Corresponding author. E-mail: mmonje@stanford.edu

cortex (Fig. 1, A and B) and subcortical white-matter projections in the corpus callosum (Fig. 2). At P35, we observed a fourfold increase in dividing cells in stimulated (ipsilateral) M2 compared with manipulated WT littermate controls (7368 ± 1228 versus 1940 ± 512 cells; $n = 3$ mice per group; $P < 0.001$) (Fig. 1C). Dividing cells, outside the immediate area of optical fiber placement in layer I, were found in the deep cortical layers near the optogenetically stimulated neurons and in the subcortical fibers of the corpus callosum (Figs. 1B and 2).

To characterize the cells proliferating in response to neuronal activity, we employed immunofluorescence staining for cell identity markers (Fig. 1, D and E, and fig. S1). We found that 54% of the dividing cells in optogenetically stimulated Thy1::ChR2 M2 express the oligodendroglial lineage marker Olig2; stimulated M2 in Thy1::ChR2 mice exhibited a significant increase in dividing Olig2$^+$ cells compared with WT controls (4032 ± 832 versus 519 ± 152 cells, respectively; $P < 0.001$) (Fig. 1D). Of the dividing cells, 24.5% were PDGFRα^+ OPCs (PDGFR, platelet-derived growth factor receptor) (Fig. 1E); a similar number of EdU-marked OPCs was detected by co-labeling with Sox2 and Olig2 (fig. S1B). A

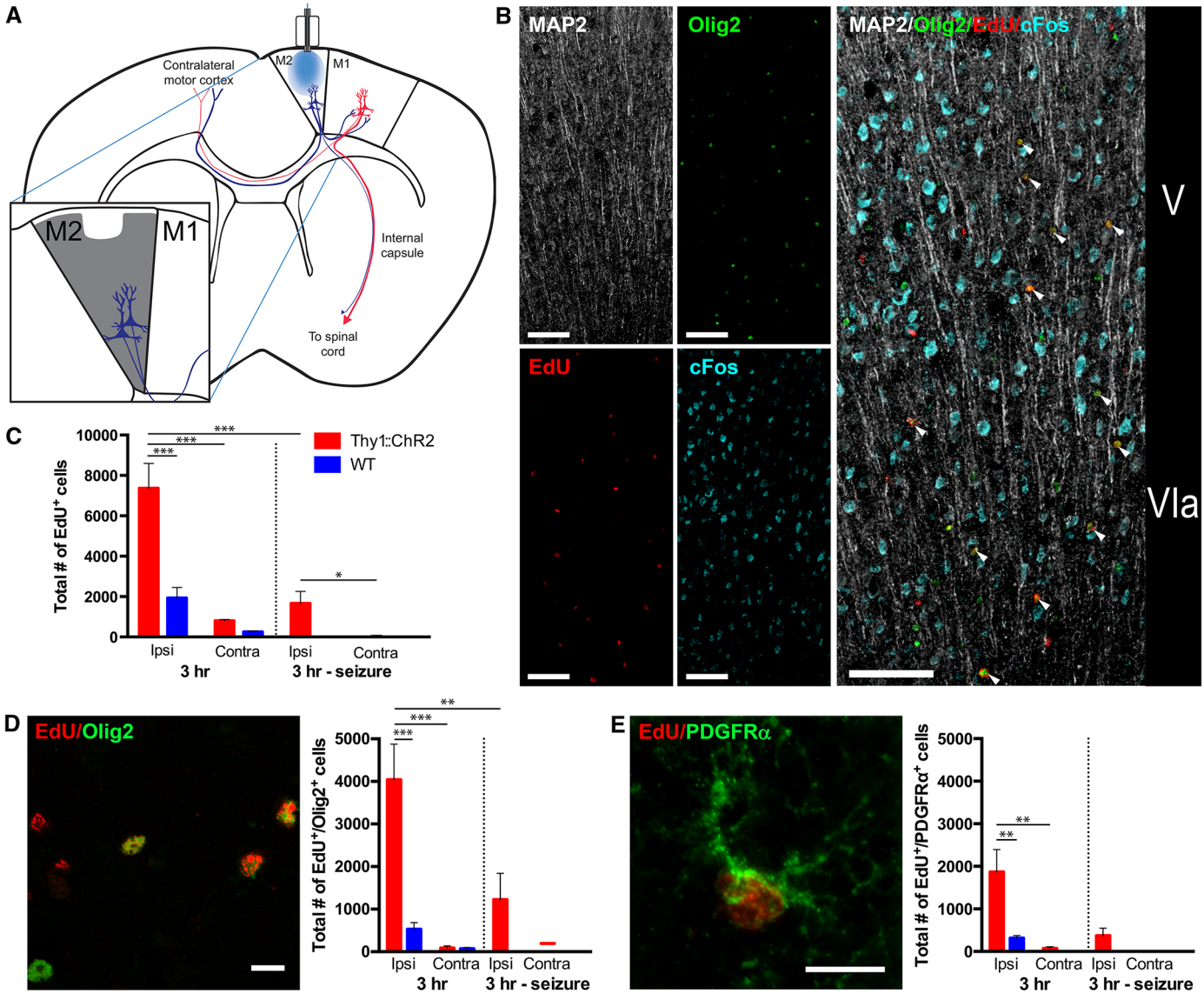


Fig. 1. Neuronal activity that elicits complex motor behavior stimulates OPC proliferation in the premotor cortex. (**A**) Schematic of optogenetic stimulation with simplified M2 circuit projections; expanded view shows the quantified area. (**B**) Proliferating oligodendroglial lineage cells are found near active neuronal cell bodies in the deep layers of the optogenetically stimulated M2 motor cortex. Confocal micrograph (split view on the left; composite image on the right) of the M2 deep cortical layers V and VIa 3 hours after optogenetic stimulation in a Thy1::ChR2 mouse. The immediate early gene c-Fos (blue) indicates recent neuronal activity. MAP2 (white) indicates neuronal cell bodies and apical dendrites. Proliferating cells marked by EdU (red) are seen throughout the deep cortical layers and frequently colocalize with the oligodendroglial lineage marker Olig2 (green; colocalized EdU$^+$/Olig2$^+$ cells are indicated by the white arrowheads.) Scale bars, 100 μm. (**C**) Total EdU$^+$ cells in M2 of P35 mice ($n = 3$ per group) 3 hours after optogenetic stimulation. The M2 regions ipsilateral (Ipsi) and contralateral (Contra) to the site of the optical fiber are quantified. (**D**) Representative confocal micrograph of EdU$^+$ cells (red) and Olig2$^+$ (green), together with the total number of EdU$^+$/Olig2$^+$ cells in M2 3 hours after optogenetic manipulation. Scale bar, 10 μm. (**E**) Representative confocal micrograph of an EdU-marked (red) PDGFRα^+ (green) OPC, together with the total number of EdU-marked OPCs in M2 3 hours after optogenetic manipulation. Scale bar, 10 μm. In all graphs, red bars indicate Thy1::ChR2 mice; blue bars denote identically manipulated WT littermate controls. Mice in whom seizures were induced rather than ambulatory behavior are shown on the right-hand side of the graphs ($n = 3$ per group). *$P < 0.05$, **$P < 0.01$, ***$P < 0.001$. Error bars indicate SEM.

significant increase in EdU-marked Sox2$^+$ neural precursor cells (NPCs) (*26*) was also observed in stimulated M2 compared to WT controls (fig. S1A). No significant fraction of the proliferating cells represented GFAP$^+$ (GFAP, glial fibrillary acidic protein) or S100β$^+$ astrocytes (fig. S1, C and D). Consistent with reports that optogenetic stimulation of ChR2-expressing neurons within the parameters used here does not induce neuronal injury or death (*21*), cleaved caspase-3 staining, indicating apoptotic cells, was not observed within optogenetically stimulated M2 (fig. S2).

We also observed an increase in proliferation in the corpus callosum of Thy1::ChR2 mice compared with manipulated WT controls (Fig. 2). Though EdU labeling was observed throughout the corpus callosum, a defined region subjacent to motor cortex and distant from the ventricular region was quantified to avoid the potential confound of EdU$^+$ cells arising from the periventricular-subventricular zone which contains a briskly mitotic and migratory population of cells that take up the EdU marker but may be distinct from those cells responding to neuronal activity (Fig. 2A). Total EdU$^+$ cell quantification revealed a twofold increase in dividing cells in the stimulated Thy1::ChR2 animals compared with manipulated WT controls (2440 ± 174 versus 916 ± 77 cells; $n = 3$ per group; $P < 0.0001$) (Fig. 2, B and C), with a significant increase in EdU-marked Olig2$^+$ oligodendroglial lineage cells in the stimulated Thy1::ChR2 animals compared with manipulated WT controls (1016 ± 68 versus 455 ± 58 cells; $n = 3$ per group; $P < 0.0001$) (Fig. 2D). Similar to M2, approximately half (42%) of the dividing cells are Olig2$^+$ (Fig. 2D), and no EdU-labeled GFAP$^+$ astrocytes or EdU-labeled S100β$^+$ astrocytes were found.

Optogenetic stimulation of opsin-expressing neurons in the motor cortex elicits expected electrophysiological and behavioral responses (*19*, *20*), but one cannot exclude the possibility of decreased neuronal health due to the presence of the opsin or to the optogenetic stimulation of firing. To control for the effects of pathological neuronal activity, we induced generalized tonic-clonic motor seizures optogenetically using the same frequency and intensity of stimulation but placing the optical fiber more medially in M2 so that light stimulates both motor cortices simultaneously. Proliferation comparable to that seen in the manipulated WT control animals was observed in the seizure animals (Fig. 1C), but not to the degree seen in animals after optogenetic stimulation that results in complex motor behavioral output ($n = 3$; $P < 0.001$) (Fig. 1, C to E). That optogenetically induced motor seizures did not elicit a proliferative response of the same magnitude indicates that pathological neuronal activity is not sufficient to account for the observed proliferative effect. Taken together, these findings show that moderate, precisely timed levels of electrical activity in neurons evoking naturalistic behavior in awake, freely behaving mice promoted the proliferation of NPC and OPC populations.

Evaluation of Inflammatory Response to Fiber Optic Manipulation

Given the effects of microglial inflammation on NPC (*27*–*29*) and OPC (*25*) proliferation and

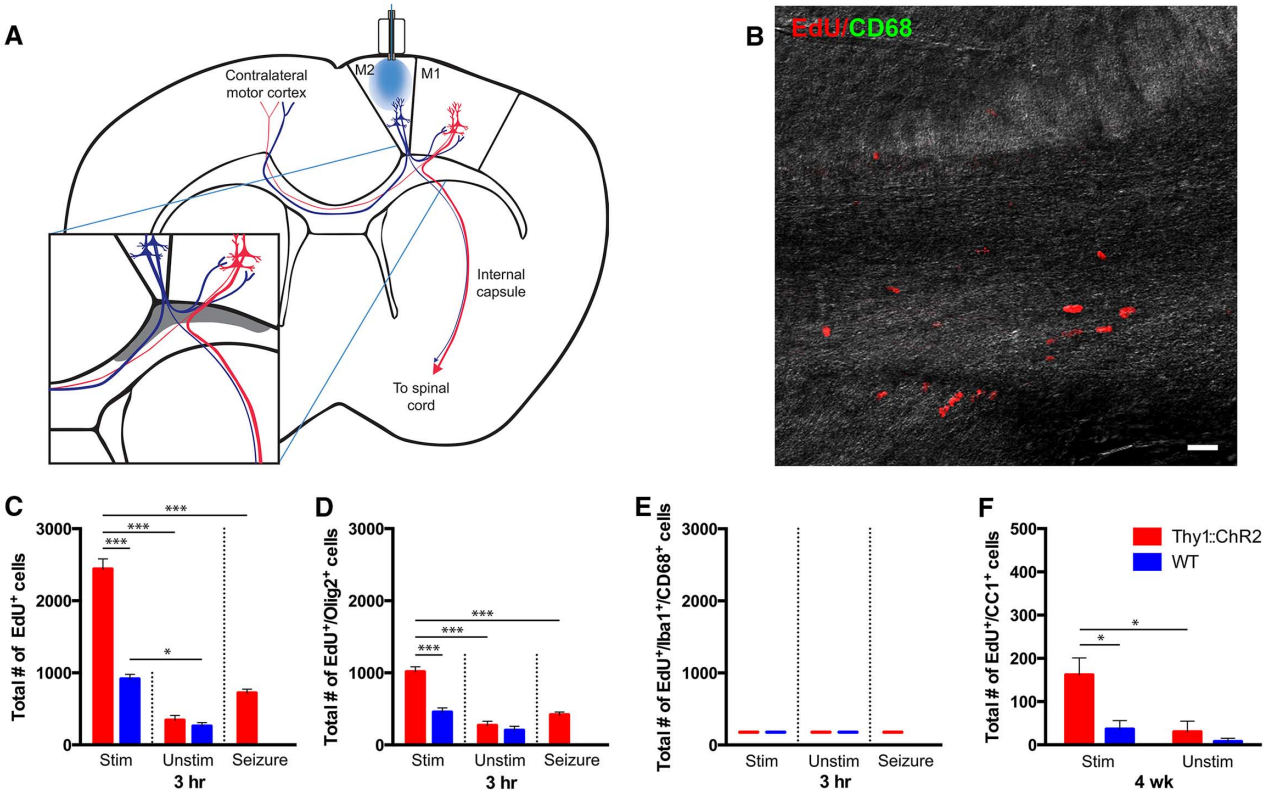


Fig. 2. Oligodendroglial lineage cells in the corpus callosum respond to premotor circuit activity. (**A**) Schematic of optogenetic stimulation with simplified M2 circuit projections; expanded view shows the area quantified in the corpus callosum (shaded gray). (**B**) Confocal micrograph from a stimulated Thy1::ChR2 corpus callosum overlaid on a differential interference contrast background to illustrate regional tissue architecture. Activated microglial marker CD68, green; EdU, red. No EdU$^+$ activated microglia were detected in the corpus callosum of stimulated or unstimulated mice. Scale bar, 20 μm. (**C** to **E**) Total EdU$^+$ (C), EdU$^+$/Olig2$^+$ (D), and EdU/Iba1$^+$/CD68$^+$ cells (E) in the indicated region of corpus callosum of P35 stimulated (Stim; $n = 3$ per group) or unstimulated (Unstim; $n = 3$ per group) mice 3 hours after optogenetic stimulation. (**F**) Total number of EdU$^+$/CC1$^+$ mature oligodendrocytes 4 weeks after premotor cortex optogenetic stimulation (or no stimulation) at P35 in Thy1::ChR2 ($n = 4$ per group) or WT ($n = 3$ per group) mice. In all graphs, red bars indicate Thy1::ChR2 mice; blue bars denote identically manipulated WT littermate controls. As the corpus callosum is a single structure, the contralateral structure does not serve as an internal control for stimulation. Thus, an unstimulated group, in which surgery was performed and the optical-neural interface was placed but no light exposure occurred, was included in corpus callosum analyses. Mice in whom seizures were induced rather than ambulatory behavior are shown on the right-hand side of the graph ($n = 3$ per group). *$P < 0.05$, ***$P < 0.001$. Error bars indicate SEM.

differentiation, the microglial response must be carefully evaluated and accounted for in this model. The majority of EdU$^+$ microglia were localized to the superficial layers of M2 near the site of the optical fiber and less in the deep layers of the cortex where the optogenetically stimulated neuronal somata reside (Fig. 3, A and B). Approximately 75% of the dividing activated microglia were localized to the superficial cortex, whereas only 25% were found in deep cortical layers in all experimental groups (Fig. 3B). To be conservative, as microglial effects such as cytokine secretion could be exerted over some distance, we quantified all microglia in M2 up to cortical layer I, excluding only those within ~100 μm of the optical fiber (Fig. 3, A to F). Consistent with the injury induced by the manipulation, we observed a significant increase in EdU-labeled dividing microglia marked by the pan-microglial marker Iba1 (*30*, *31*) and the marker of microglial "activation" CD68 (*32*, *33*) compared with the contralateral hemisphere in both WT and Thy1::ChR2 mice, as well as in the seizure control animals ($P < 0.05$ in all comparisons) (Fig. 3, C and D). The number of EdU-labeled, Iba1$^+$ and CD68$^+$ activated microglia was not different between optogenetically stimulated Thy1::ChR2 and manipulated WT mice at the 3-hour time point (1991 ± 107 versus 1412 ± 377 cells; $P = 0.10$) (Fig. 3D). Seizure animals exhibited an equivalent number of EdU-labeled, Iba1$^+$ and CD68$^+$ microglia compared to Thy1::ChR2 mice in whom locomotion was induced and compared to manipulated WT controls (Fig. 3D). By 24 hours, EdU-marked, Iba1$^+$ and CD68$^+$ activated microglia were significantly decreased in the premotor cortex compared with at the 3-hour time point (1991 ± 107 at 3 hours versus 801 ± 181 cells at 24 hours for Thy1::ChR2 animals; $n = 3$; $P = 0.005$) (Fig. 3D). There was no difference in the numbers of EdU-labeled, Iba1$^+$ and CD68$^+$ activated microglia in stimulated Thy1::ChR2 compared to manipulated WT mice at 24 hours (801 ± 181 versus 515 ± 147 cells; $n = 3$; $P = 0.07$) (Fig. 3D). The overall density (EdU$^+$ and EdU$^-$) of activated Iba1$^+$ and CD68$^+$ microglia was also not different between Thy1::ChR2 and WT at 3 or 24 hours, indicating an equal microglial inflammatory response in manipulated Thy1::ChR2 and WT littermate control mice ($P > 0.25$ in all comparisons) (Fig. 3E). In the corpus callosum, no EdU-marked, CD68$^+$ activated microglia were detected in either stimulated (or unstimulated) Thy1::ChR2 or WT mice (Fig. 2, B and E). The microglial inflammatory response was also evaluated after a 7-day stimulation paradigm (cycles of 30 s on, 2 min off over 10 min each day; see below). The overall density (EdU$^+$ and EdU$^-$) of activated Iba1$^+$ and CD68$^+$ microglia was also not different between Thy1::ChR2 and WT on day 7 of or 4 weeks after this 7-day stimulation paradigm (Fig. 3F). The microglial inflammatory response, predominantly localized to the superficial cortex, is thus equal in Thy1::ChR2 mice compared to WT littermate controls after optical fiber placement and blue light stimulation in this model.

Neuronal Activity–Regulated Oligodendrocyte Differentiation

To define the population dynamics and fate of cells dividing in response to neuronal activity, we repeated the above experiment but sacrificed P35 mice at 24 hours after a single session of optogenetic stimulation and, in a parallel cohort, sacrificed at 4 weeks after a 7-day stimulation paradigm (cycles of 30 s on, 2 min off over 10 min each day, resulting in 2.5 min of total stimulation daily). In Thy1::ChR2 mice, we observed no statistically significant change in the total number of EdU$^+$ cells from 3 to 24 hours, and only 1 to 2% of EdU$^+$ cells colabeled with either Ki67 or cleaved caspase-3 at 24 hours, indicating that the dividing cells cease proliferation soon after stimulated neuronal activity and survive in the subacute time period ($n = 3$) (Fig. 4, A and B). In contrast, 32% of the EdU$^+$ cells in WT animals remained in a proliferative state at 24 hours, evidenced by

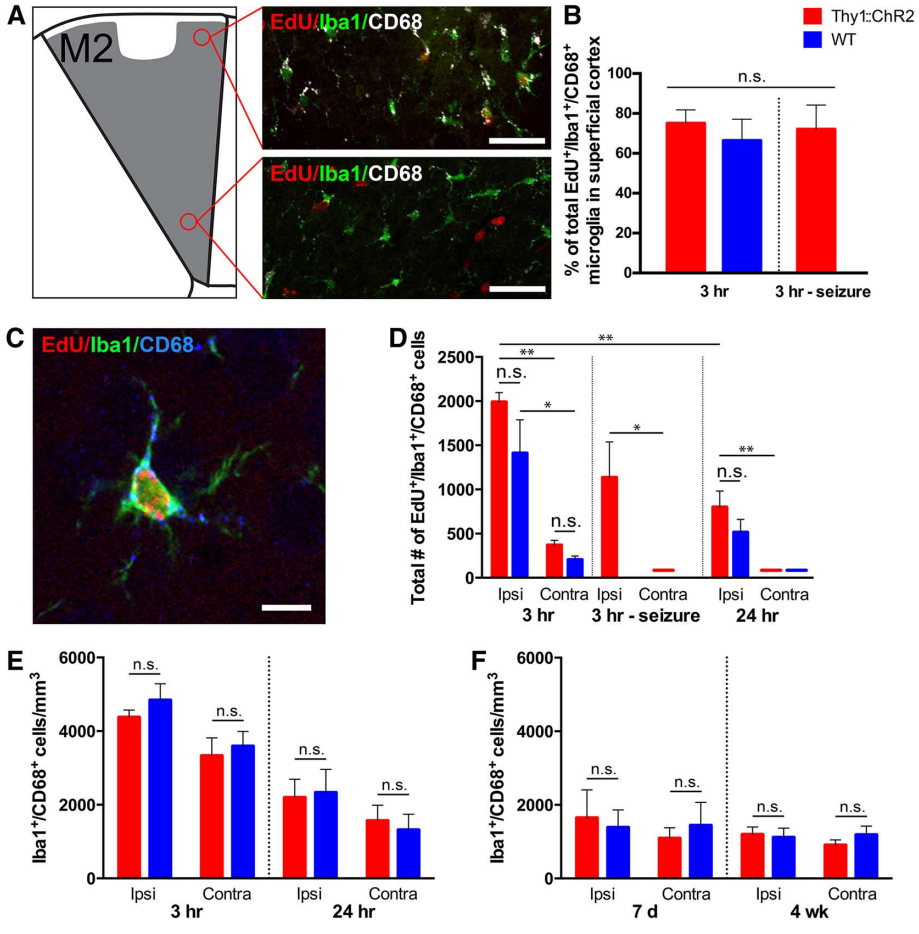


Fig. 3. Microglial inflammatory response to optical fiber manipulation is equivalent in Thy1::ChR2 and WT mice. (**A**) The majority of reactive microglia are localized to the superficial cortex (layer I), near the site of the optical fiber placement. Representative confocal micrographs illustrating CD68$^+$ activated microglia in the superficial M2 cortex in comparison to largely CD68$^-$ microglia in the deep cortex (layer V/VI). EdU, red; pan-microglial marker Iba1, green; activated microglial marker CD68, white. Scale bars, 50 μm. (**B**) Percentage of EdU-marked activated microglia (Iba1$^+$/CD68$^+$) in superficial versus deep layers of M2 cortex ipsilateral to the optical fiber, 3 hours after blue light stimulation in Thy1::ChR2 and WT littermate control mice. (**C**) Representative confocal micrograph illustrating a CD68$^+$ activated microglia marked with EdU. EdU, red; Iba1, green; CD68, blue. Scale bar, 10 μm. (**D**) Total numbers of EdU-marked activated microglia throughout the M2 cortex in Thy1::ChR2 and WT littermate control mice 3 and 24 hours after optogenetic manipulation ipsilateral and contralateral to the optical fiber placement. (**E**) Density of total CD68$^+$ microglia throughout the M2 cortex ipsilateral and contralateral to the optical fiber placement at 3 and 24 hours after a single 30-min session of optogenetic manipulation in P35 Thy1::ChR2 and WT mice. (**F**) Density of total CD68$^+$ microglia throughout the M2 cortex ipsilateral and contralateral to the optical fiber placement after a 7-day stimulation paradigm (10 min per day for 7 days) was measured on day 7 (after stimulation from P29 to P35) or 4 weeks after the completion of stimulation (from P35 to P42) in Thy1::ChR2 and WT mice. In all graphs, red bars indicate Thy1::ChR2 mice; blue bars denote identically manipulated WT littermate controls. Mice in whom seizures were induced rather than ambulatory behavior are shown to the right of the 3-hour graphs ($n = 3$ per group). n.s. (not significant) indicates $P > 0.05$. *$P < 0.05$, **$P < 0.01$. Error bars indicate SEM.

colabeling with Ki67 ($n = 3$; $P < 0.05$) (Fig. 4B). Thy1::ChR2 mice have fewer EdU$^+$ cells present in M2 at 4 weeks, which may be due to cell dispersion and death during that interval ($n = 7$ per group) (Fig. 4A and fig. S3A).

Dividing cells were localized to the motor cortex and subcortical white matter, including the corpus callosum, 3 hours after neuronal activity (Figs. 1B and 2). By 4 weeks, dispersion of EdU$^+$ cells was observed (fig. S3A), but no significant increase in EdU$^+$ cells was observed in the corresponding corticospinal tract at the level of the cervical spinal cord compared to the contralateral side ($n = 4$ Thy1::ChR2; $P = 0.48$) or to WT ($n = 3$ WT; $P = 0.16$) (fig. S3, B and C). This localization may reflect differences inherent in cortical OPCs compared with those found in the deep white matter (*34*, *35*), proximity to neuronal cell bodies (*36*), or differences in neuronal cell types (e.g., callosal projection neurons versus corticofugal projection neurons).

Because changes in the epigenetic landscape of NPCs and OPCs are necessary for progression to differentiated states (*37*, *38*), we examined population-level changes in histone modifications (Fig. 4, C and D). We found a neuronal activity–regulated increase in trimethylation of histone H3 lysine 9 (indicative of a repressive, heterochromatin state; $P < 0.05$) and a concomitant decrease in acetylated histone H3 (correlating with activating regulatory elements; $P < 0.05$) in dividing (EdU$^+$) cells between 3 and 24 hours after optogenetically stimulated neuronal activity in Thy1::ChR2 mice (Fig. 4, C and D). Thus, neuronal activity promotes a transition to a repressive chromatin state consistent with differentiation.

To evaluate the fate of the cells proliferating in response to neuronal activity, we optogenetically stimulated M2 daily as above for 7 days, then sacrificed mice 4 weeks after the end of stimulation ($n = 7$ per group). In stimulated M2, we found the absolute number of newly generated (EdU$^+$) Sox2$^+$/Olig2$^-$ NPCs and oligodendroglial (Olig2$^+$) cells remained increased compared with manipulated WT controls ($P < 0.05$ for NPCs; $P < 0.01$ for Olig2$^+$) (fig. S4 and Fig. 5A). Neuronal activity–regulated oligodendrogenesis is evidenced by an increase in the number of both EdU$^+$ early oligodendroglial cells expressing transcription factor Olig1 in a nuclear pattern (Olig1$^{nuclear+}$) and in EdU$^+$ mature oligodendrocytes expressing Olig1 in a perinuclear pattern (Olig1$^{perinuclear+}$) compared with manipulated WT controls ($P < 0.05$ for nuclear Olig1 and $P < 0.05$ for perinuclear Olig1) (Fig. 5, C and D) (*39*). Neuronal activity–regulated oligodendrogenesis was confirmed using CC1, also a marker for mature oligodendrocytes (534 ± 131 versus 39 ± 30 EdU$^+$/CC1$^+$ cells; $n = 4$ Thy1::ChR2 mice, 3 WT mice; $P < 0.01$) (Fig. 5, E and F). Supporting the interpretation that the cells dividing in response to neuronal activity had differentiated into oligodendrocytes, the EdU$^+$ OPC population (EdU$^+$/PDGFRα$^+$ and EdU$^+$/Sox2$^+$/Olig2$^+$) had diminished compared with the acute time point (Fig. 5B and fig. S4B) concomitantly with the appearance of EdU$^+$ oligodendrocytes (Fig. 5, C to F). An increase in newly generated oligodendrocytes was also found in the corpus callosum of optogenetically stimulated Thy1::ChR2 mice as compared with identically manipulated WT littermate controls (162 ± 39 versus 36 ± 19 EdU$^+$/CC1$^+$ cells; $n = 4$ Thy1::ChR2 mice, 3 WT mice; $P < 0.05$) (Fig. 2F). These results demonstrate activity-regulated oligodendrogenesis within the active neural circuit.

Histone deacetylation is required for oligodendrocyte differentiation (*37*, *38*). Blockade of histone deacetylation with trichostatin A (TSA), an inhibitor of histone deacetylases (HDACs) 1 and 2, prevented new mature oligodendrocyte production assessed with Olig1^{perinuclear} and CC1 markers ($n = 4$ per group; $P = 0.49$ for Olig1^{perinuclear} and $P = 0.44$ for CC1) (Fig. 5, C to F). TSA administration had no effect on the total number of EdU-labeled cells detected at 4 weeks after stimulation ($P = 0.3$) (fig. S5). Consistent with epigenetic blockade of differentiation, an increase in the number of EdU-labeled, Olig1$^{nuclear+}$ cells representing immature oligodendrocytes was observed at 4 weeks after stimulation ($P < 0.01$) (Fig. 5D).

Response of Oligodendroglial Lineage Cells to Neuronal Activity in Adults

Using the same model, we evaluated the effect of neuronal activity on oligodendroglial lineage cells in adult animals. At 4 weeks after the 7-day paradigm of optogenetic stimulation (commencing at age P84), we found a twofold increase in the total number of EdU-marked cells in the stimulated M2 compared with manipulated WT controls (2306 ± 337 versus 983 ± 382 cells; $n = 4$

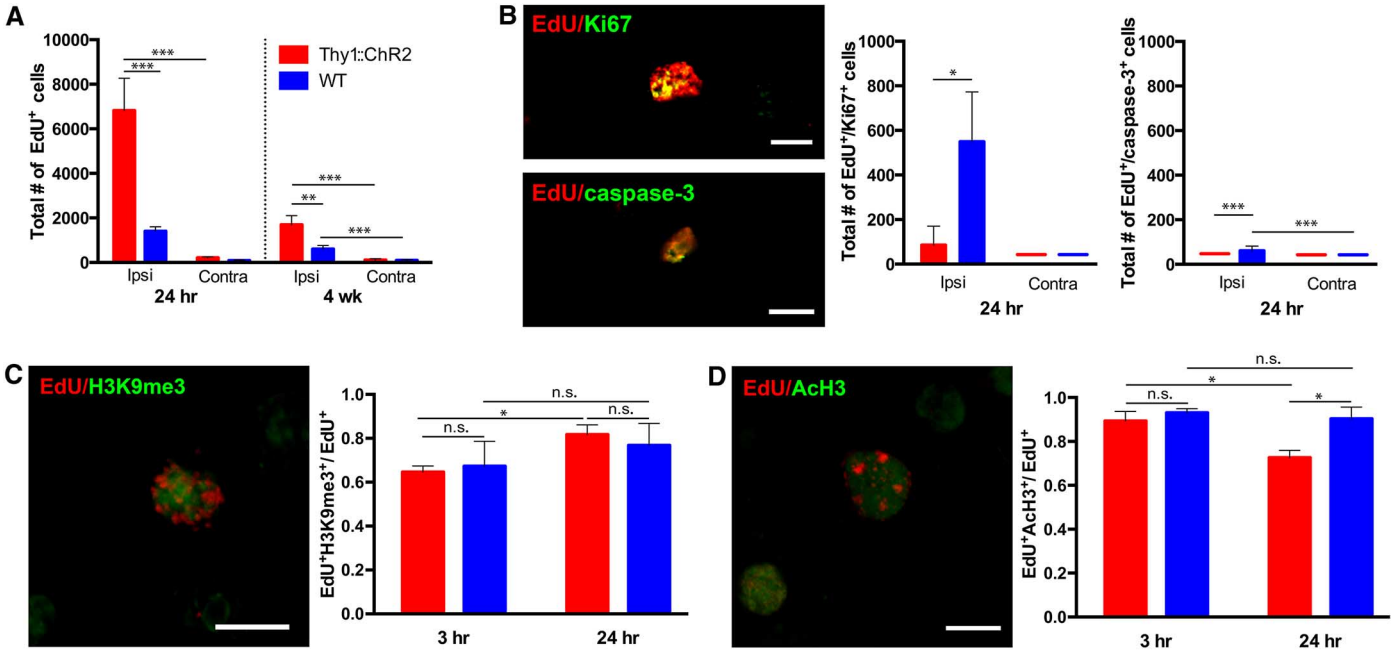


Fig. 4. Neuronal activity initiates differentiation. (**A**) Total number of EdU$^+$ cells in Thy1::ChR2 and WT mice at 24 hours ($n = 4$ per group) and 4 weeks ($n = 7$ per group) poststimulation. (**B** to **D**) Representative confocal micrographs illustrating colocalization of EdU (red) with markers (green) of cell mitosis (Ki67), apoptosis (cleaved caspase-3), or histone modification markers histone H3 lysine 9 trimethylation (H3K9me3) and histone H3 acetylation (AcH3). In all graphs, red bars indicate Thy1::ChR2 mice; blue bars denote identically manipulated WT littermate controls. *$P < 0.05$, **$P < 0.01$,***$P < 0.001$. n.s. denotes $P > 0.05$. Error bars indicate SEM. Scale bars, 10 μm. Value of (—) over x axis = 0 ± 0.

Thy1::ChR2 mice, 3 WT mice; $P < 0.05$). There was a significant increase in the number of $Olig2^+$, EdU-marked cells in both M2 (788 ± 45 versus 204 ± 71 cells; $n = 4$ Thy1::ChR2 mice, 3 WT mice; $P < 0.0001$) (fig. S6B) and in the corpus callosum (79 ± 17 versus 20 ± 9 cells; $n = 4$ Thy1::ChR2 mice, 3 WT mice; $P < 0.05$) (fig. S7B) of stimulated Thy1::ChR2 mice compared with identically manipulated WT controls. Concomitant with a decrease in EdU-marked OPCs (figs. S6C and S7C), mature oligodendrocytes marked by EdU were increased 4 weeks after the end of the stimulation paradigm in adult animals. In M2, an increase in $EdU^+/CC1^+$ mature oligodendrocytes was found in optogenetically stimulated Thy1::ChR2 mice compared with manipulated WT littermates (767 ± 106 versus 72 ± 50 cells; $n = 4$ Thy1::ChR2 mice, 3 WT mice; $P < 0.001$) (fig. S6D). Similarly, an increase in EdU-marked mature oligodendrocytes was observed in the adult corpus callosum (112 ± 32 versus 7 ± 4 $EdU^+/CC1^+$ cells; $n = 4$ Thy1::ChR2 mice, 3 WT mice, respectively; $P < 0.05$) (fig. S7D).

As above, EdU-marked, newly generated oligodendrocytes were quantified in the premotor cortex and in the corpus callosum after optogenetic stimulation at P35 or P84. Adjusting the total number of $EdU^+/CC1^+$ cells for the volume of tissue analyzed, we found more $EdU^+/CC1^+$ cells per cubic millimeter in the corpus callosum compared with M2 in mice stimulated at P35 (8983 ± 2188 cells/mm^3 in corpus callosum versus 3010 ± 737 cells/mm^3 in M2; $n = 4$ Thy1::ChR2 mice; $P < 0.05$) (fig. S8A). In animals stimulated at P84, a more comparable number of newly generated oligodendrocytes per tissue volume was found (6214 ± 1763 cells/mm^3 in corpus callosum versus 4318 ± 599 cells/mm^3 in M2; $n = 4$ Thy1::ChR2 mice; $P = 0.35$) (fig. S8B).

Neuronal Activity–Regulated Myelination

Even small changes in the thickness of the myelin sheath relative to axon caliber (i.e., *g*-ratio) can have a profound effect on impulse conduction speed (*40*). To ascertain the effect of neuronal activity on myelin thickness, we used transmission electron microscopy (TEM) to analyze myelin thickness in M2 layer VI and subcortical fibers entering the corpus callosum 4 weeks after optogenetic stimulation (Fig. 6A). Relative to axonal diameter (*g*-ratio = axon diameter/axon + myelin sheath diameter), myelin sheaths were thicker (i.e., decreased *g*-ratio) in optogenetically stimulated M2 and subcortical fibers ($g = 0.701 \pm 0.014$; $n = 4$ mice) compared with manipulated WT controls ($g = 0.756 \pm 0.003$; $n = 3$ mice; $P < 0.05$) (Fig. 6B). No difference in *g*-ratio was observed between genotypes on the side contralateral to stimulation ($P = 0.13$) (Fig. 6C). Quantification of *g*-ratios was performed by two independent blinded raters.

As supportive evidence to the TEM studies above, we examined the expression of the myelin-related protein myelin basic protein (MBP). Whereas MBP expression levels do not necessarily indicate the formation of compact myelin, as premyelinating oligodendrocytes express MBP, we found that MBP expression was also increased within M2 and subcortical white matter at 4 weeks after optogenetically stimulated neuronal activity, which is consistent with the TEM data above ($n = 10$ Thy1::ChR2, $n = 9$ WT; $P < 0.001$) (fig. S9).

Behavioral Consequences

To evaluate possible functional consequences of neuronal activity–regulated oligodendrogenesis and myelination, we tested motor behavioral performance using CatWalk gait analysis 4 weeks after the 7-day stimulation paradigm. Because demyelination or other injury to the motor system impairs limb swing speed, we hypothesized that increased myelination would result in improvement of the sensitive measure of limb swing speed (*41*). The CatWalk gait analysis test does not require any prior training. CatWalk gait analysis (Fig. 7A) indicated improvement in swing speed of the correlate (left) forelimb during normal gait (interlimb variation +4.8 ± 1.4 cm/s in Thy1::ChR2 mice versus –4.3 ± 1.7 cm/s in WT mice; $n = 5$ Thy1::ChR2,

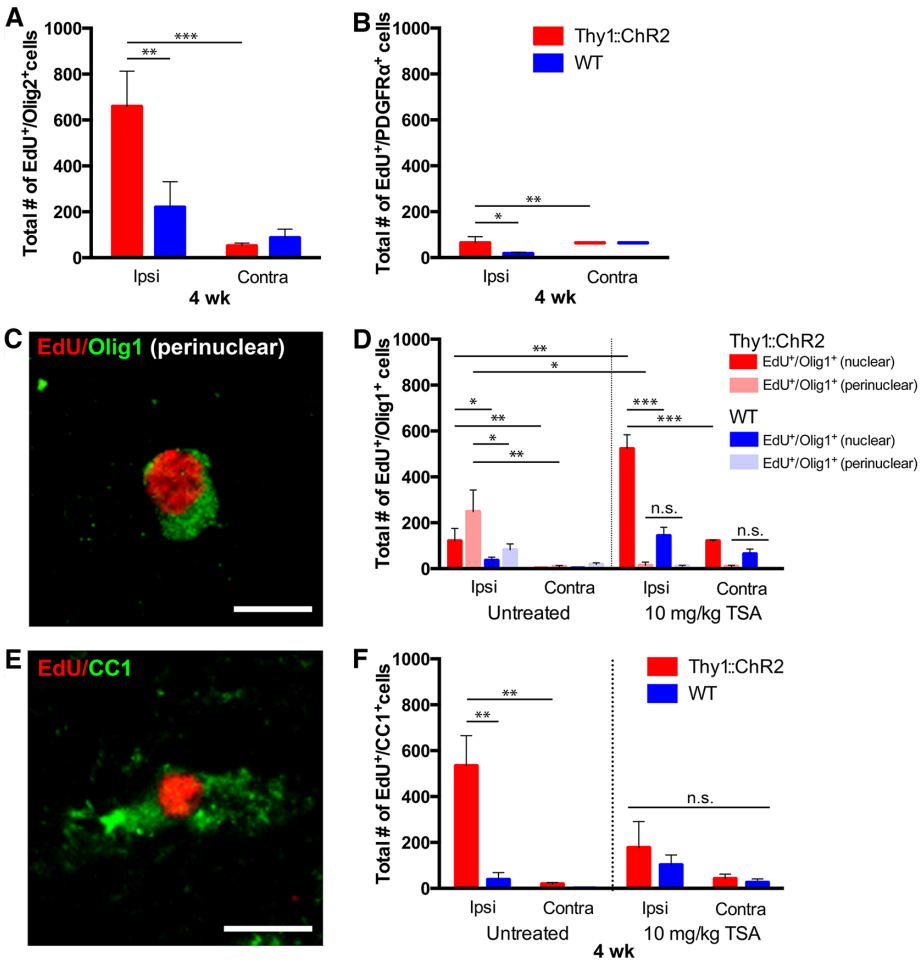


Fig. 5. Neuronal activity promotes oligodendrogenesis. Thy1::ChR2 and WT optogenetically stimulated mice sacrificed 4 weeks after a 7-day stimulation paradigm (P35 to P42) with ($n = 4$ Thy1::ChR2 and 3 WT) or without ($n = 7$ per group) exposure to TSA (10 mg/kg). (**A** to **F**) Cell identity markers of EdU-marked surviving cells quantified in the M2 cortex reveal that the majority of the remaining EdU^+ cells are in the oligodendroglial lineage [$Olig2^+$, (A)], with diminution of the oligodendrocyte precursor cell ($PDGFR\alpha^+$) population (B) and concomitant appearance of EdU^+ immature oligodendrocytes [(D); nuclear $Olig1^+$; red and dark blue bars] and mature oligodendrocytes marked by perinuclear $Olig1^+$ [(C and D), pink and light blue bars] and CC1 (E and F). (C and E) Representative confocal micrographs illustrating colocalization of EdU (red) with perinuclear Olig1 [green (C)] or CC1 [green (E)]. Scale bars, 10 μm. (D and F) Administration of the histone deacetylase inhibitor TSA during the week of optogenetic stimulation results in a blockade of mature oligodendrogenesis. TSA-treated groups are shown on the right halves of these graphs. Increased numbers of immature ($Olig1^{nuclear+}$) oligodendrocytes in the TSA group are consistent with an epigenetic blockade of precursor differentiation. In all graphs, red or pink bars indicate Thy1::ChR2 mice; blue bars denote identically manipulated WT littermate controls. $^*P < 0.05$, $^{**}P < 0.01$, $^{***}P < 0.001$. n.s. represents $P > 0.05$. Error bars indicate SEM. Value of (—) over *x* axis = 0 ± 0.

$n = 9$ WT; $P < 0.05$) (Fig. 7B), with no change in other parameters of gait such as forepaw strike intensity or stride length (Fig. 7, C and D). There was no effect of genotype on swing speed symmetry (interlimb variation for unmanipulated mice –1.8 ± 4.0 cm/s versus –1.2 ± 3.2 cm/s; $n = 6$ Thy1::ChR2, $n = 6$ WT, respectively; $P = 0.58$). Thus, oligodendrogenesis and increased myelin thickness in response to neuronal excitation correlates with altered motor function 4 weeks later.

Necessity of Myelin Changes

Do changes in myelin-forming cells account for the observed behavioral improvement? Neuronal activity could affect multiple parameters beyond oligodendrogenesis and myelination that are relevant to behavioral performance in the active circuit. One possibility is that asymmetric walking behavior led to asymmetric muscle development. However, we found that muscle mass and mean fiber diameter of the triceps and biceps brachii were unaffected by our protocol ($n = 4$ per group; $P > 0.3$) (fig. S10).

Whereas muscle structure remains unaltered by the optogenetic stimulation paradigm, other activity-dependent changes in the motor circuit such as subtle alterations in synaptic strength could account for the observed behavioral improvement. To address this question, we used HDAC inhibition with TSA, a manipulation that would be expected to enhance synaptic plasticity (*42*, *43*) but to block oligodendrogenesis (*37*, *38*), reasoning that preventing the behavioral improvement in this context would argue for the necessity of activity-induced changes in myelin-forming cells. We thus blocked oligodendrogenesis to determine if it was necessary for the increase in correlate limb swing speed. We administered TSA concomitantly with optogenetic stimulation at P35 to block oligodendrogenesis epigenetically and measured both myelination by TEM and gait performance on the CatWalk 4 weeks post stimulation. TSA administration effectively blocked oligodendrogenesis ($n = 4$ Thy1::ChR2, $n = 3$ WT; $P < 0.05$) (Fig. 5, D and F) and blocked the effect of neuronal activity on myelination (*g*-ratio = 0.756 ± 0.009 in stimulated, TSA-treated Thy1::ChR2 versus 0.762 ± 0.008 in manipulated TSA-treated WT; $n = 3$ per group; $P = 0.62$) (Fig. 6D). The observed effect on myelin thickness could be due to HDAC inhibitor–mediated blockade of new oligodendrocyte differentiation or to effects of TSA on existing oligodendrocytes. Blockade of activity-regulated oligodendrogenesis and myelination prevented the behavioral effect ($n = 6$ Thy1::ChR2, $n = 5$ WT; $P = 0.67$) (Fig. 7B). TSA administration did not affect baseline behavior or other parameters of gait (Fig. 7, C and D). As noted above, HDAC inhibition will affect many cell types, and an important consideration is whether TSA administration could itself negatively modulate motor function by effects on neurons or synaptic function. To the contrary, HDAC inhibition has been shown to improve learning and synaptic plasticity (*42*, *43*), so effects of TSA on neuronal plasticity or function would not be expected to account for the blockade of improvement in motor function. These findings support the interpretation that oligodendrocyte differentiation and/or myelination are necessary for the motor behavioral improvement observed after neuronal activity in this model.

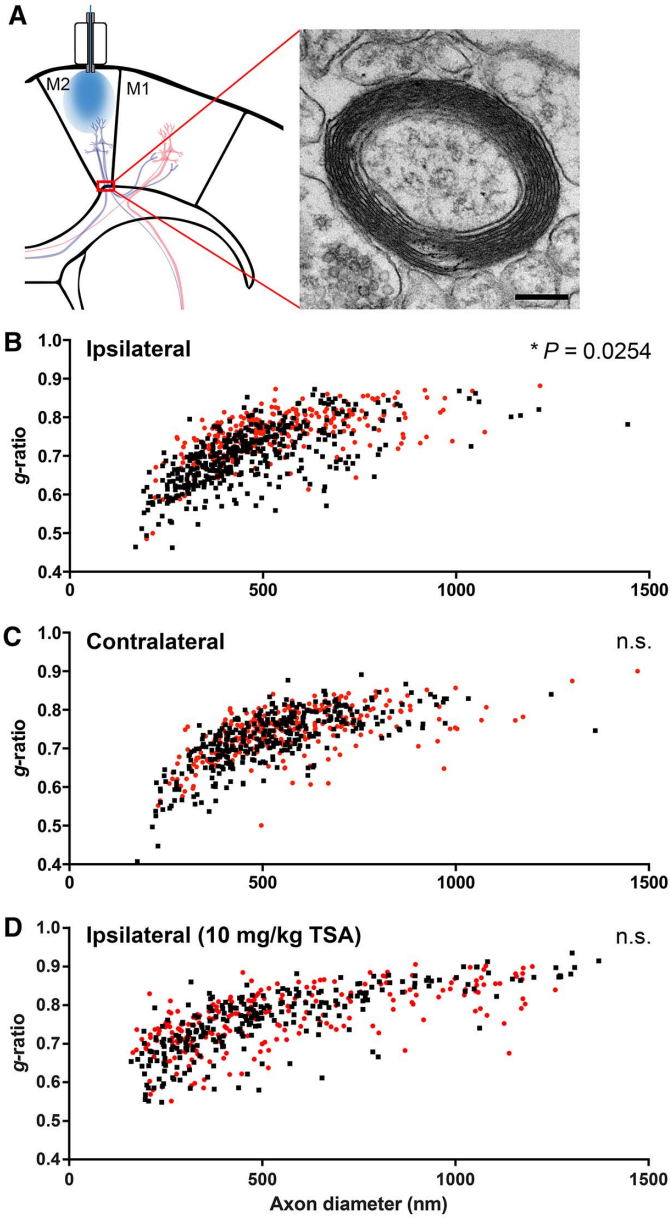


Fig. 6. Neuronal activity increases myelin thickness. (**A**) Transmission electron microscopy was performed in the projections from the premotor cortex entering the corpus callosum at the level indicated (red box). A representative TEM image of a myelinated axon at this level ipsilateral to optogenetic stimulation is shown at right (8000×, scale bar, 200 nm). (**B** to **D**) Scatter plots of *g*-ratio as a function of axon caliber in the cortical and subcortical projections from the ipsilateral (B) and contralateral (C) M2 in Thy1::ChR2 ($n = 4$ mice) and WT ($n = 3$ mice). Black squares, Thy1::ChR2; red circles, WT. (D) Scatter plot of *g*-ratios in TSA-treated Thy1::ChR2 (black squares; $n = 3$ mice) and WT (red circles; $n = 3$ mice) ipsilateral to stimulation. n.s. represents $P > 0.05$. Error bars indicate SEM.

Discussion

The results presented here demonstrate that behaviorally relevant neuronal activity in layer V projection neurons of the premotor cortex elicits a brisk proliferative response from NPCs and OPCs in the deep layers of the cortex and subcortical white matter, a subset of which differentiate into mature oligodendrocytes that persist weeks after the cessation of stimulation. Myelin thickness increases within the active circuit. These changes in myelin and myelin-forming cells are associated with an improvement in behavioral function that can be blocked by inhibition of oligodendrocyte differentiation and myelination. Taken together, these findings illustrate the plastic nature of myelin in the mammalian brain, raising numerous conceptual and mechanistic questions.

Whereas the present study provides evidence that active neurons influence OPC proliferation, differentiation, and myelination, the relation between these three aspects of myelin formation may not be linear or simple. Hughes *et al*. have demonstrated that OPCs can differentiate directly into oligodendrocytes without dividing and that OPC proliferation may occur in response to the decision to differentiate by a neighboring OPC (*24*). In the present study, those OPCs that differentiate without first proliferating would not be accounted for by EdU fate mapping, and so the number of newly generated oligodendrocytes may

have been underestimated. Similarly, whereas Young *et al*. have recently shown that adult-born oligodendrocytes contribute to ongoing myelin remodeling (*44*), it is not yet clear exactly how this occurs. In the present study, we cannot distinguish between the possibilities that neuronal activity results in myelination of previously unmyelinated axons, that new oligodendrocytes incorporate into existing sheaths, or that existing oligodendrocytes increase the thickness of the sheath. It is also interesting to note the difference in magnitude of the robust OPC proliferative response and new oligodendrocyte generation compared with the relatively small magnitude of change in myelin thickness (~10% change in average *g*-ratio), suggesting an alternative fate for some of these cells.

The paradigm used here mimics practicing a complex motor task. Would volitional, repetitive execution of a complex motor task result in the same findings? Neuroimaging studies suggest that this would be the case. A diffusion tensor imaging (DTI) study of humans before and after a 6-week period of practicing a new complex visuo-motor task (juggling) revealed changes in the microstructure of subcortical white matter within a brain region active in the task (*45*). Similarly, training in a complex motor task involving one limb was correlated with DTI-based indication of more developed white matter microstructure in the corpus callosum subjacent to the correlate motor cortex, precisely in the same location in which we observed activity-regulated oligodendrogenesis and increased thickness of myelin sheaths (*46*). The degree of complexity, directionality, or repetition necessary to elicit changes in myelin microstructure is not clear. Thus, wandering around a cage may not focally alter motor circuit myelin, but repeated episodes of a specific motor task (e.g., walking in a counterclockwise circle) may elicit a response in the relevant neural circuit that facilitates that behavior subsequently. Conversely, would hypoactivity of a circuit result in thinner myelin? Elegant studies evaluating the effects of social isolation on myelin thickness in the medial prefrontal cortex, a region important in social function, suggest that this, too, may be the case (*47*, *48*).

It may be that neuronal activity–regulated changes in myelin-forming cells are most relevant to cortical and association fiber myelin. We observed the proliferative response in the deep layers of the cortex and subcortical projections, including those in the corpus callosum projecting to the contralateral motor area, but not those in deep white-matter projections down the corticospinal tract. Similarly, the aforementioned DTI study of white-matter changes after training in a complex visuo-motor task revealed alterations in myelin microstructure consistent with improved myelination within the subcortical association fibers underlying the intraparietal sulcus (*45*). Regional differences may exist in the response of myelin-forming cells to neuronal activity that may reflect differences inherent in cortical OPCs compared with those found in the deep white matter; cortical OPCs have a distinct developmental origin (*34*), respond differentially to mitogens (*35*), appear to contribute particularly to the pathogenesis of glial tumors (*49*), and may respond differentially to activity-regulated signals. Alternatively, the localization of the observed effect on OPC proliferation and differentiation may reflect proximity to the neuronal cell bodies, as OPC mitogens can be released from the neuronal soma rather than from axons (*36*). A third possibility is that specific neuronal types (e.g., callosal neurons compared to corticofugal neurons) may interact differentially with myelin-forming cells.

How would small or localized changes in myelin structure affect neural circuit function? Subtle *g*-ratio changes in the 0.6-to-0.8 range can result in substantial changes in conduction velocity (*40*). Neural circuit function is complex and incompletely understood, but some prominent models of cortical performance (*50*) invoke the need for activity-dependent myelination as a means of balancing conductance delay and synaptic strength parameters [see (*51*) for a recent review]. It should be noted, however, that maladaptive changes in conduction delay could conversely result in perturbation of neural function by disrupting neuronal signal synchrony.

The present study may elucidate the mechanistic role of experience in brain development, defining activity-dependent adaptive changes in myelin as a dimension along which experience modulates neural function. Adult-born oligodendrocytes contribute to myelin remodeling throughout life (*44*), sensory deprivation via social isolation results in hypomyelination of the prefrontal cortex of mice (*47*, *48*), and learning a new language (*52*) or complex motor tasks (*45*) have been shown to alter white-matter structure within the relevant neural circuits in humans. These studies imply the dynamic nature of cerebral myelin throughout life and the role experience may have in modulation of the brain's infrastructure. The data presented here demonstrate that the effect of experience on myelinated fiber microstructure may result from direct effects of neuronal activity on myelin-forming cells.

The potent effects of neuronal activity on OPC proliferation, oligodendrogenesis, and myelination could have broad clinical implications. When dysregulated, neuronal activity–induced OPC proliferation may play a role in glioma pathogenesis, given that OPCs are thought to be the cell of origin for multiple subtypes of high-grade glioma in both children and adults (*49*, *53*). Pediatric high-grade gliomas appear linked to epigenetic dysregulation caused by driver mutations

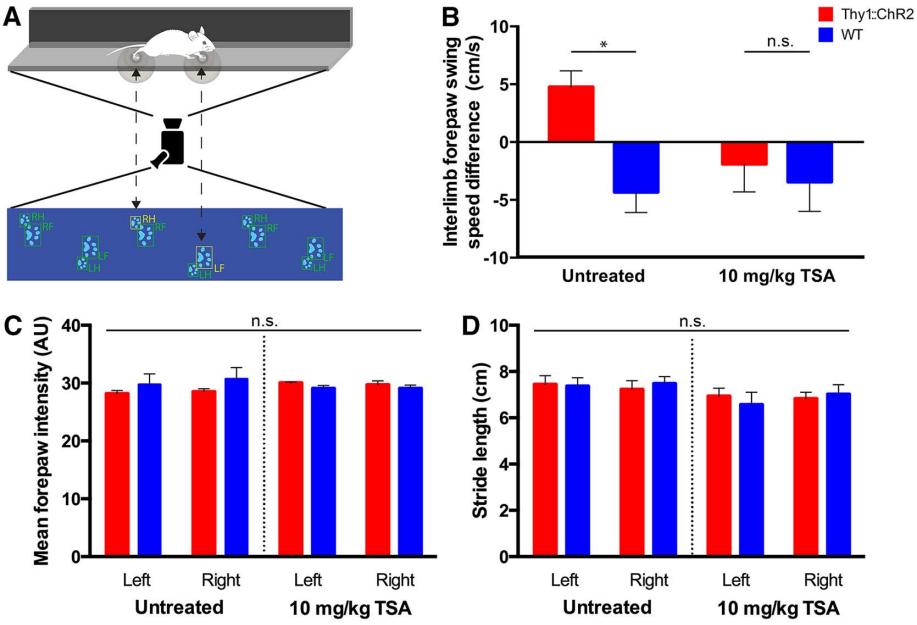


Fig. 7. Activity-regulated oligodendrogenesis and myelin remodeling correlate with improved behavioral function. CatWalk gait analysis was used to evaluate motor performance during normal gait 4 weeks after the stimulation paradigm described above. (**A**) Schematic of the CatWalk apparatus. Experimental mice walk through a long, narrow corridor on a touch-sensitive glass platform, under which a digital camera records paw print contours, allowing for software-guided reconstruction and analysis of gait. LF, left forepaw; LH, left hindpaw; RF, right forepaw; RH, right hindpaw. (**B**) Interlimb forelimb swing speed (in centimeters per second) difference of left forelimb minus right forelimb (n = 5 Thy1::ChR2 and 9 WT; n = 6 TSA-treated Thy1::ChR2 and 5 TSA-treated WT). (**C** and **D**) No alterations to paw pressure (C) or stride length (D) were observed in optogenetically stimulated Thy1::ChR2 mice or their WT littermate controls. The same is true in animals treated with the histone deacetylase inhibitor TSA (C and D). Untreated: n = 5 Thy1::ChR2 mice and 9 WT mice; TSA-treated: n = 4 Thy1::ChR2 mice and 5 WT mice. n.s. denotes $P > 0.05$. *$P < 0.05$. Error bars indicate SEM. AU, arbitrary units.

in histone H3 that may prevent effective control of such proliferation (*54*, *55*). Conversely, precisely harnessing the myelinogenic potential of neuronal-OPC interactions could yield effective regenerative strategies in diseases of myelin.

Materials and Methods

Statistical Analysis

For total EdU counts, cell identity counts, muscle morphometry analyses, and CatWalk behavioral tests (swing speed, forepaw intensity measurements, and stride length), group mean differences were assessed using two-way analysis of variance (two-way ANOVA) with Tukey or Tukey-Kramer post-hoc tests to further examine pairwise differences. Paired, two-tailed Student's *t* tests were used for analysis of mean differences between the ipsilateral and contralateral sides within the same animal in MBP intensity analyses. Unpaired, two-tailed Student's *t* tests were used for analysis of mean differences between animals in electron microscopy measurements. A level of $P < 0.05$ was used to designate significant differences.

As determined before data collection, animals were excluded from analysis if optogenetic stimulation did not result in the expected ambulation behavior (for Thy1::ChR2 animals) or, in the case of behavioral analysis, if the animal did not complete four successful runs characterized by variation under 60%, lasting no more than 5 s, and consistent movement along the CatWalk apparatus.

Mice and Housing Conditions

Male Thy1::ChR2 (The Jackson Laboratory, line 20) mice were bred with female CD1 mice (Charles River Laboratories). All experiments were performed on animals either heterozygous for Thy1::ChR2 or WT littermates housed in a 12-hour light/dark cycle with unrestricted access to food and water. Animals were housed five per cage. Male animals were used for the behavioral analysis, and both sexes were used equally for all other studies. No animals were manipulated other than as reported for that experimental group; that is, there was no history of drug exposures, surgeries, or behavioral testing for the animals used other than that reported for the given experimental group. All procedures were performed in accordance with guidelines set in place by the Stanford University Institutional Care and Use Committee.

Fiber Optic Placement and in Vivo Optogenetic Stimulation

On P32 or P33, animals were anesthetized with 1 to 4% isoflurane and placed in a stereotactic apparatus. After aseptically preparing the skin, the skull was exposed using a midline incision, and a dental drill with a 0.5-mm burr was used to expose the brain. A fiber optic ferrule (Doric Lenses) was placed over the premotor cortex (M2) and secured with dental cement. Ferrules were implanted at the following coordinates: –0.5 mm lateral to midline, 1.0 mm anterior to bregma, and –0.6 mm from the skull in the right hemisphere [as described in (*56*)]. On P35, all freely moving animals were connected to a 100-mW 473-nm diode-pumped solid-state laser system with a monofiber patch cord, and pulses of light were administered at 20 Hz. Approximately 3.7 V at 20 Hz (50-ms pulse length; 25 ms on/25 ms off) produced an output of ~1 mW, which is the minimum intensity necessary to initiate the unidirectional circling behavior of the mice. The blue light from the laser penetrates ~0.5 mm from the tip of the optical fiber and stimulates the apical dendrites of cortical layer V neurons expressing the ChR2 opsin. M2 layer V output neurons project to the M1 motor cortex (which, in turn, projects down the corticospinal tract) and also to the contralateral motor cortex via the corpus callosum. For acute (3-hour) and subacute (24-hour) time points, light was administered during a 30-min session, with alternating 30-s light exposures and 2-min recovery periods, and mice were sacrificed either 3 or 24 hours, respectively, after the start of the stimulation session. For the long-term time point (4 weeks), animals were exposed to the same alternating light exposure paradigm (30 seconds on/2 min off) for 10 min per day for 7 days beginning at P35 or P84 and sacrificed 4 weeks after the cessation of the 7-day stimulation paradigm. For the 7-day time point, P29 mice were stimulated according to the stimulation protocol used for the 4-week time point but were sacrificed 3 hours after the final stimulation session on day 7 at P35. For all stimulation sessions, all animals were given an intraperitoneal injection of EdU (40 mg/kg). To control for stimulation in the analysis of the corpus callosum, a separate group of unstimulated mice were used. In unstimulated mice, animals underwent surgery, ferrule–fiber optic implantation, and EdU injections as described above but were not exposed to 20-Hz pulses of blue light. In animals treated with a histone deacetylase inhibitor, mice were given an intraperitoneal injection of TSA (Selleck Chemicals, 10 mg/kg) concurrently with EdU administration. When the ferrule is properly placed over right M2, Thy1::ChR2 animals respond with increased locomotor behavior (circling) to the left (movie S1), whereas WT animals have no change in behavioral output.

To induce seizures without circling behavior, the ferrule was placed slightly more medially in M2 (–0.25 mm lateral to midline), with no change in stimulation intensity or frequency. Animals exhibited obvious motor seizure activity (tonic-clonic movements) of ~10 s in duration; at the onset of tonic-clonic movements the stimulation was held (blue light off), and animals were allowed to recover to behavioral baseline before further stimulation within the 30-min stimulation session. Animals had an average of 5 to 10 brief seizures, lasting 10 to 15 s each, during the single stimulation session and were sacrificed 3 hours later.

Perfusion and Immunohistochemistry

All animals were anesthetized with avertin and transcardially perfused with 15 ml phosphate-buffered saline (PBS). Brains were postfixed in 4% paraformaldehyde (PFA) overnight at 4°C before cryoprotection in 30% sucrose. Brains were embedded in optimum cutting temperature (OCT) (Tissue-Tek) and sectioned in the coronal plane at 40 μm using a sliding microtome (Leica, HM450). Spinal cords were dissected from the column and allowed to equilibrate in 30% sucrose. From each cord, transverse segments 3 mm in length were isolated and embedded in OCT, and a series of 40-μm transverse sections was collected using a sliding microtome (Leica, HM450). For immunohistochemistry, sections were stained using the Click-iT EdU cell proliferation kit and protocol (Invitrogen) to expose EdU labeling followed by incubation in blocking solution [3% normal donkey serum, 0.3% Triton X-100 in tris-buffered saline (TBS)] at room temperature for 1 hour. Goat antibody to Sox2 (anti-Sox2) (1:50; R&D Systems AF2018), rabbit anti-Olig2 (1:500; Millipore AB9610), goat anti-PDGFRα (1:500; R&D Systems AF1062), rabbit anti-Iba1 (1:2000; Wako 019-19741), rat anti-CD68 (1:200; Abcam AB53444), rabbit anti-GFAP (1:500; Dako Z0334), rabbit anti-Ki67 (1:500; Abcam AB155580), rabbit anti–caspase-3 (1:500; Cell Signaling 9662), rabbit anti-Olig1 (1:500; a generous gift from Dr. Charles Stiles), rabbit anti-histone H3K9me3 (trimethyl K9; 1:200; Abcam AB8898), rabbit anti–acetyl-histone H3 (1:200; Millipore 06-599), goat anti-cFos (1:300; Abcam AB87655), chicken anti-MAP2 (1:10,000; Abcam AB5392), mouse anti-CC1 (1:20; Calbiochem OP80), rabbit anti-S100β (100ug/ml; Sigma S2644), or rat anti-MBP (1:200; Abcam AB7349) were diluted in 1% blocking solution (normal donkey serum in 0.3% Triton X-100 in TBS) and incubated overnight at 4°C, with the exception of the anti-CC1 antibody for which a 1-week incubation was used. All antibodies have been validated in the literature and/or in Antibodypedia for use in mouse immunohistochemistry. To further validate the antibodies in our hands, we confirmed that each antibody stained in the expected cellular patterns and brain-wide distributions (e.g., nuclear Sox2 staining in the subventricular zone). For the case of cleaved caspase-3 staining, we confirmed antibody staining in ischemic brain tissue as a positive control. Secondary-only stains were performed as negative controls.

The following day, sections were rinsed three times in 1X TBS and incubated in secondary antibody solution (1:500) and 4′,6-diamidino-2-phenylindole (1:1000) in 1% blocking solution at 4°C overnight. The following secondary antibodies were used: DyLight 405 donkey anti-rabbit (Jackson ImmunoResearch), Alexa 488 donkey anti-goat (Jackson ImmunoResearch), FITC donkey anti-rabbit (Jackson ImmunoResearch), FITC donkey anti-rat (Jackson ImmunoResearch), Alexa 647 donkey anti-chicken (Jackson ImmunoResearch), Alexa 647 donkey anti-mouse (Invitrogen), or Alexa 647 donkey anti-goat (Invitrogen). The next day, sections were rinsed three times in TBS and mounted with Krystalon (HARLECO) mounting medium.

Confocal Imaging and Quantification

All cell counting was performed by experimenters blinded to the experimental conditions using a Zeiss LSM700 scanning confocal microscope (Carl Zeiss). For EdU stereology, all EdU-labeled cells in every 12th bilateral (ipsilateral and contralateral to fiber optic ferrule) section (or every 6th for the 4-week–time-point tissue) throughout the extent of M2 or the corpus callosum were counted by blinded experimenters at 200× or 400× magnification, excluding those cells in the outermost field of focus (i.e., the edge of the section), as well as those within 100 μm surrounding ferrule-induced tissue damage. The total number of EdU-labeled cells per M2 or corpus callosum was determined by multiplying the number of EdU^+ cells by 12 (or 6 for the 4-week time point). For each animal, 50 to 100 EdU^+ cells for M2 and 15 to 25 EdU^+ cells for the corpus callosum were randomly chosen and assessed for double-labeling with the aforementioned primary antibodies to determine the proportion of EdU^+ cells with specific cell identities or epigenetic markers. A minimum of three animals was assessed for each marker. Cells were considered double-labeled when they colocalized within the same plane. This proportion was then multiplied by the total number of EdU-labeled cells to determine the total number of cells within each M2 hemisphere or corpus callosum for every animal with that specific cell identity. For EdU quantification in the cervical spinal cord, EdU-labeled cells were counted at 200× magnification in representative 40-μm sections within the extent of the dorsal corticospinal tract. For MBP intensity measurements, forebrain sections surrounding the site of the fiber optic ferrule were used for the analysis. Z-stack images of the M2 area, both ipsilateral and contralateral to the optogenetically stimulated side, were acquired at 100× using a Zeiss LSM700 confocal microscope and Zen 2011 imaging software. For regional analysis of MBP expression, ImageJ software (version 1.47) was used to quantify the average fluorescent intensity of pixels in a region drawn around the entry of M2 fibers into the horn of the corpus callosum. Comparisons of intensity were made between ipsilateral and contralateral sides within a given slice. Average values across all sections were calculated for each animal and hemisphere.

For analysis of $EdU^+/CC1^+$ or $Iba^+/CD68^+$ cells per cubic millimeter, estimated volume measurements for ipsilateral and contralateral M2 and corpus callosum were obtained using MBF Bioscience StereoInvestigator version 11.01.2. Bright-field tile images of 1:6 series of M2 and corpus callosum were obtained at 50x using Zen software through areas that were quantified in EdU stereology counts, which amounted to 11 total slices. The Cavalieri Estimator probe was used to analyze the tissue, and boundaries of the regions of interest were determined using published mouse anatomical guides (*57*). A random sampling grid with dimensions of 50 μm by 50 μm was overlaid. Coefficients of error (Gunderson, $m = 0$) for the regions of interest were as follows: ipsilateral M2 = 0.071; contralateral M2 = 0.067; corpus callosum = 0.1. The number of $EdU^+/CC1^+$ cells per cubic millimeter was determined by dividing the total number of $EdU^+/CC1^+$ cells by the estimated volume analyzed for each region.

Muscle Histology and Morphometry

Thy1::ChR2 and WT mice were anesthetized with avertin, then perfused with 10 ml PBS followed by 10 ml 2% glutaraldehyde/4% PFA/100-mM sodium cacodylate 4 weeks after the 7-day optogenetic stimulation paradigm. Forelimbs were removed, and biceps and triceps brachii muscles were dissected out bilaterally and weighed with an analytical balance. Whole muscles were embedded in paraffin, sectioned at 5 μm, and stained with hematoxylin and eosin. Blinded morphometric analysis was performed at 400× magnification (SPOT Imaging Solutions) by obtaining the mean of the shortest diameter of all muscle fibers within a single field of view (80 ± 5 fibers), excluding damaged fibers.

Electron Microscopy

Four weeks after optogenetic stimulation (as above), Thy1::ChR2 or WT mice (untreated or treated with 10 mg/kg TSA as above) were sacrificed by transcardial perfusion with Karnovsky's fixative: 2% glutaraldehyde [Electron Microscopy Sciences (EMS) 16000] and 4% paraformaldehyde (EMS 15700) in 0.1 M sodium cacodylate (EMS 12300), pH 7.4. The bilateral premotor cortex (M2) was resected from the brain and postfixed in Karnovsky's fixative for at least 2 weeks. TEM was performed in the region of the M2 subcortical fibers as they exit cortical layer VI and enter the corpus callosum. The samples were then postfixed in 1% osmium tetroxide (EMS 19100) for 1 hour at room temperature, washed three times with ultrafiltered water, then en bloc stained for 2 hours at room temperature. Samples were then dehydrated in graded ethanols (50, 75, and 95%) for 15 min each at 4°C; the samples were then allowed to equilibrate to room temperature and were rinsed in 100% ethanol two times, followed by acetonitrile for 15 min. Samples were infiltrated with EMbed-812 resin (EMS 14120) mixed 1:1 with acetonitrile for 2 hours, followed by 2:1 EMbed-812:acetonitrile for 2 hours. The samples were next placed into EMbed-812 for 2 hours, then placed into TAAB capsules filled with fresh resin, which were then placed into a 65°C oven overnight. Sections were taken between 75 and 90 nm on a Leica Ultracut S (Leica, Wetzlar, Germany) and mounted on Formvar/carbon coated slot grids (EMS FCF2010-Cu) or 100 mesh Cu grids (EMS FCF100-Cu). Grids were contrast stained for 30 s in 3.5% uranyl acetate in 50% acetone, followed by staining in 0.2% lead citrate for 30 s. Samples were imaged using a JEOL JEM-1400 TEM at 120 kV, and images were collected using a Gatan Orius digital camera. With experimenters blinded to sample identity and condition, axons ipsilateral and contralateral to ferrule placement were analyzed for *g*-ratios calculated by dividing the shortest axonal diameter by the corresponding axonal-plus-sheath diameter (diameter of axon/diameter of axon plus myelin sheath). For each group, 235 to 422 axons were scored. Measurements of *g*-ratio were confirmed by a second, blinded rater.

Myelinated fiber density was analyzed by quantifying the number of myelinated axons per 8000× electron micrograph. An average of 71 such images were quantified per animal, and the average number of myelinated fibers per image was calculated for each animal. We did not find a significant change in the density of myelinated fibers (2.59 ± 0.65 myelinated axons per field in Thy1::ChR2 mice versus 1.88 ± 0.47 myelinated fibers per field in WT mice on the side ipsilateral to optogenetic stimulation; $n = 4$ Thy1::ChR2 animals and 3 WT animals; $P = 0.45$). However, this analysis is complicated by the fact that the distribution of projection axons entering the corpus callosum from the motor cortex is shaped like an inverted cone or a funnel in which the same number of axons would appear less dense superiorly at the base of the cone and denser inferiorly at the vertex of the cone. Thus, even micrometer changes in the level of analysis would affect the density of fibers observed. Whereas Thy1::ChR2 and WT mice were sampled in the same way and at the same approximate level, we believe that the variability introduced by the conformation of the structure makes it difficult to detect small changes in myelinated fiber density. Thus, we do not detect pronounced differences, but we cannot exclude small changes in myelinated fiber density after optogenetic stimulation.

Behavioral Analysis

To investigate the effect of unilateral optogenetic stimulation of the corticospinal tract on motor output, we used the CatWalk gait analysis system (Noldus, Netherlands). The apparatus consists of a glass walkway with opaque black siding that is internally illuminated with fluorescent lights via one of the long edges of the glass floor. As the mouse traverses the glass floor, the footprints cause the light to be reflected downward and are recorded by a camera positioned underneath the glass and relayed to an adjacent computer. For a detailed description of the CatWalk method, see (*41*). To ensure consistent running, mice were acclimated to handling for several weeks before recording, and all tests were run in a dark room. Only male mice were used to reduce variability in output measures between males and females, based on body weight. Animals were tested 4 weeks after the cessation of the 7-day optogenetic stimulation paradigm previously described. Male mice that did not undergo surgery and optogenetic stimulation were used to control for changes in behavior due to experimental manipulation. No behavioral training on the CatWalk apparatus was performed. Behavioral testing was performed during the light cycle. Four successful runs (with success being characterized by variation under

60%, lasting no more than 5 s, and consistent movement) were processed with the CatWalk XT 9.0 software. A sample size calculation using the ANOVA sample size calculator in SigmaPlot was used, and the numbers (the standard deviation and the minimum detectable difference in means) were based on an initial pilot study comparing untreated Thy1::ChR2 to WT animals using a power of 0.8 and an α of 0.05; this resulted in a sample size of five animals.

Our hypothesis at the outset was that swing speed, as a sensitive measure of motor system function, would be selectively improved if myelination was increased within the premotor circuit. We did not expect to see a difference in stance or paw strike intensity as a result of an increase in myelination. In this study, only the following three parameters were analyzed:

1) Swing speed: the speed (in centimeters per second) of the paw during limb swinging. Swing speed was calculated as the difference in speed between the left forepaw and the right forepaw. Thus, a positive value signifies a faster left forepaw swing speed compared with that of the right forepaw.

2) Stride length: the distance (in centimeters) between successive placements of the same paw. Calculation of stride length is based on the x coordinates of the center of the paw print of two consecutive placements of the same paw during maximum contact of the paw with the glass floor.

3) Paw intensity: the mean intensity (0 to 255, arbitrary units) of the paw print as projected onto the glass floor. The intensity of a print depends on the degree of contact between a paw and the glass plate and increases with increasing pressure.

References and Notes

1. P. I. Yakovlev, "The myelogenetic cycles of regional maturation of the brain." in *Regional Development of the Brain in Early Life*, A. Minkowski, Ed. (Blackwell Scientific Publications, Oxford, 1967), pp. 3–70.
2. C. Lebel *et al*., Diffusion tensor imaging of white matter tract evolution over the lifespan. *Neuroimage* **60**, 340–352 (2012). doi: 10.1016/j.neuroimage.2011.11.094; pmid: 22178809
3. F. M. Benes, Myelination of cortical-hippocampal relays during late adolescence. *Schizophr. Bull.* **15**, 585–593 (1989). doi: 10.1093/schbul/15.4.585; pmid: 2623440
4. E. Zuccaro, P. Arlotta, The quest for myelin in the adult brain. *Nat. Cell Biol.* **15**, 572–575 (2013). doi: 10.1038/ncb2750; pmid: 23644465
5. B. A. Barres, M. C. Raff, Proliferation of oligodendrocyte precursor cells depends on electrical activity in axons. *Nature* **361**, 258–260 (1993). doi: 10.1038/361258a0; pmid: 8093806
6. C. Demerens *et al*., Induction of myelination in the central nervous system by electrical activity. *Proc. Natl. Acad. Sci. U.S.A.* **93**, 9887–9892 (1996). doi: 10.1073/pnas.93.18.9887; pmid: 8790426
7. B. Stevens, S. Tanner, R. D. Fields, Control of myelination by specific patterns of neural impulses. *J. Neurosci.* **18**, 9303–9311 (1998).pmid: 9801369
8. T. Ishibashi *et al*., Astrocytes promote myelination in response to electrical impulses. *Neuron* **49**, 823–832 (2006). doi: 10.1016/j.neuron.2006.02.006; pmid: 16543131
9. H. Wake, P. R. Lee, R. D. Fields, Control of local protein synthesis and initial events in myelination by action potentials. *Science* **333**, 1647–1651 (2011). doi: 10.1126/science.1206998; pmid: 21817014
10. Q. Li, M. Brus-Ramer, J. H. Martin, J. W. McDonald, Electrical stimulation of the medullary pyramid promotes proliferation and differentiation of oligodendrocyte progenitor cells in the corticospinal tract of the adult rat. *Neurosci. Lett.* **479**, 128–133 (2010). doi: 10.1016/j.neulet.2010.05.043; pmid: 20493923
11. G. Goldsberry, D. Mitra, D. MacDonald, Z. Patay, Accelerated myelination with motor system involvement in a neonate with immediate postnatal onset of seizures and hemimegalencephaly. *Epilepsy Behav.* **22**, 391–394 (2011). doi: 10.1016/j.yebeh.2011.06.025; pmid: 21802995
12. D. E. Bergles, J. D. Roberts, P. Somogyi, C. E. Jahr, Glutamatergic synapses on oligodendrocyte precursor cells in the hippocampus. *Nature* **405**, 187–191 (2000). doi: 10.1038/35012083; pmid: 10821275
13. S. C. Lin *et al*., Climbing fiber innervation of NG2-expressing glia in the mammalian cerebellum. *Neuron* **46**, 773–785 (2005). doi: 10.1016/j.neuron.2005.04.025; pmid: 15924863
14. R. Káradóttir, P. Cavelier, L. H. Bergersen, D. Attwell, NMDA receptors are expressed in oligodendrocytes and activated in ischaemia. *Nature* **438**, 1162–1166 (2005). doi: 10.1038/nature04302; pmid: 16372011
15. J. L. Ziskin, A. Nishiyama, M. Rubio, M. Fukaya, D. E. Bergles, Vesicular release of glutamate from unmyelinated axons in white matter. *Nat. Neurosci.* **10**, 321–330 (2007). doi: 10.1038/nn1854; pmid: 17293857
16. J. M. Mangin, A. Kunze, R. Chittajallu, V. Gallo, Satellite NG2 progenitor cells share common glutamatergic inputs with associated interneurons in the mouse dentate gyrus. *J. Neurosci.* **28**, 7610–7623 (2008). doi: 10.1523/JNEUROSCI.1355-08.2008; pmid: 18650338
17. L. M. De Biase, A. Nishiyama, D. E. Bergles, Excitability and synaptic communication within the oligodendrocyte lineage. *J. Neurosci.* **30**, 3600–3611 (2010). doi: 10.1523/JNEUROSCI.6000-09.2010; pmid: 20219994
18. L. M. De Biase *et al*., NMDA receptor signaling in oligodendrocyte progenitors is not required for oligodendrogenesis and myelination. *J. Neurosci.* **31**, 12650–12662 (2011). doi: 10.1523/JNEUROSCI.2455-11.2011; pmid: 21880926
19. B. R. Arenkiel *et al*., In vivo light-induced activation of neural circuitry in transgenic mice expressing channelrhodopsin-2. *Neuron* **54**, 205–218 (2007). doi: 10.1016/j.neuron.2007.03.005; pmid: 17442243
20. H. Wang *et al*., High-speed mapping of synaptic connectivity using photostimulation in Channelrhodopsin-2 transgenic mice. *Proc. Natl. Acad. Sci. U.S.A.* **104**, 8143–8148 (2007). doi: 10.1073/pnas.0700384104; pmid: 17483470
21. E. S. Boyden, F. Zhang, E. Bamberg, G. Nagel, K. Deisseroth, Millisecond-timescale, genetically targeted optical control of neural activity. *Nat. Neurosci.* **8**, 1263–1268 (2005). doi: 10.1038/nn1525; pmid: 16116447
22. O. Yizhar, L. E. Fenno, T. J. Davidson, M. Mogri, K. Deisseroth, Optogenetics in neural systems. *Neuron* **71**, 9–34 (2011). doi: 10.1016/j.neuron.2011.06.004; pmid: 21745635
23. C. M. Gremel, R. M. Costa, Premotor cortex is critical for goal-directed actions. *Front. Comput. Neurosci.* **7**, 110 (2013). doi: 10.3389/fncom.2013.00110; pmid: 23964233
24. E. G. Hughes, S. H. Kang, M. Fukaya, D. E. Bergles, Oligodendrocyte progenitors balance growth with self-repulsion to achieve homeostasis in the adult brain. *Nat. Neurosci.* **16**, 668–676 (2013). doi: 10.1038/nn.3390; pmid: 23624515
25. V. E. Miron *et al*., M2 microglia and macrophages drive oligodendrocyte differentiation during CNS remyelination. *Nat. Neurosci.* **16**, 1211–1218 (2013). doi: 10.1038/nn.3469; pmid: 23872599
26. C. Y. Brazel *et al*., Sox2 expression defines a heterogeneous population of neurosphere-forming cells in the adult murine brain. *Aging Cell* **4**, 197–207 (2005). doi: 10.1111/j.1474-9726.2005.00158.x; pmid: 16026334
27. M. L. Monje, H. Toda, T. D. Palmer, Inflammatory blockade restores adult hippocampal neurogenesis. *Science* **302**, 1760–1765 (2003). doi: 10.1126/science.1088417; pmid: 14615545
28. C. T. Ekdahl, J. H. Claasen, S. Bonde, Z. Kokaia, O. Lindvall, Inflammation is detrimental for neurogenesis in adult brain. *Proc. Natl. Acad. Sci. U.S.A.* **100**, 13632–13637 (2003). doi: 10.1073/pnas.2234031100; pmid: 14581618
29. O. Butovsky *et al*., Microglia activated by IL-4 or IFN-γ differentially induce neurogenesis and oligodendrogenesis from adult stem/progenitor cells. *Mol. Cell. Neurosci.* **31**, 149–160 (2006). doi: 10.1016/j.mcn.2005.10.006; pmid: 16297637
30. Y. Imai, I. Ibata, D. Ito, K. Ohsawa, S. Kohsaka, A novel gene *iba1* in the major histocompatibility complex class III region encoding an EF hand protein expressed in a monocytic lineage. *Biochem. Biophys. Res. Commun.* **224**, 855–862 (1996). doi: 10.1006/bbrc.1996.1112; pmid: 8713135
31. D. Ito *et al*., Microglia-specific localisation of a novel calcium binding protein, Iba1. *Brain Res. Mol. Brain Res.* **57**, 1–9 (1998). doi: 10.1016/S0169-328X(98)00040-0; pmid: 9630473
32. M. B. Graeber, W. J. Streit, R. Kiefer, S. W. Schoen, G. W. Kreutzberg, New expression of myelomonocytic antigens by microglia and perivascular cells following lethal motor neuron injury. *J. Neuroimmunol.* **27**, 121–132 (1990). doi: 10.1016/0165-5728(90)90061-Q; pmid: 2332482
33. P. J. Kingham, M. L. Cuzner, J. M. Pocock, Apoptotic pathways mobilized in microglia and neurones as a consequence of chromogranin A-induced microglial activation. *J. Neurochem.* **73**, 538–547 (1999). doi: 10.1046/j.1471-4159.1999.0730538.x; pmid: 10428049
34. T. Yue *et al*., A critical role for dorsal progenitors in cortical myelination. *J. Neurosci.* **26**, 1275–1280 (2006). doi: 10.1523/JNEUROSCI.4717-05.2006; pmid: 16436615
35. R. A. Hill, K. D. Patel, J. Medved, A. M. Reiss, A. Nishiyama, NG2 cells in white matter but not gray matter proliferate in response to PDGF. *J. Neurosci.* **33**, 14558–14566 (2013). doi: 10.1523/JNEUROSCI.2001-12.2013; pmid: 24005306
36. M. Fruttiger, A. R. Calver, W. D. Richardson, Platelet-derived growth factor is constitutively secreted from neuronal cell bodies but not from axons. *Curr. Biol.* **10**, 1283–1286 (2000). doi: 10.1016/S0960-9822(00)00757-0; pmid: 11069109
37. S. Shen, J. Li, P. Casaccia-Bonnefil, Histone modifications affect timing of oligodendrocyte progenitor differentiation in the developing rat brain. *J. Cell Biol.* **169**, 577–589 (2005). doi: 10.1083/jcb.200412101; pmid: 15897262
38. M. Wu *et al*., Differential modulation of the oligodendrocyte transcriptome by sonic hedgehog and bone morphogenetic protein 4 via opposing effects on histone acetylation. *J. Neurosci.* **32**, 6651–6664 (2012). doi: 10.1523/JNEUROSCI.4876-11.2012; pmid: 22573687
39. H. A. Arnett *et al*., bHLH transcription factor Olig1 is required to repair demyelinated lesions in the CNS. *Science* **306**, 2111–2115 (2004). doi: 10.1126/science.1103709; pmid: 15604411
40. R. S. Smith, Z. J. Koles, Myelinated nerve fibers: Computed effect of myelin thickness on conduction velocity. *Am. J. Physiol.* **219**, 1256–1258 (1970). pmid: 5473105
41. F. P. Hamers, A. J. Lankhorst, T. J. van Laar, W. B. Veldhuis, W. H. Gispen, Automated quantitative gait analysis during overground locomotion in the rat: Its application to spinal cord contusion and transection injuries. *J. Neurotrauma* **18**, 187–201 (2001). doi: 10.1089/08977150150502613; pmid: 11229711
42. P. Shi *et al*., Synapse microarray identification of small molecules that enhance synaptogenesis. *Nat. Commun.* **2**, 510 (2011). doi: 10.1038/ncomms1518; pmid: 22027590
43. M. J. Morris, M. Mahgoub, E. S. Na, H. Pranav, L. M. Monteggia, Loss of histone deacetylase 2 improves working memory and accelerates extinction learning. *J. Neurosci.* **33**, 6401–6411 (2013). doi: 10.1523/JNEUROSCI.1001-12.2013; pmid: 23575838
44. K. M. Young *et al*., Oligodendrocyte dynamics in the healthy adult CNS: Evidence for myelin remodeling. *Neuron* **77**, 873–885 (2013). doi: 10.1016/j.neuron.2013.01.006; pmid: 23473318

45. J. Scholz, M. C. Klein, T. E. Behrens, H. Johansen-Berg, Training induces changes in white-matter architecture. *Nat. Neurosci.* **12**, 1370–1371 (2009). doi: 10.1038/nn.2412; pmid: 19820707
46. C. Sampaio-Baptista *et al*., Motor skill learning induces changes in white matter microstructure and myelination. *J. Neurosci.* **33**, 19499–19503 (2013). doi: 10.1523/JNEUROSCI.3048-13.2013; pmid: 24336716
47. J. Liu *et al*., Impaired adult myelination in the prefrontal cortex of socially isolated mice. *Nat. Neurosci.* **15**, 1621–1623 (2012). doi: 10.1038/nn.3263; pmid: 23143512
48. M. Makinodan, K. M. Rosen, S. Ito, G. Corfas, A critical period for social experience-dependent oligodendrocyte maturation and myelination. *Science* **337**, 1357–1360 (2012).doi: 10.1126/science.1220845; pmid: 22984073
49. C. Liu *et al*., Mosaic analysis with double markers reveals tumor cell of origin in glioma. *Cell* **146**, 209–221 (2011). doi: 10.1016/j.cell.2011.06.014; pmid: 21737130
50. P. R. Roelfsema, A. K. Engel, P. König, W. Singer, Visuomotor integration is associated with zero time-lag synchronization among cortical areas. *Nature* **385**, 157–161 (1997). doi: 10.1038/385157a0; pmid: 8990118
51. S. Pajevic, P. J. Basser, R. D. Fields, Role of myelin plasticity in oscillations and synchrony of neuronal activity. *Neuroscience* (2013). doi: 10.1016/j.neuroscience.2013.11.007; pmid: 24291730
52. A. A. Schlegel, J. J. Rudelson, P. U. Tse, White matter structure changes as adults learn a second language. *J. Cogn. Neurosci.* **24**, 1664–1670 (2012). doi: 10.1162/jocn_a_00240; pmid: 22571459
53. M. Monje *et al*., Hedgehog-responsive candidate cell of origin for diffuse intrinsic pontine glioma. *Proc. Natl. Acad. Sci. U.S.A.* **108**, 4453–4458 (2011). doi: 10.1073/pnas.1101657108; pmid: 21368213
54. G. Wu *et al*., Somatic histone H3 alterations in pediatric diffuse intrinsic pontine gliomas and non-brainstem glioblastomas. *Nat. Genet.* **44**, 251–253 (2012). doi: 10.1038/ng.1102; pmid: 22286216
55. J. Schwartzentruber *et al*., Driver mutations in histone H3.3 and chromatin remodelling genes in paediatric glioblastoma. *Nature* **482**, 226–231 (2012). doi: 10.1038/nature10833; pmid: 22286061
56. F. Zhang *et al*., Optogenetic interrogation of neural circuits: Technology for probing mammalian brain structures. *Nat. Protoc.* **5**, 439–456 (2010). doi: 10.1038/nprot.2009.226; pmid: 20203662
57. B. J. Franklin, G. Paxinos, *The Mouse Brain* (Elsevier, New York, 2008).

Acknowledgments: We gratefully acknowledge support from the National Institute of Neurological Disorders and Stroke (NINDS K08NS070926 to M.M.; R01 EY10257 to B.A.B.); California Institute for Regenerative Medicine (CIRM RB4-06093 and RN3-06510 to M.M.); Alex's Lemonade Stand Foundation (M.M.); McKenna Claire Foundation (M.M.); The Cure Starts Now (M.M.); Lyla Nsouli Foundation (M.M.); the Dylan Jewett, Connor Johnson, Zoey Ganesh, Dylan Frick, Abigail Jensen, Wayland Villars, and Jennifer Kranz Memorial Funds (M.M.); Ludwig Foundation (M.M.); Price Family Charitable Fund (M.M.); Stanford Medical Scientist Training Program (D.P., C.W.M., G.L.L.); Stanford Institute for Neuro-Innovation and Translational Neurosciences (M.M.); the Child Health Research Institute (M.M. and E.M.G.); Lucile Packard Foundation for Children's Health, Stanford University Clinical & Translation Science Award (UL1 RR025744 to E.M.G.); Howard Hughes Medical Institute Fellowship of the Life Sciences Research Foundation (J.B.Z.); the Bezos Family Foundation (I.I.); and the Child Health Research Institute at Stanford University, Anne T. and Robert M. Bass Endowed Faculty Scholarship in Pediatric Cancer and Blood Diseases (M.M.). We give special thanks to J. Perrino of the Electron Microscopy Core of the Stanford University Cell Sciences Imaging Facility for technical support with transmission electron microscopy NIH Shared Instrumentation Grant 1S10RR02678001; to S. Chen for the illustration accompanying the print summary of this work; and to J. Lennon, K. Lechtenberg, H. Venkatesh, and M. E. Freret for critical reading of the manuscript.

Supplementary Materials

www.sciencemag.org/content/344/6183/1252304/suppl/DC1
Figs. S1 to S10
Reference (*58*)
Movie S1

17 February 2014; accepted 28 March 2014
Published online 10 April 2014;
10.1126/science.1252304

Edge Nonlinear Optics on a MoS_2 Atomic Monolayer

Xiaobo Yin,[1,2]*† Ziliang Ye,[1]* Daniel A. Chenet,[3]* Yu Ye,[1]* Kevin O'Brien,[1] James C. Hone,[3] Xiang Zhang[1,2]‡

The translational symmetry breaking of a crystal at its surface may form two-dimensional (2D) electronic states. We observed one-dimensional nonlinear optical edge states of a single atomic membrane of molybdenum disulfide (MoS_2), a transition metal dichalcogenide. The electronic structure changes at the edges of the 2D crystal result in strong resonant nonlinear optical susceptibilities, allowing direct optical imaging of the atomic edges and boundaries of a 2D material. Using the symmetry of the nonlinear optical responses, we developed a nonlinear optical imaging technique that allows rapid and all-optical determination of the crystal orientations of the 2D material at a large scale. Our technique provides a route toward understanding and making use of the emerging 2D materials and devices.

The structural discontinuity at the edges and boundaries of 2D atomic materials, such as graphene and transition metal dichalcogenides, leads to complex interplay between the atomic positions and the electronic structures. Subsequently, the atomic edges and boundaries reconstruct structurally and electronically. A broad range of exceptional physical behaviors and applications including widely tunable transport gaps (*1*, *2*), unusual magnetic responses (*3*–*5*), and high-performance nanoelectronics (*6*, *7*) have been discovered. However, experimental observations of these 1D structures have been limited to scanning tunneling microscopy and transmission electron microscopy. Here, we studied the second-order nonlinear optics on the 1D edges and boundaries of hexagonal molybdenum disulfide (MoS_2) atomic membranes. The broken inversion symmetry of the atomically thin monolayer shows strong second-harmonic generation (SHG), in contrast to the centrosymmetric bulk material, which is immune to the second-order nonlinear processes. The destructive interference and annihilation of nonlinear waves from neighboring atomic membranes reveals the few-atom-wide line defects that stitch different crystal grains together, and also allows the mapping of crystal grains and grain boundaries over large areas. Our optical imaging technique enables the nonlinear optical detection of the edge states at the atomic edges of 2D crystals where the translational symmetry is broken. The observed edge resonance of SHG clearly indicates the electronic structure variation at the atomic edges, which have long been suspected to be the active sites for electrocatalytic hydrogen evolution (*8*).

Unlike gapless graphene, the monolayer form of transition metal dichalcogenides such as MoS_2 shows a direct band gap at visible frequencies, making them emergent semiconductors for nanoelectronics and optoelectronics involving photovoltaic and/or photoemission processes (*9*, *10*). In MoS_2, the unique local orbital properties of the heavy transition metal atoms and broken inversion symmetry of the monolayer crystal introduce an imbalanced charge carrier distribution in momentum space, giving rise to a novel valley-specific circular dichroism (*11*–*12, 13*). Hexagonal bulk MoS_2 has a layered structure with a single layer of molybdenum atoms sandwiched between two layers of sulfur atoms in a trigonal prismatic lattice. Each unit cell is formed by two mirrored sublattices, making the bulk crystal centrosymmetric and prohibiting the second-order nonlinear optical processes therein. However, in a monolayer consisting of one layer of molybdenum atoms and two sulfur atom layers, or few-layer MoS_2 with odd-numbered layers, the inversion center is removed, resulting in a strong second-order nonlinear optical response. The origins of the strong nonlinear optical responses and their symmetry properties have been discussed (*14*–*16*). The observed oscillatory nonlinearity between the odd-numbered and even-numbered layers is unique to all layered transition metal dichalcogenides, including MoS_2 and WSe_2 (*17*).

Because SHG is strongly affected by the lowered symmetry of a material, the structure and symmetry properties of MoS_2 atomic membranes can be probed by second-harmonic emission, which allows us to demonstrate the nonlinear optical properties of these 2D materials. Figure 1 shows the linear and nonlinear optical images of a continuous monolayer MoS_2 membrane epitaxially grown by chemical vapor deposition (CVD) (*18*). Oxide-on-silicon substrates with oxide films 285 nm thick were used for optimized optical contrast. The monolayer samples show high-quality photoluminescence and are optically uniform over large areas (Fig. 1A). In contrast, the SHG image (Fig. 1B) reveals the polycrystalline nature of the uniform monolayer, and the average grain size ranges from 20 to 40 μm. Here, the incident polarization of the pump beam is along the *y* axis and the total second-harmonic radiation is collected. The uniform SHG intensity within each grain indicates that the individual grains

[1]NSF Nanoscale Science and Engineering Center, University of California, Berkeley, CA 94720, USA. [2]Materials Sciences Division, Lawrence Berkeley National Laboratory, Berkeley, CA 94720, USA. [3]Department of Mechanical Engineering, Columbia University, New York, NY 10027, USA.

*These authors contributed equally to this work.
†Present address: Department of Mechanical Engineering, Materials Science and Engineering, University of Colorado, Boulder, CO 80309, USA.
‡Corresponding author. E-mail: xiang@berkeley.edu

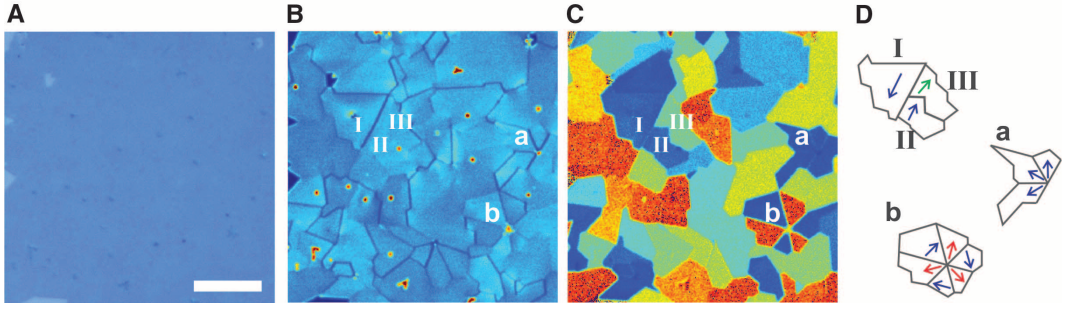


Fig. 1. All-optical determination of the crystal orientations of MoS_2 atomic membranes. (**A**) Optical image of a large area of CVD-grown monolayer MoS_2. (**B**) SHG image of a polycrystalline monolayer of MoS_2 of the same area. The grains and grain boundaries are clearly revealed by the reduced SHG intensity at the boundaries. The crystals are connected by faceted, abrupt grain boundaries. The scattered bright spots are from the nanocrystals produced in the vapor growth process. The average monolayer crystal sizes are between 20 and 50 μm. (**C**) The direct crystal orientation image shows the crystal orientations of the irregular-shaped polycrystalline aggregates. (**D**) Schematics show the flakes I and II are two crystals with opposite orientations, as they have the same contrast in crystal orientation maps but a strongly destructive interference boundary. Crystals II and III show an orientation mismatch of ~12°. The crystal groups *a* and *b* show two cyclic twin boundaries with 60° (*a*) and 30° (*b*), respectively. Scale bar, 40 μm.

are single crystals. At the grain boundaries, however, the SHG is substantially suppressed as a result of the destructive interference and annihilation of the nonlinear waves generated from the neighboring grains with different orientations. Although the grain boundaries are only a few atom sites in width, the crystal boundaries are clearly seen. Moreover, the nonlinear generation not only reveals the symmetry properties of the crystal, but also allows the rapid mapping of crystal orientations. By analyzing the polarized components of the SHG (see supplementary text and fig. S1), we can map the crystal orientation of the polycrystalline atomic membrane. This approach allows us to capture a complete map of the crystal grain structures, color-coded according to crystal orientation (Fig. 1C). Large-area CVD-grown films clearly have complex grain geometries and orientations.

Because of the threefold rotation symmetry of monolayer MoS_2, the SHG imaging without phase information does not discriminate between opposite crystal orientations. Consequently, it only determines grain rotations modulo 60°, and the measurable difference between grain orientations is from 0° to 30°. For example, crystals I and II have no contrast in the color-coded orientation maps (Fig. 1C), but the clearly visible grain boundary between them (Fig. 1B) indicates that the two crystal grains are in opposite orientations. On the other hand, the grain boundary between crystals II and III has much less contrast (Fig. 1B), but the two crystals are distinctive when looking at the crystal orientations in Fig. 1C (~12° difference in orientation). The images obtained clearly show the twin grain structures and the sixfold symmetric patterns (Fig. 1, B and C): Crystals in group *a* have a cyclic twin structure, whereas each crystal in group *b* instead has a ~30° difference in orientation with respect to its neighbors. Such a characterization process conventionally requires diffraction-filtered dark-field transmission electron microscopy as well as a sophisticated and time-consuming analysis procedure (*19*). Thus, we can directly visualize the grain structure, providing key information for optimizing synthesis strategies for large-area CVD growth. The crystal orientations determined by our nonlinear optical method correspond well to transmission electron microscopy observations on the same sample. Although the results shown here were obtained for a fundamental wavelength of 1300 nm, the symmetry and the polar patterns of SHG are ubiquitous for all pump wavelengths.

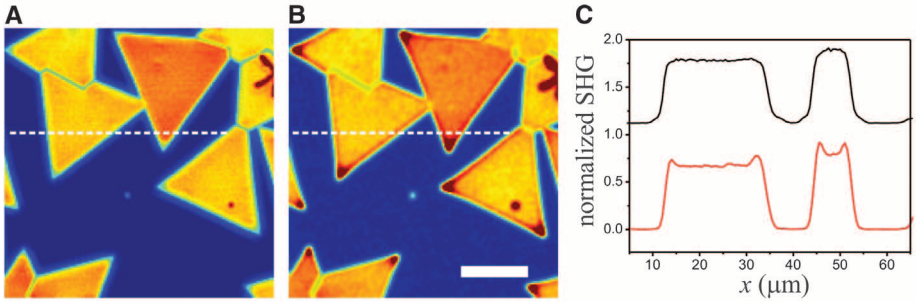


Fig. 2. SHG image of discrete triangular islands of MoS_2 crystals. (**A**) SHG image pumped at 1280 nm. (**B**) SHG image of the same sample pumped at 1300 nm. The brim of crystal shows a strong nonlinear optical (SHG) edge state. Scale bar, 20 μm. (**C**) Cross sections [white dashed lines in (A) and (B)] compare the SHG of the same crystal under pump wavelengths of 1280 nm (black) and 1300 nm (red), respectively. The enhanced edge responses are clearly shown.

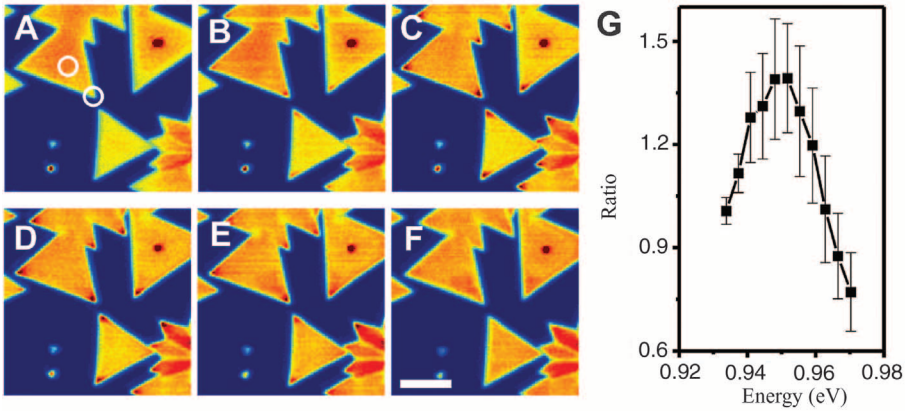


Fig. 3. Nonlinear edge resonance of MoS_2 monolayer membrane. (**A** to **F**) SHG images of the same monolayer MoS_2 sample for fundamental wavelengths of 1280 nm, 1290 nm, 1300 nm, 1310 nm, 1320 nm, and 1330 nm, respectively. Scale bar, 20 μm. (**G**) Resonance of the edge nonlinear response at ~0.947 eV (1310 nm). The ratio is determined by the integrated SHG with the areas circled in (A).

Nonlinear optical susceptibilities are highly sensitive to extremely small changes in materials' electronic properties. In a 3D crystal, breaking the translational symmetry at an interface yields appreciable electric dipolar contributions to the surface optical nonlinearity, making the highly surface- and molecular-specific second-harmonic spectroscopy an indispensable tool for noninvasive study of surface sciences (*20*). Not only does it measure dipolar width across interfaces (*21*), it also probes the real-time dynamics of a surface, such as atomic reconstructions, charge transfer, and molecular conformational transitions. We found that the broken translational symmetry at the edge of a 2D crystal potentially creates 1D atomic edges with localized electronic properties that may substantially differ from the 2D bulk. Shown in Fig. 2, A and B, are SHG images of discrete triangular CVD-grown monolayer islands at pump wavelengths of 1280 nm and 1300 nm, respectively. Although actually rough at the atomic scale, the edges of these monolayer islands are the more energetically favorable termination of molybdenum zigzag edges, and they appear straight and sharp under the optical microscope (*18*). The SHG images with two different fundamental wavelengths differ at these atomic edges. When pumped at 1300 nm, a brim of enhanced SHG is observed at the edges of the crystals (Fig. 2B), which is substantially stronger than that of the central region. At the corners, the SHG is even stronger. By comparison, no such enhancement is observed at the edges at the pump wavelength of 1280 nm. The edge-enhanced SHG is further seen in the cross sections in Fig. 2C. Structure and field discontinuities at the edges of these 2D crystals can potentially lead to enhanced in-plane nonlinear polarizability, like the surface-enhanced SHG often observed on metal and dielectric surfaces (*22*, *23*). Such enhancement, however, is equally effective for different pump wavelengths as long as there are no additional electronic states located at the edge. The stronger second-harmonic edge responses pumped at 1300 nm versus 1280 nm are therefore the results of the electronic structure variations between the sharp crystalline edges and the bulk monolayer crystals. Moreover, assuming that the region where the electronic states are affected by the existence of the atomic edges is about the same as the thickness (i.e., less than 1 nm), it requires more than three orders of magnitude of nonlinear enhancement to exceed the nonlinear generation in the central region, given an illumination pump laser spot size greater than 1 μm.

To further probe these phenomena, we imaged the SHG at the edges and corners of the

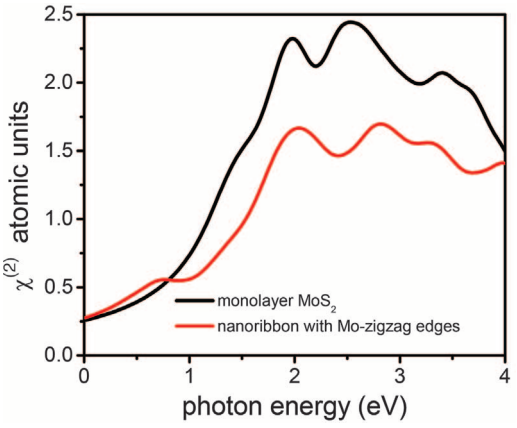


Fig. 4. Dispersion of the nonlinear permittivity for both the monolayer MoS_2 and the nanoribbon with Mo-zigzag edges derived from DFT. The monolayer (black) shows no spectroscopic features (dispersive and lossless) at the low photon energies, and the features between 1.5 and 4.0 eV are associated with interference between the one-photon and two-photon processes. The nanoribbon (red) shows a two-photon resonance at the photon energy ~0.8 eV due to the subband transitions from the valence bands to the isolated edge states originating from the Mo-zigzag edges. The nanoribbon considered here has a width of 5 unit cells, and both the edges are terminated by Mo-zigzag edges. The lattice constants were assumed to be the same as the monolayer, and the Mo edges are not passivated for simplicity. The overall nonlinear responses are averaged over the entire supercell that includes both the nanoribbon and the vacuum; the enhancement of nonlinear responses could therefore be severely underestimated.

samples at different fundamental wavelengths. We observed a resonance wavelength is about 1310 nm (~0.95 eV), a slightly higher photon energy than the half transition energy of the *A* exciton complex (Fig. 3). Quantum mechanical expression for the second-order nonlinear susceptibility of a material involves matrix elements with one occupied and two unoccupied intermediate states. When there are additional energy levels nearly coincident with virtual transition levels, the coupling between the radiation and the nonlinear optical susceptibility becomes large. The nonlinear optical transition matrix elements at the edges may involve additional occupied edge states relative to the crystalline atomic membrane, resulting in strongly enhanced second-order nonlinear susceptibilities. Density functional theory (DFT) has predicted the existence of these edge states and provides atomic-scale insight into them (*24*); such 1D edges have been identified on nanoparticulate MoS_2 clusters on single-crystal gold by scanning tunneling microscopy in ultrahigh vacuum (*25*). The existence of special electronic edge states for finite low-dimensional crystals has also been reported in graphene nanoribbons (*26*, *27*) and at the end of 1D atomic chains (end states) (*28*). We observed the strong optical nonlinear responses of such edges in 2D MoS_2 membranes, which have been suspected to be the active sites for electrocatalytic hydrogen evolution (*8*). As a control experiment, there are no extraordinary photoluminescence responses observed on these edges (fig. S6). It is also worth noting that there exist prominent excitons in thin-film MoS_2 (*29*) and that strongly correlated excitons, especially those with high binding energies, can potentially have an impact on second-order nonlinearities. Moreover, the local doping profile at the boundaries and edges introduced during the growth may also account for the difference at the edges and the center of the monolayer crystals.

The linear and nonlinear optical properties of monolayer MoS_2 can be investigated with first-principles calculations (see supplementary text). The probabilities of virtual electronic transitions can be derived from second-order perturbation theory (*30*). As shown in Fig. 4, we have calculated the dispersion of the nonlinear optical susceptibilities using the full potential linear augmented plane wave method within DFT. Because MoS_2 belongs to the point group D_{3h}, there is only one independent component, namely $\chi^{(2)} = \chi^{(2)}_{xxy} = \chi^{(2)}_{xyx} = \chi^{(2)}_{yxx} = \chi^{(2)}_{yyy}$. In Fig. 4, the tensor elements $\chi^{(2)}$ of monolayer MoS_2 and of a nanoribbon with zigzag Mo termination are compared. The monolayer shows no spectroscopic features below the band gap (~1.9 eV). In stark contrast, the zigzag nanoribbon shows a two-photon resonance at ~0.8 eV, originating from the subband transitions from the valence bands to the isolated edge states of the Mo-zigzag edges. Such a two-photon nonlinear optical resonance qualitatively explains the experimental observations at 1300 nm. In our calculations, we considered an infinitely long nanoribbon with a width of five unit cells with Mo-zigzag edge terminations. The lattice constants are assumed to be the same as the monolayer, and the Mo edges are not passivated for simplicity. The overall nonlinear responses are averaged over the entire supercell that includes both the vacuum and the nanoribbon. Therefore, the enhancement of nonlinear responses near 0.8 eV could be severely underestimated. The spectroscopic features between 1 and 4 eV are mainly associated with interference between the one-photon and two-photon processes, which are commonly observed in nonlinear semiconductors.

Our technique has revealed second-order nonlinear optics at the boundaries and edges of the atomic membranes of the hexagonal transition metal dichalcogenide MoS_2, with the strong optical resonance indicating a distinct edge state due to the translational symmetry breaking. The nonlinear response reveals the structural and symmetry information of the 2D atomic monolayer based on interference of nonlinear waves. Such a rapid nonlinear optical imaging technique will allow exploration of the structural, optical, and electronic properties of 2D atomic layers over a large area.

References and Notes

1. Y. W. Son, M. L. Cohen, S. G. Louie, *Phys. Rev. Lett.* **97**, 216803 (2006).
2. X. Li, X. Wang, L. Zhang, S. Lee, H. Dai, *Science* **319**, 1229–1232 (2008).
3. O. V. Yazyev, M. I. Katsnelson, *Phys. Rev. Lett.* **100**, 047209 (2008).
4. M. Sepioni *et al.*, *Phys. Rev. Lett.* **105**, 207205 (2010).
5. O. V. Yazyev, *Rep. Prog. Phys.* **73**, 056501 (2010).
6. O. V. Yazyev, S. G. Louie, *Nat. Mater.* **9**, 806–809 (2010).
7. A. W. Tsen *et al.*, *Science* **336**, 1143–1146 (2012).
8. T. F. Jaramillo *et al.*, *Science* **317**, 100–102 (2007).
9. B. Radisavljevic, A. Radenovic, J. Brivio, V. Giacometti, A. Kis, *Nat. Nanotechnol.* **6**, 147–150 (2011).
10. A. Splendiani *et al.*, *Nano Lett.* **10**, 1271–1275 (2010).
11. T. Cao *et al.*, *Nat. Commun.* **3**, 887 (2012).
12. H. Zeng, J. Dai, W. Yao, D. Xiao, X. Cui, *Nat. Nanotechnol.* **7**, 490–493 (2012).
13. K. F. Mak, K. He, J. Shan, T. F. Heinz, *Nat. Nanotechnol.* **7**, 494–498 (2012).
14. L. M. Malard, T. V. Alencar, A. P. M. Barboza, K. F. Mak, A. M. de Paula, *Phys. Rev. B* **87**, 201401R (2013).
15. N. Kumar, Q. Cui, F. Ceballos, H. Zhao, *Phys. Rev. B* **87**, 161403 (2013).
16. Y. Li *et al.*, *Nano Lett.* **13**, 3329–3333 (2013).
17. H. Zeng *et al.*, *Sci. Rep.* **3**, 1608 (2013).
18. A. M. van der Zande *et al.*, *Nat. Mater.* **12**, 554–561 (2013).
19. P. Y. Huang *et al.*, *Nature* **469**, 389–392 (2011).
20. Y. R. Shen, *Nature* **337**, 519–525 (1989).
21. W. H. Steel, R. A. Walker, *Nature* **424**, 296–299 (2003).
22. N. Bloembergen, P. S. Pershan, *Phys. Rev.* **128**, 606–622 (1962).
23. C. K. Chen, A. R. B. de Castro, Y. R. Shen, *Phys. Rev. Lett.* **46**, 145–148 (1981).
24. M. V. Bollinger *et al.*, *Phys. Rev. Lett.* **87**, 196803 (2001).
25. S. Helveg *et al.*, *Phys. Rev. Lett.* **84**, 951–954 (2000).
26. K. Nakada, M. Fujita, G. Dresselhaus, M. S. Dresselhaus, *Phys. Rev. B* **54**, 17954–17961 (1996).
27. C. G. Tao *et al.*, *Nat. Phys.* **7**, 616–620 (2011).
28. J. N. Crain, D. T. Pierce, *Science* **307**, 703–706 (2005).
29. K. F. Mak *et al.*, *Nat. Mater.* **12**, 207–211 (2013).
30. J. E. Sipe, D. J. Moss, H. M. Vandriel, *Phys. Rev. B* **35**, 1129–1141 (1987).

Acknowledgments: Supported by the U.S. Air Force Office of Scientific Research, Multidisciplinary University Research Initiative program, under grant FA9550-12-1-0024. The synthesis of the material was supported by the Center for Re-Defining Photovoltaic Efficiency Through Molecular-Scale Control, an Energy Frontier Research Center funded by the U.S. Department of Energy, Office of Science, Office of Basic Energy Sciences under award DE-SC0001085 (D.A.C. and J.C.H.).

Supplementary Materials

www.sciencemag.org/content/344/6183/488/suppl/DC1
Supplementary Text
Figs. S1 to S6
References (*31*–*40*)

8 January 2014; accepted 11 March 2014
10.1126/science.1250564

Probing Exchange Pathways in One-Dimensional Aggregates with Super-Resolution Microscopy

Lorenzo Albertazzi,[1,2]* Daan van der Zwaag,[1,3] Christianus M. A. Leenders,[1,3] Robert Fitzner,[4]† Remco W. van der Hofstad,[1,4] E. W. Meijer[1,2,3]*

Supramolecular fibers are prominent structures in biology and chemistry. A quantitative understanding of molecular exchange pathways in these one-dimensional aggregates was obtained by a combination of super-resolution stochastic optical reconstruction microscopy and stochastic simulation. The potential of this methodology is demonstrated with a set of well-defined synthetic building blocks that self-assemble into supramolecular fibrils. Previous ensemble measurements hid all molecular phenomena underpinning monomer exchange, but the molecular pathway determined from single-aggregate studies revealed unexpected homogeneous exchange along the polymer backbone. These results pave the way for experimental investigation of the structure and exchange pathways of synthetic and natural supramolecular fibers.

Supramolecular fibers, one-dimensional (1D) aggregates in which units are connected through noncovalent interactions, are of major interest in biology and chemistry. Biological fibers such as microtubules and actin filaments are widely studied because of their importance in controlling cell mechanical properties, migration, and differentiation (*1*). Moreover, 1D aggregates play a distinct role in several diseases (*2*). In chemistry, supramolecular polymers have potential applications in material chemistry, medicine, and molecular electronics (*3*). Because of the importance of 1D self-assembled fibers in these fields, efforts to understand the mechanism of fiber assembly and dynamics have been made (*4*, *5*). Similar theoretical models are used to explain the behavior of both natural and synthetic assemblies, despite their very different chemical nature (*6*). Based on ensemble measurements, these models usually assume that monomer exchange between fibers occurs via polymerization-depolymerization at the ends of the aggregates or through a fragmentation-recombination mechanism. However, the experimental validation of these assumptions is extremely challenging.

Super-resolution techniques are emerging as powerful tools to image cellular structures with extraordinary spatial resolution (*7*). Recent reports aim to exploit the potential of stochastic optical reconstruction microscopy (STORM) to extract quantitative information about the structure (*8*) and the dynamics (*9*) of biological machineries. We have used a combination of STORM microscopy and stochastic modeling to quantitatively study exchange pathways of 1D self-assembled structures at a single-fiber level. In particular, we present STORM imaging of supramolecular polymers based on the 1,3,5-benzenetricarboxamide (BTA) motif. BTA assemblies have been extensively studied from both a structural and a mechanistic point of view (*10*). We focus on this synthetic moiety because of the high control that can be achieved at the molecular level, in terms of structural diversity and degree of labeling. We previously reported a fluorescence resonance energy transfer (FRET)–based study of the dynamics in water of BTA supramolecular fibers (*11*). These ensemble measurements provide useful information about the time scale of the exchange but are not sufficient to unveil its mechanism.

For this study, we prepared three molecules: BTA, which self-assembled into 1D fibers, and the dye-labeled variants BTA-Cy3 and BTA-Cy5 (Fig. 1A). We chose these dyes based on their suitable photophysical properties for STORM imaging and on their high degree of molecular similarity, which minimized the effects of the labels on monomer behavior. By coassembling BTA and BTA-Cy3 or BTA and BTA-Cy5, we

[1]Institute for Complex Molecular Systems, Eindhoven University of Technology, Post Office Box 513, 5600 MD Eindhoven, Netherlands. [2]Laboratory of Chemical Biology, Eindhoven University of Technology, Post Office Box 513, 5600 MD Eindhoven, Netherlands. [3]Laboratory of Macromolecular and Organic Chemistry, Eindhoven University of Technology, Post Office Box 513, 5600 MD Eindhoven, Netherlands. [4]Department of Mathematics and Computer Science, Eindhoven University of Technology, Post Office Box 513, 5600 MD Eindhoven, Netherlands.

*Corresponding author. E-mail: l.albertazzi@tue.nl (L.A.); e.w.meijer@tue.nl (E.W.M.)

†Present address: Department of Mathematics, Stockholm University, 106 91 Stockholm, Sweden.

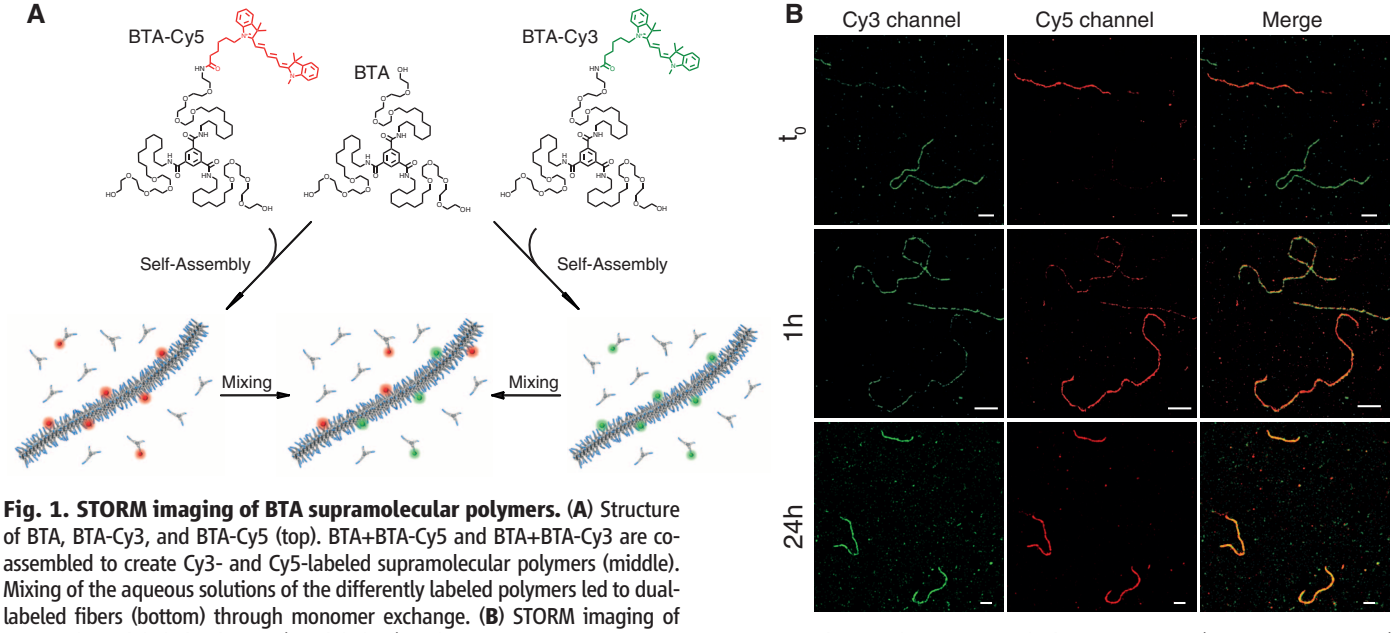


Fig. 1. STORM imaging of BTA supramolecular polymers. (**A**) Structure of BTA, BTA-Cy3, and BTA-Cy5 (top). BTA+BTA-Cy5 and BTA+BTA-Cy3 are coassembled to create Cy3- and Cy5-labeled supramolecular polymers (middle). Mixing of the aqueous solutions of the differently labeled polymers led to dual-labeled fibers (bottom) through monomer exchange. (**B**) STORM imaging of Cy5- and Cy3-labeled polymers (5% labeling) at different mixing time points. The mixing is performed in a vial while the exchange is stopped at different time points by adsorbing the fibers on the glass surface to allow STORM imaging of the samples so prepared. The separate Cy3 (excitation at 561 nm) and Cy5 (excitation at 647 nm) channels and the merge images are presented. Scale bars, 1 μm.

obtained single-color supramolecular polymers. All of the techniques we used, including cryogenic transmission electron microscopy (cryo-TEM), show incorporation of monomers into a single stack. The degree of labeling of the fibers could be accurately controlled by simple tuning of the BTA:BTA-dye ratio, which proved critical for obtaining quantitative information from the STORM analysis. Please refer to fig. S1 and supplementary materials for a detailed description of syntheses, fiber assembly, and sample preparation procedures (*12*).

We obtained STORM images of BTA-based supramolecular polymers incorporating either BTA-Cy5 or BTA-Cy3 monomers and observed fiber features down to 25 nm, as shown in fig. S2. The multicolor ability, together with the enhancement of the resolution, allowed us to resolve structural details of the fibers (see fig. S3), as well as monomer exchange on a subaggregate scale. These distinctive features of STORM provide structural insights synergistic with other high-resolution techniques such as cryo-TEM and atomic force microscopy (AFM) (*13*).

As schematically represented in Fig. 1A, after mixing single-color fibers, we monitored the exchange of monomers by imaging the migration of Cy5-labeled monomers to a Cy3-labeled fiber, and vice versa. In Fig. 1B, STORM images of a mixture of Cy3- and Cy5-labeled fibers are shown at different mixing times t. At t_0, the fibers appear either green or red because monomer exchange has not taken place, but after 24 hours, every fiber contains both monomers; what were green or red fibers are now virtually indistinguishable. The intermediate time points provide insights into the exchange mechanism. Fibers were partially mixed after 1 hour of incubation (middle row of Fig. 1B). These images unambiguously show that the exchange did not take place through fragmentation-recombination, as we did not observe any single-color blocks. Also, polymerization-depolymerization at the fiber termini could be excluded because the fluorescence intensity at the polymers ends was not appreciably higher [no more than 10% versus middle segments; see also fig. S4]. Notably, none of most expected mechanisms are operative, and these observations point toward a monomer-based mechanism.

Due to the stochastic processes involved, as well as the localization-based nature of STORM images (*14*), judging the images by eye can be very misleading. Therefore, adequate tools to extract quantitative information from STORM images are needed. Several recent papers propose approaches to quantify the distribution of molecules in isotropic samples (e.g., receptors in the plasma membrane) (*15*–*17*). To quantify the anisotropic, high–aspect-ratio objects in Fig. 1B, we developed an analytical methodology capable of evaluating structural properties of the fibers as well as their chemical composition, as shown schematically in Fig. 2A and the supplementary materials (*12*). The result is a profile of the number of localizations along the polymer backbone that contains information about density and distribution of dyes in the supramolecular fiber during monomer exchange. Moreover, mechanical properties of the polymer can be obtained from backbone fitting, similarly to AFM measurements (*18*).

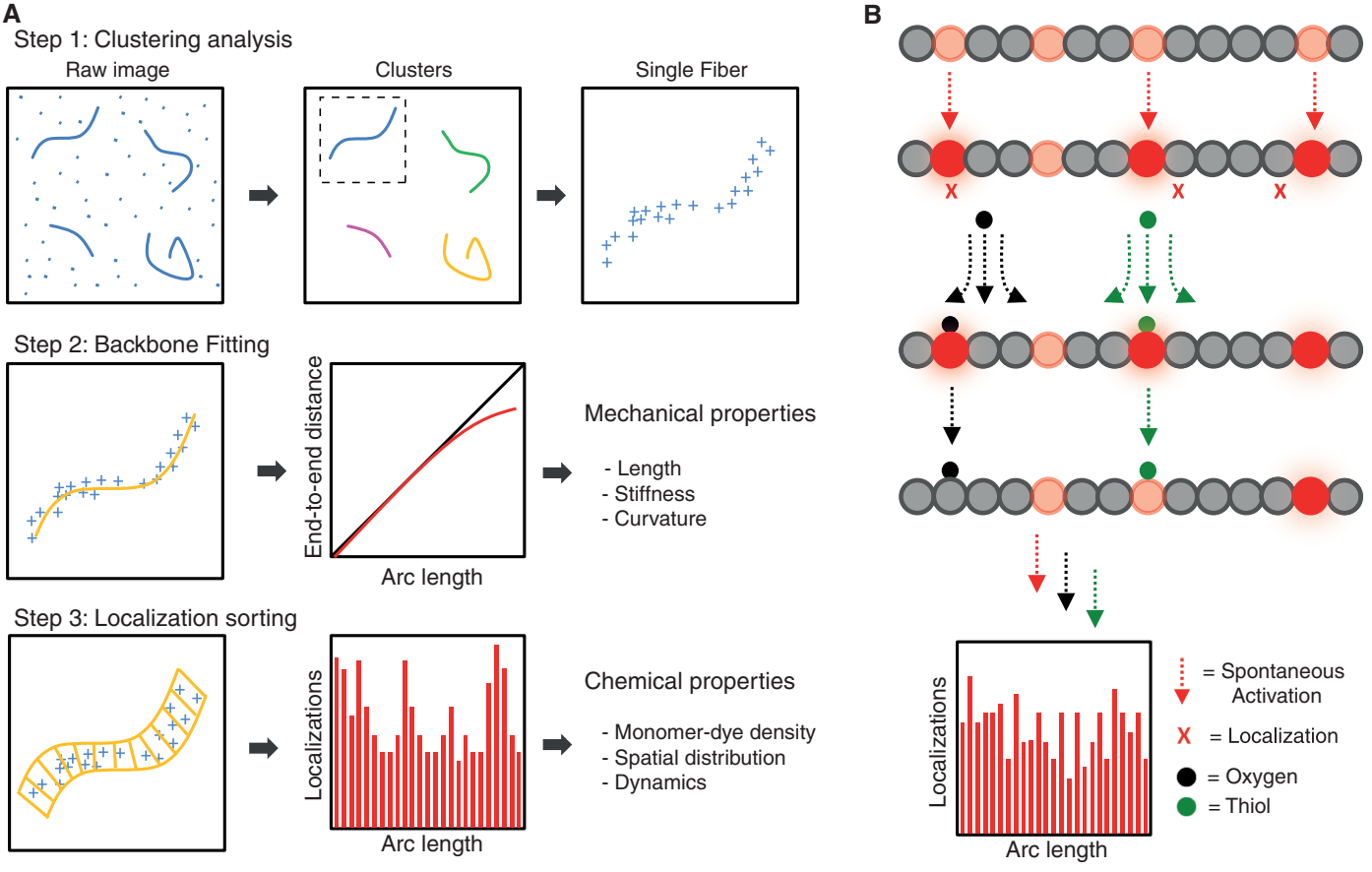


Fig. 2. STORM image analysis procedure and modeling. (**A**) Procedure for image analysis. Background removal and fiber isolation are achieved through a clustering algorithm. The fiber backbone is identified and used for analysis of mechanical properties. Finally, the fiber is divided in 25-nm sections and the number of localizations per section computed, generating a localization density profile (fig. S7). (**B**) Schematic representation of STORM stochastic model. Fibers are modeled as a 1D structure consisting of a random distribution of labeled and unlabeled monomers. Dyes are switched on stochastically and switched off reversibly and irreversibly by thiol and oxygen moieties, respectively. These chemicals are randomly distributed at every time step and act on the closest dye inside a certain range. If no dye is found within the range, the chemical produces no effect. Localizations are computed every time step, and a profile analogous to the experimental one is obtained. For a detailed description of the data treatment and the simulations, refer to appendices S1 to S3 (*12*).

We next developed a simulator to interpret the localization profiles. A schematic representation of the underlying theoretical model is depicted in Fig. 2B. These simulations take into account the different stochastic processes involved in STORM imaging (e.g., random distribution of labels, stochastic blinking and bleaching of dyes) and generate in silico localization profiles. The input parameters—namely the number of monomers and polymer size, the degree of labeling, and the photophysical properties of the dye (e.g., duty cycle and bleaching rate)—were independently determined or can be assumed from experiments, as shown in figs. S5 and S6. The comparison of the in silico profiles with the experimental ones allowed the interpretation of the stochastic processes involved. Moreover, different dye distributions, corresponding to distinct mechanisms of exchange, could be simulated and the effect on the localization profile evaluated.

We demonstrate the potential and the generality of this approach by analyzing single-color synthetic BTA-based supramolecular polymers, as well as biological fibers [microtubules in vitro (*19*) and in BSC-1 cells; see Fig. 3]. Irrespective of the chemical nature of the assemblies, we could probe both the mechanical properties and the dye distribution along the fibers. Scaling behavior, a common way to analyze fiber mechanical properties (*20*) (Fig. 3, B, H, and N), highlights the higher flexibility of BTA-based polymers compared with microtubules, as expected from previous reports on the biological fibers (*1*). For a more detailed description of the mechanical properties, see fig. S8. The localization density profiles for BTA, microtubules in vitro, and microtubules in cells are shown in Fig. 3, C, I, and O, respectively. The amplitudes of these profiles show that the fiber backbones were well-reconstructed, indicating a high image quality suitable for quantitative analysis. Also, the number of localizations along the fiber showed fluctuations around the average amplitude that matched the prediction of our simulation model (Fig. 3, D, J, and P, respectively). This demonstrates that the experimental data can be fully explained by the random distribution of monomers and their stochastic blinking in time.

Autocorrelation algorithms have been successfully used to extract the spatial distribution of labeled monomers in isotropic 2D samples from STORM images (*14*), and we extended this approach to anisotropic 1D fibers. All of the fibers showed short-range autocorrelation decays associated to multiple localizations of the same blinking dye (Fig. 3, E, K, and Q) (*21*). No other correlations appeared, indicating that the monomer distribution was purely stochastic. The fitting of the autocorrelation gave a characteristic decay length in agreement with measurements of single-molecule

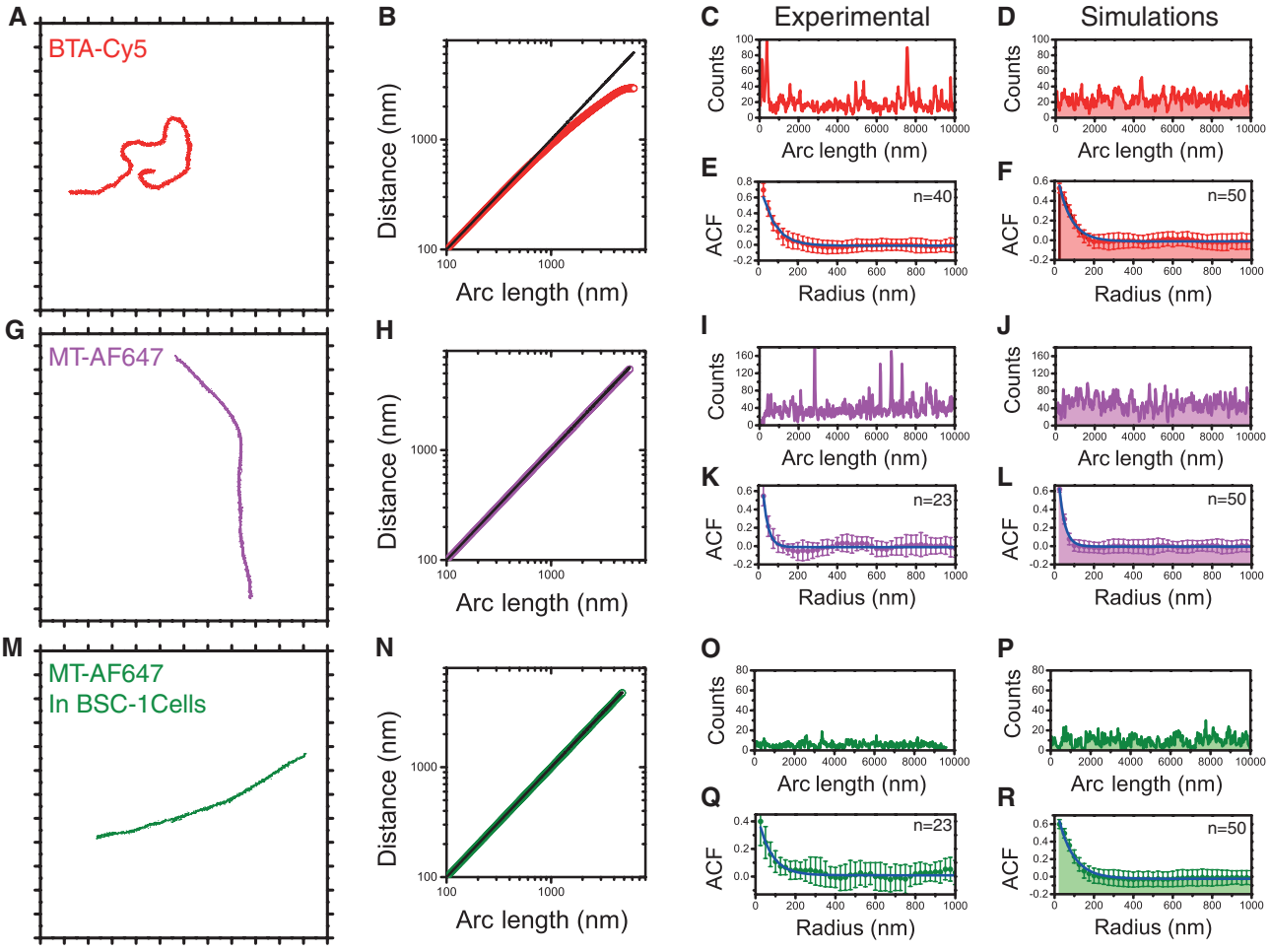


Fig. 3. Quantitative analysis of synthetic and biological supramolecular fibers. Quantitative analysis of mechanical properties and monomer composition of BTA-based polymers (**A** to **F**), microtubules in vitro (**G** to **L**), and microtubules in BSC-1 cells (**M** to **R**). The analysis was performed directly on the obtained data sets, indicating the robustness and general applicability of the methodology. Fiber images (A, G, M), scaling behavior (B, H, N), localization density profiles (C, I, O), and density profile autocorrelation function [(ACF), average of *n* imaged fibers] (E, K, Q) are presented. Analogous density profiles (D, J, P) and autocorrelation plots (F, L, R) from STORM simulations are shown. Experimental and simulated autocorrelation plots were best fit with a monoexponential decay (blue lines). Fitting of the experimental curves gave characteristic decays of 55, 26, and 67 nm for BTA, microtubules in vitro, and microtubules in vivo, respectively. Because of the unknown label densities of the microtubules, the parameters in the simulations are tuned to match the total number of localizations of the respective sample. Images size is 12 μm by 12 μm.

localizations displacement (*12*, *14*). Similar curves were obtained when the autocorrelation algorithm was applied to a simulated stochastic distribution of labels (Fig. 3, F, L, and R).

The ability to probe the monomer distribution using STORM images allows us to quantitatively address the mechanism of BTA monomer exchange presented in Fig. 1B. Figure 4 shows the analysis of BTA-mixing experiments at different time points. The localization profiles (Fig. 4B) show a rise in time in the Cy5 channels and a corresponding decrease in the Cy3 channel as a consequence of mixing. As shown in fig. S13, the curves obtained from averaging all fibers show the same trend as the previously reported FRET measurements and, thus, link ensemble measurements and single-aggregate measurements. Fitting the traces with a kinetic model yields an apparent exchange rate constant of $k'_{ex} = 5.14 \times 10^{-3}$ M^{-1} min^{-1}.

We performed correlation analyses on Cy5-localization profiles at different time points to investigate long-range order in the distribution of the monomers, that is, the occurrence of clusters formed through nonhomogeneous exchange. Simulations of dye distributions obtained from the different mechanisms proposed are presented in fig. S11. These mechanisms are characterized by a qualitatively different behavior in the autocorrelation curves that allows for the interpretation of the experimental profiles and the elucidation of the fiber-exchange mechanism. Contrary to visual observation in Fig. 1B, which suggests a clustered distribution of monomers, autocorrelation curves did not provide any evidence of long-range ordering. All curves were best fit as single decays corresponding to overcounting, in accordance with the simulation of the homogenous exchange presented in figs. S12 and S14. This finding is further corroborated by the cross-correlation analysis between the Cy5 and the Cy3 channels that also shows no ordering of monomers.

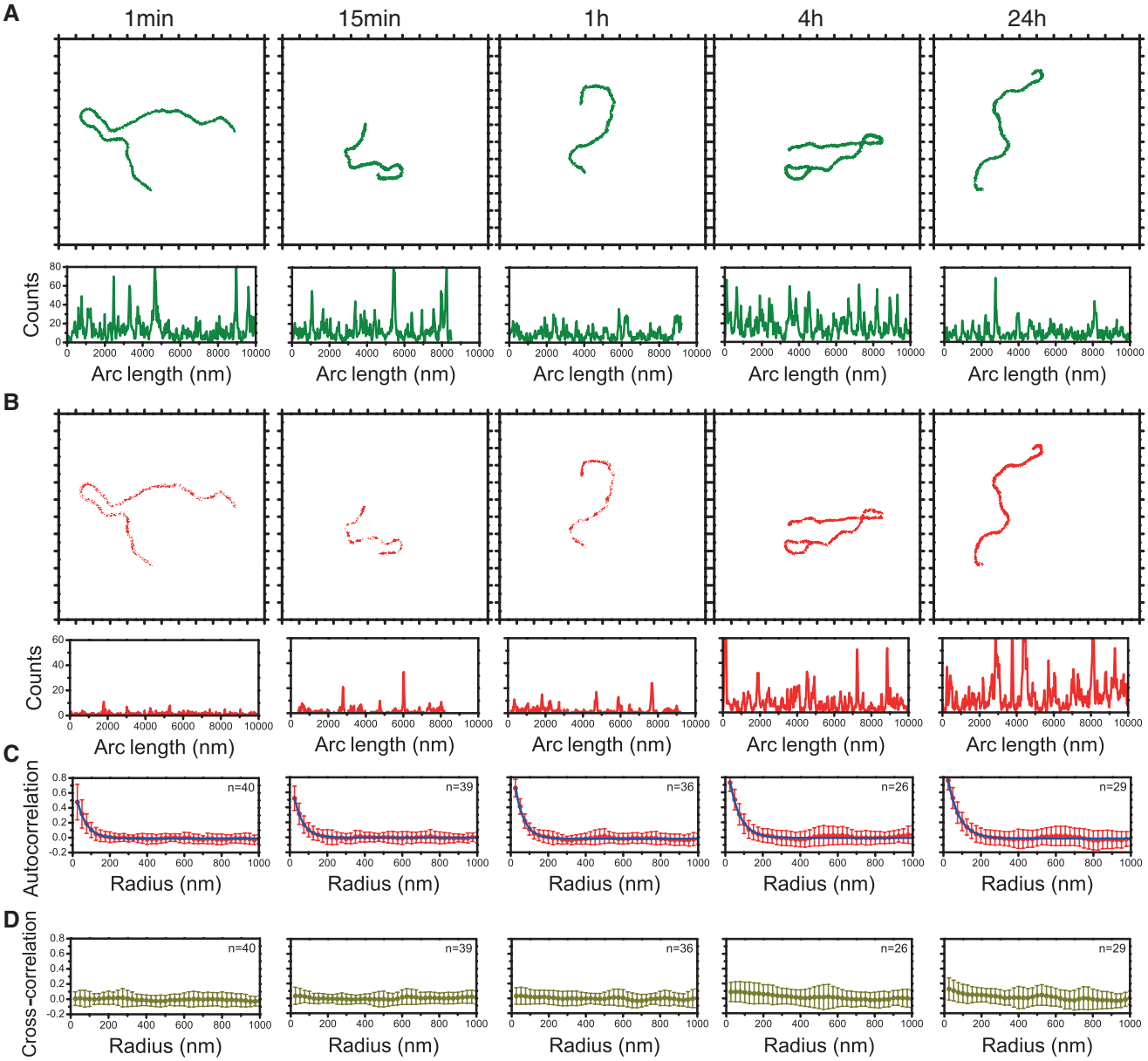


Fig. 4. BTA monomer exchange analysis at different time points. Images of BTA fibers in Cy3 (**A**) and Cy5 (**B**) channels at different time points of mixing. The corresponding localization density profile is reported below every image. Fibers initially labeled with Cy3 only that, in time, incorporate BTA-Cy5 monomers are selected. Average autocorrelation plots for the Cy5 channel are reported in (**C**). These curves contain the information about the distribution of the new monomers incorporated into a stack during mixing and, thus, on the exchange mechanism. Cross-correlation plots showed no relation between the green and red profiles at any time point (**D**). Images size is 12 μm by 12 μm.

The unexpected homogeneous exchange can be rationalized by the presence of disordered domains inside the ordered hydrogen-bonded supramolecular polymer (*13*, *22*); a more detailed description is provided in the supplementary materials (*12*). In the disordered domains the interactions between monomers are proposed to be weaker and, hence, allow an easy point for monomers to leave and enter the 1D fiber. The observed exchange rate is relatively slow compared with the dynamics of the internal order within the fiber. Therefore, within the spatial and temporal resolution of the STORM technique [down to 50 nm (fig. S14)], which corresponds to ~10 times the fiber diameter, the BTA-based supramolecular polymers presented here exchanged homogenously along the polymer backbone. No evidence is obtained for any fragmentation-fusion or polymerization-depolymerization at the chain ends. This finding suggests the need to revisit the dynamic behavior of many other supramolecular fibers (*3*).

References and Notes

1. D. A. Fletcher, R. D. Mullins, *Nature* **463**, 485–492 (2010).
2. F. Chiti, C. M. Dobson, *Annu. Rev. Biochem.* **75**, 333–366 (2006).
3. T. Aida, E. W. Meijer, S. I. Stupp, *Science* **335**, 813–817 (2012).
4. T. P. J. Knowles *et al*., *Science* **326**, 1533–1537 (2009).
5. F. Würthner, T. E. Kaiser, C. R. Saha-Möller, *Angew. Chem. Int. Ed.* **50**, 3376–3410 (2011).
6. D. Zhao, J. S. Moore, *Org. Biomol. Chem.* **1**, 3471–3491 (2003).
7. B. Huang, M. Bates, X. Zhuang, *Annu. Rev. Biochem.* **78**, 993–1016 (2009).
8. A. Szymborska *et al*., *Science* **341**, 655–658 (2013).
9. D. Pinotsi *et al*., *Nano Lett.* **14**, 339–345 (2014).
10. S. Cantekin, T. F. A. de Greef, A. R. A. Palmans, *Chem. Soc. Rev.* **41**, 6125–6137 (2012).
11. L. Albertazzi *et al*., *Proc. Natl. Acad. Sci. U.S.A.* **110**, 12203–12208 (2013).
12. Materials and methods are available as supplementary materials on *Science* Online.
13. C. M. A. Leenders *et al*., *Chem. Commun.* **49**, 1963–1965 (2013).
14. M. J. Rust, M. Bates, X. Zhuang, *Nat. Methods* **3**, 793–796 (2006).
15. P. Sengupta, T. Jovanovic-Talisman, J. Lippincott-Schwartz, *Nat. Protoc.* **8**, 345–354 (2013).
16. X. Nan *et al*., *Proc. Natl. Acad. Sci. U.S.A.* **110**, 18519–18524 (2013).
17. R. P. J. Nieuwenhuizen *et al*., *Nat. Methods* **10**, 557–562 (2013).
18. J. Adamcik *et al*., *Nat. Nanotechnol.* **5**, 423–428 (2010).
19. G. T. Dempsey, J. C. Vaughan, K. H. Chen, M. Bates, X. Zhuang, *Nat. Methods* **8**, 1027–1036 (2011).
20. F. Valle, M. Favre, P. De Los Rios, A. Rosa, G. Dietler, *Phys. Rev. Lett.* **95**, 158105 (2005).
21. S. L. Veatch *et al*., *PLOS ONE* **7**, e31457 (2012).
22. T. Shikata, D. Ogata, K. Hanabusa, *J. Phys. Chem. B* **108**, 508–514 (2004).

Acknowledgments: We thank X. Zhuang and Nikon Europe for sharing data sets. Data sets for in vitro microtubules (*18*) were provided by X. Zhuang; data sets for microtubules in BSC-1 cells were provided by Nikon Europe. We thank T. de Greef and A. Palmans for useful discussions and the Institute for Complex Molecular Systems animation studio for the artwork. This work was supported by the European Research Council; the Dutch Science Foundation (NWO); the Netherlands Initiative for Regenerative Medicine; and the Dutch Ministry of Education, Culture and Science (Gravity program 024.001.035).

Supplementary Materials

www.sciencemag.org/content/344/6183/491/suppl/DC1
Materials and Methods
Supplementary Text
Figs. S1 to S24
References (*23*–*25*)
Appendices S1 to S3

16 January 2014; accepted 7 April 2014
10.1126/science.1250945

Interfacial Effects in Iron-Nickel Hydroxide–Platinum Nanoparticles Enhance Catalytic Oxidation

Guangxu Chen,[1] Yun Zhao,[1] Gang Fu,[1]* Paul N. Duchesne,[3] Lin Gu,[2]* Yanping Zheng,[1] Xuefei Weng,[1] Mingshu Chen,[1] Peng Zhang,[3] Chih-Wen Pao,[4] Jyh-Fu Lee,[4] Nanfeng Zheng[1]*

Hybrid metal nanoparticles can allow separate reaction steps to occur in close proximity at different metal sites and accelerate catalysis. We synthesized iron-nickel hydroxide–platinum (transition metal-OH-Pt) nanoparticles with diameters below 5 nanometers and showed that they are highly efficient for carbon monoxide (CO) oxidation catalysis at room temperature. We characterized the composition and structure of the transition metal–OH-Pt interface and showed that Ni^{2+} plays a key role in stabilizing the interface against dehydration. Density functional theory and isotope-labeling experiments revealed that the OH groups at the Fe^{3+}-OH-Pt interfaces readily react with CO adsorbed nearby to directly yield carbon dioxide (CO_2) and simultaneously produce coordinatively unsaturated Fe sites for O_2 activation. The oxide-supported PtFeNi nanocatalyst rapidly and fully removed CO from humid air without decay in activity for 1 month.

The fabrication of multicomponent active sites (*1*–*15*), particularly metal-metal hydroxide and oxide interfaces (*1*–*11*), to facilitate the activation of reagents has been emerging as an effective method for preparing heterogeneous catalysts with improved activities. For example, Pt/FeO_x interfaces exhibit excellent performance in CO oxidation and CO preferential oxidation (PROX) (*1*, *2*), Au/CeO_x and Au/TiO_x interfaces improve the activity of the water-gas shift reaction (*5*–*7*), and $Pt/M(OH)_2$ (where M is metal) interfaces enhance the performance of H_2 evolution reaction (*10*, *11*). The structure and reactivity of such catalysts can be modeled with well-defined synthetic nanoparticles (NPs) (*16*–*18*). For instance, rational design of nanoscaled metal–metal oxide interfaces in nanostructured catalysts has been successfully achieved by controlled assembly of metal and metal oxide nanocrystals (NCs) (*8*). Monodisperse Pd NCs were deposited on ceria to investigate the $Pd\text{-}CeO_2$ interfacial effect on catalysis (*19*). However, assembling metal NPs with oxide NPs or depositing metal NPs on oxide supports introduced rather limited metal-metal (hydr)oxide interfaces.

We report on a wet-chemical method for fabricating M-OH-Pt interfaces (M-OH, where M is Fe and Ni) by partially covering the surface of monodisperse Pt NCs (which are <5 nm in diameter) with atomically thick M-OH layers. The Fe^{3+}-OH-Pt interfaces increased room-temperature catalytic CO oxidation by generating coordinatively unsaturated iron sites for activating O_2, and the Ni^{2+} incorporation dramatically enhanced the long-term catalyst stability by stabilizing the Fe^{3+}-OH-Pt interfaces during catalysis. Based on this understanding, an alloy-assisted strategy was developed to produce a practical Pt nanocatalyst with catalytic M-OH-Pt sites over 50% of total Pt atoms in the catalyst.

To create the iron (hydr)oxide interface, monodisperse Pt NCs capped by organic amine (fig. S1) were synthesized by thermally reducing $Pt(acac)_2$ (where acac is acetylacetonate) in the presence of CO. A small amount of $Fe(acac)_3$ was then introduced and thermally decomposed to deposit submonolayer $Fe(OH)_x$ onto the surface of the premade Pt NCs, yielding the $Pt/Fe(OH)_x$ composite (*20*). Aberration-corrected scanning transmission electron microscopy (STEM) images (Fig. 1, B and C, and fig. S2) revealed the deposition of a less electron-dense layer on the Pt NCs; energy-dispersive spectroscopy (EDS) analysis showed that this layer contained iron (fig. S3). Although the surface of the Pt NCs was covered by iron

[1]State Key Laboratory for Physical Chemistry of Solid Surfaces, Collaborative Innovation Center of Chemistry for Energy Materials, National Engineering Laboratory for Green Chemical Productions of Alcohols, Ethers, and Esters, and Department of Chemistry, College of Chemistry and Chemical Engineering, Xiamen University, Xiamen 361005, China. [2]Institute of Physics, Chinese Academy of Sciences, Beijing 100190, China. [3]Department of Chemistry, Dalhousie University, Halifax, NS, B3H 4R2, Canada. [4]National Synchrotron Radiation Research Center, Hsinchu 30076, Taiwan.

*Corresponding author. E-mail: nfzheng@xmu.edu.cn (N.F.Z.); l.gu@iphy.ac.cn (L.G.); gfu@xmu.edu.cn (G.F.)

species, lattice fringes with interplanar distances of 0.23 nm, corresponding to Pt(111) planes, were observed. The Fe x-ray photoelectron spectroscopy (XPS) spectra suggested an Fe^{3+} oxidation state (Fig. 1C and fig. S4). The O1s XPS spectra are best fitted by the presence of Fe-OH and bridging oxo groups (*21*) in a 4.2:1 ratio (Fig. 1D). X-ray absorption near-edge structure (XANES) analysis (fig. S5) at the pre-edge of the Fe K-edge at 7.114 keV showed that the Fe-O coordination sphere is a slightly distorted octahedron (*22*). Extended x-ray absorption fine structure (EXAFS) revealed that the bond distances of Fe-O and Fe-Fe in the overgrown $Fe(OH)_x$ layer were 1.97 ± 0.02 Å and 3.01 ± 0.02 Å, respectively (fig. S5 and table S1), and an Fe-O coordination of 6 ± 1. Low-energy ion scattering spectroscopy (LEISS) (fig. S6) showed that the as-obtained $Pt/Fe(OH)_x$ NPs still had open Pt sites at their edges and corners.

Given the strong binding of CO to Pt (*1*), we studied CO oxidation to evaluate the Fe^{3+}-OH-Pt interfacial effect. TiO_2-supported Pt NCs displayed negligible CO oxidation activity at room temperature (Fig. 1E); 100% CO conversion was achieved only at temperatures above 373 K. However, TiO_2-supported $Pt/Fe(OH)_x$ NPs (fig. S7) readily achieved 100% CO conversion at room temperature, even with a space velocity (SV) as high as ~400 L g^{-1} Pt h^{-1} (Fig. 1E). The enhanced activity of $Pt/Fe(OH)_x$ NPs was also observed in a humid stream with less oxidizing reactant (reducing the O_2/CO ratio from 16 to 4) (fig. S8). The activity was lost when the $Pt/Fe(OH)_x$ catalyst was simply treated with nitric acid (fig. S9). A decline in activity from 100 to 27% in 70 min occurred when the reaction was switched from humid air to dry air (fig. S10). Even in a humid reaction stream with a relative humidity of 50%, the $Pt/Fe(OH)_x$ catalyst began to degrade after 8 hours at room temperature. We propose that the activity decrease was caused by instability of the interfacial Fe^{3+}-OH-Pt sites with respect to dehydration. Because CO oxidation is exothermic, we subjected the $Pt/Fe(OH)_x$ catalyst to thermal treatment at 453 K in dry air for 2 hours. The OH:O ratio from the O1s XPS was reduced to only 2.7 (fig. S11), suggesting the loss of water. The $Fe(OH)_x$ submonolayers dehydrated into three-dimensional iron oxide-hydroxide or iron oxide.

To prevent the dehydration-induced loss of Fe^{3+}-OH-Pt sites, Ni^{2+}, which forms a stable, layered structure of $Ni(OH)_2$ with nearly perfect octahedral coordination, was incorporated into the $Fe(OH)_x$ submonolayer. The ready formation of hydrotalcite-like Ni/Fe hydroxides (*23*, *24*) was expected to stabilize catalytically active Fe^{3+}-OH-Pt interfacial sites through the strong interaction between $Ni(OH)_x$ and $Fe(OH)_x$. Moreover, $Ni(OH)_2$ species are active in the dissociation of adsorbed water molecules and in proton transport

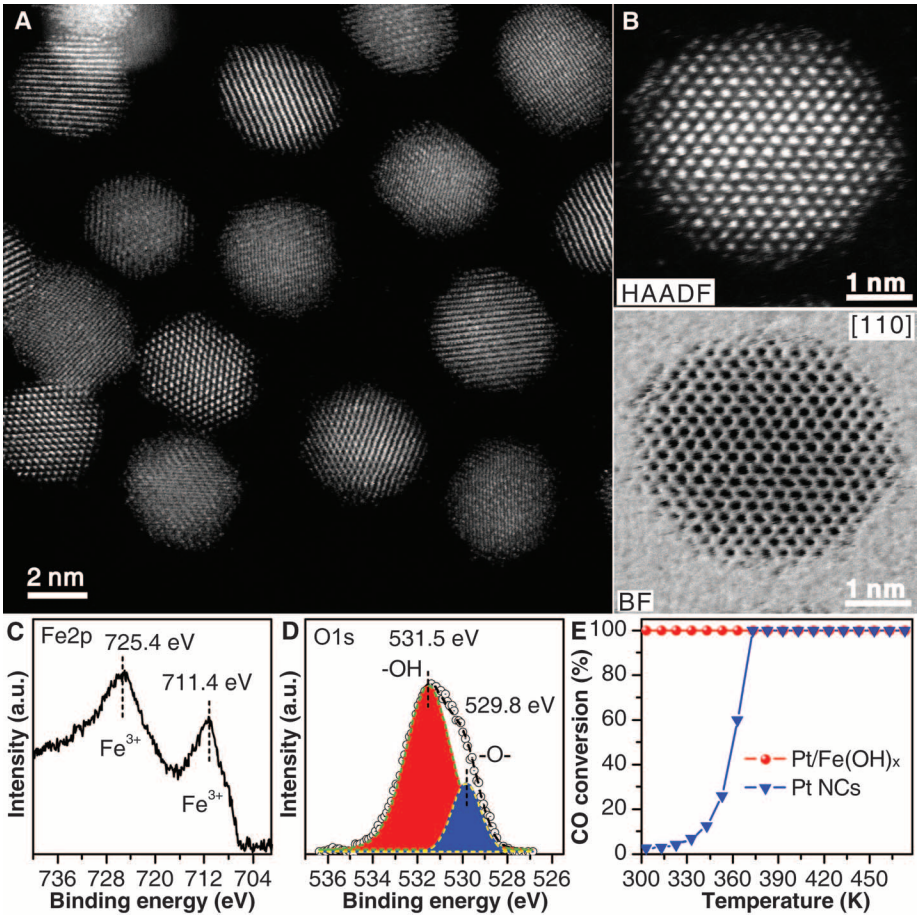
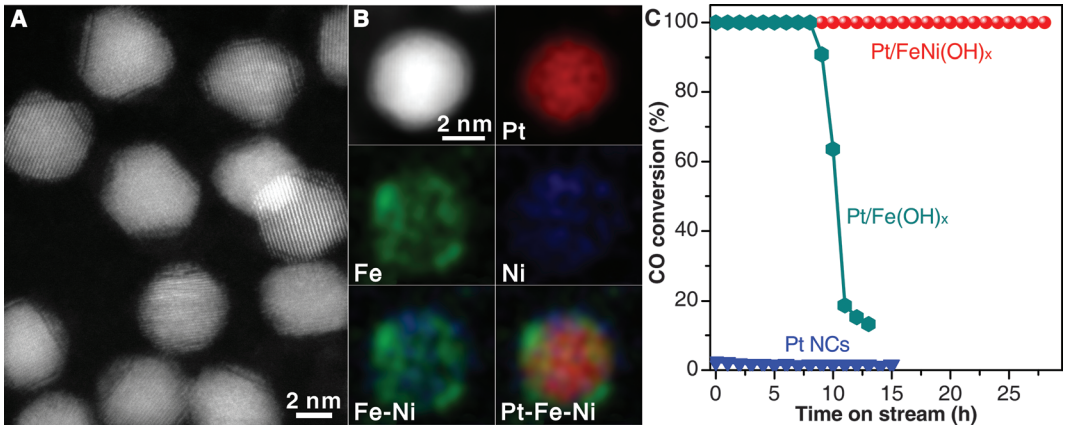


Fig. 1. Structural characterizations and catalytic performance of the $Pt/Fe(OH)_x$ nanoparticles. (**A**) Representative high-angle annular dark-field (HAADF) STEM image of $Pt/Fe(OH)_x$ NPs. (**B**) High-resolution HAADF-STEM image projected along [110] axis and the corresponding bright-field image of an individual $Pt/Fe(OH)_x$ NP. (**C** and **D**) XPS core-level spectra of Fe2p and O1s, respectively. (**E**) CO conversions as a function of reaction temperature over TiO_2-supported $Pt/Fe(OH)_x$ NPs and Pt NCs. Reaction conditions: 1% CO; 16% O_2; N_2 balance; SV = 400 L g^{-1} Pt h^{-1}; pressure = 0.1M Pa.

Fig. 2. Structural characterizations and catalytic performance of the $Pt/FeNi(OH)_x$ nanoparticles. (**A**) Representative HAADF-STEM image of $Pt/FeNi(OH)_x$ NPs. (**B**) STEM-EDS elemental mapping of a single $Pt/FeNi(OH)_x$ NP. (**C**) Catalytic performances of TiO_2-supported $Pt/FeNi(OH)_x$ NPs, Pt NCs, and $Pt/Fe(OH)_x$ NPs as a function of time-on-stream. Reaction conditions: 1% CO; 16% O_2; N_2 balance; T = 303 K; SV = 400 L g^{-1} Pt h^{-1}; relative humidity = 50%; pressure = 0.1M Pa.



(*11*, *25*). The addition of a $Ni(acac)_2$ precursor during the thermal overgrowth process deposited $FeNi(OH)_x$ hybrid submonolayers on Pt NCs with a boundary gap of 3 Å (Fig. 2A). STEM-EDS measurements showed that the $Fe(OH)_x$ and $Ni(OH)_x$ were mixed on the surface (Fig. 2B). As identified by LEISS (fig. S12), open Pt sites were present with Ni and Fe on the outermost surface of the $Pt/FeNi(OH)_x$ NPs. The XANES and EXAFS analyses of $Pt/FeNi(OH)_x$ (fig. S13) indicated that $Ni(OH)_2$ was present in a nearly perfect octahedral coordination environment with Ni-O distances of 2.05 ± 0.01 Å (table S2), and iron was still present as Fe^{3+}. The O1s XPS spectrum indicated an OH:O ratio of 7.5 (fig. S14A).

The $Pt/FeNi(OH)_x$ NPs exhibited greater stability in CO oxidation. When loaded onto supports (fig. S15), the $Pt/FeNi(OH)_x$ catalyst was stable in the reaction stream for more than 28 hours without any decrease in its activity at room temperature (Fig. 2C) and achieved 100% CO conversion (fig. S16). After a 2-hour heat treatment at 453 K under reaction atmosphere, the OH:O ratio in the $Pt/FeNi(OH)_x$ catalyst was maintained at 5.3 (fig. S14B). In comparison, NPs with $Ni(OH)_x$ submonolayer grown on Pt NCs, denoted as $Pt/Ni(OH)_x$, performed poorly at room temperature relative to $Pt/Fe(OH)_x$ (figs. S17 and S18).

To understand how the Fe^{3+}-OH-Pt interface promoted the activity of the catalysts, structural models of periodic Pt [n(111)×(111)] and [n(111)×(100)] stepped surfaces with the overgrowth of $Fe(OH)_x$ on (111) terraces (figs. S19 to S21 and table S3) were built to simulate the hydroxide overgrowth structures on Pt NCs and optimized by using Vienna Ab-initio Simulation Package (VASP) code. Density functional theory (DFT) calculations suggested that CO oxidation at the interfacial Fe^{3+}-OH-Pt site could be triggered by the coupling reaction between the adsorbed CO and interfacial –OH moieties (Fig. 3A), leading to formation of CO_2 either directly or via –COOH intermediate (figs. S22 to S24) with a low energy barrier of 0.69 eV (or 0.93 eV). On the [n(111)×(111)] stepped surface, the release of CO_2 created a vacancy at the interface (i.e., Fe-Vac-Pt, where Vac is a vacancy) with an activation barrier and reaction energy of 0.16 and –0.66 eV (Fig. 3A), respectively. The proton on the reacted interfacial –OH was transferred to nearby –OH to form adsorbed H_2O. On the interfacial Fe-Vac-Pt site, O_2 adsorption was preferential to CO adsorption (–1.34 versus –0.87 eV) (fig. S21), suggesting that the created interfacial vacancy readily served as an effective adsorption site to convert O_2 into highly reactive –OOH species (table S3). The produced –OOH species readily coupled with the second CO directly to form CO_2, simultaneously recovering the Fe^{3+}-OH-Pt interfaces and completing the catalytic cycle. Such H_2O-mediated proton transfer often occurs on the surface of solid oxides (e.g., iron oxide) (*26*) and in our case facilitates the whole catalytic oxidation process (fig. S10).

The reported mechanisms for CO oxidation over $Pt\text{-}FeO_x$ catalysts begin with O_2 activation, either at coordinatively unsaturated Fe^{2+} sites on Pt (*1*) or at an oxygen vacancy on the hematite surface (*2*). These coordinatively unsaturated O_2 activation sites were mainly generated by thermally prereducing the $Pt\text{-}FeO_x$ catalysts in H_2 and were unstable in air. However, our Fe^{3+}-OH-Pt mechanism suggests that these Fe^{2+} sites are not a prerequisite for CO oxidation and that coordinatively saturated Fe^{3+} species are more stable under ambient conditions. We verified the above mechanism by using isotope-labeling experiments (*20*). In the absence of O_2, 55% of the total CO_2 yielded in the first five pulses was determined by mass spectroscopy to be singly ^{18}O-labeled CO_2 ($C^{16}O^{18}O$) when $C^{16}O$ was pulsed into the $H_2{}^{18}O$ pretreated $Pt/Fe(OH)_x$ catalyst (Fig. 3B). The production of $C^{16}O^{18}O$ declined with the increased number of CO pulses because of the continuous consumption of the interfacial $-{}^{18}OH$ groups. In comparison, the reaction of a $C^{16}O$ pulse with the untreated $Pt/Fe(OH)_x$ catalyst yielded negligible $C^{16}O^{18}O$ (Fig. 3C). While confirming that CO could directly react with the interfacial Fe^{3+}-OH-Pt sites to yield CO_2, this result also suggested that ^{18}O-labeled interfacial Fe^{3+}-^{18}OH-Pt sites were readily obtained by treating the $Pt/Fe(OH)_x$ catalyst with $H_2{}^{18}O$. Thus, it was not surprising that the reaction of pulses containing CO, O_2, and $H_2{}^{18}O$ in N_2 with the $Pt/Fe(OH)_x$ catalyst steadily yielded much more $C^{16}O^{18}O$ than those pulses containing CO, O_2, and non-^{18}O–labeled H_2O (Fig. 3, D and E). In all of our isotope-labeling experiments, no detectable isotope exchange between H_2O and O_2 was observed (fig. S25).

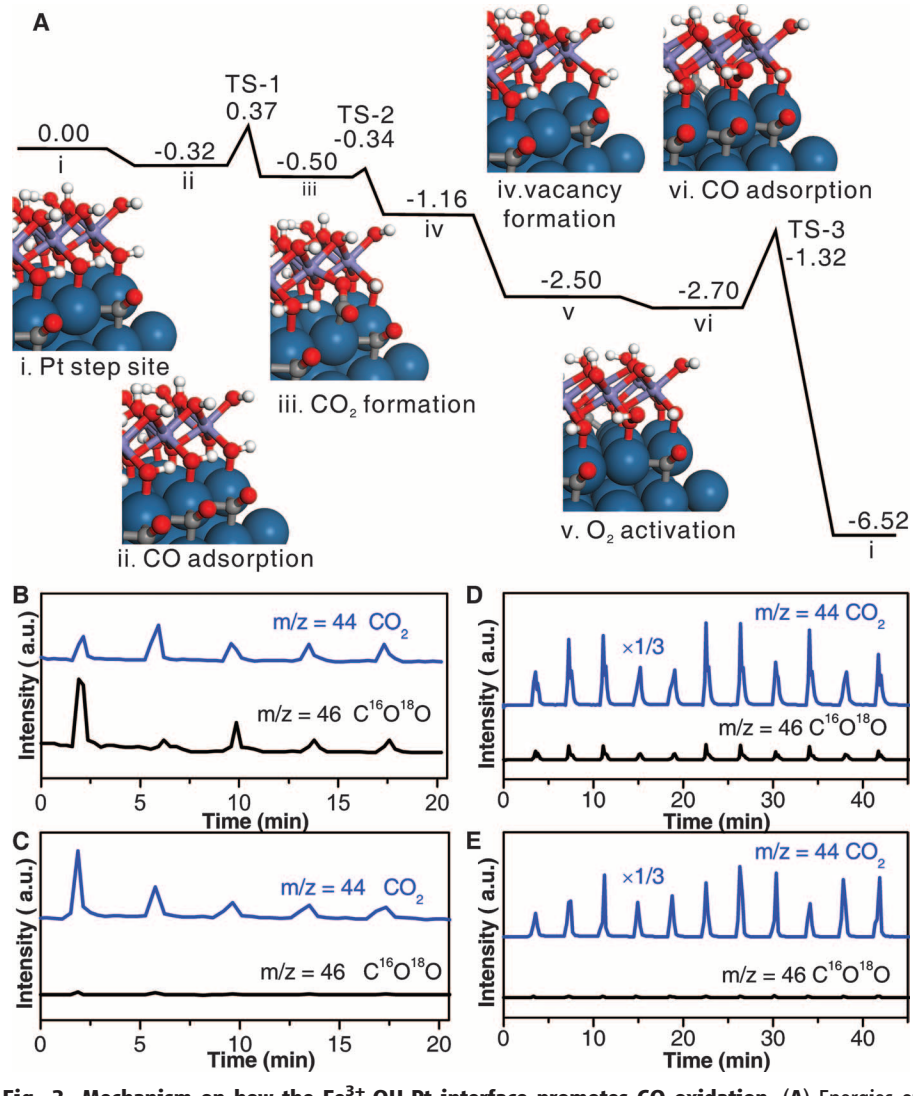


Fig. 3. Mechanism on how the Fe^{3+}-OH-Pt interface promotes CO oxidation. (**A**) Energies of intermediates and transition states in the mechanism of CO oxidation at the Fe^{3+}-OH-Pt[n(111)×(111)] interfaces from DFT calculation. (**B** and **C**) Time-dependent mass spectra of $C^{16}O_2$ and $C^{16}O^{18}O$ species during the pulse experiments by pulsing CO into the $Pt/Fe(OH)_x$ catalyst with (B) and without (C) $H_2{}^{18}O$ pretreatment. (**D** and **E**) Time-dependent mass spectra of $C^{16}O_2$ and $C^{16}O^{18}O$ species during the pulse experiments by reacting the $Pt/Fe(OH)_x$ catalyst with pulses containing a mixture of CO, O_2, and $H_2{}^{18}O$ (D) or normal H_2O (E) in N_2.

Our Fe^{3+}-OH-Pt mechanism was also confirmed by kinetic studies. Over the catalysts incorporated with $Fe(OH)_x$, the activation energies of CO oxidation were reduced to 16 kJ/mol compared with 51 kJ/mol for TiO_2-supported Pt NCs (fig. S26). The incorporation of Ni^{2+} did not reduce the activation energy further. Over TiO_2-supported Pt/$Fe(OH)_x$, the introduction of humidity reduced the activation energy to 12 kJ/mol. Moreover, CO oxidation was determined to be close to zero order for CO and first order for O_2 (fig. S27), which is expected from the Fe^{3+}-OH-Pt mechanism. These results are consistent with CO oxidation triggered by CO oxidative coupling with interfacial OH groups at Fe^{3+}-OH-Pt that also creates coordinatively unsaturated Fe sites for O_2 activation.

In terms of Pt use, the core-shell overgrowth structure described above is not an ideal structure because most Pt atoms are not located on the surface (Fig. 4A) (*1*, *27*). To maximize Pt use and Fe/Ni-OH-Pt interfaces as well, we developed an alloy-assisted strategy to maximize the use of Pt. In this strategy, ternary alloy PtFeNi NCs were prepared by thermally reducing metal precursors [i.e., $Pt(acac)_2$, $Fe(acac)_3$, and $Ni(acac)_2$] under 1 atm CO atmosphere and then aged in the air for 3 days to yield the highly active catalyst (denoted as PtFeNi) (Fig. 4A). The mean diameter of the PtFeNi NPs was 4.9 ± 0.5 nm. When the thermal reduction time at 513 K was 30 min, STEM analyses revealed that the PtFeNi NPs were mainly core-shell structures with Pt-enriched cores (Fig. 4, B and C, and fig. S28). However, Pt-enriched cores were not present in the PtFeNi NPs when the thermal reduction time at 513 K was extended to 1 hour (fig. S29). Each individual NP apparently had a single-crystalline face-centered cubic structure. However, more careful STEM-EDS investigations revealed an interwoven, highly irregular structure to the surface of the air-aged PtFeNi NPs (Fig. 4D and fig. S30) that improved the Pt use compared with those from both Pt NCs and Pt/$Fe(OH)_x$ or Pt/$FeNi(OH)_x$ NPs with the core-shell overgrowth structure.

As characterized by elemental mapping (Fig. 4E), the PtFeNi NPs exhibited compositional heterogeneities in the form of small interwoven domains (less than 3.5 Å) on their surfaces. The LEISS spectra (fig. S31) confirmed that Pt, Fe, and Ni were all exposed on the outermost surface. Both XANES and XPS spectra confirmed the presence of Fe^{3+} and Ni^{2+} oxidation states. EXAFS analyses (fig. S32) revealed that Fe and Ni in the PtFeNi catalyst were both six-coordinate with respect to oxygen, with average Fe-O and Ni-O bond distances of 1.99 ± 0.01 and 2.04 ± 0.01 Å, respectively (table S4). The O1s XPS spectrum indicated an OH:O ratio of 13 (fig. S33). These EXAFS and XPS studies demonstrated that PtFeNi NPs possessed the same interfacial sites discussed above for the Pt/$FeNi(OH)_x$ catalyst, which were active and stable for CO oxidation. As suggested by the temperature-programmed desorption measurements (fig. S34), besides the catalytically active sites that readily reacted with CO to yield CO_2, no further CO chemical adsorption sites were available on the surface of the PtFeNi catalyst. CO titration was thus used to determine the percentage of catalytic sites over the total Pt sites in the catalyst. As illustrated in table S5 (*20*), the numbers of catalytic sites depended on the composition and also the thermal reduction conditions of the NPs. The PtFeNi catalysts with high percentages of Pt-OH-M sites (up to 54% over the total Pt atoms) were readily prepared by extending the thermal reduction time at 513 K. The high percentage of catalytic sites is also supported by the rough NP surfaces with highly dispersed Pt, and the high coordination number (up to 1.6) of O on Pt (table S4) that would allow surface Pt atoms to form more than one Pt-OH-M active center. As compared to the overgrown Pt/$FeNi(OH)_x$ catalyst with the same amount of Pt, the catalytic performance of TiO_2-supported PtFeNi NPs (fig. S35) for CO oxidation was indeed enhanced by a factor of 1.4 to 1.8 (fig. S36). The PtFeNi catalyst exhibited the highest activity with a Fe/Ni molar ratio of ~0.5 (fig. S37). The PtFeNi catalyst exhibited very high stability, both in the reaction stream and during prolonged storage. No decay in the activity of the catalyst was experienced after more than 1 month in the reaction stream of CO with humid air (fig. S38).

The enhanced catalysis of the PtFeNi NPs over pure Pt NCs was also observed when γ-Al_2O_3 was used as the support (fig. S39). Even after being stored at room temperature in ambient air for 2 years, no deterioration of catalytic performance was found for the PtFeNi catalyst prepared by the alloy-assisted strategy. The excellent catalytic performance of the PtFeNi catalyst makes it a promising candidate for applications to remove CO in

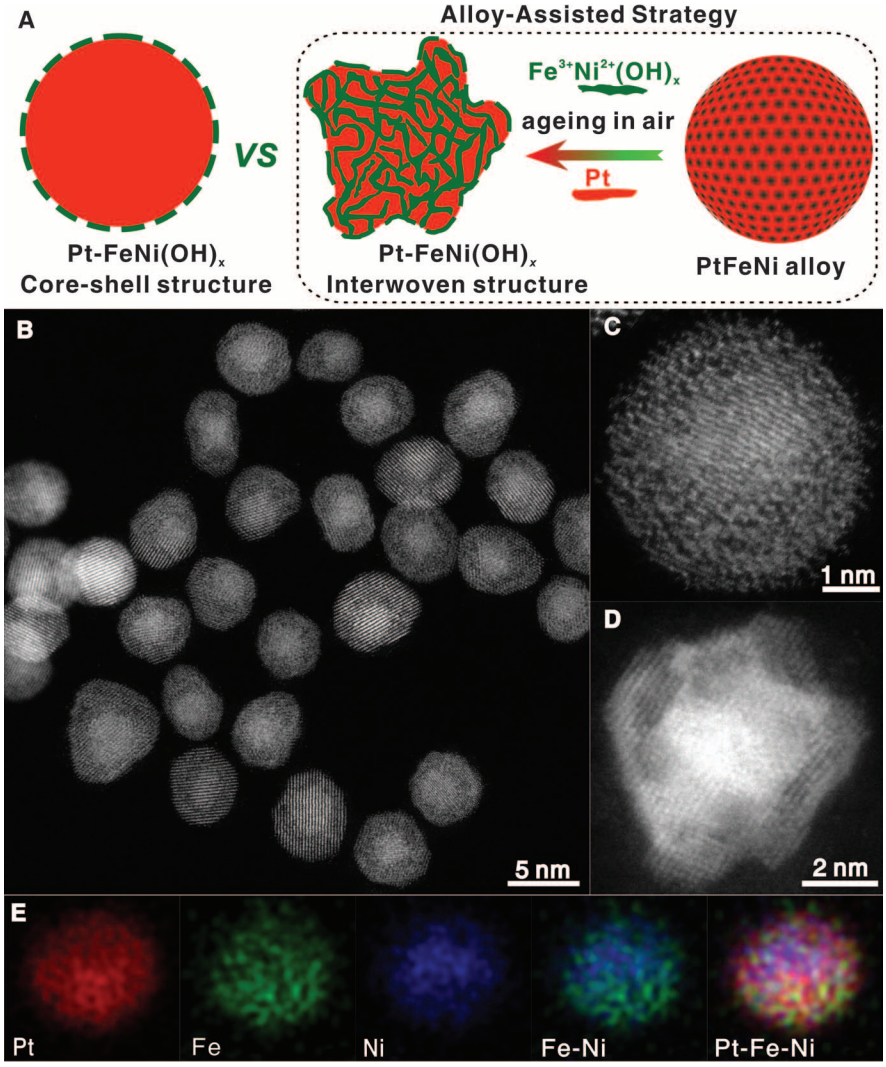


Fig. 4. Synthetic strategy, characterizations, and catalysis of a practical PtFeNi catalyst. (**A**) Cartoon showing the structural difference between the core-shell overgrowth Pt/$FeNi(OH)_x$ catalyst and the interwoven PtFeNi catalyst, and the alloy-assisted strategy for the synthesis of the PtFeNi catalyst. (**B**) Representative HAADF-STEM image of PtFeNi NPs. (**C** and **D**) High-resolution HAADF-STEM image of PtFeNi NPs before (C) and after (D) aging in air, respectively. (**E**) STEM-EDS elemental mapping of a single PtFeNi NP.

humid air or H_2-rich stream and trace H_2 in air (figs. S40 and S41). Creating submonolayer metal hydroxides on noble metal NCs is expected to provide an effective method to prepare efficient noble metal nanocatalysts for oxidative catalysis.

References and Notes

1. Q. Fu *et al.*, *Science* **328**, 1141–1144 (2010).
2. B. Qiao *et al.*, *Nat. Chem.* **3**, 634–641 (2011).
3. I. X. Green, W. Tang, M. Neurock, J. T. Yates Jr., *Science* **333**, 736–739 (2011).
4. M. S. Chen, D. W. Goodman, *Science* **306**, 252–255 (2004).
5. J. B. Park *et al.*, *Proc. Natl. Acad. Sci. U.S.A.* **106**, 4975–4980 (2009).
6. J. A. Rodriguez *et al.*, *Science* **318**, 1757–1760 (2007).
7. Q. Fu, H. Saltsburg, M. Flytzani-Stephanopoulos, *Science* **301**, 935–938 (2003).
8. Y. Yamada *et al.*, *Nat. Chem.* **3**, 372–376 (2011).
9. M. Cargnello *et al.*, *Science* **337**, 713–717 (2012).
10. R. Subbaraman *et al.*, *Nat. Mater.* **11**, 550–557 (2012).
11. R. Subbaraman *et al.*, *Science* **334**, 1256–1260 (2011).
12. V. R. Stamenkovic *et al.*, *Nat. Mater.* **6**, 241–247 (2007).
13. J. Zhang, K. Sasaki, E. Sutter, R. R. Adzic, *Science* **315**, 220–222 (2007).
14. G. W. Huber, J. W. Shabaker, J. A. Dumesic, *Science* **300**, 2075–2077 (2003).
15. H. Zhang, T. Watanabe, M. Okumura, M. Haruta, N. Toshima, *Nat. Mater.* **11**, 49–52 (2012).
16. B. H. Wu, N. F. Zheng, *Nano Today* **8**, 168–197 (2013).
17. G. A. Somorjai, A. M. Contreras, M. Montano, R. M. Rioux, *Proc. Natl. Acad. Sci. U.S.A.* **103**, 10577–10583 (2006).
18. T. S. Ahmadi, Z. L. Wang, T. C. Green, A. Henglein, M. A. El-Sayed, *Science* **272**, 1924–1926 (1996).
19. M. Cargnello *et al.*, *Science* **341**, 771–773 (2013).
20. See supplementary materials on *Science* Online.
21. B. J. Tan, K. J. Klabunde, P. M. A. Sherwood, *Chem. Mater.* **2**, 186–191 (1990).
22. T. E. Westre *et al.*, *J. Am. Chem. Soc.* **119**, 6297–6314 (1997).
23. M. Gong *et al.*, *J. Am. Chem. Soc.* **135**, 8452–8455 (2013).
24. Y. Han *et al.*, *Chem. Mater.* **20**, 360–363 (2008).
25. M. A. Henderson, *Surf. Sci. Rep.* **46**, 1–308 (2002).
26. L. R. Merte *et al.*, *Science* **336**, 889–893 (2012).
27. Q. Fu, F. Yang, X. Bao, *Acc. Chem. Res.* **46**, 1692–1701 (2013).

Acknowledgments: We appreciate the financial support from the Ministry of Science and Technology of China (2011CB932403) and the National Nature Science Foundation of China (21131005, 20925103, 21373167, 21033006, and 21333008). P.Z. appreciates the funding from Natural Sciences and Engineering Research Council of Canada. We also thank L. S. Zheng, Z. Q. Tian, X. Lu, Y. Wang, and S. C. Lin for helpful discussions, and Shanghai Supercomputer Center (SSC) for providing computational resources. X-ray absorption spectroscopy studies were carried out at the beamline 17C1 of the National Synchrotron Radiation Research Center (NSRRC) in Taiwan.

Supplementary Materials

www.sciencemag.org/content/344/6183/495/suppl/DC1
Materials and Methods
Figs. S1 to S41
Tables S1 to S5
References (*28*–*40*)

24 February 2014; accepted 9 April 2014
10.1126/science.1252553

Manipulation of Discrete Nanostructures by Selective Modulation of Noncovalent Forces

Takahiro Fukino,[1] Hyunho Joo,[1] Yuki Hisada,[1] Maiko Obana,[1] Hiroshi Yamagishi,[1] Takaaki Hikima,[2] Masaki Takata,[2] Norifumi Fujita,[1] Takuzo Aida[1,3]*

Covalent organic synthesis commonly uses the strategy of selective bond cleavage and formation. If a similar approach can be applied stepwisely to noncovalent synthesis, more exotic or challenging nanostructures might become achievable. Here, we report that ferrocene-based tetratopic pyridyl ligands, which can dynamically change their geometry by means of thermal rotation of their cyclopentadienyl rings in solution, assemble with $AgBF_4$ into discrete metal-organic nanotubes with large and uniform diameters. The nanotubes can be cut into metal-organic nanorings through selective attenuation of the inter-nanoring interaction via ferrocene oxidation. The resultant nanorings can be transferred onto inorganic substrates electrostatically or allowed to reassemble to form the original nanotube by the reductive neutralization of their oxidized ferrocene units.

In covalent organic synthesis, bond cleavage and formation are commonly used for the construction of complicated molecular structures. However, for noncovalent architectures, manipulation of the assembled structure is difficult because selective in situ attenuation and/or enhancement of noncovalent forces is hard to achieve. Although a variety of beautiful nanostructures have been noncovalently synthesized (*1*–*6*), even more exotic or hardly accessible self-assembled motifs might become available if there were methods to cut, paste, or merge assembled structures. With stepwise noncovalent synthesis, several exotic nanostructures were recently synthesized by using inorganic clusters (*7*, *8*), block copolymers (*9*–*12*), and small organic molecules (*13*) as assembling components, and some of those nanostructures were indeed shown to break up into thermodynamically inaccessible, low-symmetry pieces (*14*, *15*). However, such selective cutting requires prior stabilization of parent nanostructures by means of partial cross-linking, so that cut pieces are covalently linked.

We report the noncovalent synthesis of a large-diameter metal-organic nanotube, which can be preferentially "cut" into its constituent nanorings with a metal-organic structure. A key for the success in cutting the nanotube was the redox-active ferrocene motif used for our metal-ligating units $\mathbf{FcL_1}$ and $\mathbf{FcL_2}$ (Fig. 1A and figs. S1 to S4). Ligands $\mathbf{FcL_1}$ and $\mathbf{FcL_2}$, derived from 1,1′-bis(4-bromophenyl)-3,3′-bis(4-iodophenyl)ferrocene (*16*), carry a metal-coordinating 4-pyridyl group at each terminus of the four aromatic arms. Hence, they are tetratopic ligands. The triethylene glycol (TEG) side chains are for enhanced solubility of the ligands and better dispersibilities of assembled products in common organic solvents. Because ferrocene derivatives thermally rotate their cyclopentadienyl rings freely in solution (*17*), both ligands have the possibility of changing their tetratopic geometry dynamically (Fig. 1B, top). This "geometrical uncertainty" might give rise to the formation of ill-defined metal-organic structures but might also allow for more scope for modifying the assembled structures. As a metal ion source, we chose $AgBF_4$ (Fig. 1C) because its coordination chemistry with pyridine (Py) derivatives, forming a linear Py(N)–Ag(I)–(N)Py array, has been well established (*18*–*21*). If the ligand adopts an entropically favored noneclipsed geometry in solution, a sheet-like two-dimensional (2D) structure (Fig. 1B, bottom left) would result, in which the ligands are connected together by single Py(N)–Ag(I)–(N)Py bonds. On the other hand, if the ligand adopts an eclipsed geometry, the formation of a doubly bridged coordination polymer (Fig. 1B, bottom center) is expected. The doubly bridged connection should be more stable than the singly bridged one because of its multivalency and can also take an enthalpic gain as a consequence of possible π-stacking and Ag(I)–Ag(I) metallophilic interactions (Fig. 1D) (*18*–*20*). Although linear coordination polymers might be able to cyclize (Fig. 1B, bottom right), such a cyclization event, in general, is entropically disfavored.

Rather than any of the three anticipated products, the assembly of $AgBF_4$ with $\mathbf{FcL_1}$ yielded large-diameter nanotube $\mathbf{FcNT_1}$ (Fig. 1, C and E). As a typical example, an acetonitrile (MeCN) solution of a mixture of $\mathbf{FcL_1}$ (2.0 mM) and two equivalents of $AgBF_4$ (figs. S6, S7, S9, and S11) was allowed to stand at 25°C without stirring. After 4 hours, an aliquot of the reaction mixture was diluted with water, and the resultant suspension, negatively stained with uranyl acetate, was air-dried and then subjected to transmission electron microscopy (TEM). As shown in Fig. 2A, hollow cylinders ($\mathbf{FcNT_1}$) with a uniform "wall center–to–wall center" distance (nanotube diameter)

[1]Department of Chemistry and Biotechnology, School of Engineering, The University of Tokyo, 7-3-1 Hongo, Bunkyo-ku, Tokyo 113-8656, Japan. [2]RIKEN SPring-8 Center, 1-1-1 Kouto, Sayo, Hyogo 679-5198, Japan. [3]RIKEN Center for Emergent Matter Science, 2-1 Hirosawa, Wako, Saitama 351-0198, Japan.

*Corresponding author. E-mail: aida@macro.t.u-tokyo.ac.jp

of 7.5 nm were observed. Most nanotubes thus formed were 50 nm to 2 μm long (fig. S14). Tapping-mode atomic force microscopy (AFM) on highly ordered pyrolytic graphite (HOPG) displayed two-dimensionally bundled cylindrical objects (Fig. 2C), whose thickness (8.5 nm) and cylinder-to-cylinder distance (9.5 nm) are reasonable from the TEM image of a single piece of **FcNT$_1$** (Fig. 2A). Small-angle x-ray scattering (SAXS) analysis of the assembled mixture in MeCN (Fig. 2E) showed a distinct oscillation lasting to a large scattering vector q, indicating that the nanotubes have a uniform diameter (*22*, *23*). The observed SAXS pattern was nicely fitted by the form factor of a hollow cylinder model with a

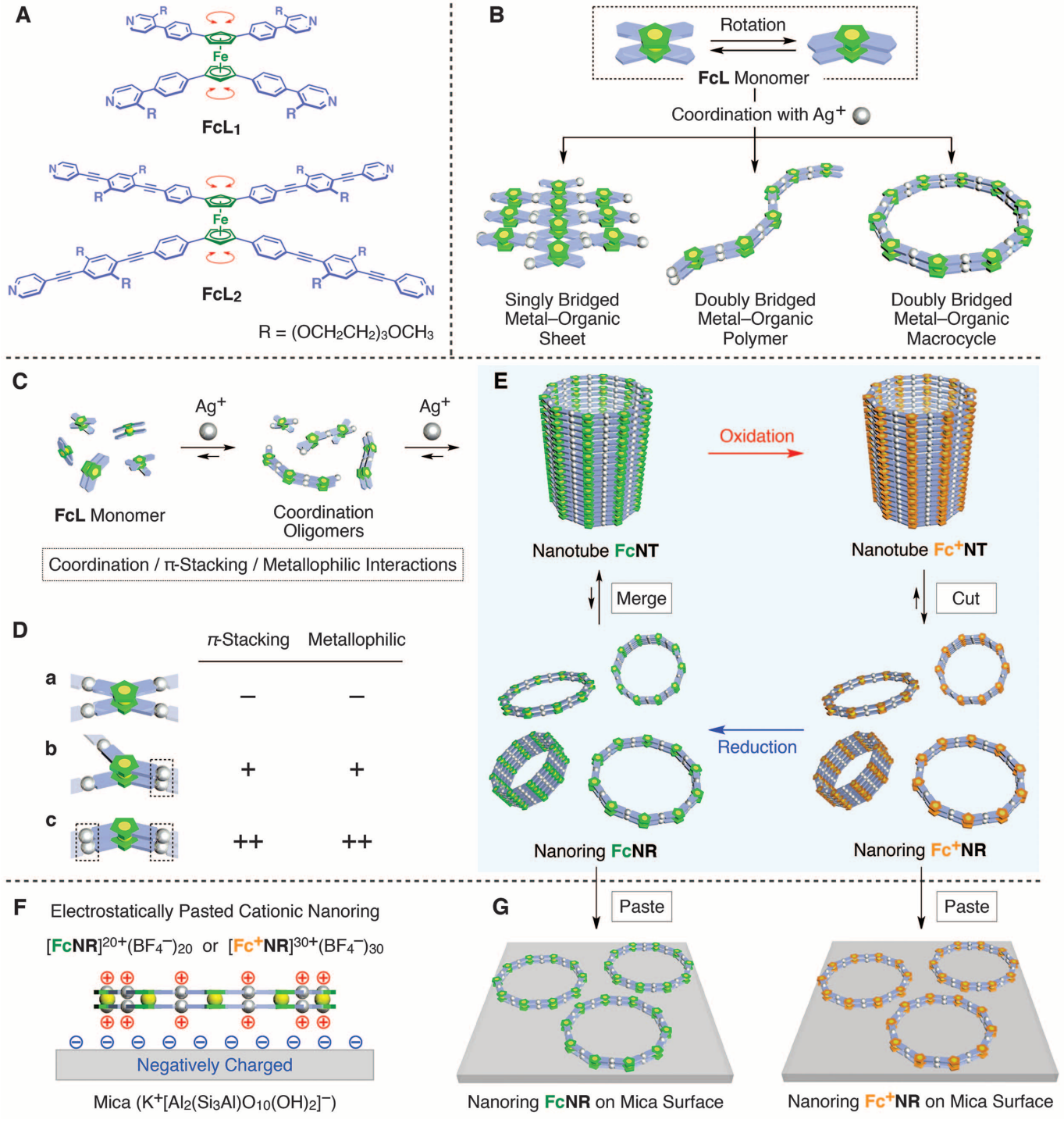


Fig. 1. Formation and manipulation of ferrocene-based metal-organic architectures. (**A**) Schematic molecular structures of ferrocene-based tetratopic double-decker pyridyl ligands **FcL$_1$** and **FcL$_2$**. (**B**) Schematic illustrations of possible noncovalent structures from geometrically uncertain **FcL** upon complexation with Ag(I) ions. Blue, silver, and green/yellow-fused objects represent pyridyl arms, Ag(I) ions, and ferrocene units, respectively. (**C**) A schematic representation of the $AgBF_4$-mediated assembly of **FcL** to form **FcNT**. (**D**) Geometry-dependent possible interactions in **FcL** upon complexation with Ag(I) ions. (**E**) A schematic illustration of the polymerization/depolymerization equilibrium between nanorings **FcNR** and nanotubes **FcNT** biased by redox chemistry of ferrocene. Orange and yellow objects represent oxidized ferrocene units. (**F**) A schematic illustration of how cationic nanoring **FcNR** is electrostatically pasted onto a negatively charged mica (muscovite) surface. (**G**) Schematic illustrations of cationic nanorings **FcNR** (left) and **Fc$^+$NR** (right) immobilized on mica.

diameter of 7.5 nm (*24*). Taking into account the bent angle of **FcL$_1$** (144°), this nanotube diameter allows for the construction of a molecular model with a decagonal cross section (vertex angle; 144°) composed of 10 bent-shaped **FcL$_1$** ligands and 20 Ag(I) ions (Fig. 2G). In this molecular model, the diagonal Fe···Fe and Ag···Ag distances in its cross section are 7.7 and 7.3 nm, respectively, whose mean value of 7.5 nm agrees well with the nanotube diameter actually observed. We also constructed nanotubular molecular models with nonagonal and undecagonal cross sections (fig. S20) and found that their calculated diameters of 6.8 and 8.2 nm, respectively, do not match the observed one. Furthermore, SAXS patterns simulated for the corresponding hollow-cylinder models (fig. S21) were clearly different from that actually observed for **FcNT$_1$**. The Py(N)–Ag(I)–(N)Py coordination angles of the nanotube models with nonagonal and undecagonal cross sections are slightly but definitely deviated from an ideal value of 180°.

Two-dimensional wide-angle x-ray diffractometry (2D WAXD) of oriented films is informative of how assembled components are arranged in the solid state. For the purpose of obtaining such an oriented film from **FcNT$_1$**, we attempted several different methods and found that the use of a magnetic field works well. Typically, one drop of a dispersion of **FcNT$_1$** in MeCN ([**FcL$_1$**] = 4.0 mM) was cast on a sapphire plate and air-dried under a 10-T magnetic field. When the resultant thin film was rotated around its normal axis in polarized optical microscopy, bright and dark images appeared alternately every 45° (fig. S12), indicating that the nanotubes are oriented one-dimensionally

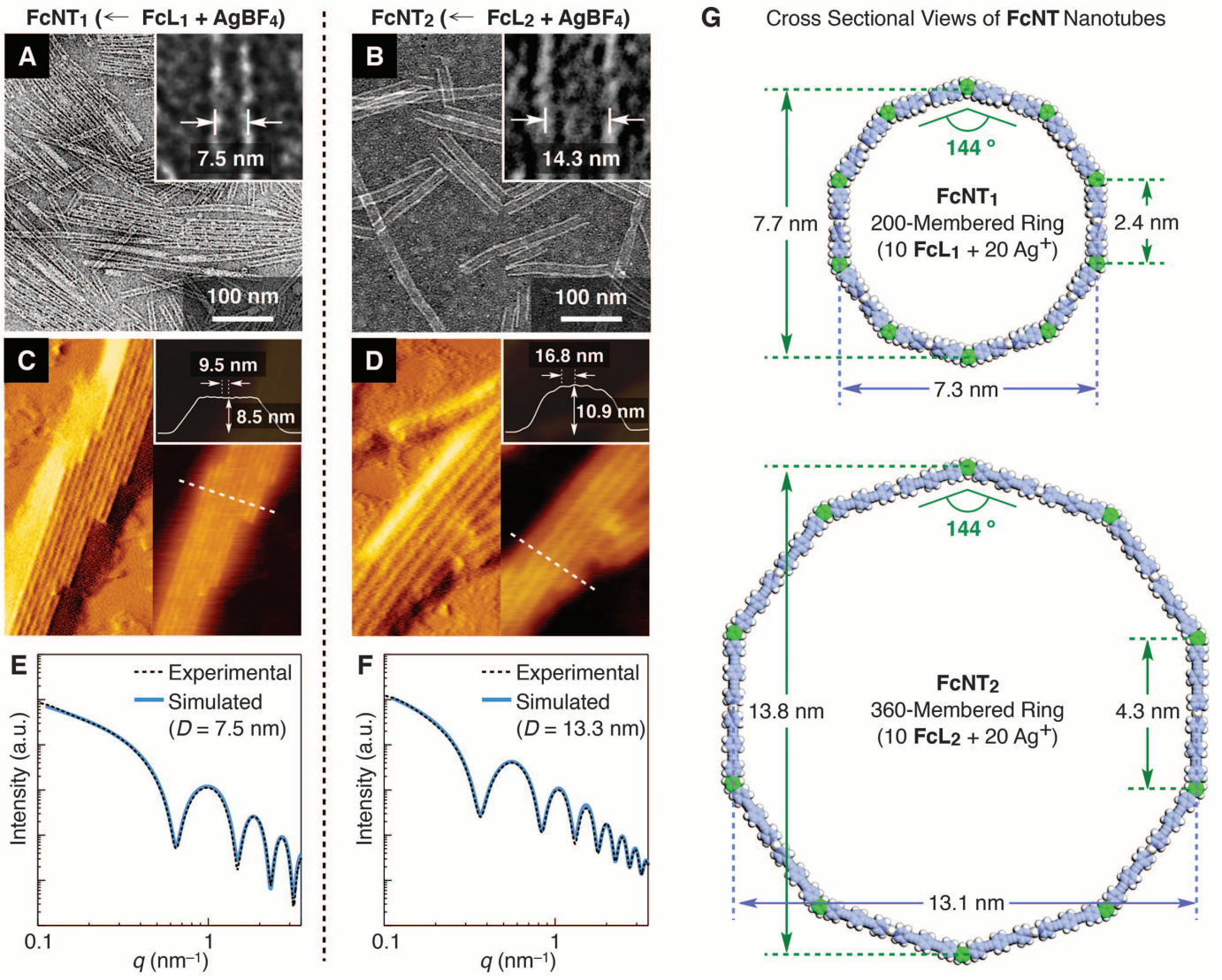


Fig. 2. Metal-organic nanotubes with large and uniform diameters. (**A** and **B**) TEM micrographs of air-dried MeCN/water dispersions of (A) **FcNT$_1$** (prepared in MeCN; [**FcL$_1$**] = 2.0 mM; [$AgBF_4$] = 4.0 mM) and (B) **FcNT$_2$** (prepared in MeCN; [**FcL$_2$**] = 5.0 mM; [$AgBF_4$] = 10 mM). Samples were negatively stained with uranyl acetate. (Insets) Magnified TEM images (35 by 35 nm). Lower-magnification images are provided in fig. S14. (**C** and **D**) Tapping-mode AFM amplitude-error (left) and height (right) images (200 by 400 nm) of air-dried MeCN/CH_2Cl_2 dispersions of (C) **FcNT$_1$** (prepared in MeCN; [**FcL$_1$**] = 2.0 mM; [$AgBF_4$] = 4.0 mM) and (D) **FcNT$_2$** (prepared in MeCN; [**FcL$_2$**] = 5.0 mM; [$AgBF_4$] = 10 mM). Samples were prepared by drop-casting on a HOPG substrate. (Insets) Cross-section profiles along the white broken lines drawn on the height images. (**E** and **F**) Experimental SAXS profiles (black broken curves) of MeCN dispersions of (E) **FcNT$_1$** ([**FcL$_1$**] = 4.0 mM; [$AgBF_4$] = 8.0 mM) and (F) **FcNT$_2$** ([**FcL$_2$**] = 5.0 mM; [$AgBF_4$] = 10 mM) at 25°C and their simulated scattering patterns (blue solid curves) for hollow cylinder models plotted against scattering vector $q = 4\pi\sin\theta/\lambda$. Parameters for the hollow cylinder models were (E) D = 7.5 nm, W = 0.50 nm, and L = 2000 nm and (F) D = 13.3 nm, W = 0.50 nm, and L = 2000 nm, where D, W, and L denote diameter (wall center–to–wall center distance), wall thickness, and cylinder length, respectively. Other simulated SAXS patterns are provided in figs. S21 and S23 to S25. (**G**) Computer-generated molecular (CPK) models for the cross sections of **FcNT$_1$** and **FcNT$_2$** using optimized **FcL** structures from molecular mechanics calculations (figs. S20 and S22). Counter anions and side chains are omitted for clarity.

in the film (Fig. 3A). This film successfully displayed a distinct 2D WAXD pattern (Fig. 3C), featuring a set of diffuse spots along the direction of the applied magnetic field. These spots were indexed as 100, 200, 210, 220, 320, and 330 planes of a 2D hexagonal lattice, with a lattice parameter a = 8.7 nm (Fig. 3D, blue, and table S1). This 2D hexagonal lattice indicates that the nanotubes are oriented perpendicularly to the applied magnetic field and hexagonally packed, with an interpore distance of 8.7 nm. The observed interpore distance is reasonable considering that the nanotubes with a diameter of 7.5 nm are wrapped by their TEG side chains and counterion species. Meanwhile, along the longer axis of **FcNT$_1$** two distinct diffraction arcs (Fig. 3C) with d-spacings of 0.70 and 0.35 nm (Fig. 3D, red) were observed. Taking into account the molecular structure and dimensions of bent-shaped **FcL$_1$**, this diffraction pattern is attributable to a wall structure illustrated in Fig. 3B, in which **FcL$_1$** with an eclipsed geometry stacks up normally on top of each so as to maximize the intermolecular π-stacking and metallophilic interactions. Aromatic rings, in principle, can align parallel to the magnetic field because they exert a large anisotropy in diamagnetic susceptibility (*25*, *26*). Thus, the assembled geometry of the **FcL$_1$** units in **FcNT$_1$** (Fig. 3B) can reasonably explain why the nanotube aligns perpendicularly to the applied magnetic field.

We explored the possibility of assembling longer-armed **FcL$_2$** (Fig. 1A) for constructing a larger-diameter nanotube. If **FcL$_2$** likewise assembles with $AgBF_4$, the cross section of the resultant nanotube (**FcNT$_2$**) would be a 360-membered decagonal ring with an estimated diameter of 13.4 nm (Fig. 2G). According to a method analogous to that for the formation of **FcNT$_1$**, we mixed **FcL$_2$** (5.0 mM) with two equivalents of $AgBF_4$ in MeCN at 25°C. After being allowed to stand for 12 hours without stirring, an aliquot of the assembling mixture was subjected to microscopic [TEM (Fig. 2B and fig. S14) and AFM (Fig. 2D)] and scattering [SAXS (Fig. 2F)] analyses. Analogous to **FcL$_1$** upon coordination with $AgBF_4$, **FcL$_2$** exclusively formed metal-organic nanotubes with large and uniform diameters. Theoretical fitting of the oscillatory SAXS pattern (Fig. 2F) by using a hollow cylinder model indicates that this nanotube again has a uniform diameter of 13.3 nm, which matches the predicted value from the decagonal cross section (Fig. 2G). As shown in Fig. 2B, TEM visualized discrete nanotubes **FcNT$_2$** (stained with uranyl acetate) with a diameter of 14.3 nm. On the other hand, tapping-mode AFM on HOPG displayed 10.9-nm-thick 2D bundles of cylindrical objects (Fig. 2D), which are thinner than the nanotube diameter we evaluated with SAXS (13.3 nm) and TEM (14.3 nm; stained). We consider that this mismatch is caused by the poor mechanical strength of **FcNT$_2$** originating from the thin dimensions of its wall structure.

By analogy with self-assembled organic nanotubes of small molecules (*27*, *28*), we initially thought that the nanotubes from **FcL$_1$** and **FcL$_2$** are composed of their helically stranded doubly bridged metal-organic polymer chains. However, the wall structure in Fig. 3B suggests the possibility that they are composed of uniaxially stacked giant nanorings (Fig. 1B, bottom right). We were inspired by the idea that this nanotube might possibly be cut into its constituent nanorings if an attractive force among the nanorings is selectively attenuated. In general, ferrocene derivatives are reversibly oxidized into their cationic ferrocenium species. Thus, we envisioned that one-electron oxidation of the ferrocene units in the nanotube may preferentially allow electrostatic attenuation of the nanoring-nanoring interaction without breaking the Ag(I)–N(Py) coordination

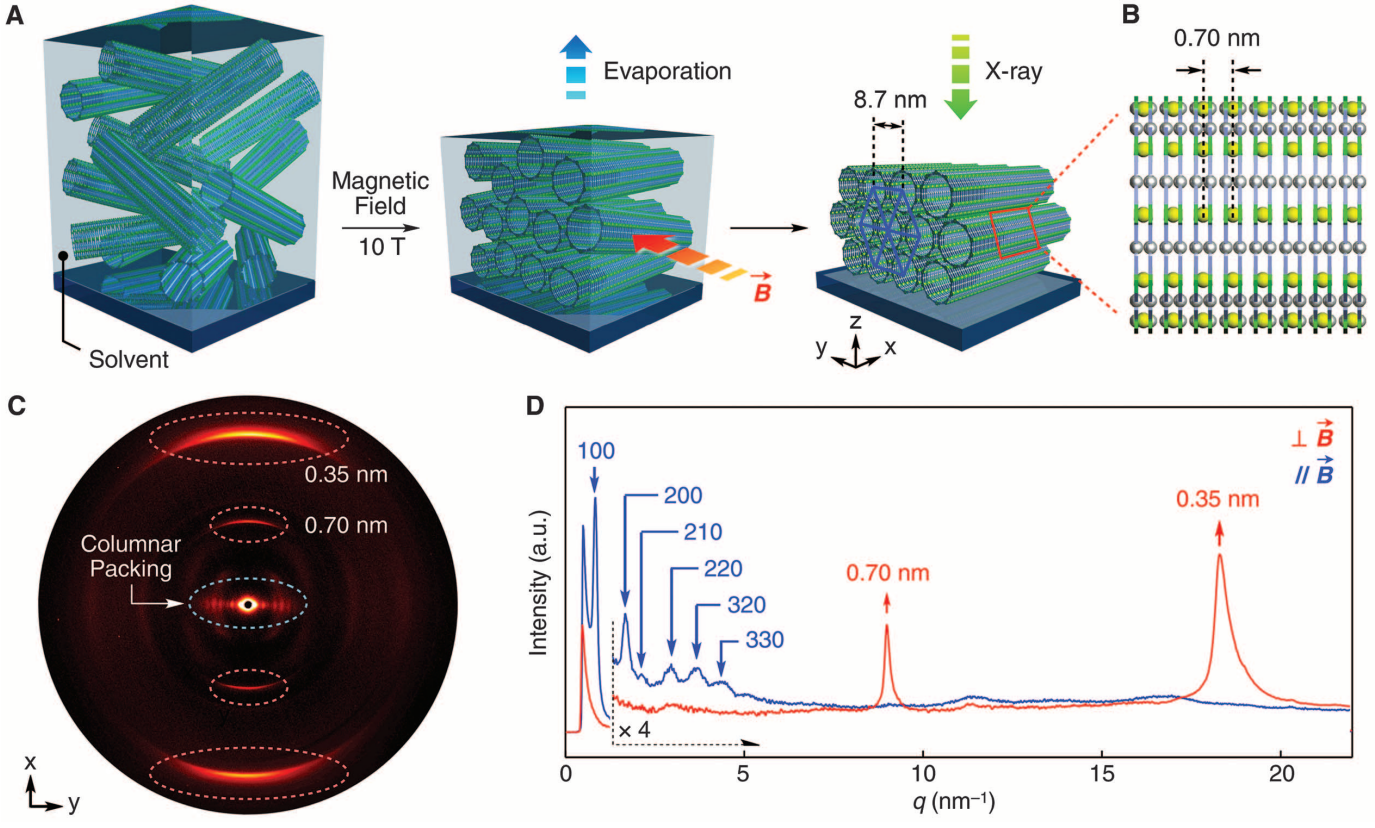


Fig. 3. Magnetic orientation and x-ray diffraction profiles of FcNT$_1$. (**A**) A schematic procedure for the preparation of a film sample of one-dimensionally oriented **FcNT$_1$** nanotubes. A MeCN dispersion of **FcNT$_1$** was air-dried at 25°C in a 10-T magnetic field generated by a superconducting magnet. (**B**) A possible wall structure of **FcNT$_1$**. Blue, silver, green, and yellow objects represent pyridyl arms, Ag(I) ions, cyclopentadienyl rings, and Fe(II) ions, respectively. (**C**) A 2D WAXD pattern of a film sample of one-dimensionally oriented **FcNT$_1$** nanotubes, prepared according to (A) ([**FcL$_1$**] = 4.0 mM; [$AgBF_4$] = 8.0 mM; [TBAOTf] = 8.0 mM). (**D**) Meridional (red) and equatorial (blue) plots from the 2D diffraction pattern shown in (C). Numerical values in blue and red colors denote Miller indices and d spacings, respectively. The oriented **FcNT$_1$** film, prepared by combined use of TBAOTf with $AgBF_4$, was better qualified than that prepared without TBAOTf. The SAXS pattern of **FcNT$_1$** in the presence of TBAOTf was virtually identical to that in the absence of TBAOTf (fig. S26).

bonds. In cyclic voltammetry, ligand **FcL$_1$** itself was oxidized and reduced reversibly under appropriate conditions (fig. S8). So, we attempted to oxidize the ferrocene units in **FcNT$_1$**. Typically, an MeCN dispersion of **FcNT$_1$** was diluted with CH_2Cl_2, and the resultant mixture (CH_2Cl_2/MeCN; 99.5:0.5 v/v, [**FcL$_1$**] = 10 μM) was titrated at 25°C with a mild oxidant such as 1,1′-dichloroferrocenium tetrafluoroborate ($Cl_2Fc^+BF_4^-$) (fig. S10). As shown in Fig. 4A, the reaction mixture displayed a quick absorption spectral change, in which new absorption bands emerged at 282, 344, 385, and 502 nm at the expense of the original absorption bands at 329 and 435 nm. The spectral change subsided when the molar ratio of $Cl_2Fc^+BF_4^-$ to **FcL$_1$** exceeded unity. The observed spectral change profiles indicate that the ferrocene units in **FcNT$_1$** are oxidized with $Cl_2Fc^+BF_4^-$ cleanly and quantitatively. Upon oxidation, **FcNT$_1$** underwent selective disassembly in CH_2Cl_2/MeCN (Fig. 1E). Dynamic light scattering (DLS) analysis upon oxidation showed a substantial drop of the apparent hydrodynamic diameter from 182 to 11 nm (Fig. 4J). We then transferred an aliquot of the oxidized dispersion onto an amorphous carbon film and analyzed the resultant air-dried solid residue by means of TEM. Together with short-chain nanotubes, toroidal objects with a uniform diameter of 7.4 ± 0.4 nm (average of 86 toroids examined) (fig. S16) were visualized (Fig. 4G). This value is close to the diameter of precursor **FcNT$_1$** (7.5 nm) with a decagonal cross section, indicating that the toroidal objects observed in Fig. 4G form as a consequence of the oxidative cutting of nanotubular **FcNT$_1$**.

The nanorings can be stably pasted onto metal oxide substrates (Fig. 1G). For example, when mica was used as the substrate, tapping-mode AFM visualized a large number of uniform-diameter toroidal objects entirely on the mica surface (Fig. 4D). In contrast, when HOPG was used in place of mica, such toroidal objects were hardly observed. Considering that mica is negatively charged, pasting of the polycationic nanorings (30+) onto the mica surface was driven by a strong electrostatic interaction (Fig. 1F). The precursor nanotube is polycationic and potentially interactive with mica electrostatically. However, unless the nanotubes in the dispersion are oxidized before the AFM observation on mica, no toroidal objects but only cylinders are visualized (Fig. 4C). Namely, mica does not induce the nanotube/nanoring conversion. Cross-section AFM analysis (Fig. 4I) showed that single toroids (Fig. 4H), on average (31 toroids examined) (fig. S18), are 0.6 ± 0.2 nm high. This height profile is consistent with the expected molecular thickness of **FcL$_1$** with a double-decker architecture. The decagonal nanoring **Fc$^+$NR$_1$** thus obtained is a 200-membered gigantic macrocycle consisting of 10 oxidized **FcL$_1$** ligands and 20 Ag (I) ions (Fig. 1E).

We investigated what happens to nanoring **Fc$^+$NR$_1$** if its oxidized ferrocene units are neutralized. When a reducing agent such as bis(pentamethylcyclopentadienyl)iron(II) (Fc*) (fig. S10) was added to an oxidized dispersion of **FcNT$_1$** in CH_2Cl_2/MeCN, a backward absorption spectral change immediately took place (Fig. 4B). Thus, the oxidized ferrocene units in the assembly are

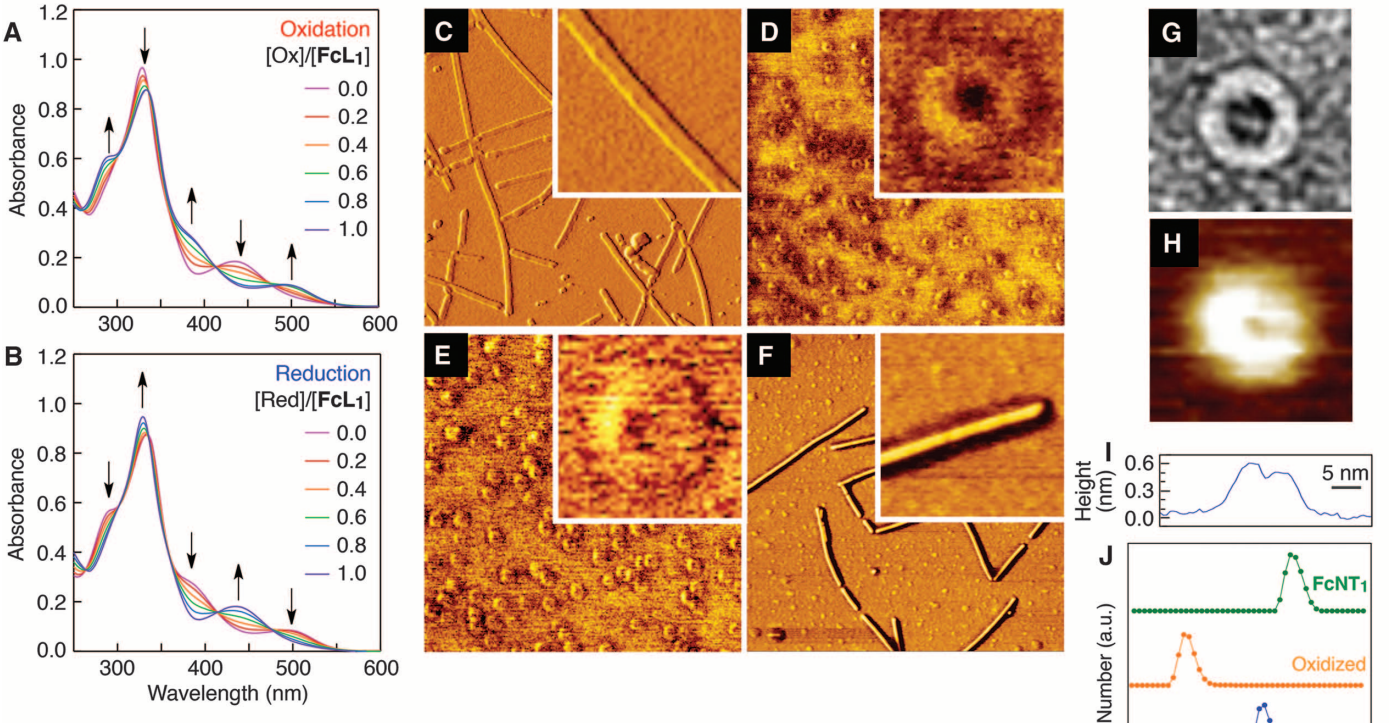


Fig. 4. Oxidative cutting of FcNT$_1$ and reductive reassembly of resultant Fc$^+$NR$_1$. (**A** and **B**) Electronic absorption spectra at 23°C of (A) a CH_2Cl_2/MeCN (99.5:0.5 v/v) dispersion of **FcNT$_1$** ([**FcL$_1$**] = 10 μM; [$AgBF_4$] = 20 μM) upon titration with oxidant $Cl_2Fc^+BF_4^-$ (mole ratio to constituent **FcL$_1$** = 0 to 1) and (B) those of the resultant dispersion of **Fc$^+$NT$_1$** upon titration with reductant bis(pentamethylcyclopentadienyl)iron(II) (Fc*) (mole ratio to constituent **Fc$^+$L$_1$** = 0 to 1). Arrows indicate the directions of spectral changes. Contributions of the absorption bands due to added reagents (250 to 400 nm) were subtracted for clarity. (**C** to **F**) Tapping-mode AFM phase images of an air-dried CH_2Cl_2/MeCN (99.5:0.5 v/v) dispersion of **FcNT$_1$** ([**FcL$_1$**] = 10 μM); (C) as-formed (2 by 2 μm; inset, 400 by 400 nm); (D) in 5 min after mixing with oxidant $Cl_2Fc^+BF_4^-$ (1 equivalent to constituent **FcL$_1$**) (**Fc$^+$NR$_1$**; 500 by 500 nm; inset, 30 by 30 nm); and (E) in 30 min (**FcNR$_1$**; 500 by 500 nm; inset, 40 by 40 nm) and (F) 28 hours (**FcNT$_1$** reconstructed; 2 by 2 μm; inset, 300 by 300 nm) after subsequent mixing with reductant Fc* (1 equivalent to constituent **Fc$^+$L$_1$**). Samples were spin-coated onto a mica substrate. Lower-magnification images of (D) are provided in fig. S17. (**G** to **I**) TEM and tapping-mode AFM images of nanoring **Fc$^+$NR$_1$**. For sample preparation, a CH_2Cl_2/MeCN (99.5:0.5 v/v) dispersion of **Fc$^+$NR$_1$** [described for (D)] was drop-cast and spin-coated for TEM and AFM observations, respectively. (G) A TEM micrograph (20 by 20 nm; selected from fig. S16) of **Fc$^+$NR$_1$** negatively stained with uranyl acetate. (H) A high-resolution tapping-mode AFM height image (20 by 20 nm) of **Fc$^+$NR$_1$** on a mica substrate and (I) its cross-section profile. Lower-magnification images of (G) and (H) are provided in figs. S15 and S18, respectively. (**J**) DLS profiles at 20°C of CH_2Cl_2/MeCN (95:5 v/v) dispersions of **FcNT$_1$** ([**FcL$_1$**] = 20 μM) in 12 hours after preparation (green), 2 hours after oxidation with $Cl_2Fc^+BF_4^-$ (1 equivalent to constituent **FcL$_1$**) (orange), and 48 hours after subsequent reduction with Fc* (1 equivalent to constituent **Fc$^+$L$_1$**) (blue).

rapidly and cleanly neutralized. The reaction mixture obtained after the incubation for 48 hours at 25°C showed in DLS a marked increase in apparent hydrodynamic diameter from 11 to 82 nm (Fig. 4J). Therefore, we carried out tapping-mode AFM of an aliquot of the reaction mixture on mica and found that long cylindrical objects are reconstructed (Fig. 4F). These observations indicate that reduced nanorings **FcNR$_1$** are equilibrated with their uniaxially "merged" nanotubular assembly of **FcNT$_1$** (Fig. 1E). The uniaxial merging event of **FcNR$_1$** appears rather sluggish, certainly due to its large entropic loss. When the reaction mixture, incubated for 0.5 hours after the complete reduction of the ferrocene units of **Fc$^+$NR$_1$**, was air-dried on mica and analyzed with tapping-mode AFM, only toroidal objects were visualized (Fig. 4E). Analogous to the case of **FcNT$_1$**, we attempted oxidative cutting of larger-diameter **FcNT$_2$** by using $Cl_2Fc^+BF_4^-$. However, a mixture of ill-defined structures resulted. We consider that **FcNT$_2$** cannot satisfy a requisite for the selective attenuation of noncovalent forces, most likely because of an insufficient structural robustness originating from its large and thin-wall dimensions.

Considering a possible entropic penalty for the formation of giant nanorings through the direct self-assembly of small molecules, we suppose that the Ag(I)–mediated nanotubular assembly of **FcL** (Fig. 1C) probably occurs stochastically, without preceding formation of the corresponding nanorings (**FcNR**). In the crystalline state, tetraarylferrocene derivatives are known to adopt an eclipsed geometry (*29*, *30*). By means of ^{1}H nuclear magnetic resonance (NMR) spectroscopy in CD_3CN, we confirmed that the geometry of **FcL$_1$** in solution is more biased to the eclipsed form at lower temperatures. However, even at –40°C its ^{1}H NMR spectral feature was still dynamic (fig. S5). Meanwhile, when **FcL** is bound to Ag(I) ions a metallophilic interaction may occur, so that its tendency to form the eclipsed geometry is enhanced. The resultant Ag(I)–bound bent-shaped ligands are connected together to form a doubly bridged metal-organic oligomer (Fig. 1B, bottom center). Such oligomers may start to stack up bilaterally via amplified π-stacking and metallophilic interactions. Consequently, curvy sheet-like intermediates would form and grow up stochastically to furnish nanotubular **FcNT$_1$** at the final stage. In regard to the stochastic assembling mechanism thus proposed, neither nanotubes nor nanorings were detected with AFM when oxidized **FcL$_1$** (**Fc$^+$L$_1$**) with an attenuated stacking ability was likewise treated with $AgBF_4$ (fig. S19). As highlighted in the present work, 200-membered metal-organic decagonal nanorings (**Fc$^+$NR$_1$**), obtained by oxidative cutting of the nanotube, are unlikely to form directly with conventional self-assembling protocols. Together with the results of electrostatic pasting (Fig. 1G) and reductive merging (Fig. 1E) of **Fc$^+$NR$_1$**, we believe that the idea of stepwise noncovalent synthesis—involving cutting, pasting, and merging operations—may open additional routes for nanoscale synthesis.

References and Notes

1. J.-M. Lehn, *Supramolecular Chemistry* (Wiley-VCH, Weinheim, ed. 1, 1995).
2. L. J. Prins, D. N. Reinhoudt, P. Timmerman, *Angew. Chem. Int. Ed.* **40**, 2382–2426 (2001).
3. R. Chakrabarty, P. S. Mukherjee, P. J. Stang, *Chem. Rev.* **111**, 6810–6918 (2011).
4. H. Furukawa, K. E. Cordova, M. O'Keeffe, O. M. Yaghi, *Science* **341**, 1230444 (2013).
5. Q.-F. Sun *et al.*, *Science* **328**, 1144–1147 (2010).
6. T. Aida, E. W. Meijer, S. I. Stupp, *Science* **335**, 813–817 (2012).
7. A. Müller, S. Q. N. Shah, H. Bögge, M. Schmidtmann, *Nature* **397**, 48–50 (1999).
8. T. Liu *et al.*, *Science* **331**, 1590–1592 (2011).
9. X. Wang *et al.*, *Science* **317**, 644–647 (2007).
10. T. Gädt, N. S. Ieong, G. Cambridge, M. A. Winnik, I. Manners, *Nat. Mater.* **8**, 144–150 (2009).
11. A. H. Gröschel *et al.*, *Nature* **503**, 247–251 (2013).
12. A. H. Gröschel *et al.*, *Nat. Commun.* **3**, 710 (2012).
13. W. Zhang *et al.*, *Science* **334**, 340–343 (2011).
14. R. Erhardt *et al.*, *Macromolecules* **34**, 1069–1075 (2001).
15. P. A. Rupar, L. Chabanne, M. A. Winnik, I. Manners, *Science* **337**, 559–562 (2012).
16. T. Muraoka, K. Kinbara, T. Aida, *Nature* **440**, 512–515 (2006).
17. E. W. Abel, N. J. Long, K. G. Orrell, A. G. Osborne, V. Šik, *J. Organomet. Chem.* **403**, 195–208 (1991).
18. A. N. Khlobystov *et al.*, *Coord. Chem. Rev.* **222**, 155–192 (2001).
19. D. Braga *et al.*, *Chem. Commun. (Camb.)* **10**, 1080–1081 (2002).
20. C. Y. Chen, J. Y. Zeng, H. M. Lee, *Inorg. Chim. Acta* **360**, 21–30 (2007).
21. S. Shin *et al.*, *J. Am. Chem. Soc.* **135**, 2156–2159 (2013).
22. C. Tarabout *et al.*, *Proc. Natl. Acad. Sci. U.S.A.* **108**, 7679–7684 (2011).
23. G. Oster, D. P. Riley, *Acta Crystallogr.* **5**, 272–276 (1952).
24. Materials and methods are available as supplementary materials on *Science* Online.
25. I. O. Shklyarevskiy *et al.*, *Langmuir* **21**, 2108–2112 (2005).
26. W. H. de Jeu, in *Physical Properties of Liquid Crystalline Materials* (Gordon and Breach, New York, 1980), pp. 24–33.
27. W. Jin *et al.*, *Proc. Natl. Acad. Sci. U.S.A.* **102**, 10801–10806 (2005).
28. D. M. Eisele *et al.*, *Nat. Chem.* **4**, 655–662 (2012).
29. H. Schumann, A. Lentz, R. Weimann, *J. Organomet. Chem.* **487**, 245–252 (1995).
30. T. Muraoka, K. Kinbara, Y. Kobayashi, T. Aida, *J. Am. Chem. Soc.* **125**, 5612–5613 (2003).

Acknowledgments: T.F. thanks the Japan Society for the Promotion of Science Young Scientist Fellowship (23•9024). We acknowledge Grant-in-Aid for Specially Promoted Research on "Physically Perturbed Assembly for Tailoring High-Performance Soft Materials with Controlled Macroscopic Structural Anisotropy" (25000005) and for Scientific Research on Innovative Areas "Coordination Programming" (21108012). The synchrotron x-ray diffraction experiments were performed at the BL45XU in the SPring-8 with the approval of the RIKEN SPring-8 Center (proposal 20130079).

Supplementary Materials

www.sciencemag.org/content/344/6183/499/suppl/DC1
Materials and Methods
Figs. S1 to S26
Tables S1 to S3
References (*31*–*41*)

11 February 2014; accepted 26 March 2014
Published online 10 April 2014;
10.1126/science.1252120

Vibrationally Promoted Dissociation of Water on Ni(111)

P. Morten Hundt,[1]† Bin Jiang,[2]† Maarten E. van Reijzen,[1] Hua Guo,[2]* Rainer D. Beck[1]*

Water dissociation on transition-metal catalysts is an important step in steam reforming and the water-gas shift reaction. To probe the effect of translational and vibrational activation on this important heterogeneous reaction, we performed state-resolved gas/surface reactivity measurements for the dissociative chemisorption of D_2O on Ni(111), using molecular beam techniques. The reaction occurs via a direct pathway, because both the translational and vibrational energies promote the dissociation. The experimentally measured initial sticking probabilities were used to calibrate a first-principles potential energy surface based on density functional theory. Quantum dynamical calculations on the scaled potential energy surface reproduced the experimental results semiquantitatively. The larger increase of the dissociation probability by vibrational excitation than by translation per unit of energy is consistent with a late barrier along the O-D stretch reaction coordinate.

Water dissociation on transition-metal surfaces (*1*, *2*) is an essential part in the steam reforming process used on a large scale by the chemical industry to convert natural gas [methane (CH_4)] to H. In the first step, CH_4 and water vapor (steam) react on a Ni catalyst to produce a mixture of CO and H_2 (syngas). The CO is reacted again with water, and this water-gas shift reaction produces additional H_2 and CO_2. The H_2 is used as a clean fuel and for the industrial production of important chemicals such as ammonia and methanol. In both reactions, the dissociative chemisorption of H_2O on the catalyst surface to form chemisorbed OH(ads) and H(ads) is an essential fundamental step, so an in-depth understanding of the adsorption and dissociation of water on a transition-metal catalyst surface is highly desirable. Although the dissociative chemisorption of CH_4 has been extensively studied by quantum-state–resolved experiments (*3*–*9*), until now, few experimental studies of water dissociation on transition metals have been available (*2*). We report a quantum-state–resolved study for D_2O dissociative chemisorption on Ni(111), jointly with a quantum-dynamical

[1]Laboratoire de Chimie Physique Moléculaire, Ecole Polytechnique Fédérale de Lausanne, 1015 Lausanne, Switzerland. [2]Department of Chemistry and Chemical Biology, University of New Mexico, Albuquerque, NM 87131, USA.

*Corresponding author. E-mail: hguo@unm.edu (H.G.); rainer.beck@epfl.ch (R.D.B.)
†These authors contributed equally to this work.

investigation on a density functional theory (DFT)–based global potential energy surface (PES), with the aim of progressing toward a predictive understanding of this important reaction.

Dissociative chemisorption of both water and CH_4 on Ni surfaces occurs via a direct mechanism in which the incident molecules either dissociate on the surface on initial impact or are scattered back to the gas phase intact. For CH_4, earlier experiments have shown that the dissociative chemisorption is activated by both the translational and vibrational energy of the incident molecule [(*3*) and references therein]. Quantum-state–resolved experiments for CH_4 have later revealed several signatures of nonstatistical reaction dynamics. The dissociation reaction of several isotopologues of CH_4 on Ni and Pt surfaces was observed to be both mode-specific (*4*–*6*) and bond-selective (*7*, *8*). Furthermore, the vibrational efficacy $\eta(v_i)$, which compares reactivity enhancement for vibrational excitation of a specific quantum state v_i with the effect of increasing the incident translational energy by an equivalent amount, took values both above and below unity, depending on the vibrational state of CH_4 and the type of metal surface. Finally, experiments with laser-aligned incident CH_4 molecules uncovered a hitherto unexplained steric effect in the CH_4 reactivity on several different Ni surfaces (*9*, *10*). All these observations show the inadequacy of statistical models (*11*, *12*) for a realistic microscopic description of CH_4 chemisorption and provide stringent tests for classical and/or quantum-dynamics calculations on multidimensional PESs (*13*–*16*).

Recently, theoretical studies of water dissociative chemisorption have predicted strong mode specificity (*17*), bond selectivity (*18*), and steric effects (*19*, *20*) for water on Cu(111) and Ni(111) (*21*). In addition, experiments have demonstrated mode specificity and bond selectivity in bimolecular reactions of water with H (*22*–*24*) and Cl atoms (*25*) in the gas phase. The strong vibrational enhancement in these gas-phase processes has been attributed, according to Polanyi's rules (*26*), to the "late" barrier along the reaction path, a characteristic that is shared by the dissociative chemisorption of both CH_4 and water. Challenged by the theoretical predictions, we investigated the effects of translational and vibrational excitation on the dissociation probability of water on the Ni(111) surface. We used single- and double-resonance excitation by infrared (IR) laser pumping in a molecular beam (*27*) to prepare surface-incident D_2O selectively either with one or two vibrational quanta of antisymmetric O-D stretch excitation (ν_3 or $2\nu_3$) in order to measure its state-resolved dissociation probability on a Ni(111) single-crystal surface. Such a selective quantum-state preparation by population inversion only became feasible recently for D_2O because of the availability of tunable high-power IR laser sources that emit light in the O-D stretching region. To better understand the experimental results, a six-dimensional (6D) PES was developed based on a large number of DFT points on Ni(111), and the dissociative chemisorption dynamics of D_2O were investigated with a 6D quantum wave-packet method. As demonstrated below, the synergistic interplay between state-resolved experiment and high-level quantum theory leads to a much deeper understanding of this prototypical surface reaction.

Details of the experimental setup have been described in previous publications (*28*, *29*). Briefly, a continuous molecular beam of D_2O was generated by skimming a supersonic expansion of a gas mixture of 3% D_2O in He obtained by bubbling He gas through a reservoir containing liquid D_2O. D_2O was chosen over H_2O because our available IR sources only allowed the preparation of O-D stretching states. The molecular beam speed was controlled by variation of the nozzle temperature and was measured using a fast chopper wheel together with a quadrupole mass spectrometer located in the molecular beam path. The surface-incident D_2O molecules were prepared with either one or two quanta of antisymmetric O-D stretch vibration (ν_3) by rapid adiabatic passage (*27*) with IR radiation from two optical parametric oscillators for either single- or double-resonance excitation. We measured state-resolved reaction probabilities on a clean Ni(111) surface [surface temperature ($T_{surface}$) = 300 K] for the dissociative chemisorption of D_2O according to $D_2O(v,J,E_t) \rightarrow OD(ads) + D(ads)$ (v and J designate the vibrational and rotational quantum states of the D_2O reactant) as a function of incident translational energy (E_t) for the ν_3 and $2\nu_3$ states, as well as without laser excitation by quantifying the coverage of the surface-bound OD(ads) product with Auger electron spectroscopy (AES) resulting from a known dose of incident D_2O [additional experimental details can be found in the supplementary materials (SM) (*30*)].

For a theoretical description of water dissociation on Ni(111), we developed a 6D flat rigid surface model (Fig. 1), following our earlier work on Cu(111) (*17*). The 6D global PES was constructed from ~22,000 spin-polarized DFT points on a three-layer slab with a 2 × 2 unit cell, using the PW91 functional (*31*) implemented in VASP (the Vienna Ab-initio Simulation Package) (*32*, *33*). These points were fit using the permutation-invariant polynomial approach (*34*), with a root mean square deviation of 2.0 kJ/mol for the dynamically relevant region (points below 145 kJ/mol). The resulting PES reproduces the geometries, energies, and frequencies for stationary points obtained in the DFT calculations quite well and are also consistent with earlier electronic structure calculations (*30*). The quantum dynamics were represented in Jacobi coordinates (shown in Fig. 1) by a 6D Chebyshev real wave-packet method (*20*, *35*). Specifically, an initial wave packet was launched for a rovibrational state of reactant (D_2O) above the surface and propagated on the PES using the Chebyshev three-term recursion formula. The total reaction probability was computed with a flux method on a dividing surface placed beyond the saddle point. The effects of surface corrugation, impact site, and lattice motion are approximately treated based on the approaches of Jackson and co-workers (*14*, *36*, *37*). A more detailed description of the theoretical calculations is given in the SM (*30*).

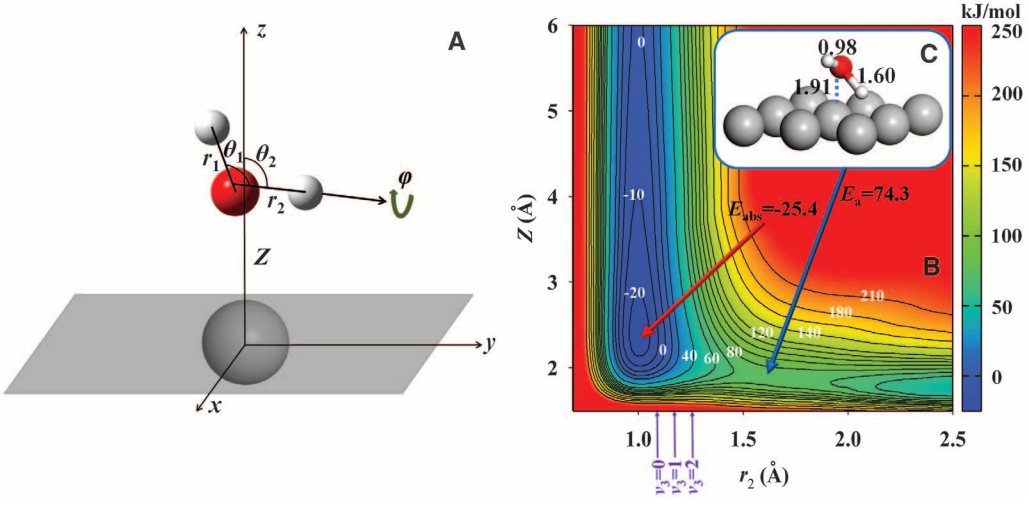


Fig. 1. Potential energy surface. (**A**) Definition of the six Jacobi coordinates used in the theoretical model, (**B**) Contour plot of the 6D scaled PES as a function of Z and r_2, with all other coordinates optimized. The adsorption well and transition state are indicated in red and blue arrows with the corresponding energies. (**C**) The geometry of the transition state in the Jacobi coordinates r_1 = 0.98 Å, r_2 = 1.60 Å, Z = 1.91 Å (where r_1 is the bond length of the nondissociative OD bond, r_2 is the distance between the centers of mass of OD and D, and Z is the distance between the D_2O center of mass and the surface). The contours are in kilojoules per mole relative to the D_2O in the gas phase, and the outer turning points of the O-D bond for ν_3 = 0, 1, and 2 are indicated by purple arrows.

Figure 2 shows a comparison of the AES-detected OD coverage on the Ni(111) surface resulting from two D_2O depositions at E_t = 36.5 kJ/mol with and without laser excitation of the incident molecular beam. For the laser-off deposition, the absence of substantial OD coverage in the region where the molecular beam struck the Ni(111) surface (Fig. 2, right, labeled laser-off) shows that 36.5 kJ/mol of translational energy normal to the surface was insufficient for the incident D_2O to overcome the reaction barrier and to dissociate to produce OD(ads). For the laser-on deposition (Fig. 2, left, labeled laser-on), rovibrational excitation of 30% of the incident D_2O in the molecular beam with two quanta of the antisymmetric O-D stretch normal mode ($2\nu_3$) added 66.8 kJ/mol of vibrational energy to the reactant molecules and led to dissociation of 0.05% of the incident vibrationally excited D_2O ($2\nu_3$) as detected by the AES signal. The data presented in Fig. 2 show that water dissociation on Ni(111) is strongly activated by vibrational energy, which is consistent with the results of earlier simulations for the H_2O/Cu(111) system (*17*).

In order to probe for translational activation and to compare the effect of translational and vibrational energy, we performed reactivity measurements at several incident energies E_t in the range of 36.5 to 75 kJ/mol for ν_3 and $2\nu_3$ excitation of the incident D_2O and in the range of 55 to 75 kJ/mol without laser excitation. The average E_t of the molecular beam was controlled by changing the temperature of the expansion nozzle T_n in steps of 100 K from 373 to 773 K. Figure 3 shows a summary of our state-resolved D_2O reactivity measurements on a Ni(111) surface at a surface temperature of 300 K. Because we varied E_t by increasing T_n, and vibrational relaxation in a supersonic expansion is inefficient, the measured laser-off D_2O reactivity contained an unknown contribution from the dissociation of vibrationally excited D_2O from the hot nozzle. Thus, the measured laser-off reactivity can only be taken as an upper limit to the $v = 0$ reactivity, which, depending on the fraction of vibrationally excited D_2O and the vibrational efficacies, may be substantially lower. The experimental state-resolved ν_3 and $2\nu_3$ reactivities were not affected by the effect of heating the expansion nozzle, because they were obtained from the difference between laser-on and laser-off measurements, where the contributions of thermally excited vibrations cancel.

For comparison of the effect of translational and vibrational excitation, we parameterized the state-resolved data by fitting S-shaped reactivity curves, initially suggested by Luntz (*38*), to each of the ν_3 and $2\nu_3$ data sets. For the laser-off data, which represent an average of different vibrational states populated at a given T_n, the same analysis is not suitable. These S-shaped curves are based on the assumption of a Gaussian distribution of reaction barrier heights of width W about an average barrier E_0. The width of the barrier reflects the combined effect of different initial orientations of the incident D_2O, the distribution of impact sites of D_2O within the unit cell of the Ni(111) surface lattice, and the distribution of thermal surface atom displacement along the surface normal. The fitted curves are represented by the dotted lines in Fig. 3. The horizontal shift of 37 kJ/mol between the state-resolved S-shaped reactivity curves for ν_3 and $2\nu_3$ excitation along the E_t axis can be used to compare the effects of translational and vibrational energy on the reaction probability. The ratio of the translational energy shift to the vibrational energy of 33.2 kJ/mol gives the vibrational efficacy $\eta(2\nu_3\text{-}\nu_3)$. For the second quantum of ν_3 excitation, the efficacy is 1.1 ± 0.05, indicating that vibrational excitation from ν_3 to $2\nu_3$ is more efficient in promoting reactivity than is adding an equal amount of translational energy to the incident molecule. Because the efficacy for the second quantum of ν_3 excitation is expected to be lower than that of the first (*3*), we would expect $\eta(\nu_3)$ to be larger than 1.1, although we cannot determine it directly from the laser-off data for the reasons stated above. Given such a large effect of vibrational energy on the reactivity, we can conclude that the laser-off reactivity is dominated by thermal vibrationally excited molecules, which is consistent with the theoretical results presented below.

The state-resolved reactivity data for ν_3 and $2\nu_3$ excitation reported here provide stringent tests for theoretical models. The 6D model used here contains all important degrees of freedom for water dissociative chemisorption, including all three vibrational modes of D_2O. Although the theoretical sticking probabilities calculated on the PW91 PES display appreciable mode specificity, they were systematically larger than the experimental results. The discrepancy was attributed to the underestimation of the barrier height (64.6 kJ/mol relative to free H_2O) by the PW91 functional. Indeed, a higher (99.1 kJ/mol) barrier was found with

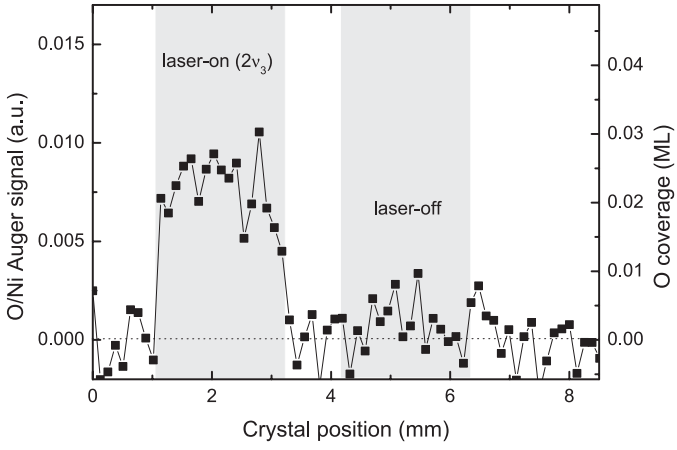


Fig. 2. Product detection. Auger-detected surface-bound OD after depositions of a molecular beam of D_2O (36.5 kJ/mol) with and without selective rovibrational excitation. $2\nu_3$ excitation is achieved by a sequential double-resonance pumping of a ν_3-$R_{11}(1)$ transition, followed by an $R_{12}(2)$ transition from ν_3 to $2\nu_3$. The surface temperature was 300 K. a.u., arbitrary units; ML, monolayer units.

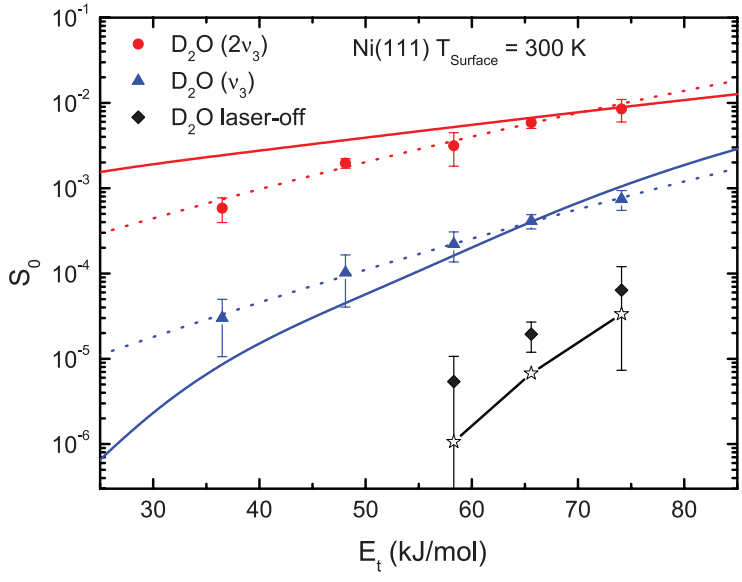


Fig. 3. State-resolved initial dissociation probabilities of D_2O on a Ni(111) surface. The solid points represent the experimental data, and the dotted lines are fitted S-shaped reactivity curves [see text and SM (*30*)]. Solid lines are the results of quantum dynamics calculations on the 6D scaled PES, and the open stars are calculated laser-off reactivities, including the thermal vibrational excitation for the nozzle temperature used in each experiment.

the revised Perdew-Burke-Ernzerhof (RPBE) functional (*39*). Similar observations have been reported by Kroes and co-workers on H_2 dissociative chemisorption, and these authors have corrected the PES using a combination of PW91 and RPBE functionals (*40*, *41*). We elected to scale the PW91 PES with a simple function of the distance (Z) between D_2O and the surface $\{V_{scaled} = V \times [1 + \exp(-\lambda Z)]$, with scaling parameter $\lambda = 1$ Å$^{-1}\}$, which resulted in a barrier of 74.3 kJ/mol, between the values predicted by the PW91 and RPBE functionals. The resulting PES shown in Fig. 1 features a saddle point with an elongated O-D bond (1.54 Å versus 0.97 Å for the equilibrium in D_2O), similar to that for H_2O on Cu(111) (*17*).

The simulations of the laser-off data were done with nozzle temperatures of 573, 673, and 773 K, at which several vibrational states of D_2O are significantly populated. The calculated sticking probabilities are thus a Boltzmann average of the contributions from these states. This approach has been used previously by Kroes and co-workers in their studies for H_2 dissociative chemisorption processes (*42*). For the simulation of state-resolved experiments, only the specific vibrational state (ν_3 or $2\nu_3$) prepared by the IR laser is considered. The calculated sticking probabilities obtained on the scaled PES are compared with the experimental results in Fig. 3, reproducing both the promotional effects for the translational and vibrational modes. Quantitatively, the calculated sticking probabilities for the ν_3 and $2\nu_3$ excited D_2O are in good agreement with the experimental counterparts between 55 and 75 kJ/mol, but theory overestimates and underestimates the vibrational enhancement in the low- and high-energy wings, respectively. The discrepancies can probably be attributed to the approximately treated degrees of freedom and uncertainties in the DFT functionals. We emphasize that the experiment-theory agreement underscores the importance of experimental calibration of the theoretical model.

As discussed above, the experimental data alone are insufficient to provide a reliable ν_3 efficacy $\eta(\nu_3)$. Fortunately, theory complements experiment by providing estimates of the vibrational efficacies for all vibrational states. As shown in the SM (*30*), all three vibrational modes of D_2O promote the reaction more effectively than translation. As a result, even when the thermal populations of the excited vibrational states of D_2O are relatively small, the laser-off reactivity is dominated by these highly reactive states. Similar vibrational efficacies have also been found for the gas-phase reaction between H and stretch-excited H_2O, and the rate constants were likewise dominated by excited vibrational states (*43*).

The theoretical estimate of the vibrational efficacy $\eta(\nu_3)$ for the antisymmetric stretch is about 1.65 to 1.78, substantially larger than vibrational efficacies observed in CH_4 dissociative chemisorption on Ni surfaces, which fall in the range of 0.5 to 1.4 (*3*–*6*). The vibrational enhancement of the reactivity can be understood by the recently proposed sudden vector projection (SVP) model, which assumes that the reaction occurs in the sudden limit, and the enhancement of reactivity by a reactant mode reflects its coupling with the reaction coordinate at the transition state (*35*, *44*). Such coupling can be estimated by the projection of the reactant mode vector onto the reaction coordinate vector at the transition state. The high vibrational efficacy for D_2O dissociative chemisorption can be rationalized by the fact that the SVP projection for the antisymmetric stretching mode (0.65) is substantially larger than that for the translation (0.34). As discussed elsewhere (*44*), the stronger coupling between the reactant vibration and the reaction coordinate is related to the late barrier and thus is consistent with Polanyi's rules (*26*). Indeed, it is shown in Fig. 1 that the classical outer turning point of the $\nu_3 = 0$, 1, or 2 state progressively approaches the saddle point, allowing better access of the transition state.

There has been substantial progress in understanding dissociative chemisorption of diatomic molecules on metal surfaces in recent years (*45*). The theory-experiment agreement in these systems has reached an unprecedented level, thanks to the chemical accuracy (<1 kcal/mol) of the PESs (*41*). However, it is still extremely challenging to repeat such success for heterogeneous reactions involving polyatomic molecules. The in-depth understanding of the reaction dynamics for water dissociation provided by the present synergistic experimental-theoretical work has important implications in advancing our understanding and control of prototypical polyatomic surface reactions beyond their well-understood diatomic counterparts. The mode specificity demonstrated in the dissociative chemisorption of water on Ni(111) suggests that such a phenomenon is not restricted to CH_4 and might be quite prevalent in many surface reactions. A key determinant of mode specificity and bond selectivity is the slow rate of surface-induced intramolecular vibrational energy redistribution of the reactant, which is related to its sparse density of states (*46*). Both CH_4 and H_2O, and many other molecules, obviously possess these properties. More interestingly, the results presented here suggest that water dissociation in high-temperature (700° to 1100°C) steam reforming is dominated by Boltzmann populated excited vibrational states, thanks to their high vibrational efficacies. Further experimental and theoretical work will be needed to investigate mode specificity, bond selectivity, and steric effects in water chemisorption, with the goal of developing a predictive understanding of this important gas/surface reaction.

References and Notes

1. P. A. Thiel, T. E. Madey, *Surf. Sci. Rep.* **7**, 211–385 (1987).
2. M. A. Henderson, *Surf. Sci. Rep.* **46**, 1 (2002).
3. L. B. F. Juurlink, D. R. Killelea, A. L. Utz, *Prog. Surf. Sci.* **84**, 69–134 (2009).
4. R. D. Beck *et al.*, *Science* **302**, 98–100 (2003).
5. P. Maroni *et al.*, *Phys. Rev. Lett.* **94**, 246104 (2005).
6. L. B. F. Juurlink, R. R. Smith, D. R. Killelea, A. L. Utz, *Phys. Rev. Lett.* **94**, 208303 (2005).
7. D. R. Killelea, V. L. Campbell, N. S. Shuman, A. L. Utz, *Science* **319**, 790–793 (2008).
8. L. Chen, H. Ueta, R. Bisson, R. D. Beck, *Faraday Discuss.* **157**, 285–295, discussion 375–398 (2012).
9. B. L. Yoder, R. Bisson, R. D. Beck, *Science* **329**, 553–556 (2010).
10. B. L. Yoder, R. Bisson, P. Morten Hundt, R. D. Beck, *J. Chem. Phys.* **135**, 224703 (2011).
11. V. A. Ukraintsev, I. Harrison, *J. Chem. Phys.* **101**, 1564 (1994).
12. A. Bukoski, D. Blumling, I. Harrison, *J. Chem. Phys.* **118**, 843 (2003).
13. S. Nave, B. Jackson, *Phys. Rev. B* **81**, 233408 (2010).
14. B. Jackson, S. Nave, *J. Chem. Phys.* **135**, 114701 (2011).
15. B. Jiang *et al.*, *Chem. Sci.* **4**, 3249 (2013).
16. F. Nattino *et al.*, *J. Phys. Chem. Lett.* **5**, 1294–1299 (2014).
17. B. Jiang, X. Ren, D. Xie, H. Guo, *Proc. Natl. Acad. Sci. U.S.A.* **109**, 10224–10227 (2012).
18. B. Jiang, D. Xie, H. Guo, *Chem. Sci.* **4**, 503 (2013).
19. A. Mondal, H. Seenivasan, A. K. Tiwari, *J. Chem. Phys.* **137**, 094708 (2012).
20. B. Jiang, J. Li, D. Xie, H. Guo, *J. Chem. Phys.* **138**, 044704 (2013).
21. H. Seenivasan, A. K. Tiwari, *J. Chem. Phys.* **139**, 174707 (2013).
22. A. Sinha, M. C. Hsiao, F. F. Crim, *J. Chem. Phys.* **92**, 6333 (1990).
23. M. C. Hsiao, A. Sinha, F. F. Crim, *J. Phys. Chem.* **95**, 8263–8267 (1991).
24. M. J. Bronikowski, W. R. Simpson, R. N. Zare, *J. Phys. Chem.* **97**, 2194–2203 (1993).
25. A. Sinha, J. D. Thoemke, F. F. Crim, *J. Chem. Phys.* **96**, 372 (1992).
26. J. C. Polanyi, *Science* **236**, 680–690 (1987).
27. H. Chadwick, P. M. Hundt, M. E. van Reijzen, B. L. Yoder, R. D. Beck, *J. Chem. Phys.* **140**, 034321 (2014).
28. M. P. Schmid, P. Maroni, R. D. Beck, T. R. Rizzo, *Rev. Sci. Instrum.* **74**, 4110 (2003).
29. P. M. Hundt, R. Bisson, R. D. Beck, *J. Chem. Phys.* **137**, 074701 (2012).
30. Materials and methods are available as supplementary materials on *Science* Online.
31. J. P. Perdew, K. A. Jackson, M. R. Pederson, D. J. Singh, C. Fiolhais, *Phys. Rev. B* **46**, 6671–6687 (1992).
32. G. Kresse, J. Furthmuller, *Phys. Rev. B* **54**, 11169–11186 (1996).
33. G. Kresse, J. Furthmuller, *Comput. Mater. Sci.* **6**, 15–50 (1996).
34. J. M. Bowman, G. Czakó, B. Fu, *Phys. Chem. Chem. Phys.* **13**, 8094–8111 (2011).
35. B. Jiang, H. Guo, *J. Am. Chem. Soc.* **135**, 15251–15256 (2013).
36. D. Han, S. Nave, B. Jackson, *J. Phys. Chem. A* **117**, 8651–8659 (2013).
37. A. K. Tiwari, S. Nave, B. Jackson, *J. Chem. Phys.* **132**, 134702 (2010).
38. A. C. Luntz, *J. Chem. Phys.* **113**, 6901 (2000).
39. B. Hammer, L. B. Hansen, J. K. Nørskov, *Phys. Rev. B* **59**, 7413–7421 (1999).
40. G.-J. Kroes, *Phys. Chem. Chem. Phys.* **14**, 14966–14981 (2012).
41. C. Díaz *et al.*, *Science* **326**, 832–834 (2009).
42. L. Sementa *et al.*, *J. Chem. Phys.* **138**, 044708 (2013).
43. D. H. Zhang, M. A. Collins, S.-Y. Lee, *Science* **290**, 961–963 (2000).
44. B. Jiang, H. Guo, *J. Chem. Phys.* **138**, 234104 (2013).
45. G.-J. Kroes, *Science* **321**, 794–797 (2008).
46. D. R. Killelea, A. L. Utz, *Phys. Chem. Chem. Phys.* **15**, 20545–20554 (2013).

Acknowledgments: P.M.H., M.v.R., and R.D.B. gratefully acknowledge financial support from the Swiss National Science Foundation (grant no. 146487/1) and the Ecole Polytechnique Fédérale de Lausanne. B.J. and H.G. thank the U.S. NSF (grant no. CHE-0910828) for support. The experiments were done by the Lausanne group, and the theory was developed by the Albuquerque group.

Supplementary Materials

www.sciencemag.org/content/344/6183/504/suppl/DC1
Materials and Methods
Figs. S1 to S8
Tables S1 to S6
References (*47*–*83*)

24 January 2014; accepted 3 April 2014
10.1126/science.1251277

Faster Decomposition Under Increased Atmospheric CO_2 Limits Soil Carbon Storage

Kees Jan van Groenigen,[1,2]* Xuan Qi,[3] Craig W. Osenberg,[4] Yiqi Luo,[3,5] Bruce A. Hungate[1,6]

Soils contain the largest pool of terrestrial organic carbon (C) and are a major source of atmospheric carbon dioxide (CO_2). Thus, they may play a key role in modulating climate change. Rising atmospheric CO_2 is expected to stimulate plant growth and soil C input but may also alter microbial decomposition. The combined effect of these responses on long-term C storage is unclear. Combining meta-analysis with data assimilation, we show that atmospheric CO_2 enrichment stimulates both the input (+19.8%) and the turnover of C in soil (+16.5%). The increase in soil C turnover with rising CO_2 leads to lower equilibrium soil C stocks than expected from the rise in soil C input alone, indicating that it is a general mechanism limiting C accumulation in soil.

Carbon exchange between land and the atmosphere is a major focus of Earth system models, because the C cycle is sensitive to environmental change and because alterations of the C cycle affect our climate. Earth system models project that rising atmospheric CO_2 will promote C uptake by the terrestrial biosphere (*1*). The resulting increase in C stocks in plant biomass and soil organic matter (*2*) would slow the rise in atmospheric CO_2 concentrations and may help to slow climate change. Data support part of these model predictions: Experimentally increased CO_2 concentrations usually stimulate photosynthesis and plant growth (*3*). However, the response of soil C stocks is less well understood, because changes in soil C content are difficult to detect (*4*, *5*). Thus, global models projecting future C dynamics of the biosphere have strong empirical support for the effects of CO_2 on plant growth (*3*) but limited empirical support for assumed effects on soil C accumulation.

Soil C stocks are determined by the balance between plant growth and the subsequent input of plant detritus to soil and C losses through microbial decomposition. Earth system models typically treat decomposition as a function of temperature and water content (*1*) and do not include direct effects of increased CO_2, which are generally assumed to be small (*6*). These models commonly describe soil C dynamics with first-order kinetics (*7*), such that C loss from soil increases proportionally with the size of the soil C pool (*8*) (Eq. 1). Thus, if increased CO_2 enhances C input to soil, these models project that decomposition will also increase. Consistent with these expectations, CO_2 enrichment is frequently found to increase CO_2 efflux from soil (*9*). However, in some cases this increase was greater than the first-order expectation (*10*, *11*), suggesting that increased CO_2 may stimulate decomposition beyond what is expected from increased substrate availability alone. It is not known whether this disproportionate response to increased atmospheric CO_2 is general across ecosystems.

Disentangling C input to and loss from soil is possible in short-term laboratory experiments using isotopic tracers (*10*) and can be inferred from mass balance calculations (*12*). However, synthetic approaches disentangling C inputs and losses across broad data sets from the field have not been developed. Here, we use an approach that combines measurements of plant production, microbial respiration, and soil C stocks to estimate CO_2 effects on soil C turnover, thereby providing insight into the mechanisms determining long-term soil C storage (*13*). We derived effect sizes from a one-pool biogeochemical model of soil C cycling (*8*), the same form used by several global C cycling models (*1*, *2*)

$$C_t = C_0[\exp(-kt)] + I/k[1 - \exp(-kt)] \quad (1)$$

where C_t is the soil C content (g C m^{-2}) at time t (year); C_0 is the soil C content at the start of a CO_2 enrichment experiment (g C m^{-2}); k is the decomposition rate constant ($year^{-1}$, the rate at which C leaves the soil system); and I is the annual input of C to soil (g C m^{-2} $year^{-1}$). The model was constrained by multiple independent data streams from 53 CO_2 enrichment experiments (see table S1 and databases S1 to S4). We then used meta-analysis to synthesize the results (*13*).

Using this approach, the data indicate that CO_2 enrichment increased soil C input (I in Eq. 1) by 19.8% (Fig. 1A), with lower responses in cropland (10.9%) compared with grassland (20.1%) and forest (23.3%) (table S2). These estimates are consistent with past syntheses of the responses of plant production to experimental CO_2 enrichment (*3*).

If the decomposition rate constant k of soil C in Eq. 1 were unaffected by CO_2 enrichment, then microbial decomposition would change proportionally with the size of the soil C pool. That is, C loss from decomposition would increase with CO_2 enrichment because the pool of soil C increased, not because the rate of decomposition (i.e., k) increased. However, our meta-analysis showed that CO_2 enrichment significantly increased k by 16.5% (Fig. 1A). The average effect

[1]Center for Ecosystem Science and Society, Northern Arizona University, Flagstaff, AZ 86011, USA. [2]Department of Botany, School of Natural Sciences, Trinity College Dublin, Dublin 2, Ireland. [3]Department of Microbiology and Plant Biology, University of Oklahoma, Norman, OK 73019–0245, USA. [4]Department of Biology, University of Florida, Gainesville, FL 32611–8525, USA. [5]Center for Earth System Science, Tsinghua University, Beijing 100084, China. [6]Department of Biological Sciences, Northern Arizona University, Flagstaff, AZ 86011, USA.

*Corresponding author. E-mail: cjvangroenigen@nau.edu

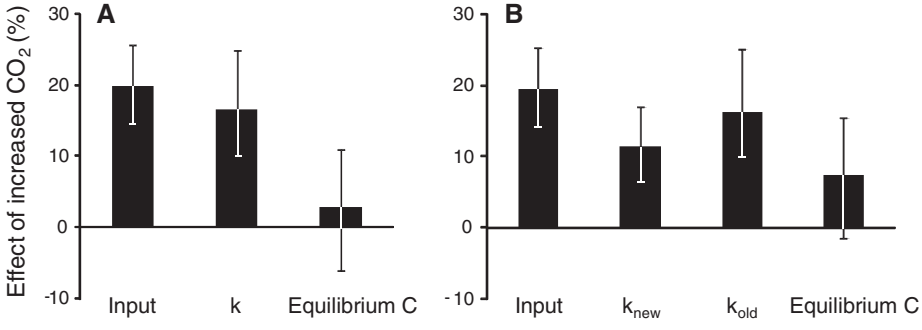


Fig. 1. Results of a meta-analysis on the response of soil C dynamics to increased levels of atmospheric CO_2. (**A**) The effect of increased CO_2 on soil C input (input), soil C turnover (k), and projected equilibrium soil C, based on a one-pool soil C model (Eq. 1). (**B**) The effect of increased CO_2 on soil C input, new soil C turnover (k_{new}), old soil C turnover (k_{old}), and projected equilibrium soil C, based on a two-pool soil C model (Eq. 2). Results are based on 53 experimental comparisons. Effect sizes were weighted by replication, adjusted by the number of comparisons per experimental site. All error bars represent 95% confidence intervals.

of increased CO_2 was similar in grasslands, forests, and croplands, although the effect in the latter category was not significant (see table S2). Correspondingly, increased atmospheric CO_2 significantly reduced soil residence time ($1/k$, the average time that a C atom spends in the soil) by 2.4 years (95% confidence interval, 1.5 to 3.8 years) (see table S3).

Why does increased atmospheric CO_2 stimulate the turnover of soil C? Larger soil C input rates under increased CO_2 cause an enhanced supply of easily metabolized substrates (*10*), which can stimulate the decomposition of native soil organic matter, mobilizing C reserves assumed to be protected from microbial attack (*14*). This process, commonly called "priming" (*15*), has previously been described as short-term and idiosyncratic (*16*). However, recent studies indicate that it is a widespread and persistent phenomenon (*17*, *18*). Our results now suggest that it is also a general and prolonged response to increased atmospheric CO_2.

Furthermore, atmospheric CO_2 enrichment can increase soil water content (*19*), due to improved efficiency of water use by plants, which reduces soil water loss through transpiration (*20*). Because low water availability limits the physiological performance of soil microbes and their access to substrate, a CO_2-induced increase in soil water content may increase decomposition rates in arid and semiarid ecosystems (*21*).

Our results are based on a one-pool soil C model, but two- or three-pool soil C models that distinguish labile and recalcitrant C pools may describe changes in soil C stocks over time more accurately (*22*); however, parameters in a conventional multipool soil C model could not be estimated with the available data (*13*). Thus, we took a slightly different approach and applied a model that distinguished the k of soil C initially present at each experimental site (k_{old}) from the k of soil C added after CO_2 enrichment started (k_{new}).

$$C_t = C_0[\exp(-k_{old} \times t)] + I/k_{new}[1 - \exp(-k_{new} \times t)] \quad (2)$$

Based on this approach, we found that CO_2 enrichment increased both k_{old} and k_{new} (Fig. 1B and table S4) to similar degrees. These findings corroborate recent studies suggesting that increased CO_2 stimulates the decomposition of old soil C (*10*, *11*) as well as new soil C pools (*23*).

Given enough time, soil C stocks will eventually reach equilibrium of I/k (Eq. 1) or I/k_{new} (Eq. 2), where soil C input through plant growth is balanced by soil C loss through decomposition. If increased CO_2 alters only I and not k, an assumption made in early Earth system models (*1*), predicted equilibrium soil C contents for the experiments in our database would increase to the same degree as soil C input rates, that is, by 19.8%. However, when we take into account the effect of CO_2 on k, increased CO_2 does not significantly affect the predicted equilibrium soil C contents (Fig. 1, A and B). In other words, the observed increase in k largely negates the predicted soil C accumulation due to increased atmospheric CO_2. Although increased CO_2 stimulates plant growth and C input to soil, the microbial response counteracts this response, thereby reducing the net effect of rising CO_2 levels on soil C stocks.

The effect of increased CO_2 on I/k and I/k_{new} (which represent projected long-term responses) are quantitatively similar to the effect of increased CO_2 on soil C contents found in several recent meta-analyses focusing on short-term responses (*24*, *25*). This suggests that studies that are focused on processes (and thus allow estimation of I and k) and those focused on soil C storage provide complementary answers. Importantly, our approach allows the separation of inputs and losses and thus explains the apparent mismatch between the stimulation of plant growth and the limited response of soil C (*25*, *26*).

Current Earth system models include only some of the possible processes underlying the response of k to increased atmospheric CO_2. In most models, atmospheric CO_2 enrichment could influence decomposition by altering soil moisture (*1*). Furthermore, some Earth system models partition plant litter into multiple pools with different decomposition rates. Increased CO_2 could drive changes in k due to shifts in vegetation composition, because the ratio of these pools differs between vegetation types (*1*). However, because of their relative short duration, experiments in our data set did not allow for the large shifts in vegetation composition that affect soil C dynamics in these models (*27*). Therefore, this mechanism does not explain our findings. Alternatively, Earth system models that include a nitrogen (N) cycle can simulate changes in C to N ratio and decomposability of litter (*28*). However, because atmospheric CO_2 enrichment generally has little effect on litter quality (*6*), this mechanism probably plays a limited role in explaining the response of k. The priming effect itself is not explicitly represented in any Earth system model. Including priming in ecosystem models captures increased decomposition rates with increased atmospheric CO_2 (*29*), a result consistent with our findings. Future Earth system models might improve by incorporating the priming effect in their land surface mode as well.

References and Notes

1. P. Friedlingstein *et al.*, *J. Clim.* **19**, 3337–3353 (2006).
2. P. E. Thornton, J.-F. Lamarque, N. A. Rosenbloom, N. M. Mahowald, *Global Biogeochem. Cycles* **21**, GB4018 (2007).
3. E. A. Ainsworth, S. P. Long, *New Phytol.* **165**, 351–372 (2005).
4. B. A. Hungate, R. B. Jackson, C. B. Field, F. S. Chapin III, *Plant Soil* **187**, 135–145 (1995).
5. P. Smith, *Soil Use Manage.* **20**, 264–270 (2004).
6. R. J. Norby, M. F. Cotrufo, P. Ineson, E. G. O'Neill, J. G. Canadell, *Oecologia* **127**, 153–165 (2001).
7. W. J. Parton, D. S. Schimel, C. V. Cole, D. S. Ojima, *Soil Sci. Soc. Am. J.* **51**, 1173–1179 (1987).
8. J. S. Olson, *Ecology* **44**, 322–331 (1963).
9. D. R. Zak, K. S. Pregitzer, J. S. King, W. E. Holmes, *New Phytol.* **147**, 201–222 (2000).
10. E. Paterson *et al.*, *Soil Biol. Biochem.* **40**, 2434–2440 (2008).
11. K. M. Carney, B. A. Hungate, B. G. Drake, J. P. Megonigal, *Proc. Natl. Acad. Sci. U.S.A.* **104**, 4990–4995 (2007).
12. J. E. Drake *et al.*, *Ecol. Lett.* **14**, 349–357 (2011).
13. Materials and methods are available as supplementary materials on *Science* Online.
14. S. Fontaine *et al.*, *Nature* **450**, 277–280 (2007).
15. E. Blagodatskaya, Y. Kuzyakov, *Biol. Fertil. Soils* **45**, 115–131 (2008).
16. J. W. Dalenberg, G. Jager, *Soil Biol. Biochem.* **21**, 443–448 (1989).
17. F. A. Dijkstra, W. Cheng, *Ecol. Lett.* **10**, 1046–1053 (2007).
18. E. J. Sayer, M. S. Heard, H. K. Grant, T. R. Marthews, E. V. J. Tanner, *Nature Clim. Change* **1**, 304–307 (2011).
19. K. J. van Groenigen, C. W. Osenberg, B. A. Hungate, *Nature* **475**, 214–216 (2011).
20. S. D. Wullschleger, T. J. Tschaplinski, R. J. Norby, *Plant Cell Environ.* **25**, 319–331 (2002).
21. E. Pendall *et al.*, *Global Biogeochem. Cycles* **17**, GB1046 (2003).
22. E. A. Davidson, S. E. Trumbore, R. Amundson, *Nature* **408**, 789–790 (2000).
23. R. P. Phillips *et al.*, *Ecol. Lett.* **15**, 1042–1049 (2012).
24. B. A. Hungate *et al.*, *Glob. Change Biol.* **15**, 2020–2034 (2009).
25. W. M. A. Sillen, W. I. J. Dieleman, *Biogeosciences* **9**, 2247–2258 (2012).
26. K. J. van Groenigen *et al.*, *Proc. Natl. Acad. Sci. U.S.A.* **103**, 6571–6574 (2006).
27. Y. Luo *et al.*, *Glob. Change Biol.* **17**, 843–854 (2011).
28. V. K. Arora *et al.*, *J. Clim.* **26**, 5289–5314 (2013).
29. N. Perveen *et al.*, *Glob. Change Biol.* **20**, 1174–1190 (2014).

Acknowledgments: This research was supported by the Biological and Environmental Research program, Office of Science, U.S. Department of Energy; the Western Regional Center of the National Institute for Climatic Change Research; and the Irish Research Council, cofunded by Marie Curie Actions under the Seventh Framework Program (FP7). X.Q. and Y.L. received financial support from the U.S. Department of Energy, Terrestrial Ecosystem Sciences grant DE SC0008270. We thank M. Hoosbeek, K. Sturner, A. Talhelm, and D. Zak for sharing unpublished data with us. Many thanks go to T. Xu for assisting us with writing the Matlab code. The data reported in this paper are available online as supplementary materials.

Supplementary Materials

www.sciencemag.org/content/344/6183/508/suppl/DC1
Materials and Methods
Figs. S1 to S3
Tables S1 to S4
Databases S1 to S6
References (*30*–*106*)

10 December 2013; accepted 4 April 2014
Published online 24 April 2014;
10.1126/science.1249534

Genomic Signatures of Specialized Metabolism in Plants

Lee Chae, Taehyong Kim, Ricardo Nilo-Poyanco, Seung Y. Rhee*

All plants synthesize basic metabolites needed for survival (primary metabolism), but different taxa produce distinct metabolites that are specialized for specific environmental interactions (specialized metabolism). Because evolutionary pressures on primary and specialized metabolism differ, we investigated differences in the emergence and maintenance of these processes across 16 species encompassing major plant lineages from algae to angiosperms. We found that, relative to their primary metabolic counterparts, genes coding for specialized metabolic functions have proliferated to a much greater degree and by different mechanisms and display lineage-specific patterns of physical clustering within the genome and coexpression. These properties illustrate the differential evolution of specialized metabolism in plants, and collectively they provide unique signatures for the potential discovery of novel specialized metabolic processes.

Plants produce compounds that contribute to human health and survival. More than one-third of human drugs have originated from products synthesized by plant metabolism (*1*). Understanding the origins, evolution, and diversity of plant metabolites has been a long-standing goal in plant biology. Metabolic diversification may play a key role in plant evolution, particularly those genes that encode proteins that function as novel specialized (or secondary) metabolites that mediate interactions between a given plant and its environment (*2*, *3*).

In order to apply advances in genomic and computational resources, both systematically and quantitatively, to assess the relationship between metabolic diversity and plant evolution (*4*, *5*), we performed a comparative analysis of the metabolic networks of 16 green plants with high-quality genome annotations from major groups in the green plant lineage. These included six chlorophyte algae (*Chlamydomonas reinhardtii*, *Volvox carteri*, *Coccomyxa subellipsoidea*, *Micromonas pusilla CCMP1545* and *RCC299*, *Ostreococcus lucimarinus*), two early-diverging land plants [*Physcomitrella patens* (moss), *Selaginella moellendorfii*], three grasses [*Oryza sativa* ssp. *japonica* (rice), *Sorghum bicolor*, *Zea mays* (maize)], and five eudicots [*Arabidopsis thaliana*, *Manihot esculenta* (cassava), *Populus trichocarpa* (poplar), *Glycine max* (soybean), *Vitis vinifera* (grapevine)] (*6*) (table S1 and fig. S1). We annotated enzymes encoded in the genomes of the 16 species with four-part Enzyme Commission (EC) numbers (*6*), implementing an ensemble classification algorithm to integrate molecular function predictions (fig. S2) (*6*). Pipeline validation produced results of 86% precision, 87% recall, and 86% F_1 measure, compared to the individual methods (54 to 81% precision, 57 to 82% recall, and 55 to 79% F_1 measure) (figs. S3 and S4). The identified enzyme inventories ranged in size from 1295 in *Ostreococcus* (16.6% of protein-coding genes) to 12,124 in soybean (21.7% of protein-coding genes), covering 1219 distinct EC numbers (table S2, fig. S5, and data file S1). Annotated enzymes were used to reconstruct bidirectional, reaction-centric metabolic networks (*7*). Enzymes and reactions were manually classified into 13 functional classes, including primary metabolism-related categories such as amino acid, nucleotide, and energy metabolism, as well as specialized metabolism (fig. S6 and data file S2) (*6*).

To assess divergence among the genome-scale metabolic networks, we investigated differences in their structure and content. The size (diameter) and density (clustering coefficient and betweenness centrality distributions) (*7*) of the metabolic networks were statistically similar across the species (fig. S7). However, land plant networks contain a significantly larger number of reaction nodes than algal networks (fig. S8A). Given the similarity in network size and density, the increase in reaction nodes suggests a more complex set of networks in land plants, with higher levels of connectivity, as seen by differences in the degree and average neighbor degree distributions ($P < 0.0001$, Kruskal-Wallis test) (fig. S8, B and C) (*8*).

Comparisons of network content, reflecting species phylogeny, grouped the prasinophycea apart from chlorophycea algae and separated moss and *Selaginella* from grasses and eudicots, respectively (Fig. 1A). This suggests that the evolution of plant metabolic networks followed a pattern of descent with modification, with closely related species sharing more similar sets of metabolic reactions. If true, phylogenetic comparisons of genome-scale metabolic networks may offer a predictive tool for discovering metabolic properties in different plant

Department of Plant Biology, Carnegie Institution for Science, Stanford, CA 94305, USA.

*Corresponding author. E-mail: srhee@carnegiescience.edu

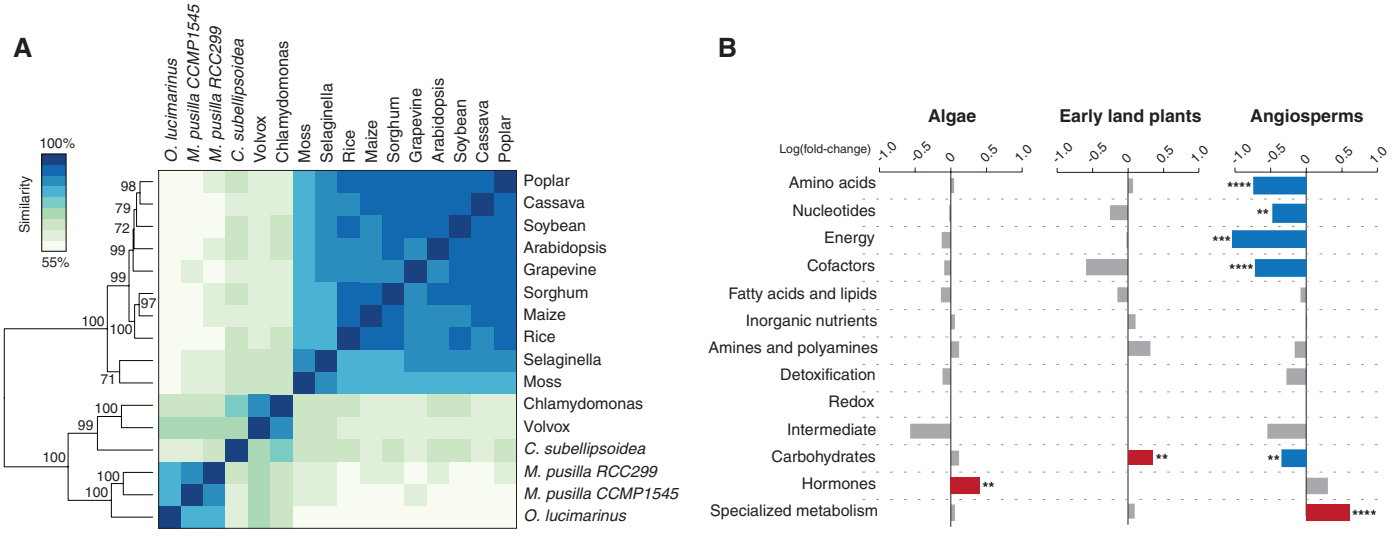


Fig. 1. Diversification of metabolism in the green plant lineage. (**A**) Heat map depicting the similarity of reaction node sets among species (*6*). Numbers indicate support from 1000 bootstrap rounds. (**B**) Enrichment (red) or depletion (blue) of functional classes in lineage-specific groupings of metabolic reactions (algae, 6 species, 154 reactions; early land plants, 2 species, 32 reactions; angiosperms, 8 species, 137 reactions). The *x* axes depict $\log_{10}$ transformations of relative change ratios for reactions unique to each group versus all reactions in each group. $^{**}P \leq 0.01$, $^{***}P \leq 0.001$, $^{****}P \leq 0.0001$ (hypergeometric test).

species. However, reconstructing events leading to differences in metabolic reaction sets across a deep phylogeny, as represented by the 16 species, is challenged by the paucity of high-quality genome sequence data across the plant kingdom (*9*).

If metabolic networks evolved by descent with modification, lineage-based groupings of enzymatic reactions may reveal how metabolic functionality diverged after important junctures in plant evolution. We investigated the functional composition of the set of reactions unique to algae, the early land plants, and angiosperms (323 reactions, 19.9% of the network reactions). Algae were enriched in hormone-related reactions (P = 0.001, hypergeometric test), whereas early land plant reactions were enriched in carbohydrate metabolism (P = 0.003, hypergeometric test) (Fig. 1B). Reactions unique to the angiosperms were enriched for specialized metabolism ($P \approx 0$, hypergeometric test), whereas primary metabolism-related reactions were significantly underrepresented in this set ($P < 0.01$ for amino acid, carbohydrate, cofactor, energy, and nucleotide metabolism; hypergeometric test).

Several serotonin- and melatonin-related reactions were found in the algal groups examined (data file S3). However, other reactions typically comprising these metazoan pathways, such as the decarboxylation of 5-hydroxytryptophan or the acetylation of serotonin, were not found. Similarly, mosses and bryophytes contained a number of carbohydrate-related reactions not associated with any known pathway (*6*). The lack of genome sequences for other members of these lineages makes it hard to reconstruct events that may have led to the appearance of these reactions in these species. On one hand, they may reflect a mosaic pattern of metabolic evolution, where ancestral pathways are unevenly conserved across reactions and lineages. Conversely, some proportion of the reactions may represent the appearance of newfound metabolic functionality in a particular species.

The enrichment pattern in the angiosperm grouping suggests that the predominant metabolic innovations after the appearance of the vascular plants dealt with specialized metabolism, while those processes related to primary metabolism were likely established earlier in the evolution of plants. The extent of specialized metabolism evolution in basal plant lineages is difficult to ascertain, as much of our knowledge of plant specialized metabolism derives from angiosperms. Consequently, it is likely that a number of specialized processes unique to basal lineages have not yet been discovered, which ultimately may demonstrate a greater role for specialized metabolism in the basal plant lineages (*10*).

The functional enrichment analysis suggests that specialized metabolic capacity expanded after the divergence of early land plants into more derived lineages, including the angiosperms. We thus examined whether specialized metabolism exhibited different patterns of evolution among

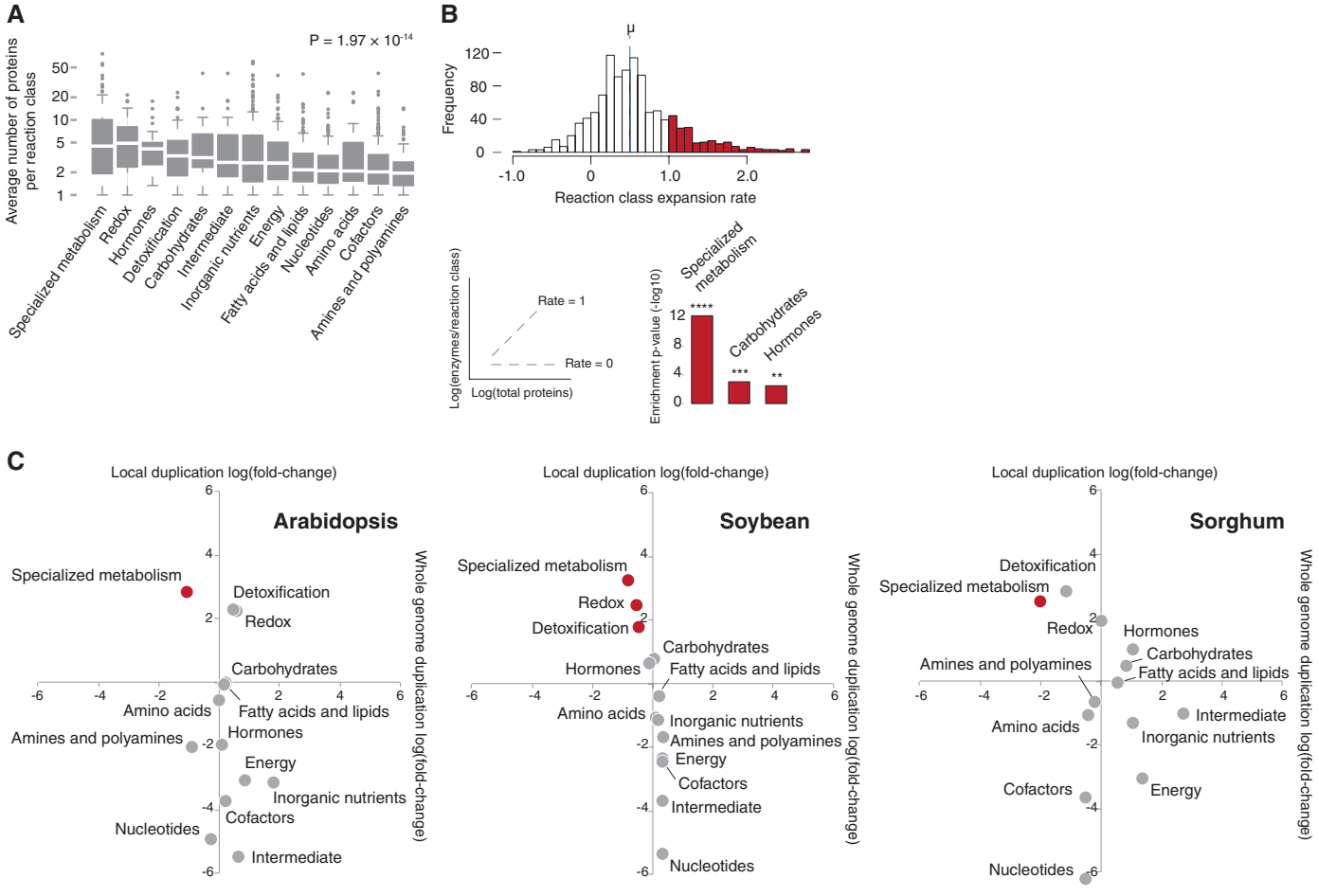


Fig. 2. Differential evolution of specialized metabolism in plants. (**A**) Differences in the distributions of the number of enzymes per EC-based reaction class for each functional category in all 16 species ($P = 1.97 \times 10^{-14}$, Kruskal-Wallis test). (**B**) Histogram of expansion rates for all reaction classes found in two or more species (*6*). Inset is an example plot for one reaction class. Rate = 0, enzyme number remained constant; rate = 1, enzyme number increased linearly with protein number. Specialized metabolism ($P = 5.64 \times 10^{-13}$, hypergeometric test), carbohydrate ($P = 8.40 \times 10^{-4}$, hypergeometric test), and hormone (P = 0.003, hypergeometric test) reactions are enriched in the set of reactions with expansion rates ≥ 1. The y axis represents negative $\log_{10}$ transformations of the P value. (**C**) Enrichment or depletion of genes annotated to a given functional class after local duplication (LD, y axis) versus whole-genome duplication (WGD, x axis). Axes represent $\log_{10}$ transformations of relative change ratios for LD or WGD genes in each functional grouping versus all metabolic LD or WGD genes. Red markers indicate LD enrichment and WGD depletion at $P \leq 0.0001$ (hypergeometric test).

enzyme families. Overall, the total number of enzymes observed for each species increased linearly with respect to the total number of proteins ($R^2 = 0.947$, $P = 6.17 \times 10^{-7}$, Student's t test) (fig. S5). However, this increase is biased toward specialized metabolism, as specialized metabolism reactions catalyzed by specific four-digit EC numbers tended to have larger enzyme inventories relative to other functional classes ($P = 1.97 \times 10^{-14}$, Kruskal-Wallis test) (Fig. 2A and table S3). Furthermore, a number of metabolic reactions experienced enzyme number expansions at a rate greater than the rate of change in the total number of proteins (Fig. 2B) (*6*). Several functional classes were enriched in this set of metabolic reactions, most notably specialized metabolism ($P = 5.64 \times 10^{-13}$, hypergeometric test), along with carbohydrates ($P = 8.40 \times 10^{-4}$, hypergeometric test) and hormones ($P = 0.003$, hypergeometric test). Similar expansions in enzyme number related to specialized metabolism have been observed, notably within some subfamilies of the cytochrome P450s and glycosyltransferases (*11*, *12*). These results suggest that specialized metabolism is under selection driving the expansion of gene families coding for specific enzymatic processes in plants, in contrast to genes underlying the function of primary metabolism-related processes.

This growth in enzyme families is the result of selection for gene duplication for specialized metabolic genes. In general, gene duplication events, such as whole-genome duplications (WGDs) and local (tandem) duplication (LDs), increase gene content in plant genomes (*13*). We investigated the impact of WGD and LD events on amplifying metabolic genes across functional categories. In *Arabidopsis*, specialized metabolic genes were the only metabolic functional class significantly enriched in LD genes ($P \approx 0$, hypergeometric test) that were also significantly depleted in the WGD-derived gene set ($P = 4.80 \times 10^{-7}$, hypergeometric test) (Fig. 2C). Similar enrichment of LD genes was reported for three *Arabidopsis* specialized metabolic pathways but suggested that whole-genome duplications contributed significantly to these pathways (*14*). We tested whether whole-genome duplications have contributed significantly to the specialized metabolic gene sets in soybean and sorghum (*6*). Both species exhibited significant depletions of WGD-derived specialized metabolic genes ($P = 2.23 \times 10^{-37}$ and 6.77×10^{-14}, respectively; hypergeometric test) but displayed significant enrichment in LD-derived specialized metabolic genes ($P \approx 0$ for both species, hypergeometric test) (Fig. 2C).

Although the LD versus WGD dynamic was the same among the three species, the functional impact of local duplication on specialized metabolic genes differed. For example, a local duplication of genes involved in sinapate ester production was seen in *Arabidopsis*, whereas local duplications of terpenoid genes associated with phytoalexins were observed in sorghum (data files S1 and S4). These duplications appeared to affect a number of flavonol-related genes in each species, including those associated with quercetin and rhutin in *Arabidopsis* and kaempferol in soybean (data files S1 and S4). Thus, the expansion of specialized metabolic plant genes appears to be due to local gene duplication.

We also examined the genomic colocation, or clustering, of genes whose products function together to synthesize specialized metabolites (*15*). Reports thus far have focused on specific metabolic gene clusters, but it is unknown whether clustering plays a major role in specialized metabolism evolution. Consequently, we analyzed the extent of metabolic gene clustering and tested whether clusters are biased for specialized metabolism (*6*). From this we observed that approximately one-third of the metabolic genes in *Arabidopsis* (30.1%), soybean (30.2%), and sorghum (30.5%), and one-fifth of the genes in rice (22.4%), were situated in clusters (data file S5). For each species, the extent of clustering was greater than expected by chance ($P < 2.20 \times 10^{-16}$, χ^2 test) (Fig. 3A) (*6*). The *Arabidopsis* and soybean clusters were significantly enriched for specialized metabolic genes ($P = 1.38 \times 10^{-3}$ and 7.06×10^{-3}, respectively; hypergeometric test), as well as fatty acids and lipids in *Arabidopsis* ($P = 2.01 \times 10^{-3}$, hypergeometric test) and carbohydrates in soybean ($P = 4.34 \times 10^{-4}$, hypergeometric test) (Fig. 3B). In contrast, no such enrichment was found in sorghum or rice (table S4).

Clustering patterns differed across species and different classes of specialized metabolic compounds (*6*). Genes involved in phenylpropanoid and terpenoid metabolism were more likely to be found in *Arabidopsis* clusters ($P = 0.043$ and 0.040, hypergeometric test), whereas genes involved in nitrogen-containing specialized compound metabolism were enriched in the nonclustered gene set ($P = 0.002$, hypergeometric test) (Fig. 3C). The enrichment pattern differed in soybean, where the clustered genes were enriched for metabolism of nitrogen-containing compounds ($P = 0.037$, hypergeometric test) (Fig. 3C). Clustered genes in sorghum were enriched in terpenoid metabolism ($P = 0.012$, hypergeometric test), whereas phenylpropanoid metabolism was enriched in the

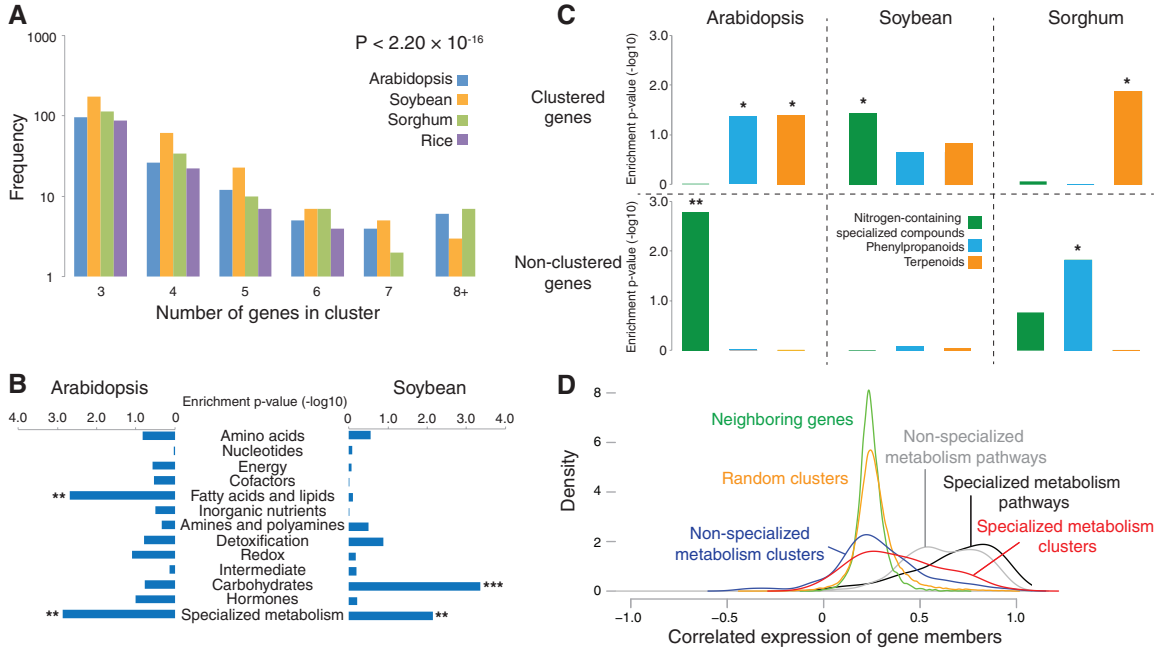


Fig. 3. Clustering and coexpression of specialized metabolic genes. (**A**) Distribution of metabolic gene cluster sizes (number of genes per cluster) in four plant genomes. Clusters of size 3 and greater were statistically significant for all four genomes ($P < 2.20 \times 10^{-16}$, χ^2 test) (*6*). (**B**) Enrichment of functional classes in metabolic gene clusters of *Arabidopsis* and soybean. The x axes represent negative $\log_{10}$ transformations of the P value. (**C**) Enrichment of three main classes of specialized metabolism compounds in clustered versus nonclustered gene sets in *Arabidopsis*, soybean, and sorghum (*6*). $^*P \leq 0.05$, $^{**}P \leq 0.01$, $^{***}P \leq 0.001$ (hypergeometric test). The y axes represent negative $\log_{10}$ transformations of the P value. (**D**) Coexpression values for clusters containing specialized metabolic gene(s) (red), nonspecialized metabolism-related clusters (blue), known specialized metabolic pathways (black), nonspecialized metabolism-related pathways (gray), randomized clusters (orange), and neighboring genes (green).

nonclustered genes ($P = 0.014$, hypergeometric test) (Fig. 3C). Rice exhibited no enrichment patterns in either gene set. The differing results among the four species suggest that specialized metabolic gene clusters are a product of independent, lineage-specific metabolic evolution, rather than a broad mechanism underlying specialized metabolism evolution.

We used a large-scale microarray data set to test whether the *Arabidopsis* clusters exhibit coexpression (*6*, *16*). Of the 128 clusters with at least three genes, 62 contained at least one specialized metabolism-related gene. The mean coexpression value for the specialized metabolic gene-containing clusters (0.390) was significantly higher than the mean for the remaining clusters (0.289) ($P = 0.020$, Wilcoxon rank sum test) (Fig. 3D). Coexpression of genes within the 62 specialized metabolism–related clusters differed significantly from randomized clusters of genes ($P = 2.71 \times 10^{-7}$, Wilcoxon rank sum test) and neighboring genes in the *Arabidopsis* genome ($P = 3.56 \times 10^{-5}$, Wilcoxon rank sum test) (Fig. 3D) (*6*). In contrast, coexpression values within the 66 nonspecialized metabolism-related clusters were similar to the examined controls (random clusters, $P = 0.191$; neighboring genes, $P = 0.817$). These results indicate that gene clusters containing specialized metabolic genes are more likely to be coexpressed than their nonspecialized counterparts. Given that genes in the same metabolic pathway tend to coexpress with each other, newly identified clusters exhibiting high degrees of gene coexpression may represent novel metabolic pathways (fig. S9).

Our findings indicate that the major innovations across plant networks pertain to the emergence of specialized metabolic processes, which, relative to primary metabolic processes, exhibit larger numbers of associated enzymes, increased enzyme proliferation rates, and preferential retention after local gene duplication versus whole-genome duplication. Furthermore, specialized metabolic genes exhibit lineage-specific patterns of genome colocation and specialized metabolism-related gene clusters display heightened levels of gene coexpression in *Arabidopsis*. Collectively, these properties constitute a set of genomic signatures of specialized metabolic genes that may serve as a tool for the accelerated and rational discovery of genes involved in the synthesis of novel specialized compounds (*4*, *5*, *17*).

References and Notes

1. B. M. Schmidt, D. M. Ribnicky, P. E. Lipsky, I. Raskin, *Nat. Chem. Biol.* **3**, 360–366 (2007).
2. P. R. Ehrlich, P. H. Raven, *Evolution* **18**, 586–608 (1964).
3. M. Wink, *Biochemistry of Plant Secondary Metabolism* (Wiley-Blackwell, Chichester, UK, 2010).
4. A. L. Schilmiller, E. Pichersky, R. L. Last, *Curr. Opin. Plant Biol.* **15**, 338–344 (2012).
5. J.-K. Weng, R. N. Philippe, J. P. Noel, *Science* **336**, 1667–1670 (2012).
6. See supplementary materials on *Science* Online.
7. A.-L. Barabási, Z. N. Oltvai, *Nat. Rev. Genet.* **5**, 101–113 (2004).
8. B. C. M. van Wijk, C. J. Stam, A. Daffertshofer, *PLOS ONE* **5**, e13701 (2010).
9. B. D. Mishler, *Taxon* **49**, 661–683 (2000).
10. J.-K. Weng, J. P. Noel, *Front. Plant Sci.* **4**, 119 (2013).
11. D. Nelson, D. Werck-Reichhart, *Plant J.* **66**, 194–211 (2011).
12. K. Yonekura-Sakakibara, K. Hanada, *Plant J.* **66**, 182–193 (2011).
13. R. C. Moore, M. D. Purugganan, *Curr. Opin. Plant Biol.* **8**, 122–128 (2005).
14. D. J. Kliebenstein, *PLOS ONE* **3**, e1838 (2008).
15. H. Y. Chu, E. Wegel, A. Osbourn, *Plant J.* **66**, 66–79 (2011).
16. T. Obayashi, K. Nishida, K. Kasahara, K. Kinoshita, *Plant Cell Physiol.* **52**, 213–219 (2011).
17. K. Yonekura-Sakakibara, K. Saito, *Nat. Prod. Rep.* **26**, 1466–1487 (2009).

Acknowledgments: We thank A. Osbourn, E. Sattely, and K. Dreher for comments. Supported by a Becas Chile-Conicyt postdoctoral fellowship (R.N.-P.) and by NSF grants DBI-0640769 and IOS-1026003. Data are available as supplementary data files S1 to S5. The enzyme annotation program is available for download at https://dpb.carnegiescience.edu/labs/rhee-lab/software.

Supplementary Materials

www.sciencemag.org/content/344/6183/510/suppl/DC1
Materials and Methods
Figs. S1 to S9
Tables S1 to S4
Data Files S1 to S5
References (*18*–*51*)

11 February 2014; accepted 7 April 2014
10.1126/science.1252076

Deception by Flexible Alarm Mimicry in an African Bird

Tom P. Flower,[1,2]* Matthew Gribble,[2] Amanda R. Ridley[1,3]

Deception is common in nature, but victims of deception discriminate against and ultimately ignore deceptive signals when they are produced too frequently. Flexible variation of signals could allow evasion of such constraints. Fork-tailed drongos (*Dicrurus adsimilis*) use false alarm calls to scare other species away from food that they then steal. We show that drongos mimic the alarms of targeted species. Further, target species reduce their response to false alarm calls when they are repeated. However, the fear response is maintained when the call is varied. Drongos exploit this propensity by changing their alarm-call type when making repeated theft attempts on a particular species. Our results show that drongos can evade the frequency-dependent constraints that typically limit deception payoffs through flexible variation of their alarm calls.

Animal signals tend to be honest (*1*–*3*), but deception can persist where it is beneficial for individuals to respond to a signal type on average (*4*). Such deception stops working when deceptive signals occur too often relative to their honest counterparts (*5*, *6*). This balance imposes a constraint on payoffs for individuals possessing a single inflexible deceptive signal whose success depends on the abundance of honest models (*5*). Novel deceptive signals can confer benefits because individuals that produce rare signals are at a selective advantage (*7*, *8*). Nevertheless, individual success still declines as signal frequency increases (*7*, *8*). Some deceivers can tune their signal to better deceive their host (*9*, *10*). However, the benefits available from flexibly alternating between different deceptive signal types remain unknown. We tested whether such flexible variation enables individuals to produce the specific signal most likely to deceive hosts, and to evade frequency-dependent constraints on deception, by changing their signal when hosts habituate to a previously used signal.

We investigated the deceptive tactics of an African bird, the fork-tailed drongo (*Dicrurus*

[1]Department of Science and Technology/National Research Foundation Centre of Excellence at the Percy FitzPatrick Institute, University of Cape Town, Rondebosch 7701, South Africa. [2]Department of Zoology, University of Cambridge, Cambridge CB2 3EJ, UK. [3]Centre for Evolutionary Biology, School of Animal Biology (M092), University of Western Australia, Crawley 6009, Australia.

*Corresponding author. E-mail: thomas.flower@uct.ac.za

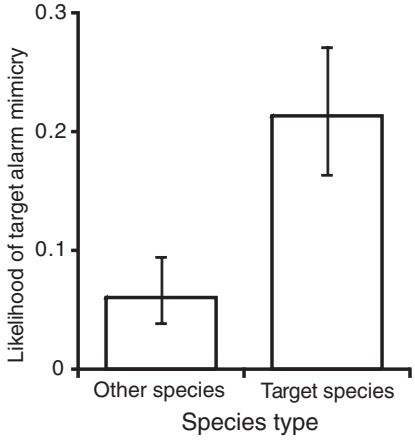
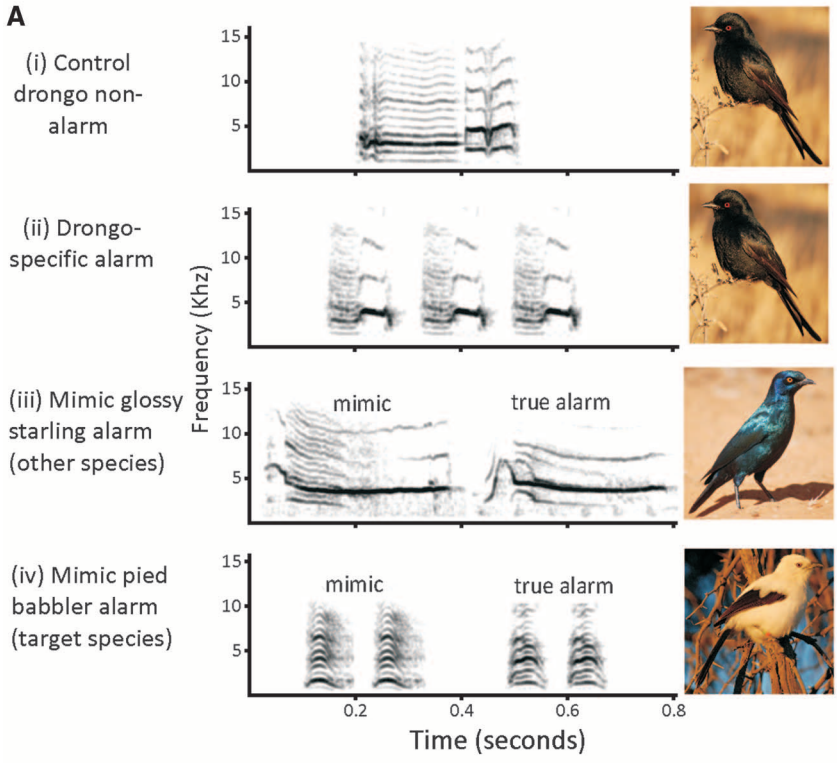


Fig. 1. Mimicry of target species alarm calls in food-theft attempts. Drongos mimicked a target species' alarm calls more often in food-theft attempts on them (target species) than in attempts on other target species (other species) [generalized linear mixed model (GLMM) (binomial), $\chi^2_1 = 2.55$, $P = 0.011$, $n = 147$ food-theft attempts by 10 drongos (table S1)]. Error bars indicate SEM.

adsimilis), which uses false alarm calls, including mimicked alarm calls, to scare and steal food from a variety of targeted species (*11*–*13*). We hypothesized that wild drongos use vocal mimicry to flexibly vary their false alarm calls and thereby (i) increase the likelihood of target deception and (ii) maintain target deception during repeated interactions. Our research was conducted in the Kalahari Desert on 64 wild drongos habituated to observers and individually recognizable by color rings (*14*). Drongos in this population spend over a quarter of their time following target species, including habituated groups of individually recognizable southern pied babblers (*Turdoides bicolor*) and meerkats (*Suricata suricatta*) (*11*, *12*). When doing so, drongos honestly produce true alarm calls when they observe approaching predators (*11*, *12*). Target species eavesdrop on these alarm calls, as well as those of other species in the environment, and flee to cover in response just as they do to conspecific alarms (*11*, *12*, *15*). Additionally, target species benefit from drongo sentries by reducing their vigilance and increasing their foraging returns (*12*, *16*). When a target individual finds a large food item, however, attending drongos may produce false alarm calls, causing the target to flee to cover and enabling the drongo



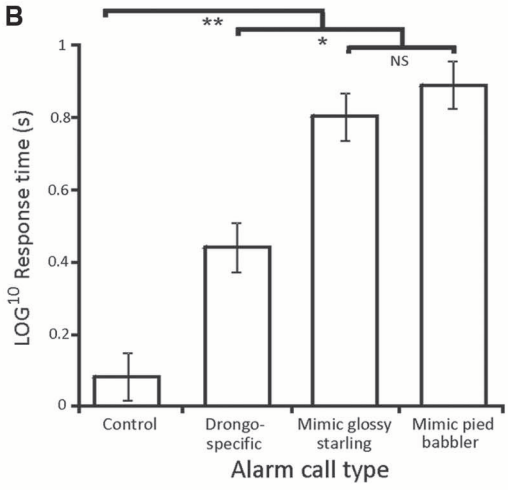
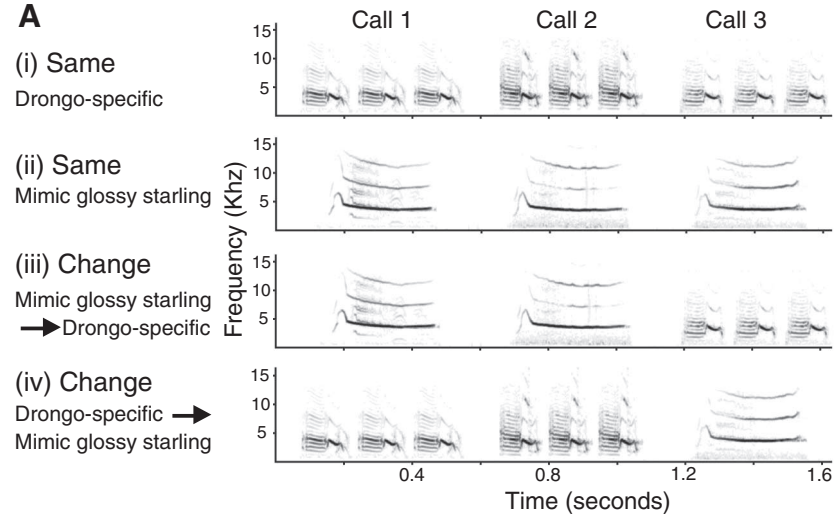


Fig. 2. Effect of alarm mimicry on target response. (**A**) Spectrograms of call types played to pied babblers (i to iv) to determine whether mimicry of alarm calls increases target alarm response. Drongo mimics of glossy starling and babbler alarm calls (mimic) are shown alongside these species' alarm calls (true alarm). (**B**) Response duration was longer to mimicked babbler (target species) or starling (other species) alarm calls than to drongo-specific alarm calls [LMM, $\chi^2_1 = 38.38$, $P < 0.001$, Tukey tests, $^*P < 0.001$; $n = 80$ alarm responses by 20 babblers (table S2)] and longer to all alarms than to control nonalarm calls [Tukey tests, $^{**}P < 0.001$ (table S2)]. NS, not significant.



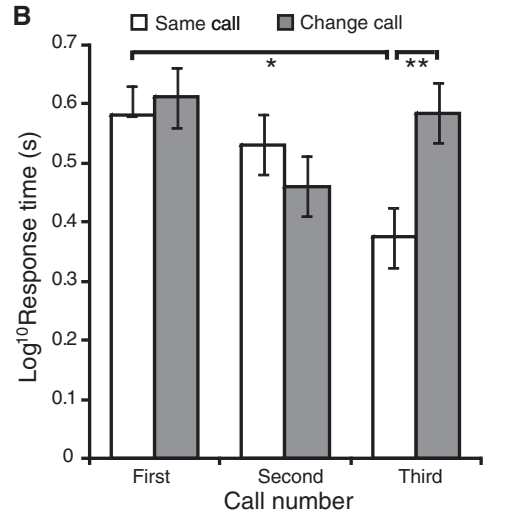


Fig. 3. Effect of alarm variation on target response. (**A**) Spectrograms of call treatments (i to iv) played to pied babblers to determine whether targets reduce their alarm response when the same alarm call is repeated (i and ii) but not when it is changed (iii and iv). (**B**) Response duration declined when the same alarm call was made three times in succession [LMM interaction: $\chi^2_1 = 5.73$, $P = 0.004$, $n = 264$ alarm responses by 22 babblers; Tukey test, $^*P < 0.004$ (table S3)] but not when the third call was changed [Tukey test, $P < 0.996$ (table S3)], regardless of whether drongo-specific or mimicked starling alarm calls were made. The response to the third call was longer when changed than when it was kept the same [Tukey test, $^{**}P < 0.002$ (table S3)].

to steal the abandoned food (*11*, *12*). Drongos associate with a target species for several hours each day, during which time they give multiple true and false alarms and food theft accounts for 23% of drongo biomass intake (*17*).

Drongos produce a diversity of alarm call types (*11*). Individual repertoires range from 9 to 32 different calls (mean ± SE = 17 ± 1), and a total of 51 different alarm call types have been recorded in false alarms (*11*). Six calls are drongo-specific, but 45 mimic other species' alarm calls, including those of target species (*11*). Highlighting the importance of alarm mimicry, drongos exclusively produce mimicked alarm calls in 42% of false alarms and combine mimicked and drongo-specific alarm calls in a further 27% of false alarms (*11*). However, the specific benefit drongos gain from producing such a large array of mimetic alarm calls is unclear.

One possibility is that target species are more likely to be deceived by mimicked versions of their own calls than by drongo-specific alarm calls. Observations of 688 food theft attempts made during 847.5 hours of focal observations on 64 drongos (10.75 ± 1.62 attempts per drongo) (*7*) revealed that drongos able to mimic a specific target's alarm call more frequently mimicked the target in food-theft attempts on them, as compared with their attempts on other species (Fig. 1 and table S1). We experimentally tested our hypothesis that mimicry of target species alarms increases the intensity of target responses by playing four different call types at 20-min intervals [equivalent to natural alarm rates (*7*)] to individual pied babblers (n = 20 babblers in 10 groups) experimentally provisioned with a food item. The drongo-generated calls were (i) a nonalarm territory call (control), (ii) a drongo-specific alarm call, (iii) a mimicked Cape glossy starling (*Lamprotornis nitens*) alarm call (other species), and (iv) a mimicked pied babbler alarm call (target species) (Fig. 2A). Mimicked starling alarms were selected because starlings are common throughout the study site and are frequently mimicked by drongos (*11*). We measured the babbler's response time (seconds) from when a call was played and the individual stopped handling the food item (looked up, moved toward cover, or combined these behaviors) to when it resumed foraging (0 s when calls ignored) (*7*).

Babblers were slower to resume foraging in response to mimicked alarm calls than to drongo-specific alarm calls (Fig. 2B and table S2). Alarm mimicry therefore increased target deception, but there was no difference between the babbler's response to their own mimicked alarms relative to those of starlings (table S2). Starlings may be reliable alarm callers, accurately signaling threatening predators. Nevertheless, in a dynamic environment where drongos target numerous species and the value of different alarm calls is likely to vary with recent usage (*15*), target-specific mimicry could represent a reliable heuristic rule of thumb (*18*).

Although these results indicate that alarm mimicry by drongos increases target deception, targets are still predicted to habituate to repeated use of the same false alarm call regardless of its type (*5*). We used a second experiment to test our hypothesis that, by flexibly varying their false alarm calls during repeated food-theft attempts, drongos maintain the intensity of target responses. We played four treatments of three alarm calls to individual babblers (n = 22 babblers in 11 groups) provisioned with a food item and measured their response time (3 days between treatments and 20 min between calls). Of the four treatments, two contained three alarm calls of the same type, either drongo-specific or mimicked starling, whereas in the other two treatments the third call was changed to the opposite type, either drongo-specific to mimicked starling or vice versa (Fig. 3A) (*7*). Babblers decreased their response when the same alarm call type was played three times in succession but maintained their response when the third alarm was changed (Fig. 3B and table S3). Furthermore, the duration of their response to the third alarm was greater when it was changed relative to when it was kept the same (Fig. 3B and table S3).

Drongos thus could benefit by flexibly varying their call type to maintain target deception. We tested whether drongos exploit this possibility under natural circumstances by changing their false alarm calls during repeated food-theft attempts on a target and, more specifically, whether they change their call type when their previous food-theft attempt failed. We observed repeated food-theft attempts by drongos on the same target on 151 occasions (n = 42 drongos) and found that they changed their alarm call type on 74 ± 6% of occasions (*7*). In particular, drongos were more likely to change the type of false alarm call when their previous food-theft attempt failed (Fig. 4A and table S4). Furthermore, when drongos changed their false alarm-call type after a failed food-theft attempt, they were more likely to successfully steal food than when they made the same alarm call (Fig. 4B and table S5).

Our results suggest that, by flexibly varying their deceptive signal, drongos benefit in two ways. First, they produce signals more likely to deceive their targets. Second, they avoid target habituation to repeated use of the same deceptive signal and thereby evade the frequency-dependent constraints that typically limit payoffs from deceptive communication. Such benefits are analogous to those provided by antigenic variation, whereby infectious organisms, including those responsible for influenza, sleeping sickness (*Trypanosomiasis brucei*), and malaria (*Plasmodium falciparum*), vary cell-surface proteins to evade host immune responses (*19*).

Flexible variation maintained deception because target habituation to one alarm signal did not result in habituation to other signals. This finding is similar to that of research on habituation mechanisms in bird song systems (*20*). However, flexible variation might not maintain deception indefinitely because deceived species may ultimately habituate to all the deceptive signals in an individual's repertoire. Furthermore, species able to recognize individuals could combat deception by assessing signaler reputation across different signals (*21*, *22*). Selection may therefore favor mechanisms that enable deceivers to elaborate their signal repertoire and disguise their identity.

Our results suggest a deceptive function for vocal mimicry, a behavior for which few adaptive benefits have been demonstrated (*23*). Further, we found that drongos specifically change their alarm calls to both mimic targets and exploit feedback from target alarm responses, thereby increasing their success. This shows that attending to feedback in deceptive communication may be adaptive, complementing recent research on feedback in other communication systems where individuals repeatedly interact (*21*, *24*, *25*). Such deceptive flexibility and the drongos' production of both honest and dishonest alarms, termed tactical deception (*26*), are considered evidence that species possess cognitive abilities, including mental state attribution, akin to theory of mind (*26*–*28*). However, the evolved mechanisms responsible for similar behavior in different species are not necessarily the same and likely vary with species' ecology. Determining what different mechanisms enable the production of complex behavior and when these are selectively advantageous remain key questions in evolutionary biology.

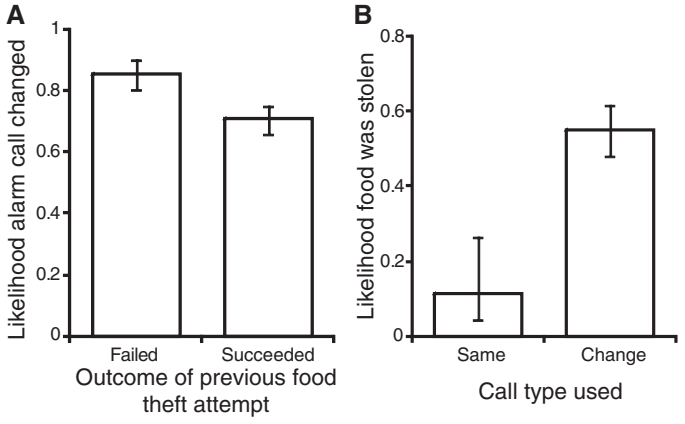


Fig. 4. Repeated food-theft attempts by individual drongos. (**A**) Drongos were more likely to change their false alarm call type in food-theft attempts when they had failed in their previous attempt on that target species [GLMM (binomial): χ^2_1 = 2.15, P = 0.039, n = 151 (table S4)] and (**B**) were more successful when they did so compared with when they made the same call type [GLMM (binomial), χ^2_1 = 2.01, P = 0.045, n = 60 (table S5)].

References and Notes

1. A. Zahavi, *J. Theor. Biol.* **53**, 205–214 (1975).
2. A. Grafen, *J. Theor. Biol.* **144**, 517–546 (1990).
3. M. Broom, G. D. Ruxton, H. M. Schaefer, *Proc. Biol. Sci.* **280**, 20131560 (2013).
4. R. A. Johnstone, A. Grafen, *Anim. Behav.* **46**, 759–764 (1993).
5. D. W. Pfennig, W. R. Harcombe, K. S. Pfennig, *Nature* **410**, 323 (2001).
6. R. A. Fisher, *The Genetical Theory of Natural Selection* (Clarendon, Oxford, 1930).
7. R. Thorogood, N. B. Davies, *Science* **337**, 578–580 (2012).
8. P. M. Sheppard, *Cold Spring Harb. Symp. Quant. Biol.* **24**, 131–140 (1959).
9. R. R. Jackson, R. S. Wilcox, *Behaviour* **127**, 21–36 (1993).
10. N. E. Langmore, G. Maurer, G. J. Adcock, R. M. Kilner, *Evolution* **62**, 1689–1699 (2008).
11. T. Flower, *Proc. Biol. Sci.* **278**, 1548–1555 (2011).
12. A. R. Ridley, N. J. Raihani, *Behav. Ecol.* **18**, 324–330 (2007).
13. C. A. Munn, *Nature* **319**, 143–145 (1986).
14. See supplementary materials on *Science* Online.
15. R. D. Magrath, B. J. Pitcher, J. L. Gardner, *Behav. Ecol.* **20**, 745–752 (2009).
16. A. N. Radford, M. B. V. Bell, L. I. Hollén, A. R. Ridley, *Evolution* **65**, 900–906 (2011).
17. T. P. Flower, M. F. Child, A. R. Ridley, *J. Anim. Ecol.* **82**, 245–255 (2013).
18. J. Hutchinson, G. Gigerenzer, *Behav. Process.* **69**, 97–124 (2005).
19. K. W. Deitsch, S. A. Lukehart, J. R. Stringer, *Nat. Rev. Microbiol.* **7**, 493–503 (2009).
20. S. Dong, D. F. Clayton, *Neurobiol. Learn. Mem.* **92**, 183–188 (2009).
21. R. Bshary, A. S. Grutter, *Nature* **441**, 975–978 (2006).
22. D. L. Cheney, R. M. Seyfarth, *Anim. Behav.* **36**, 477–486 (1988).
23. L. A. Kelley, R. L. Coe, J. R. Madden, S. D. Healy, *Anim. Behav.* **76**, 521–528 (2008).
24. E. S. Fortune, C. Rodríguez, D. Li, G. F. Ball, M. J. Coleman, *Science* **334**, 666–670 (2011).
25. G. L. Patricelli, J. A. C. Uy, G. Walsh, G. Borgia, *Nature* **415**, 279–280 (2002).
26. A. Whiten, R. W. Byrne, *Behav. Brain Sci.* **11**, 233 (1988).
27. R. W. Mitchell, N. S. Thompson, Eds., *Deception: Perspectives on Human and Nonhuman Deceit* (State Univ. New York Press, Albany, NY, 1986).
28. D. L. Cheney, R. M. Seyfarth, *How Monkeys See the World: Inside the Mind of Another Species* (Univ. Chicago Press, Chicago, 1990).

Acknowledgments: The Kalahari Research Trust, T. H. Clutton-Brock, and M. Manser kindly provided study site access. Northern Cape Conservation provided research permission (FAUNA 270/2008), and the University of Cape Town provided ethical permission (2010/V20/TF). We thank N. Davies for supervision and M. Nelson-Flower, A. Thornton, R. Sutcliffe, J. Samson, and three anonymous reviewers for their help and comments. Work was funded by a Natural Environment Research Council grant awarded to T.P.F. Data available from the Dryad Digital Repository (10.5061/dryad.f60j5).

Supplementary Materials

www.sciencemag.org/content/344/6183/513/suppl/DC1
Materials and Methods
Tables S1 to S5
References (*29*–*34*)

13 December 2013; accepted 2 April 2014
10.1126/science.1249723

Greater Sensitivity to Drought Accompanies Maize Yield Increase in the U.S. Midwest

David B. Lobell,[1]* Michael J. Roberts,[2] Wolfram Schlenker,[3] Noah Braun,[4] Bertis B. Little,[5] Roderick M. Rejesus,[4] Graeme L. Hammer[6]

A key question for climate change adaptation is whether existing cropping systems can become less sensitive to climate variations. We use a field-level data set on maize and soybean yields in the central United States for 1995 through 2012 to examine changes in drought sensitivity. Although yields have increased in absolute value under all levels of stress for both crops, the sensitivity of maize yields to drought stress associated with high vapor pressure deficits has increased. The greater sensitivity has occurred despite cultivar improvements and increased carbon dioxide and reflects the agronomic trend toward higher sowing densities. The results suggest that agronomic changes tend to translate improved drought tolerance of plants to higher average yields but not to decreasing drought sensitivity of yields at the field scale.

Drought is currently one of the main constraints to crop production in rainfed systems throughout the world, including in the United States. As a result, much breeding and agronomic research has been designed, at least in part, to improve performance under drought conditions (*1*). However, success in experimental fields does not always easily or completely translate to yield progress in farmers' fields because drought characteristics in farmers' commercial fields can differ substantially from trial conditions (*2*) and because different drought scenarios can favor different genotypes or management practices (*3*, *4*).

In the United States, which typically supplies 40% of global annual maize production and 35% of global soybean production (*5*), several factors could be affecting drought sensitivity in farmers' fields. On the positive side, increased use of low or no-till systems has likely increased soil moisture in dry years, and increasing CO_2 concentrations typically lead to higher plant water-use efficiencies, thereby reducing drought sensitivity (*6*, *7*). At the same time, in maize, modern genetics has facilitated increased sowing density because individual plants are better able to develop ears under stress (*8*, *9*), roots are able to penetrate deeper and access more water (*10*), and genetically engineered pest resistance has reduced root damage from soil insects (*11*). All of these have contributed to historical gains in biomass and yields, but increased density can be detrimental under drought conditions because of excessive stress exposure for individual plants (*12*). Thus, the net effect of recent genetic, agronomic, and environmental changes on drought sensitivity remains an open empirical question.

An obstacle to measuring progress in farmers' fields has been lack of accurate field-level data on both environmental conditions and yield performance that span a range of drought conditions and time. Here, we use a data set of field-level records

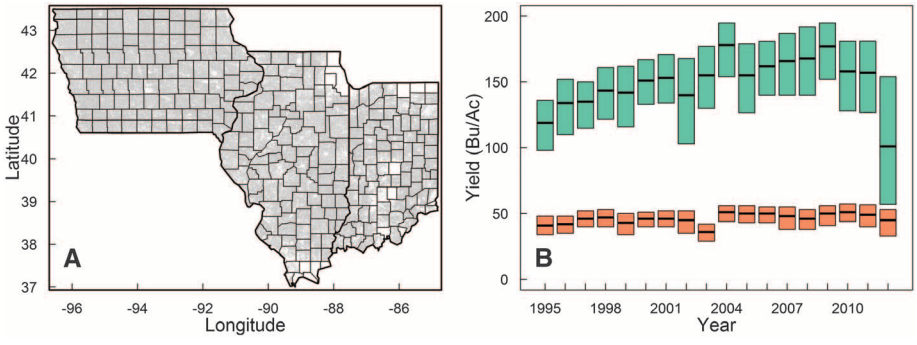


Fig. 1. Study area and yield distributions. (**A**) Map of main study region, with individual points showing locations of fields for maize in the USDA data. (**B**) Summary statistics of field-level maize (green) and soybean (orange) yields over the study period. Horizontal bands indicate sample median, and bars show interquartile range (25th to 75th percentile). Bu/Ac, bushels per acre.

[1]Department of Environmental Earth System Science and Center on Food Security and the Environment, Stanford University, Stanford, CA 94305, USA. [2]Department of Economics, University of Hawaii at Manoa, Honolulu, HI 96822, USA. [3]School of International and Public Affairs, Columbia University, New York, NY 10027, USA. [4]Department of Agricultural and Resource Economics, North Carolina State University, Raleigh, NC 27695, USA. [5]Department of Mathematics, Office of the Provost, and Division of Academic Affairs, Tarleton State University, Stephenville, TX, USA. [6]The University of Queensland, Queensland Alliance For Agriculture and Food Innovation, Brisbane, Qld 4072, Australia.

*Corresponding author. E-mail: dlobell@stanford.edu

on yields and sowing dates collected by the U.S. Department of Agriculture (USDA) Risk Management Agency since 1995 (Fig. 1) and combine that with 800-m-resolution daily weather data sets (see supplementary materials). These data are used to identify and group "location-year" combinations that have similar drought stress levels and measure yield progress over time for different stress levels. The study was conducted for maize and soybean, the two major field crops in the region.

Tracking yield progress at different levels of stress requires a clear and accurate measure of stress experienced by a crop. In field trials, stress levels are often quantified as the average yield across all cultivars grown at a given site and season, sometimes referred to as an environment index (*13*, *14*). A plot of a cultivar's yield versus environment index is then used to measure the sensitivity of that cultivar's yield to stress. To define the environment index, we use the USDA data to calibrate a statistical model relating yields to weather. To allow for potential nonlinearities, asymmetries, and interactions between different variables, we employ multivariate adaptive regression splines (*15*). As candidate predictors for the regression splines, we use four weather variables [minimum and maximum temperatures, precipitation, and daytime vapor pressure deficit (VPD)] averaged over five successive 30-day periods spanning from 30 days before sowing to 120 days after sowing, resulting in a total of 20 candidate weather predictors (*16*). VPD is a widely used measure of atmospheric water demand that depends on air temperature and humidity and has a strong influence on plant growth rates in these systems (*17*, *18*). We also repeated the analysis using the Palmer Drought Severity Index (*16*).

Figures S1 and S2 summarize the regression model calibrated for the maize and soybean data, respectively. The maize model selected six variables, with the most influential being VPD in the third month after sowing, which is typically July for a field sown in early May. An increase in VPD has a negative and nonlinear effect, with high values especially damaging, both of which are consistent with physiological understanding and previous empirical and crop modeling studies (*17*, *19*). Some of the effects of high VPD may be associated with direct effects on pollen and grain set (*20*), but this mechanism appears to play a minor role in this region relative to VPD effects on water stress and overall plant growth rates (*17*). For soybean, five variables were selected, with VPD again the most important, and with precipitation playing a more important role than in maize.

The regression models are then used to calculate an environment index for each field in each year, which is defined as the predicted yield assuming a constant level of technology (year is fixed at 2000 for all predictions). As seen for maize in Fig. 2A (or fig. S3 for soybean), most years have the full range of conditions experienced throughout the region, but the exact locations of low or high stress change each year.

Mean yields for each quintile of the environment index exhibit significantly positive trends ($P < 0.05$) over time in absolute yields for all stress quintiles (Fig. 2B). In an absolute sense, yields under drought conditions have steadily improved over time, as emphasized in previous analyses of improved stress tolerance in maize (*8*, *9*). However, yields have been rising more slowly at the lowest quintile than other stress levels, even when expressed as a percentage of yields at the start of the study period (1995), so that yields in the most stressed quintile have been declining relative to other quintiles (Fig. 2C).

A possible confounding factor in the above analysis is the fact that some locations are more frequently exposed to stress than others (Fig. 2A),

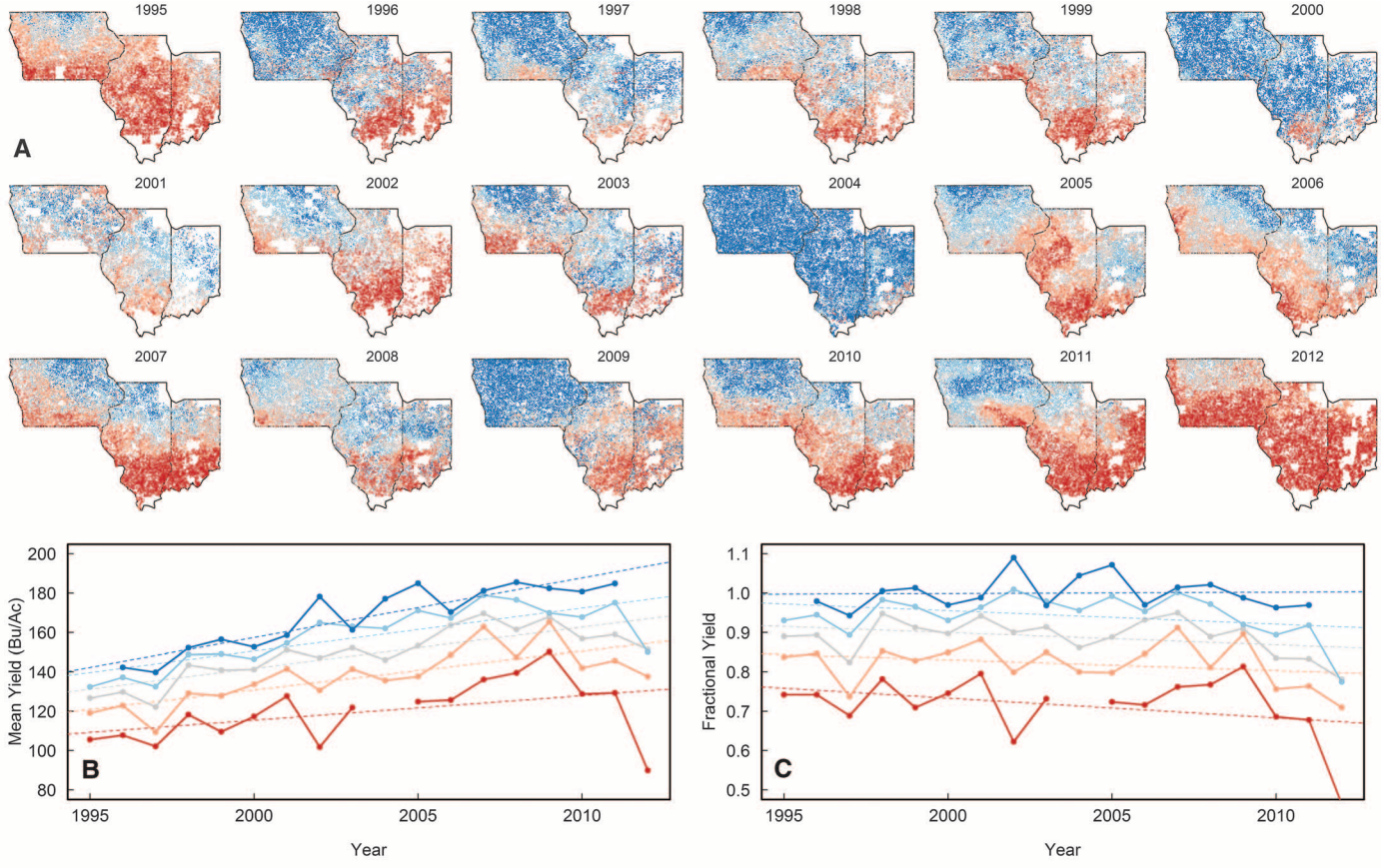


Fig. 2. Maize yields in different environments over time. (**A**) The locations of environment index quintiles for maize for each study year. Red indicates the lowest environment index values, indicating the worst yield conditions, and blue indicates the best conditions. (**B**) Average maize yields (Bu/Ac) for each environment index quintile by year. Dashed lines show best-fit linear regression for each quintile. (**C**) Same as in (B) but expressed as fraction of trend yield under good conditions (i.e., highest quintile).

and therefore trend differences that arise from location-specific factors that are unrelated to stress could either obscure or enhance any trend differences due to changes in stress sensitivity. As a robustness check, we therefore repeat the analysis of Fig. 2B, but first removing all time trends for each county and for all variables. This "detrended" analysis therefore considers whether positive yield anomalies when conditions are anomalously good have been rising over time. Consistent with Fig. 2B, we find that absolute anomalies are indeed growing over time (fig. S4).

Conditions of high VPD 61 to 90 days after sowing are the most important driver of a low environment index in this region, and we find that yield trends for the highest quintile of VPD are significantly lower than for the lowest quintile ($P = 0.04$) (Fig. 3A). Importantly, this finding is robust to the exclusion of 2012, which was a particularly low-yielding and high-VPD year (fig. S5). In contrast, the second most important factor for maize yields, late sowing, exhibits yield trends that are actually higher than trends for the more favorable early sow dates (Fig. 3B), although these differences are not significant. Thus, the overall slower progress under low-yielding conditions is the net effect of significantly slower progress for high VPD relative to low VPD, countered by slightly better progress for late relative to early sowing. Similar to maize, yield trends in soybean are higher in absolute value under good conditions than in poor conditions (fig. S5). However, soybean yield trends do not exhibit any significant dependence on VPD or other environment index predictors.

Repeating the analysis for the Palmer drought index rather than VPD leads to qualitatively similar results, with yield trends lower for the lowest quintile of the Palmer index (fig. S6). However, the Palmer index is a poorer predictor of yields than VPD, and as a result trend differences between low and high values of the Palmer index are less statistically significant. This agrees with previous work showing that the Palmer index, although a common variable used to measure drought, is actually a relatively poor predictor of crop water stress as simulated by a crop model (*21*).

As an alternative test of whether sensitivity to VPD has indeed been increasing over time in this region for maize, a cross-sectional regression model between yield and VPD was fit separately for each year. The coefficient on VPD becomes increasingly negative over time, with a significant negative time slope even if excluding 2012, and even if including county-fixed effects in the cross-section regressions to control for omitted variables (Fig. 4A and fig. S7). All other predictors of maize yields showed insignificant time trends in cross-sectional regressions (fig. S7).

Although this study is focused on the core Corn Belt states, USDA data are also available for other states. When our analysis is repeated for a broader group of Corn Belt states, the slower trends for high VPD persists (fig. S8). We also consider separately the western Corn Belt, where seed companies have arguably focused more of their efforts to test and release drought-tolerant seeds in the past decade (*22*), and one might expect more progress for drought conditions. Figs. S9 and S10 show the analysis repeated for rainfed maize fields in Nebraska, South Dakota, and Kansas. Similar variables are identified as important for maize in this region, with VPD 61 to 90 days after sowing the most critical, and precipitation in that period also important. The disparity between yield trends in low- and high-stress conditions is even more evident in this region than in the eastern states, with significantly slower yield progress under high VPD conditions.

One likely explanation for the increased sensitivity to VPD is the continuing trend toward denser sowing of maize crops. In Illinois, for example, average plant populations have gone from slightly under 24,000 plants per acre in 1995 to 30,000 by 2012 (a 25% increase over our study period) (*23*, *24*). Similar trends have occurred in other Corn Belt states (*23*). To evaluate this

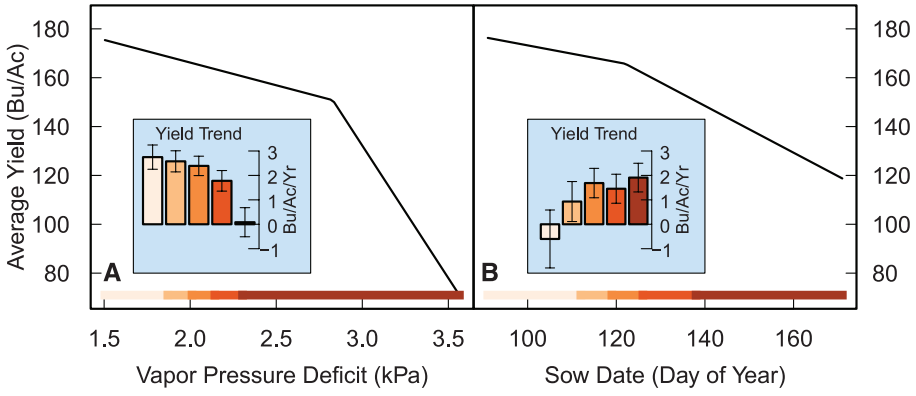


Fig. 3. Effects of vapor pressure deficit (VPD) and sowing date on maize yields. (**A**) Yield response curves for VPD from multivariate adaptive regression spline model (see fig. S1 for explanation). Colors at bottom of figure indicate ranges for each quintile of that variable. (Inset) Yield trends for 1995 to 2012 corresponding to each quintile of VPD. (**B**) Same as in (A) but for sowing date. Error bars, mean ± 1 SE. Time trends for the highest quintile of VPD are significantly lower than for the lowest quintile ($P = 0.04$). Response curves and yield trends for other predictors and for soybean are shown in figs. S1, S2, and S5.

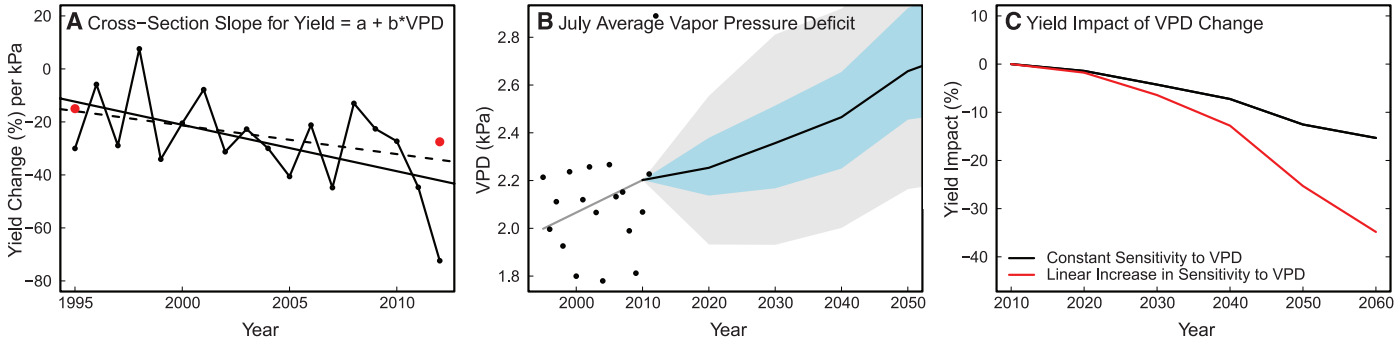


Fig. 4. Changes in vapor pressure deficit and its impacts. (**A**) Estimates of maize yield sensitivity to VPD 61 to 90 days after sowing from a cross-sectional regression for each year in the study period, along with best-fit trend lines with (solid) or without (dashed) including 2012 for computing the trend. Red dots indicate sensitivity estimates from APSIM simulations with sowing densities corresponding to the start and end of the study period. (**B**) Average July VPD in the study region for historical and projected periods. Dots show individual year observations, gray line shows linear trend for 1995 to 2012, black line shows mean VPD projected using 29 climate models, blue shading indicates 25th to 75th percentile of model projections, and gray shading indicates 5th to 95th percentiles. (**C**) Estimated impact of mean VPD projections on average maize yields using either constant yield sensitivity of −27.5% per kPa or a linear increase in sensitivity at the historical rate of 7% per kPa per decade.

mechanism more directly, we simulated maize yields using the Agricultural Production Systems Simulator (APSIM) model for a representative site under sowing densities of 24,000 and 35,000 plants per acre, or 6.0 and 7.5 plants per m^2, respectively. Simulations under higher density exhibited higher average yields, but significantly higher sensitivity to VPD than simulations for lower density (fig. S11). The estimated yield response to high VPD 61 to 90 days after sowing in the simulations (–15% and –28% per kPa, respectively) agreed with the cross-sectional analysis of the USDA data (Fig. 4A). The importance of density is also suggested by the fact that soybeans, which show weaker evidence of increased drought sensitivity, have exhibited relatively constant sowing densities since 1995 in this region (*24*, *25*).

Our results agree with the general notion that as farmers become more adept at removing all nonwater constraints to crop production, the sensitivity to drought generally increases (*26*). Given the dominant role of temperature (via VPD) in driving water stress in this region, our results are also consistent with the finding that heat sensitivity of maize yields in Indiana increased in recent decades (*27*). One implication is that climate change effects may be more severe than predicted by models that assume current crop genetics and management. Climate model projections indicate that July VPD for this region will become more severe, with an expected increase in average VPD of roughly 20% over the next 50 years (Fig. 4B), driven both by higher temperatures and reduced relative humidity. At current VPD sensitivity, these VPD trends would reduce yields by about 15% over the next 50 years. If maize yields continue to become increasingly sensitive to VPD, then yield losses from VPD trends could be as much as 30% (Fig. 4C).

Overall, we find no evidence to support the notion that farmers' yields are becoming less sensitive to drought in the main maize- and soybean-growing states. Instead, we find evidence that drought sensitivity in maize, in particular sensitivity to high VPD, has steadily increased over the past 18 years. Whether the recent push by seed companies to develop and market drought-tolerant seeds will reverse this trend remains to be seen. It is clear that cultivar changes are not the only relevant factor for changes in drought sensitivity, because agronomic trends—often facilitated by the cultivar changes—can be as or more important. It is also clear that new, field-level data sets on farm performance can complement field-based experiments in efforts to understand changes in drought sensitivity in this important production region.

References and Notes

1. H. Campos, M. Cooper, J. E. Habben, G. O. Edmeades, J. R. Schussler, *Field Crops Res.* **90**, 19–34 (2004).
2. C. M. Löffler *et al.*, *Crop Sci.* **45**, 1708 (2005).
3. K. Chenu, R. Deihimfard, S. C. Chapman, *New Phytol.* **198**, 801–820 (2013).
4. F. Tardieu, *J. Exp. Bot.* **63**, 25–31 (2012).
5. Food and Agriculture Organization of the United Nations (FAO), FAO Statistical Databases (2013); http://faostat.fao.org.
6. J. McGrath, D. B. Lobell, *Glob. Change Biol.* **17**, 2689–2696 (2011).
7. R. J. Donohue, M. L. Roderick, T. R. McVicar, G. D. Farquhar, *Geophys. Res. Lett.* **40**, 3031–3035 (2013).
8. D. N. Duvick, *Adv. Agron.* **86**, 83–145 (2005).
9. M. Tollenaar, J. Wu, *Crop Sci.* **39**, 1597 (1999).
10. G. Hammer *et al.*, *Crop Sci.* **49**, 299 (2009).
11. NRC, *The Impact of Genetically Engineered Crops on Farm Sustainability in the United States* (National Research Council, Washington, DC, 2010).
12. D. J. Lyon, G. L. Hammer, G. B. McLean, J. M. Blumenthal, *Agron. J.* **95**, 884 (2003).
13. M. Tollenaar, E. Lee, *Field Crops Res.* **75**, 161–169 (2002).
14. M. Bänziger, P. S. Setimela, D. Hodson, B. Vivek, *Agric. Water Manage.* **80**, 212–224 (2006).
15. J. H. Friedman, *Ann. Stat.* **19**, 1–67 (1991).
16. Materials and methods are available as supplementary materials on *Science* Online.
17. D. B. Lobell *et al.*, *Nat. Clim. Change* **3**, 497–501 (2013).
18. J. D. Ray, R. W. Gesch, T. R. Sinclair, L. Hartwell Allen, *Plant Soil* **239**, 113–121 (2002).
19. B. Barnabás, K. Jäger, A. Fehér, *Plant Cell Environ.* **31**, 11–38 (2008).
20. A. E. Fonseca, M. E. Westgate, *Field Crops Res.* **94**, 114–125 (2005).
21. P. Woli, J. W. Jones, K. T. Ingram, C. W. Fraisse, *Agron. J.* **104**, 287 (2012).
22. C. D. Messina, D. Podlich, Z. Dong, M. Samples, M. Cooper, *J. Exp. Bot.* **62**, 855–868 (2011).
23. National Agriculture Statistics Service, Corn Objective Yield Survey Data, 1992-2006 (NASS, U.S. Department of Agriculture, Washington, DC, 2007); http://usda.mannlib.cornell.edu/MannUsda/viewDocumentInfo.do?documentID=1749.
24. National Agriculture Statistics Service, Soybean Objective Yield Survey Data, 1992-2006 (NASS, U.S. Department of Agriculture, Washington, DC, 2007); http://usda01.library.cornell.edu/usda/current/SoyObjYield/SoyObjYield-07-27-2007.pdf.
25. National Agriculture Statistics Service, 2013 Illinois Annual Statistics Bulletin (NASS, U.S. Department of Agriculture, Washington, DC, 2013); www.nass.usda.gov/Statistics_by_State/Illinois/Publications/.Annual_Statistical_Bulletin/2013/toc.html#fieldcrops.
26. D. J. Connor, R. S. Loomis, K. G. Cassman, *Crop Ecology: Productivity and Management in Agricultural Systems* (Cambridge Univ. Press, Cambridge, 2011).
27. M. J. Roberts, W. Schlenker, in *The Economics of Climate Change: Adaptations Past and Present*, G. D. Libecap, R. H. Steckel, Eds. (Univ. of Chicago Press, Chicago, 2011), pp. 225–251.

Acknowledgments: We thank G. McLean for assistance with APSIM simulations and acknowledge the modeling groups, the Program for Climate Model Diagnosis and Intercomparison, and the Working Group on Coupled Modelling of the World Climate Research Programme (WCRP) for their roles in making available the WCRP CMIP5 multimodel data set. This work was supported by NSF grant SES-0962625 and National Oceanic and Atmospheric Administration grant NA11OAR4310095. B.B.L. was supported by a Research Services Agreement from USDA's Risk Management Agency, and G.L.H. by grant LP100100495 from the Australian Research Council. Data used in this study are available as supplementary materials on *Science* Online.

Supplementary Materials

www.sciencemag.org/content/344/6183/516/suppl/DC1
Materials and Methods
Figs. S1 to S12
Database S1
References (*28*, *29*)

28 January 2014; accepted 20 March 2014
10.1126/science.1251423

Polarization of the Effects of Autoimmune and Neurodegenerative Risk Alleles in Leukocytes

Towfique Raj,[1,2,3,4] Katie Rothamel,[5] Sara Mostafavi,[6] Chun Ye,[4] Mark N. Lee,[3,4] Joseph M. Replogle,[1,4] Ting Feng,[5] Michelle Lee,[1] Natasha Asinovski,[5] Irene Frohlich,[1] Selina Imboywa,[1] Alina Von Korff,[1] Yukinori Okada,[2,3,4,7,8] Nikolaos A. Patsopoulos,[1,2,3,4] Scott Davis,[5] Cristin McCabe,[1,4] Hyun-il Paik,[5] Gyan P. Srivastava,[1,2,3,4] Soumya Raychaudhuri,[2,3,4,9] David A. Hafler,[4,10] Daphne Koller,[6] Aviv Regev,[4,11] Nir Hacohen,[4,12] Diane Mathis,[5] Christophe Benoist,[5]* Barbara E. Stranger,[13,14]* Philip L. De Jager[1,2,3,4]*

To extend our understanding of the genetic basis of human immune function and dysfunction, we performed an expression quantitative trait locus (eQTL) study of purified $CD4^+$ T cells and monocytes, representing adaptive and innate immunity, in a multi-ethnic cohort of 461 healthy individuals. Context-specific cis- and trans-eQTLs were identified, and cross-population mapping allowed, in some cases, putative functional assignment of candidate causal regulatory variants for disease-associated loci. We note an over-representation of T cell–specific eQTLs among susceptibility alleles for autoimmune diseases and of monocyte-specific eQTLs among Alzheimer's and Parkinson's disease variants. This polarization implicates specific immune cell types in these diseases and points to the need to identify the cell-autonomous effects of disease susceptibility variants.

It is necessary to understand the functional consequences of disease-associated genetic variation as we strive to unravel the causal chain of events linking genetic risk factors to clinical syndromes. Because most disease-associated variants localize to noncoding regions of the genome, an initial role of their function can be inferred from their proximity to a gene and association to gene expression levels (*1*–*6*) or to epigenomic features derived from representative tissues and cell types (*7*, *8*). Given the central role of inflammation in many diseases, we leveraged differences in the

genetic structure of human populations to systematically interrogate the role of peripheral blood cell types that represent the lymphoid ($CD4^+$ T lymphocyte) and myeloid ($CD14^+CD16^-$ monocyte) arms of the immune system. These distinct programs of gene expression were profiled as part of the of Immune Variation (ImmVar) Project.

We used a rigorous sampling and cell purification protocol, minimizing circadian and experimental noise, to generate gene expression profiles from blood cells of 461 healthy individuals sampled in Boston, Massachusetts, including African Americans (AA), European Americans (EU), and East Asian Americans (EA) (Table 1, fig. S1, and table S1) (see also supplementary materials and methods). We purified naïve $CD4^+$ $CD62L^{hi}$ T cells, chosen to minimize experiential or environment-linked variation in effector/memory pools. Similarly, $CD14^+CD16^-$ monocytes are a recent and short-lived cell population that is less likely to reflect an individual's life history. We quantified the extent of differential gene expression between each pairwise combination of populations using the V_{ST} statistic for each of the 19,114 genes passing quality control (fig. S2). V_{ST} (range: 0 to 1) is similar to the fixation index (F_{ST}): It quantifies the proportion of expression-level variance explained by population-level differences (*1*). The low median pairwise V_{ST} estimates (ranging from 0.005 to 0.009) suggest minimal gene expression variance between populations. Nonetheless, several genes are highly differentiated ($V_{ST} > 0.2$; top 1% of all V_{ST} scores) in expression between pairs of human populations (Fig. 1, A and B, and tables S2 and S3).

For each human population and cell type, we associated residual RNA expression phenotypes with genotyped or imputed (using reference haplotypes from The 1000 Genomes Project) (*9*) SNPs in a ±1-Mb window around the transcription start

Table 1. Significant cis-eQTLs detected at FDR = 0.05. N/A, not applicable.

Population	Monocyte		$CD4^+$ T cell		Shared
	No. of participants	No. of genes	No. of participants	No. of genes	No. of genes
European American	211	3090	213	2352	1178
African American	112	1318	112	722	259
East Asian	78	1181	82	592	215
≥Two populations	N/A	1352	N/A	739	328
Three populations	401	537	407	255	102
Nonredundant	401	3703	407	2672	1372
Meta-analysis	401	6210	407	4975	2789

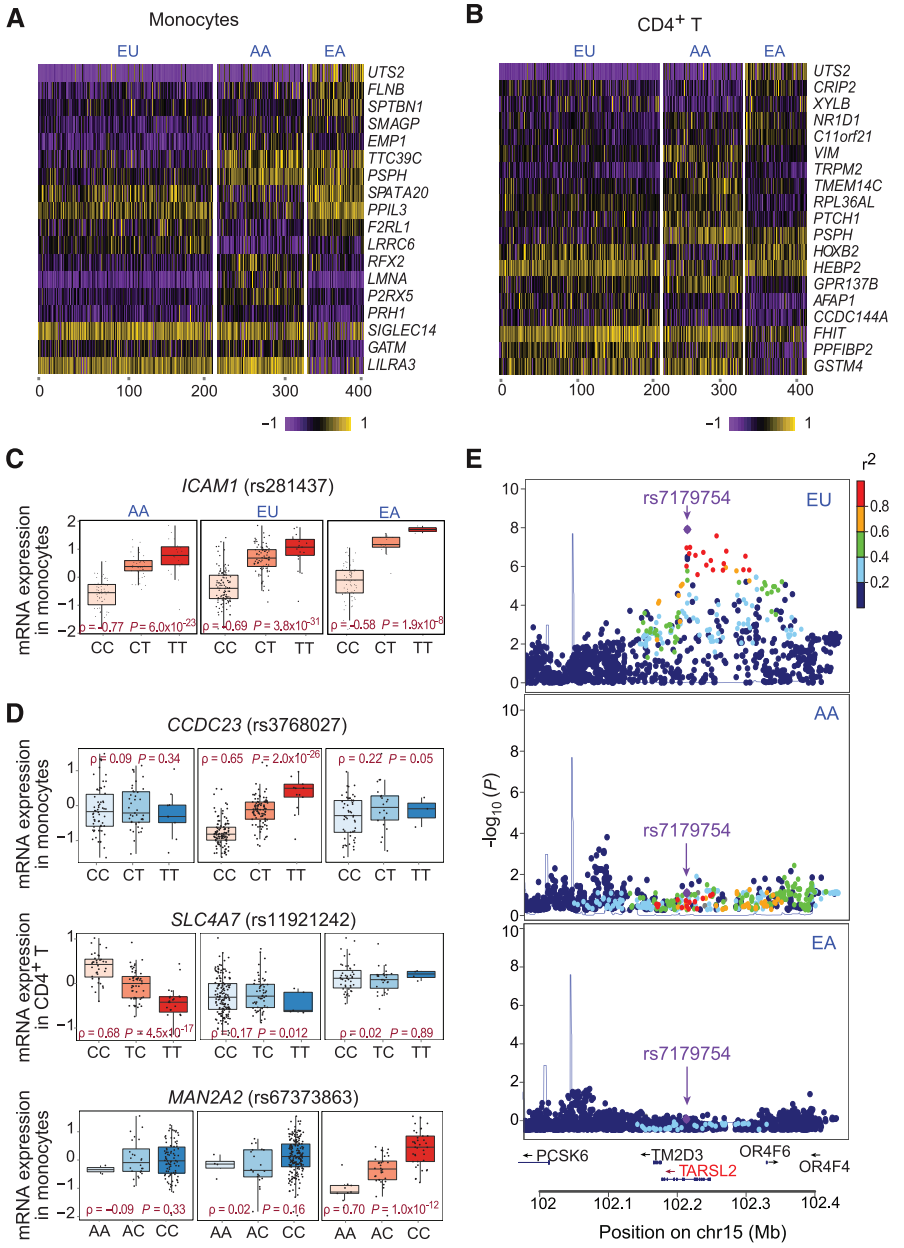


Fig. 1. Transcriptome variation among human populations. Heat map of genes that are differentially expressed ($V_{ST} > 0.2$) in monocytes (**A**) and T cells (**B**). (**C**) Example of a cis-eQTL shared across populations. (**D**) Examples of population-specific cis-eQTLs. (**E**) Regional association plots of an EU-specific cis-eQTL in the *TARSL2* locus.

[1]Program in Translational NeuroPsychiatric Genomics, Institute for the Neurosciences, Departments of Neurology and Psychiatry, Brigham and Women's Hospital, Boston, MA 02115, USA. [2]Division of Genetics, Department of Medicine, Brigham and Women's Hospital, Boston, MA 02115, USA. [3]Harvard Medical School, Boston, MA 02115, USA. [4]The Broad Institute of MIT and Harvard, Cambridge, MA 02142, USA. [5]Department of Microbiology and Immunobiology, Division of Immunology, Harvard Medical School, Boston, MA 02115, USA. [6]Department of Computer Science, Stanford University, Stanford, CA 94305, USA. [7]Department of Human Genetics and Disease Diversity, Graduate School of Medical and Dental Sciences, Tokyo Medical and Dental University, Tokyo, Japan. [8]Laboratory for Statistical Analysis, RIKEN Center for Integrative Medical Sciences, Yokohama, Japan. [9]Division of Rheumatology, Immunology and Allergy, Department of Medicine, Brigham and Women's Hospital, Boston, MA 02115, USA. [10]Departments of Neurology and Immunobiology, Yale School of Medicine, New Haven, CT 06520, USA. [11]Department of Biology, Massachusetts Institute of Technology, and Howard Hughes Medical Institute, Cambridge, MA 02139, USA. [12]Center for Immunology and Inflammatory Diseases, Massachusetts General Hospital, Charlestown, MA 02129, USA. [13]Section of Genetic Medicine, Department of Medicine, University of Chicago, IL 60637, USA. [14]Institute for Genomics and Systems Biology, University of Chicago, Chicago, IL 60637, USA.

*Corresponding author. E-mail: christophe_benoist@hms.harvard.edu (C.B.); bstranger@medicine.bsd.uchicago.edu (B.E.S.); pdejager@partners.org (P.L.D.J.)

site of each gene. Of the 19,114 genes tested in T cells, we detected 2352, 592, and 722 genes with evidence of a cis expression quantitative trait locus (eQTL) effect in EU, EA, and AA participants, respectively [false discovery rate (FDR) = 0.05] (Table 1 and tables S4 to S6). In monocytes, we detected more genes with cis-eQTLs: 3090, 1181, and 1318 in EU, EA, and AA participants, respectively (Table 1 and tables S7 to S9). Up to 70% of the genes with cis-eQTLs in monocytes replicate associations noted in a previous study (*4*) (fig. S3).

We used a Bayesian model average (BMA) and a hierarchical model (HM) (*10*) to jointly analyze the three human populations in a single framework. This method was applied separately to each cell type. With BMA-HM, we observed a high degree of cross-population sharing, with 96% [95% confidence interval (CI): 89 to 100%] and 94% (95% CI: 83 to 100%) of cis-eQTLs being shared by all three populations in monocytes

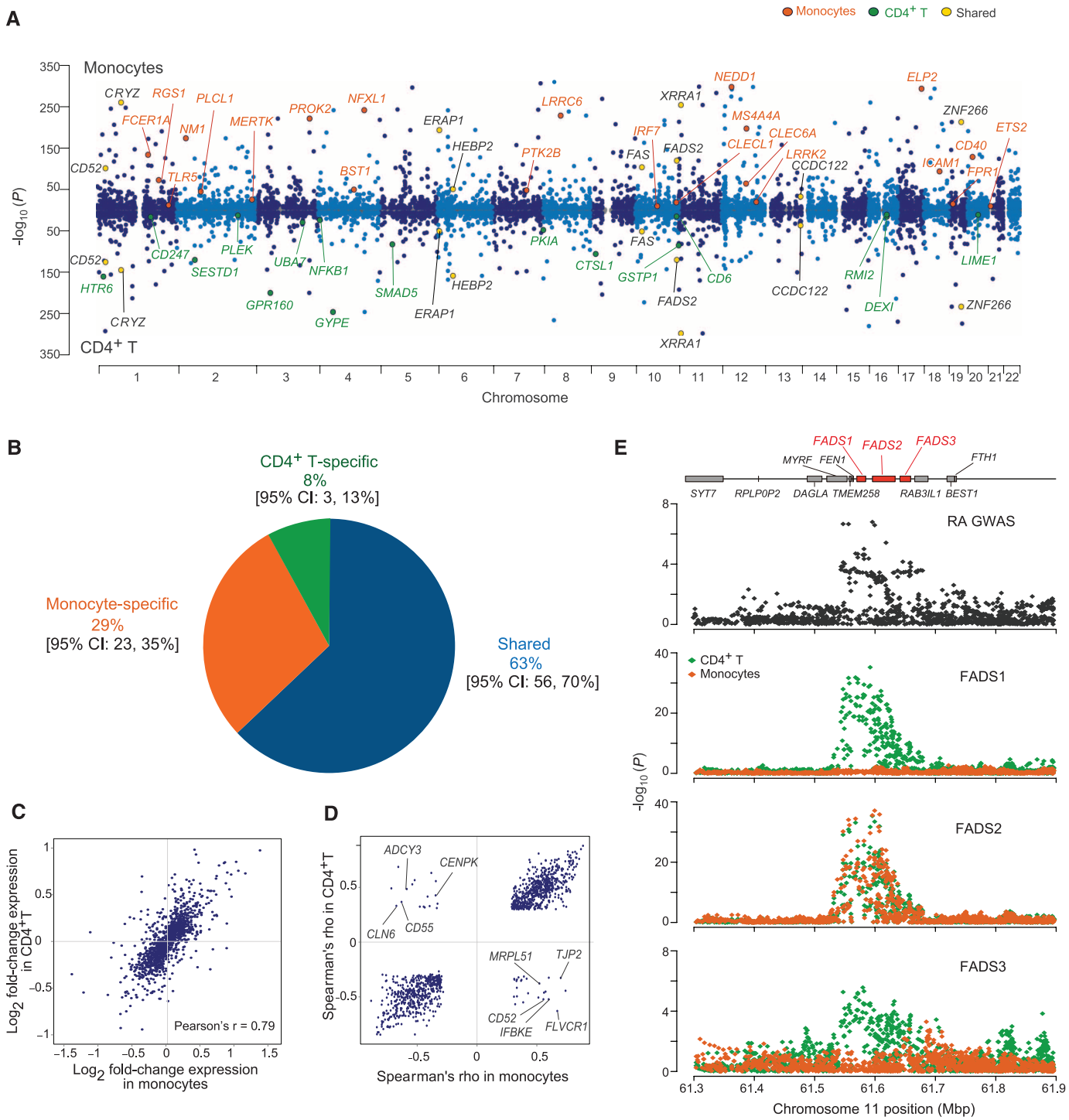


Fig. 2. Comparison of meta-analysis results from each cell type. (**A**) Manhattan plots of the most significant cis-eQTL per gene in monocytes (top) and T cells (bottom). The highlighted genes are representative of genes that (i) are shared, (ii) are cell-specific, or (iii) overlap with a disease association. (**B**) Inference of the proportion of cis-eQTL sharing between the two cell types using a Bayesian hierarchical model. (**C**) Expression-level fold-change for the most significant cis-eQTLs in T cells and monocytes. (**D**) Spearman's ρ (direction of allelic effect on gene expression) for the most significant cis-eQTLs shared by the two cell types. We highlight genes that have discrepant directions of effect. (**E**) Example of a context-specific cis-eQTL in a rheumatoid arthritis locus. Mbp, megabase pairs.

and T cells, respectively (Fig. 1C). A small number of population-specific cis-eQTLs were found (Fig. 1, D and E). Using a different approach, a measure of the proportion of overlap estimated from the enrichment of low *P* values (π_1) (*11*), we observe a similarly high degree of pairwise population sharing of cis-eQTLs (70 to 90%) (table S10).

The direction of allelic effect [that is, whether a given cis-eQTL is associated with an allele in the same (or opposite) direction across pairs of populations] is highly conserved: When the top single-nucleotide polymorphism (SNP)–gene pair is shared across pairs of populations, all cis-eQTLs are concordant, suggesting that causal regulatory variation generally affects gene expression in the same direction in all populations (figs. S4 and S5). Similarly, the effect size of shared cis-eQTLs is significantly correlated (Pearson's r = 0.70 to 0.87) in each pairwise combination of populations for the same cell type (figs. S6 and S7), suggesting little population-specific modulation of eQTL effect.

A meta-analysis maximized our power to detect cis-eQTLs in 401 participants with monocyte data and 407 with T cell data; we used a random effects model optimized to detect associations under heterogeneity (*12*). We detected 50% more genes with cis-eQTLs in the meta-analysis: 6210 genes in monocytes and 4975 genes in T cells (Fig. 2A and tables S11 and S12). Up to 17% of genes in monocytes and 14% of genes in T cells demonstrate multiple independent eQTL effects (figs. S8 and S9). In addition, among the genes with shared effects across populations, the number of candidate causal variants in strong linkage disequilibrium (LD) with the lead SNP was reduced by more than 50% to an average of 21.2 SNPs when an LD threshold of $r^2 > 0.8$ with the lead SNP is considered in the meta-analysis (fig. S10).

To identify trans-eQTLs in which a SNP is associated with expression of a distal gene (>1 Mb from the SNP or on a different chromosome), we performed a trans-eQTL meta-analysis in our data. At a conservative Bonferroni-corrected threshold of $P < 3 \times 10^{-12}$, we identified 482 trans-eQTL associations (427 are interchromosomal) involving 55 genes specific to monocytes, 31 genes specific to T cells, and 4 genes shared by both cell types (figs. S11 and S12 and tables S13 and S14). Our results support the existence of trans-eQTLs, but their mechanism remains largely unknown.

We assessed the proportion of cell type–specific cis-eQTLs with BMA-HM (*10*) and estimated that 29% of cis-eQTLs are specific to monocytes, whereas 8% are specific to T cells, with 63% shared across cell types (Fig. 2B). Using a different approach that estimates the likelihood of eQTL rediscovery (*11*), we obtain similar estimates of sharing: π_1 = 69, 68, and 62% in the EU, AA, and EA participants (table S15). With reference epigenomic data from the ENCODE project (*13*), the cell type–specific cis-eQTLs were relatively enriched (quantified by relative risk) in the histone marks and deoxyribonuclease (DNase) I sites derived from the pertinent cell type (fig. S13). For instance, T cell–specific cis-eQTLs were more likely to coincide with DNase I sites derived from naïve CD4$^+$ T cells than from monocytes. This confluence of epigenomic annotations and functional analysis results strengthens the interpretation of such epigenomic annotations, which are inferred to relate to functional effects of given variants.

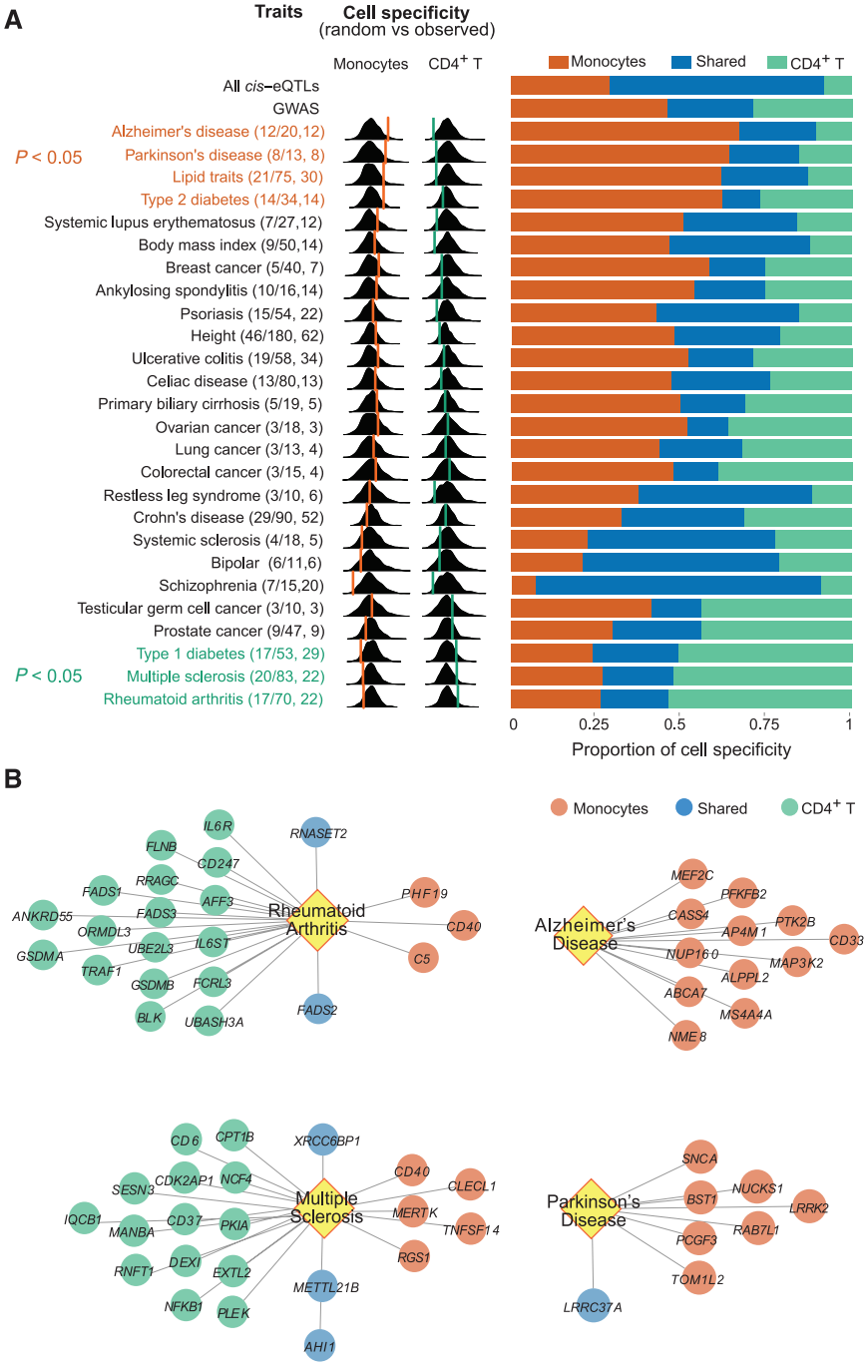


Fig. 3. Polarization of cis-regulatory effects for disease-associated variants. (**A**) (Left) For each evaluated trait, we report, in parentheses, the number of trait-associated (GWAS) SNPs with cis-eQTL effects over the total number of SNPs, and the number of genes influenced by one or more of these SNPs. For each trait, we present the distribution of the proportion of cell specificity (estimated using a Bayesian hierarchical model) observed for each of 1000 random samplings of matched SNP sets. The proportion of cell-specific cis-eQTL effects observed for a given trait is shown over this distribution using an orange line for monocytes and a green line for T cells. (Right) We report the proportion of cis-eQTLs that are monocyte-specific (orange), shared (blue), and T cell–specific (green). (**B**) Four diseases with significant polarization (FDR < 0.05) in the distribution of cis-eQTLs: Multiple sclerosis and rheumatoid arthritis are enriched in T cell effects (green), whereas Alzheimer's and Parkinson's diseases are enriched in monocyte effects (orange).

We went on to examine whether cis-eQTLs shared across cell types have similar direction and effect sizes. The comparison of the effect size for an eQTL (most significant SNP per gene) in the two cell types (Fig. 2C) showed concordance in effect size for most eQTLs (Pearson's $r = 0.79$). However, in 42 genes, the most significant SNP was associated with discordant directional effects across cell types: The allele associated with higher expression in one cell type is associated with lower expression in the other (Fig. 2D and fig. S14). We identified another dimension of cell type specificity: 6% of genes with cis-eQTLs shared across cell types are influenced by different, independent SNPs in each of the two cell types. Furthermore, 7% of independent SNPs in T cells and 11% in monocytes were associated with expression levels of more than one gene, with several SNPs affecting different genes in a cell type–dependent manner (Fig. 2E).

Leveraging 6341 SNPs (LD-pruned to $r^2 < 0.4$) associated with one or more of 415 human diseases or traits [National Institutes of Health genome-wide association study (GWAS) catalog] (*14*), we note 887 independent SNPs that influence expression of 1088 genes in cis (tables S16 and S17). To distinguish coincidental colocalizations of GWAS and eQTL associations, we used regulatory trait concordance (RTC) scores (*15*), which assesses whether a cis-eQTL and a trait association are tagging the same functional variant. Applying a stringent RTC threshold of 0.9, we identified 106 GWAS SNPs in T cells for which the trait and expression associations may be tagging the same effect; in monocytes, 123 GWAS SNPs met this criterion. Given the cell types profiled in our study, we found the expected significant enrichment (permutation $P < 1 \times 10^{-4}$) for cis-eQTLs among autoimmune disease–associated variants: Of the 425 GWAS SNPs associated with one or more autoimmune disease, 143 have cis-regulatory effects on 164 genes in monocytes and/or T cells (fig. S15 and tables S18 and S19).

Disease and trait-associated cis-eQTLs show more cell type specificity than average cis-eQTLs. Using BMA-HM, we find that 46% of all trait-associated variants are monocyte-specific, 29% are T cell–specific, and 25% are shared (Fig. 3A). In addition, variants associated with some diseases display a preponderance of T cell–specific cis-regulatory effects: These include susceptibility alleles for multiple sclerosis, rheumatoid arthritis, and type 1 diabetes (Fig. 3, A and B). On the other hand, Alzheimer's disease (AD), Parkinson's disease (PD), lipid traits, and type 2 diabetes susceptibility alleles are enriched in monocyte-specific effects (Fig. 3, A and B). In fact, the AD susceptibility alleles are significant eQTLs only in monocytes (Fig. 3B and figs. S16 and S17). Because the targeted genes are mostly expressed in both monocytes and T cells, this observed polarization is not driven by the lack of expression of the implicated genes in T cells (fig. S18).

On the basis of these results, we suggest that the inflammatory component of susceptibility to neurodegenerative diseases may be more strongly driven by the myeloid compartment of the immune system. This is consistent with the altered phagocytic function that we have reported in monocytes of individuals carrying the *CD33* AD susceptibility variant (*16*). The putative role of inflammation has previously been invoked in aging-related neurodegenerative diseases such as AD and PD (*17*), but our results bring a genetic underpinning and candidate pathways to these observations. Because our study examines young and healthy individuals, we provide support for a role of myeloid cells in the prodromal phase of neurodegenerative diseases. Functionally, we cannot say that blood-derived monocytes themselves are the key cell type; they are likely to be proxies for the infiltrating macrophages (which differentiate from monocytes) and/or resident microglia found at the sites of neuropathology. Both of these cell types share many of the transcriptome patterns of monocytes.

Despite its inherent logistic challenges, the profiling of purified primary cells from multiple human populations was clearly beneficial in several respects, including the reduction of the credible set of variants associated with a given trait. Though the majority of eQTLs are shared, the ImmVar study provides clear examples of context specificity of eQTLs and has yielded insights into the relative role of two representative cell types in exerting the functional consequences of disease-associated variants. Further, the depletion of disease-associated eQTLs with effects in both cell types is intriguing and suggests that the evolutionary history of cell-specific and pleiotropic variants is an important area of future investigation. Overall, this component of the ImmVar Project represents a strong foundation for future explorations of the role of disease susceptibility variants in an increasingly diverse matrix of cell types, stimuli, and in vivo contexts.

References and Notes

1. B. E. Stranger *et al.*, *PLOS Genet.* **8**, e1002639 (2012).
2. T. Lappalainen *et al.*, *Nature* **501**, 506–511 (2013).
3. A. Battle *et al.*, *Genome Res.* **24**, 14–24 (2014).
4. B. P. Fairfax *et al.*, *Nat. Genet.* **44**, 502–510 (2012).
5. H. J. Westra *et al.*, *Nat. Genet.* **45**, 1238–1243 (2013).
6. D. L. Nicolae *et al.*, *PLOS Genet.* **6**, e1000888 (2010).
7. G. Trynka *et al.*, *Nat. Genet.* **45**, 124–130 (2013).
8. M. T. Maurano *et al.*, *Science* **337**, 1190–1195 (2012).
9. G. R. Abecasis *et al.*, *Nature* **491**, 56–65 (2012).
10. T. Flutre, X. Wen, J. Pritchard, M. Stephens, *PLOS Genet.* **9**, e1003486 (2013).
11. J. D. Storey, R. Tibshirani, *Proc. Natl. Acad. Sci. U.S.A.* **100**, 9440–9445 (2003).
12. B. Han, E. Eskin, *Am. J. Hum. Genet.* **88**, 586–598 (2011).
13. B. E. Bernstein *et al.*, *Nature* **489**, 57–74 (2012).
14. L. A. Hindorff *et al.*, *Proc. Natl. Acad. Sci. U.S.A.* **106**, 9362–9367 (2009).
15. A. C. Nica *et al.*, *PLOS Genet.* **6**, e1000895 (2010).
16. E. M. Bradshaw *et al.*, *Nat. Neurosci.* **16**, 848–850 (2013).
17. C. K. Glass, K. Saijo, B. Winner, M. C. Marchetto, F. H. Gage, *Cell* **140**, 918–934 (2010).

Acknowledgments: We thank the study participants in the Phenogenetic Project for their contributions. We are grateful to T. Flutre and X. Wen for assistance with running the Bayesian model averaging software. This work was supported by U.S. National Institute of General Medical Sciences grant RC2 GM093080 (C.B.). T.R. is supported by the NIH F32 Fellowship (F32 AG043267). Gene expression data are deposited in the National Center for Biotechnology Information Gene Expression Omnibus under accession no. GSE56035.

Supplementary Materials

www.sciencemag.org/content/344/6183/519/suppl/DC1
Materials and Methods
Figs. S1 to S25
Tables S1 to S19
References (*18*–*31*)

11 December 2013; accepted 8 April 2014
10.1126/science.1249547

Reconstructing the DNA Methylation Maps of the Neandertal and the Denisovan

David Gokhman,[1] Eitan Lavi,[1] Kay Prüfer,[2] Mario F. Fraga,[3] José A. Riancho,[4] Janet Kelso,[2] Svante Pääbo,[2] Eran Meshorer,[1,5]* Liran Carmel[1]*

Ancient DNA sequencing has recently provided high-coverage archaic human genomes. However, the evolution of epigenetic regulation along the human lineage remains largely unexplored. We reconstructed the full DNA methylation maps of the Neandertal and the Denisovan by harnessing the natural degradation processes of methylated and unmethylated cytosines. Comparing these ancient methylation maps to those of present-day humans, we identified ~2000 differentially methylated regions (DMRs). Particularly, we found substantial methylation changes in the HOXD cluster that may explain anatomical differences between archaic and present-day humans. Additionally, we found that DMRs are significantly more likely to be associated with diseases. This study provides insight into the epigenetic landscape of our closest evolutionary relatives and opens a window to explore the epigenomes of extinct species.

The high-coverage genomes of the Denisovan (*1*) and the Neandertal (*2*), from whom present-day humans split 550,000 to 765,000 years ago (*2*), allowed the comparison of our DNA to that of our closest extinct relatives. However, differences could be sought exclusively at the sequence level and consequently did not provide direct insights regarding epigenetic

regulation, which likely underlies many of the traits that distinguish these human groups.

DNA methylation is a key hallmark of gene activity in mammals, where it occurs almost exclusively in cytosines in the context of CpG dinucleotides. In promoters, it is inversely correlated with expression level, and in intergenic regions it is linked to the activity of enhancers and insulators and to silencing transposable elements (*3*, *4*).

Classic methods to measure full methylomes are impracticable to apply to archaic samples because of damage to the ancient DNA. However, the natural process of cytosine deamination, in which unmethylated cytosines decay with time to uracils and methylated cytosines decay to thymines (*5*), has been shown to carry information regarding general trends of genome methylation (*5*, *6*). Sequencing protocols of ancient DNA trim uracils but leave thymines unprocessed (*5*). Therefore, positions in which cytosines were methylated premortem are expected to have a higher fraction of reads with thymines compared with unmethylated positions. Consequently, the fraction of CpG→TpG substitutions (hereinafter, C→T ratio) may serve as a proxy for the levels of methylation in ancient DNA (Fig. 1A and fig. S1).

We computed, for every CpG in the human genome, a C→T ratio in each of the archaic human genomes. Positions that were expected to represent true premortem thymines rather than postmortem deamination were excluded (*7*). We then compared the Neandertal and Denisovan C→T ratios to experimentally measured methylation in bone (osteoblast) cells of a present-day human (*8*). The samples were obtained from the femur, costae, and tibia bones of a young female and therefore highly resemble the Neandertal and Denisovan samples [obtained from limb bones of young females (*1*, *2*)]. For both ancient genomes, the correlation between binned present-day methylation and archaic C→T ratios was ~0.98 (*7*) (Fig. 1B).

In order for deamination to serve as a reliable proxy for DNA methylation, it should display a stochastic behavior that is homogenous along the genome. By using the genome of a ~4000-year-old Eskimo, the sequencing protocol of which provides a direct measure for deamination rates (*9*), we show that every region in the genome has the same probability to undergo deamination (*7*). Such homogeneity is expected given the fast postmortem degradation of cellular structure and proteins that are therefore unlikely to bias deamination across tens of thousands of years.

In order to account for the stochastic nature of deamination, we computed for each CpG a mean C→T ratio by using a sliding window over neighboring CpGs (*7*) (fig. S2 and table S1). The correlation between the C→T ratio and present-day human methylation is apparent also when examining specific genomic regions (Fig. 2A and fig. S3A). Furthermore, our method is highly robust not only to coverage variation, which could potentially bias C→T ratio through reduced coverage in uracil-trimmed regions, but also to potential differences in deamination rate between methylated and unmethylated cytosines (*7*) (fig. S4).

[1]Department of Genetics, Alexander Silberman Institute of Life Sciences, Hebrew University of Jerusalem, Jerusalem 91904, Israel. [2]Department of Evolutionary Genetics, Max Planck Institute for Evolutionary Anthropology, D-04103 Leipzig, Germany. [3]Cancer Epigenetics Laboratory, University Institute of Oncology of Asturias–Cajastur Social Program (IUOPA), University of Oviedo, Oviedo and Centro Nacional de Biotecnologia–Consejo Superior de Investigaciones Científicas, Madrid, Spain. [4]Department of Medicine, Hospital Universitario Marqués de Valdecilla, University of Cantabria, Instituto de Investigación Marqués de Valdecilla, Santander, Spain. [5]Edmond and Lily Safra Center for Brain Sciences, Hebrew University of Jerusalem, Jerusalem 91904, Israel.

*Corresponding author. E-mail: liran.carmel@huji.ac.il (L.C.); meshorer@huji.ac.il (E.M.)

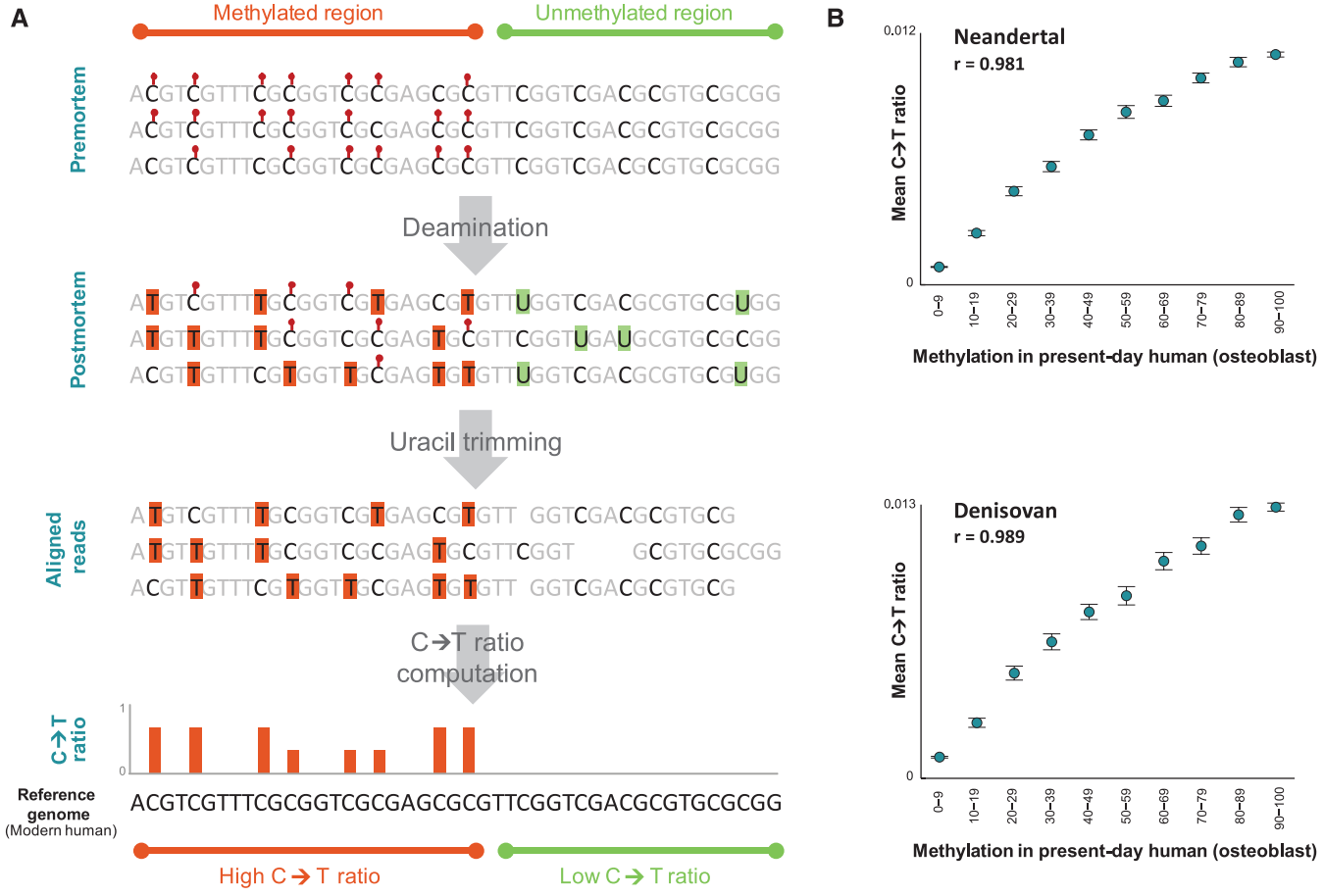


Fig. 1. C→T ratio is a proxy for ancient DNA methylation. (**A**) Scheme of the processes that enable the reconstruction of ancient methylation by using C→T ratios. (**B**) C→T ratios in archaic humans are highly correlated with measured methylation in present-day humans. CpGs were binned according to their measured methylation level in human osteoblast cells, and for each bin a mean C→T ratio was computed. Error bars represent one standard deviation.

We then scaled the C→T ratios to represent premortem methylation percentages (*7*). The reconstructed archaic methylation in single CpGs shows strong correlation to measured present-day methylation ($r = 0.77$ in the Denisovan; $r = 0.79$ in the Neandertal) (Fig. 2B). Next, we investigated CpG islands, which tend to be hypomethylated in mammalian genomes (*3*). The reconstructed methylation in CpG islands falls within the range of values in present-day humans (fig. S3B). We also investigated 3804 housekeeping genes (*10*), whose promoters are constitutively hypomethylated (*4*). The reconstructed methylation shows strong hypomethylation and falls within the range of 16 present-day human tissues taken from 20 individuals (*11*) (Fig. 3A and fig. S3C). Taken together, these results suggest that the C→T ratio can be used as a proxy for premortem methylation and that genome-wide methylation maps can be reconstructed after tens of thousands of years.

As expected from groups that diverged recently, over 99% of both archaic genomes show no significant methylation differences compared to the present-day human. However, in each archaic human we found ~1100 differentially methylated regions (DMRs) (*7*). We divided the DMRs according to where the methylation change has likely occurred, that is, into Neandertal-specific, Denisovan-specific, and present-day human–specific DMRs. DMRs that could not be confidently assigned to a specific lineage were tagged as unclassified DMRs (*7*) (Fig. 3B and table S2). Because housekeeping genes serve fundamental functions in all cells, we expected them to present low rates of methylation changes. Reassuringly, despite constituting ~10% of genes, none of the housekeeping genes harbors DMRs ($P = 1.7 \times 10^{-36}$, hypergeometric test). Last, when comparing differences in methylation to differences in sequence, we observed a significant overlap between the two, as expected if some of the methylation changes were driven by sequence changes ($P < 10^{-6}$, randomization test).

A difference in methylation between an archaic and a present-day human does not necessarily imply a fixed difference between the human groups. This difference can stem from variability within a population or from the comparison of close, yet not identical, cell types (osteoblasts versus whole bones). Hence, we compared the archaic methylation to 37 bones samples taken from osteoblasts and whole bones (*12*–*14*). We sought reliable DMRs, in which the archaic methylation significantly differs from that in modern bones. These samples were measured with 27K arrays and provided information for ~5% of DMRs. In most DMRs, archaic methylation was significantly different from the 37 bones and therefore classified as reliable [false discovery rate (FDR) < 0.01, z-test] (tables S2 and S3).

DMRs for which data from bones was not available were compared with 25 samples of 23 tissues from 20 individuals representing both sexes, different ethnicities, and ages ranging from 6 to 88 (*8*). Over 50% of DMRs had stable methylation levels across modern samples, but were significantly different in the archaic humans, and are thus likely to represent reliable DMRs (*7*) ($FDR < 0.01$ (tables S2 and S3).

A key regulator of limb development is the 5′ HOXD cluster (*15*), which includes five genes (*HOXD9* to *HOXD13*). We identified three DMRs within the HOXD locus (Fig. 4) and two intergenic DMRs located 20- and 25-kb upstream to the cluster in a putative enhancer region (*16*) (table S2). In both archaic humans, we detected hypermethylation in the *HOXD9* promoter and in the *HOXD10* gene body, whereas in present-day humans these regions are hypomethylated in all 37 bone samples (methylation = 5 ± 2%;

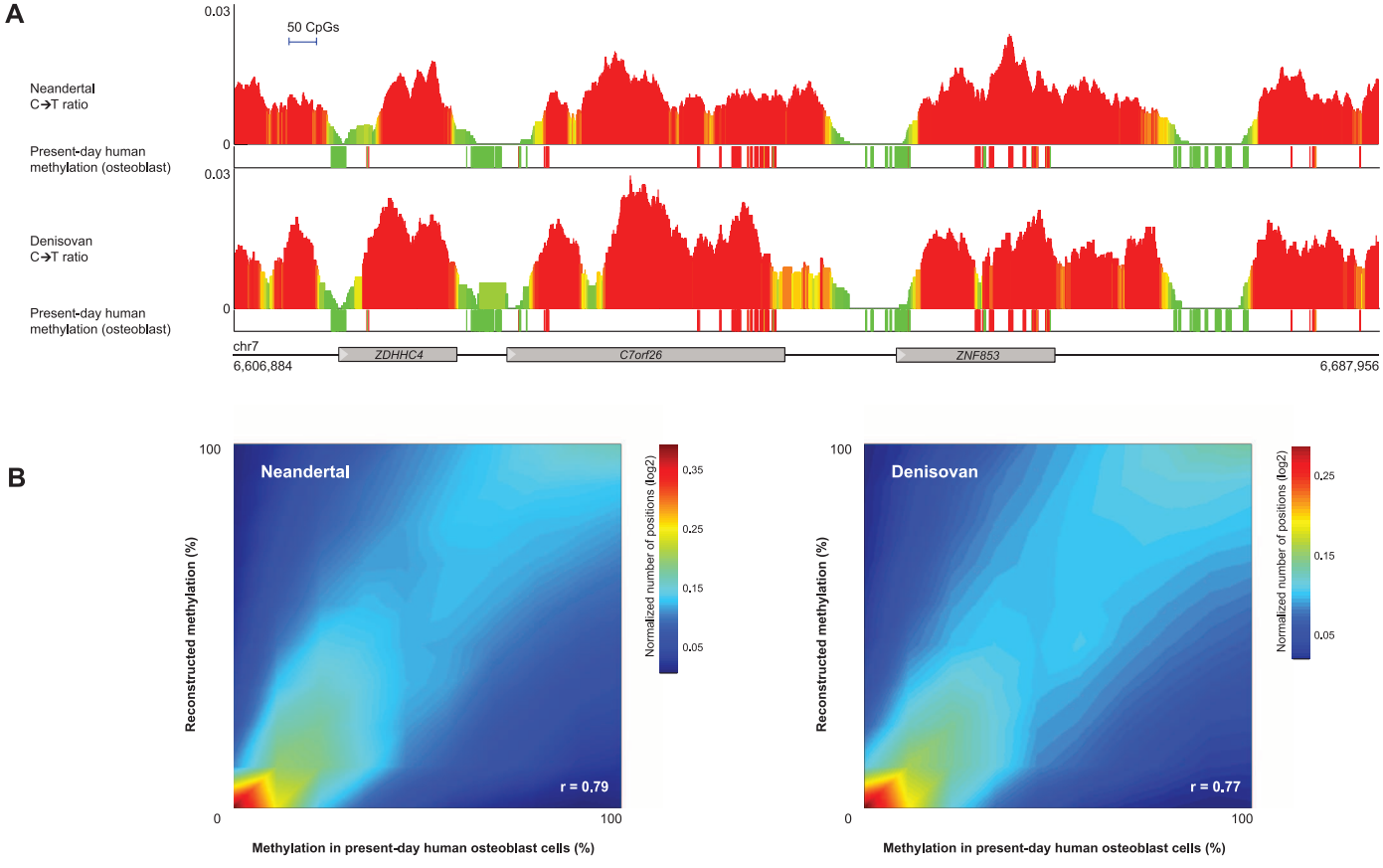


Fig. 2. Reconstructed archaic methylation relative to present-day human methylation. (**A**) An exemplary region (chromosome 7, 6,606,884 to 6,687,956) demonstrating that reconstructed archaic methylation patterns follow present-day human patterns. C→T ratio and measured methylation are color-coded with a gradient from green (unmethylated) to red (methylated). The bottom line shows genes in the region. For visual clarity, osteoblast methylation in present-day humans appears twice, below each of the C→T ratio lanes. (**B**) Normalized heat maps of present-day human methylation versus archaic reconstructed methylation for all single CpG positions across the genome. The hot region along the diagonal line shows that, in most CpG positions, reconstructed methylation matches measured present-day methylation.

$FDR < 1.7 \times 10^{-30}$, z-test). In addition, we found the gene body of *HOXD9* to be hypermethylated in the Denisovan (Fig. 4 and table S2). These DMRs imply linked regulation of *HOXD9* and *HOXD10*, consistent with observations in mouse (*17*). Distinctions between present-day and Neandertal limbs include larger femur articulations (*18*), robust hands and fingers (*19*), broader elbow and knee joints (*18*, *20*), more-curved radius and femur (*18*, *20*), and shorter limbs (*18*, *20*). All of these features were shown in mouse and human to result from changes in the HOXD

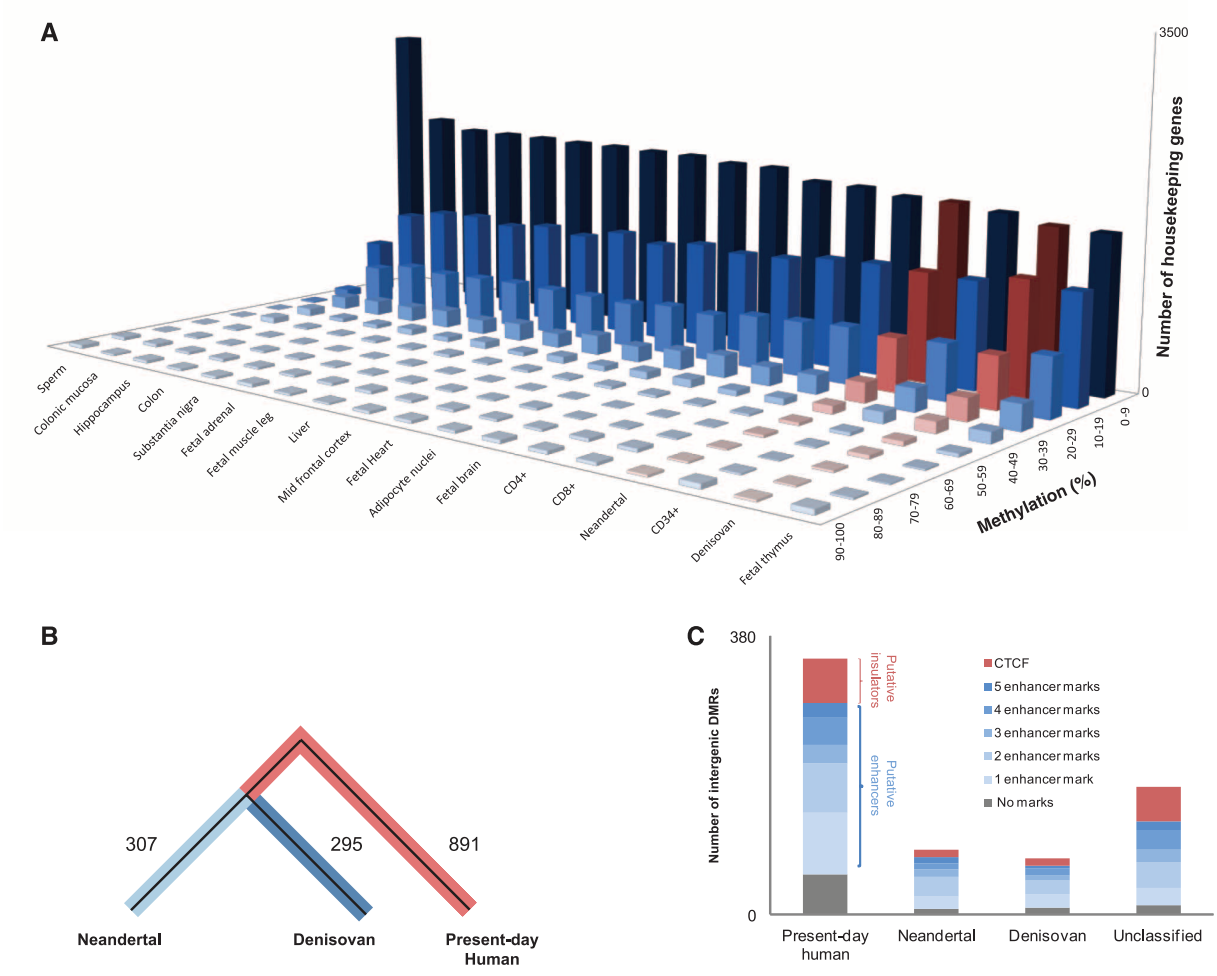


Fig. 3. Characteristics of DMRs. (**A**) Distribution of methylation in housekeeping promoters in various human tissues (blue) and in the Neandertal and the Denisovan (red). The distribution of methylation in the Neandertal and the Denisovan falls within the variability across human tissues. (**B**) The numbers of present-day human–, Neandertal-, and Denisovan-specific DMRs. (**C**) Intergenic DMRs colocalize with enhancer and insulator marks. Overlap of intergenic DMRs with insulator mark (CTCF) and with five different enhancer marks (histone modifications H3K4me1 and H3K27ac, histone variant H2A.Z, binding by p300, and DNase I sensitivity). DMRs are divided according to the number of enhancer marks they overlap.

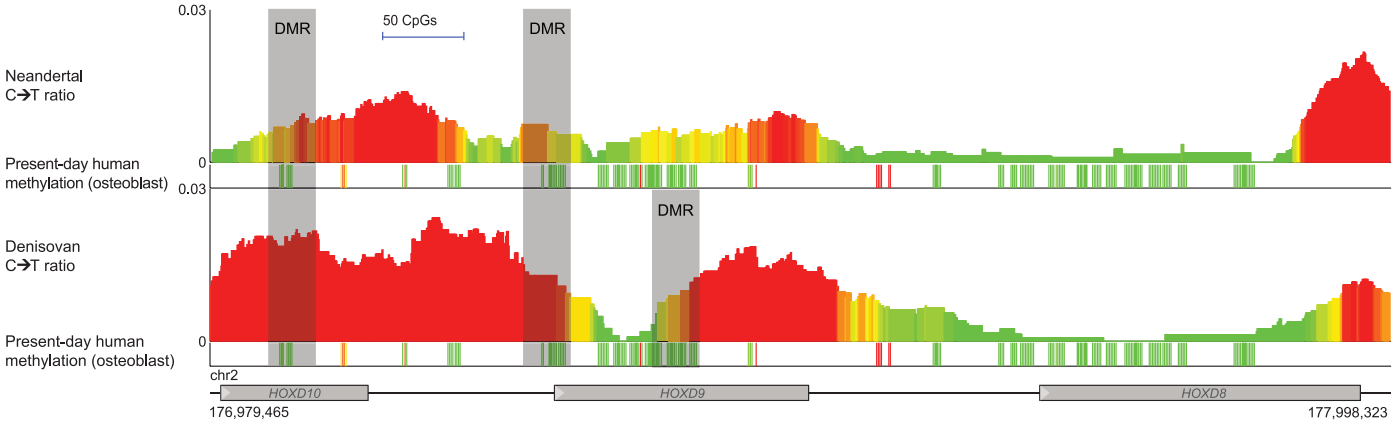


Fig. 4. The HOXD cluster is hypermethylated in archaic humans. C→T ratio in archaic humans, and present-day human methylation (see caption of Fig. 1C). Gray rectangles mark DMRs. A minimum of 10 positions with measured osteoblast methylation was required for a region to be denoted a DMR.

cluster in general and in *HOXD9* and *HOXD10* in particular (*15*, *21*–*23*). Together, these findings suggest that the HOXD cluster might have played a key role in the recent evolution of human limbs.

Enhancers are often deoxyribonuclease I (DNase I)–sensitive regions bound by p300 and histone variant H2A.Z and marked by the histone modifications H3K4me1 and H3K27ac (*24*, *25*). For insulators, CCCTC binding factor (CTCF) plays a major role as a buffer between active and inactive regions. By using a randomization test, we found a significant enrichment for enhancer marks and for CTCF binding in the intergenic DMRs, with over 80% having these marks (Fig. 3C, fig. S5, and tables S2 and S4). We show that this cannot be explained by length, CG-content, CpG density, or coverage (*7*). This suggests that many of the intergenic DMRs may affect gene activity through distal elements. Additionally, both of the intergenic DMRs upstream of the HOXD cluster possess enhancer marks (table S2), suggesting that they might have affected the methylation of the HOXD cluster through distal regulation.

DNA methylation affects, as well as is affected by, the binding of transcription factors (TFs) (*3*, *4*). To test whether multiple DMRs may be associated with a change in a single TF, we looked for TF-encoding genes that are differentially methylated and whose targets are enriched with DMRs (*7*) (tables S5 and S6). In the Neandertal, we identified sterol regulatory element binding protein 1 (SREBP-1), a regulator of lipid homeostasis ($FDR = 5.5 \times 10^{-3}$; Fisher's exact test), and aryl hydrocarbon receptor (AHR), a receptor of environmental toxins ($FDR = 3.7 \times 10^{-8}$). In present-day humans, we identified early growth response 3 (EGR3), which regulates biorhythm and development of muscles, lymphocytes, and neurons ($FDR = 4.2 \times 10^{-10}$); and Meis homeobox 1 (MEIS1), a regulator of limb development that forms complexes with both HOXD9 and HOXD10 ($FDR = 5.6 \times 10^{-8}$). This enrichment is independent of CpG density, GC content, and coverage (*7*). Additionally, the number of TFs that passed this test is significantly higher than would be expected by random ($P = 0.018$, hypergeometric test). These TFs could provide a lead to the mechanism behind the methylation changes and possibly offer a model of burstlike evolution, where multiple genes changed their activity after a single evolutionary event.

Last, we found that DMR-containing genes in present-day humans are almost twice as likely as genes that do not contain DMRs to be disease-related (18.1% compared with 10.8%, $P = 1.9 \times 10^{-7}$, Fisher's exact test) (fig. S6 and table S7). More than a third of the disease-linked genes (30/81) are involved in neurological and psychiatric disorders. Here, too, the enrichment is independent of gene length, CpG density, GC content, and coverage (*7*). This could potentially point to a link between recent changes in regulation and the emergence of diseases or to a scenario where disease-linked genes (i.e., genes in which a change is not embryonic lethal) are possibly more prone to methylation changes.

Current techniques for measuring genome-wide methylation result in the destruction of the examined DNA (*3*) and are therefore impracticable in the study of ancient DNA. Our method allows for the reconstruction of methylation maps directly from ancient DNA reads without the need to use additional ancient material. We hope that the differences in methylation elucidated here will help to uncover the epigenetic basis for phenotypic differences between present-day and archaic humans and shed light on the role of epigenetics in the recent evolution of our lineage.

References and Notes

1. M. Meyer *et al.*, *Science* **338**, 222–226 (2012).
2. K. Prüfer *et al.*, *Nature* **505**, 43–49 (2014).
3. P. A. Jones, *Nat. Rev. Genet.* **13**, 484–492 (2012).
4. Z. D. Smith, A. Meissner, *Nat. Rev. Genet.* **14**, 204–220 (2013).
5. A. W. Briggs *et al.*, *Nucleic Acids Res.* **38**, e87 (2010).
6. J. S. Pedersen *et al.*, *Genome Res.* **24**, 454–466 (2014).
7. Methods are available as supplementary materials on *Science* Online.
8. ENCODE Project Consortium, *PLOS Biol.* **9**, e1001046 (2011).
9. M. Rasmussen *et al.*, *Nature* **463**, 757–762 (2010).
10. E. Eisenberg, E. Y. Levanon, *Trends Genet.* **29**, 569–574 (2013).
11. M. J. Ziller *et al.*, *Nature* **500**, 477–481 (2013).
12. J. E. Ohm *et al.*, *Cancer Res.* **70**, 7662–7673 (2010).
13. S. H. Kresse *et al.*, *PLOS ONE* **7**, e48262 (2012).
14. C. García-Ibarbia *et al.*, *Gene* **532**, 165–172 (2013).
15. J. Zakany, D. Duboule, *Curr. Opin. Genet. Dev.* **17**, 359–366 (2007).
16. P. Tschopp, D. Duboule, *Annu. Rev. Genet.* **45**, 145–166 (2011).
17. F. M. Rijli, P. Dollé, V. Fraulob, M. LeMeur, P. Chambon, *Dev. Dyn.* **201**, 366–377 (1994).
18. T. D. Weaver, *Proc. Natl. Acad. Sci. U.S.A.* **100**, 6926–6929 (2003).
19. E. S. Mittra, H. F. Smith, P. Lemelin, W. L. Jungers, *Am. J. Phys. Anthropol.* **134**, 449–459 (2007).
20. I. De Groote, *J. Hum. Evol.* **61**, 396–410 (2011).
21. B. Dlugaszewska *et al.*, *J. Med. Genet.* **43**, 111–118 (2006).
22. M. Fujimoto *et al.*, *J. Hum. Genet.* **43**, 32–36 (1998).
23. C. C. de la Cruz, A. Der-Avakian, D. D. Spyropoulos, D. D. Tieu, E. M. Carpenter, *Dev. Biol.* **216**, 595–610 (1999).
24. C. T. Ong, V. G. Corces, *Nat. Rev. Genet.* **12**, 283–293 (2011).
25. M. Ku *et al.*, *Genome Biol.* **13**, R85 (2012).

Acknowledgments: We thank S. Shifman, Y. Stelzer, M. Choder, O. Amster-Choder, U. Ben-David, M. Meyer, Y. Aaronson, and Y. N. Harari for critical comments. Supported by the Israel Science Foundation FIRST individual grant (ISF 1430/13 to L.C. and E.M.), the Israel Science Foundation (ISF 1252/12, 657/12 to E.M.), a European Union Marie Curie Reintegration grant (IRG-248639 to L.C.), the Abisch-Frenkel Foundation (to E.M.), the European Research Council (ERC-281781 to E.M.), the Presidential Innovation Fund of the Max Planck Society (to S.P.), and the Spanish Health Ministry (Instituto de Salud Carlos III-FIS PI09/539, PI12/615). Software (RoAM, after Reconstruction of Archaic Methylation) can be found at http://carmelab.huji.ac.il/software/RoAM/roam.html and data at http://carmelab.huji.ac.il/data.html. The authors declare no competing financial interests. Requests for data should be addressed to Liran Carmel (liran.carmel@huji.ac.il) and Eran Meshorer (meshorer@huji.ac.il).

Supplementary Materials

www.sciencemag.org/content/344/6183/523/suppl/DC1
Materials and Methods
Figs. S1 to S6
Tables S1 to S10
References (*26*–*43*)

2 January 2014; accepted 4 April 2014
Published online 17 April 2014;
10.1126/science.1250368

Chemical Inhibition of NAT10 Corrects Defects of Laminopathic Cells

Delphine Larrieu,[1] Sébastien Britton,[1]* Mukerrem Demir,[1] Raphaël Rodriguez,[2]† Stephen P. Jackson[1,3]†

Down-regulation and mutations of the nuclear-architecture proteins lamin A and C cause misshapen nuclei and altered chromatin organization associated with cancer and laminopathies, including the premature-aging disease Hutchinson-Gilford progeria syndrome (HGPS). Here, we identified the small molecule "Remodelin" that improved nuclear architecture, chromatin organization, and fitness of both human lamin A/C–depleted cells and HGPS-derived patient cells and decreased markers of DNA damage in these cells. Using a combination of chemical, cellular, and genetic approaches, we identified the acetyl-transferase protein NAT10 as the target of Remodelin that mediated nuclear shape rescue in laminopathic cells via microtubule reorganization. These findings provide insights into how NAT10 affects nuclear architecture and suggest alternative strategies for treating laminopathies and aging.

Mutations in *LMNA*, which encodes lamin A and C, cause pathologies known as laminopathies (*1*), including the accelerated-aging disease Hutchinson-Gilford progeria syndrome (HGPS) (*2*, *3*). Deregulation of A-type lamins expression or localization also occurs in various cancers (*4*–*6*). Lamin A/C depletion or *LMNA* mutations cause enlarged, misshapen nuclei and altered chromatin organization (*7*). Whereas some of these pathologies might reflect cell fragility, many likely result from downstream effects on chromatin structure, gene

expression, DNA replication, or DNA repair. Improving nuclear architecture of laminopathic cells can ameliorate defects in chromatin structure and other processes, thus improving some disease phenotypes (*8*, *9*).

[1]The Wellcome Trust/Cancer Research UK (CRUK) Gurdon Institute and Department of Biochemistry, University of Cambridge, CB2 1QN Cambridge, UK. [2]Institut de Chimie des Substances Naturelles, CNRS, 91198 Gif-sur-Yvette, France. [3]The Wellcome Trust Sanger Institute, Hinxton, CB10 1SA Cambridge, UK.

*Present address: Université de Toulouse-Université Paul Sabatier, CNRS, Institut de Pharmacologie et de Biologie Structurale, 31077 Toulouse, France.

†Corresponding author. E-mail: s.jackson@gurdon.cam.ac.uk (S.P.J.); raphael.rodriguez@cnrs.fr (R.R.)

Lamin A/C depletion by small interfering RNA (siRNA) transfection (siLMNA) caused nuclear-shape defects (Fig. 1, A and B, and fig. S1, A and B), global chromatin relaxation, and increased nuclear area (fig. S1, C and D). We therefore reasoned that modulating chromatin organization by lysine acetyltransferase (KAT) or lysine deacetylase (KDAC) inhibition might improve nuclear architecture defects of siLMNA cells. Compound screening identified the KAT inhibitor 4-(4-chlorophenyl)-2-(2-cyclopentylidenehydrazinyl) thiazole (**1**) (Fig. 1C), which restored nuclear circularity and global chromatin compaction in siLMNA cells (Fig. 1, D and E, and fig. S1, E to G). Although molecule **1** was identified in *Saccharomyces cerevisiae* as a GCN5 (general control of amino acid synthesis protein 5-like 2) network inhibitor (*10*), nuclear shape rescue was GCN5-independent because the benchmark GCN5 inhibitor MB-3 had no effect on nuclear circularity. Complete nuclear-shape rescue by molecule **1** occurred within 12 hours of treatment (Fig. 1F), independently of mitosis (fig. S2A and movie S1) and without markedly affecting the cell cycle (fig. S2, B and C). Moreover, compound **1** improved the nuclear morphology of several cancer cell lines displaying reduced lamin A/C expression (fig. S2, D and E), indicating that its effects were not specific to siRNA-mediated lamin A/C depletion.

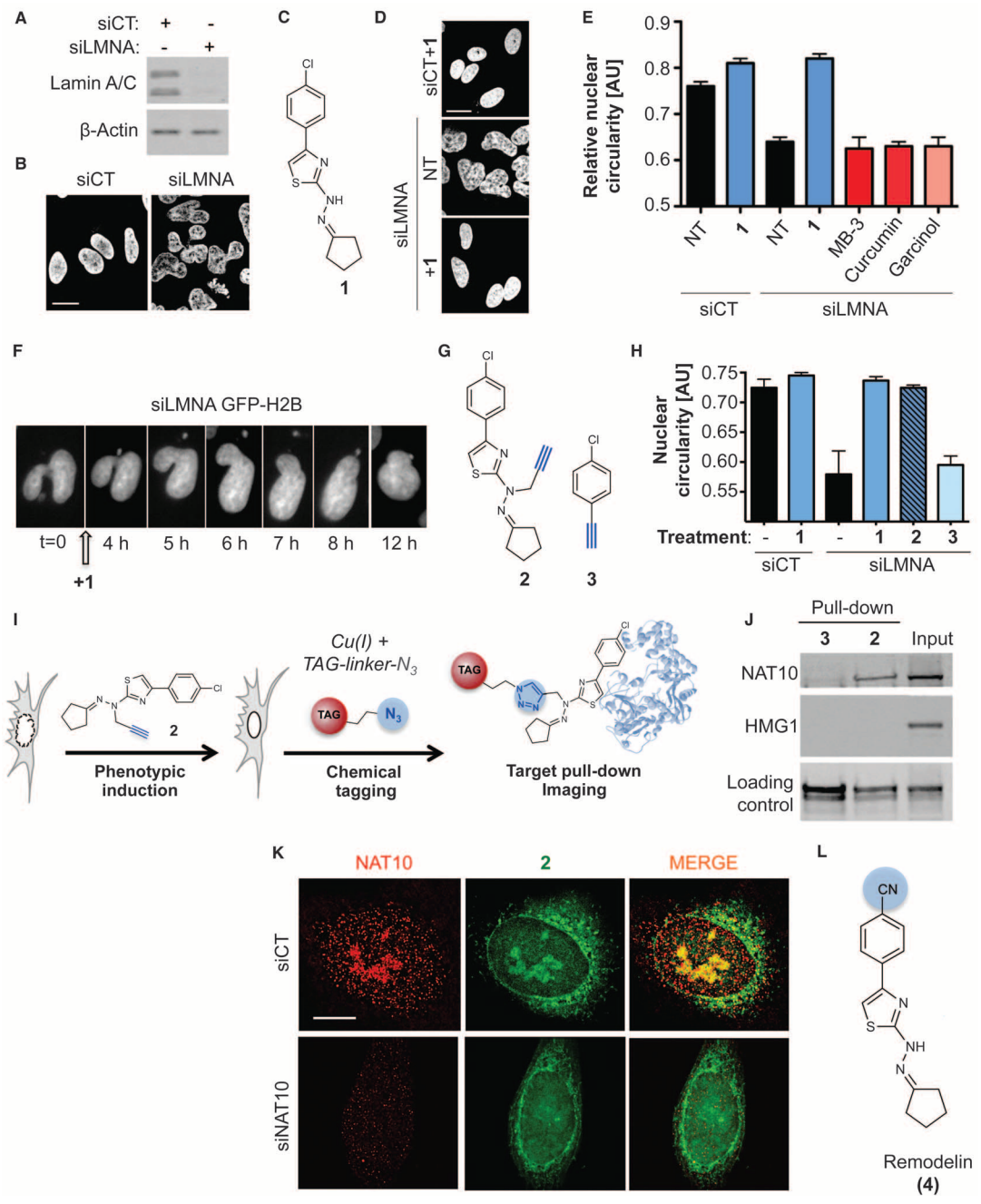


Fig. 1. A small molecule restores nuclear shape in lamin A/C–depleted cells and targets the acetyltransferase NAT10. (**A**) Lamin A/C depletion (siLMNA) in U2OS cells compared with negative control (siCT). (**B**) Nuclear shape observed with 4′,6-diamidino-2-phenylindole (DAPI) staining. (**C**) Molecular structure of compound **1**. (**D**) Nuclear shape rescue observed with DAPI staining after treatment with **1**. (**E**) Quantification of nuclear circularity in nontreated (NT) cells or cells treated with the indicated compounds (means of three independent experiments with $n > 212$ nuclei ± SD). (**F**) Live imaging pictures of nuclear shape rescue in green fluorescent protein (GFP)–H2B expressing U2OS cells transfected with siLMNA and treated with **1**. (**G**) Molecular structure of clickable analog **2** and clickable inactive control molecule **3**. (**H**) Quantification of U2OS nuclear circularity (means of three independent experiments with $n > 224$ nuclei ± SD) (**I**) Principle of click-chemistry strategy for small-molecule tagging. (**J**) Pull-down of clickable molecules **2** and **3** preincubated in U2OS cells and analysis of bound proteins. (**K**) Representative high-resolution microscopy pictures of NAT10 (red) and fluorescently labeled **2** (green) in control or NAT10-depleted cells (siNAT10). Scale bars, 10 μm. (**L**) Molecular structure of Remodelin (**4**), a stable and more potent analog of **1**.

To identify putative targets of **1**, we synthesized a "clickable" cell-active analog **2** and used inactive molecule **3** as a negative control (Fig. 1, G and H). We then used "click-chemistry" to retrieve and validate drug-associated proteins. The alkyne moiety selectively reacts with an azide group upon copper exposure, allowing tagging of the clickable molecules in cells (Fig. 1I). First, we incubated a biotinylated derivative of **2** in cell extracts (fig. S3A), retrieved associated proteins with streptavidin beads, and identified several protein species whose staining intensities were reduced by an excess of competitor **1** (fig. S2B). These proteins were then identified by means of liquid chromatography–mass spectrometry (LC-MS)/MS (fig. S2C). *N*-acetyltransferase 10 (NAT10) was the only KAT protein identified, thus being the only likely relevant target of **1**. NAT10 was previously linked with the SUN1 nuclear envelope protein (*11*), whose depletion rescues nuclear shape in cells in which LMNA had been knocked out (*8*), and NAT10 KAT activity has been demonstrated toward microtubules and histones (*12*).

Preincubating clickable molecules with live cells followed by click pull-down identified NAT10 as a specific target of **2** in vivo (Fig. 1J), establishing our protocol as a framework for identifying specific partners without photo-cross-linking agents (*13*). In parallel, we visualized subcellular localizations of clickable molecules by means of fluorescence microscopy (Fig. 1K) (*14*). This revealed that **2** specifically accumulated in nucleoli and also localized at the nuclear periphery and in the cytoplasm (Fig. 1K and fig. S4A). Corroborating the binding studies, this distribution overlapped with that of NAT10, and moreover, NAT10 depletion (fig. S4B) led to a marked reduction of molecule **2** in the nucleolus (Fig. 1K) without changes in nucleolar architecture [NAT10 localization was not affected by treatment with **1** or siLMNA (fig. S4C)]. Furthermore, we established direct physical interaction between **1** and NAT10 using circular dichroism spectroscopy (fig. S4D). Because molecule **1** was rapidly degraded upon light and air exposure, we explored its structural derivatives for their ability to rescue nuclear shape of siLMNA cells (fig. S5A). The most potent and stable analog identified (**4**) (fig. S5B) was named "Remodelin" on the basis of its ability to remodel nuclear architecture of siLMNA cells (Fig. 1L).

Consistent with a model in which Remodelin affects siLMNA cells through NAT10 targeting,

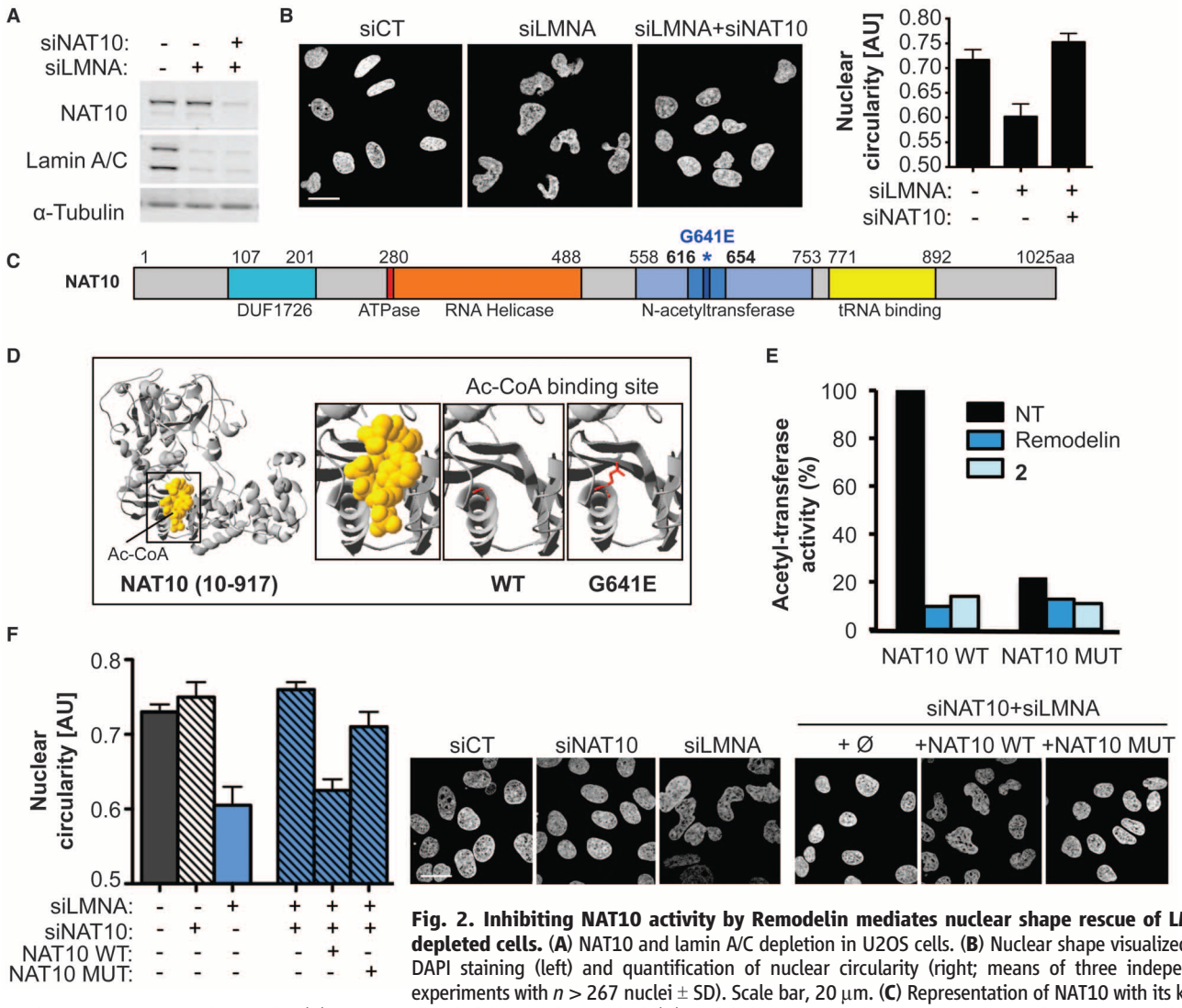


Fig. 2. Inhibiting NAT10 activity by Remodelin mediates nuclear shape rescue of LMNA-depleted cells. (**A**) NAT10 and lamin A/C depletion in U2OS cells. (**B**) Nuclear shape visualized with DAPI staining (left) and quantification of nuclear circularity (right; means of three independent experiments with $n > 267$ nuclei ± SD). Scale bar, 20 μm. (**C**) Representation of NAT10 with its known domains. The G641E mutation identified in (D) is indicated in dark blue and asterisked. (**D**) Modeled 3D structure of human NAT10 residues 10 to 917 showing the acetyl-CoA binding site (left) and disruption of Ac-CoA binding by NAT10 G641E mutation (right) visualized with Swiss-Prot PDB Viewer. (**E**) In vitro acetylation assay showing the activity of NAT10 toward tubulin. (**F**) Quantification of nuclear circularity (left) in cells stably expressing siRNA-resistant FLAG-NAT10 wild type or FLAG-NAT10 G641E (NAT10 MUT; means of three independent experiments with $n > 198$ nuclei ± SD) and nuclear shape visualized with DAPI staining (right). Scale bar, 20 μm.

we found that NAT10 depletion (Fig. 2A) corrected the aberrant nuclear morphology of siLMNA cells (Fig. 2B). Because **1**, the analog of Remodelin, was identified as a KAT inhibitor, we assessed whether Remodelin affected NAT10 KAT activity. Aligning human NAT10 with the three-dimensional (3D) structure of its bacterial homolog in complex with acetyl–coenzyme A (acetyl-CoA) (*15*) led us to mutate conserved glycine-641 to glutamate (G641E), which was predicted to impair acetyl-CoA binding (Fig. 2, C and D, and fig. S6A). Indeed, this mutation blocked NAT10 activity (Fig. 2E and fig. S6B). Moreover, wild-type NAT10 activity was inhibited by Remodelin or clickable molecule **2**, establishing Remodelin as a bona fide NAT10 inhibitor. Complementation assays with siRNA-resistant wild-type (NAT10 WT) or G641E mutant NAT10 (NAT10 MUT) (fig. S6, C and D) showed that rescue of nuclear circularity in siLMNA cells required loss of NAT10 catalytic

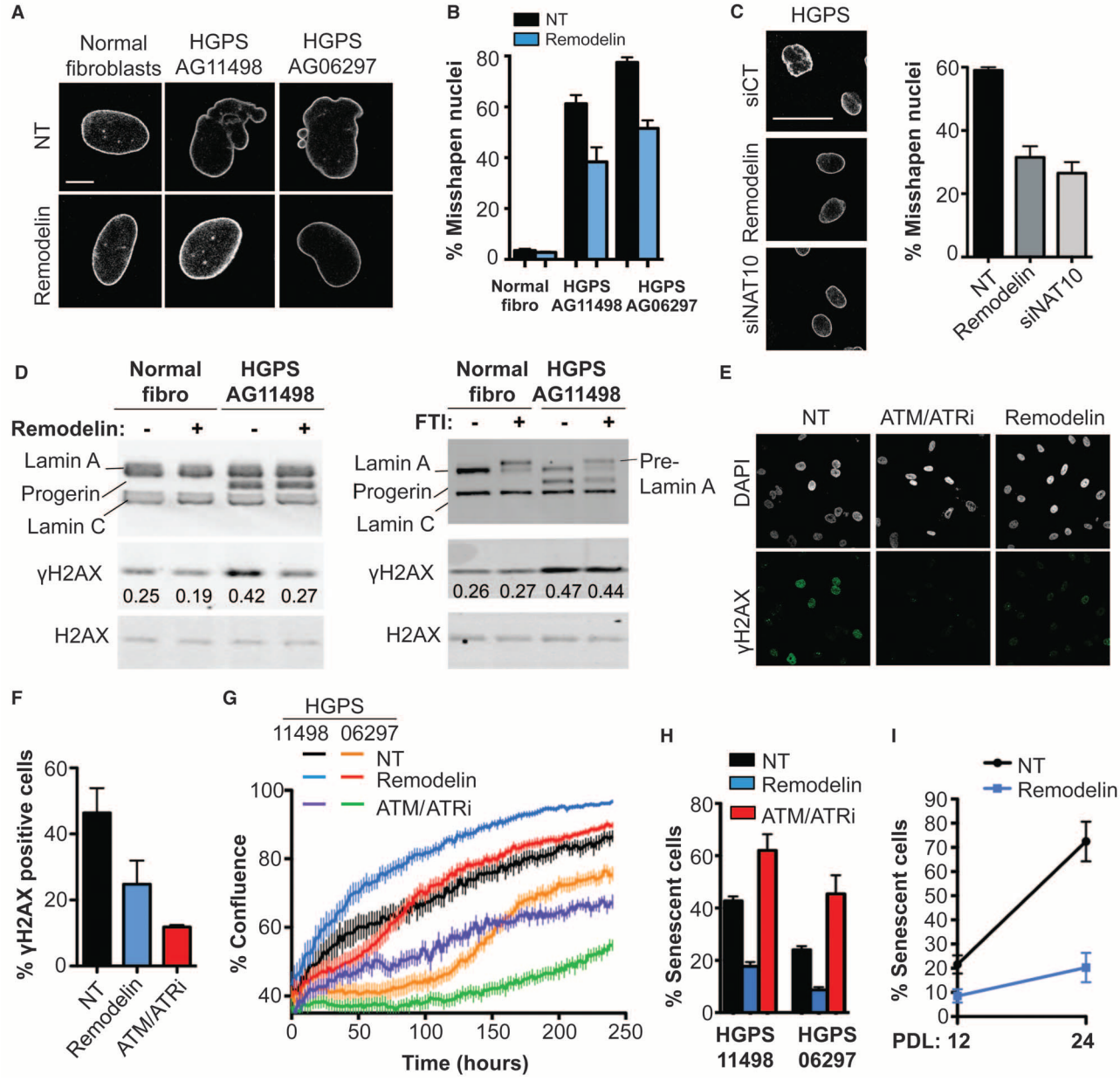


Fig. 3. Remodelin targets NAT10 to improve nuclear shape and fitness of HGPS cells. (**A**) Representative immunofluorescence (IF) pictures of lamin A/C in HGPS cell lines compared with matched normal fibroblasts at the same population doubling. Scale bar, 10 μm. (**B**) Quantification of misshapen nuclei upon Remodelin treatment (means of three independent experiments with $n >$ 213 nuclei ± SEM). (**C**) Lamin A/C staining in HGPS AG11498 cells (left) and quantification of misshapen nuclei (right; means of three independent experiments with $n >$ 176 nuclei ± SEM). Scale bar, 50 μm. (**D**) Western blotting analysis of γH2AX after Remodelin or FTI treatment. (**E**) Immunofluorescence analysis of γH2AX staining upon Remodelin or ATM/ATR inhibition (ATM/ATRi). (**F**) Quantification of γH2AX-positive cells observed with IF (means of three independent experiments with $n >$ 127 cells ± SEM). (**G**) HGPS proliferation upon Remodelin or ATM/ATR-inhibitor treatment (means of nine replicates ± SEM). (**H**) Quantification of senescence-associated β-galactosidase positive cells (means of three independent experiments with $n >$ 257 cells ± SEM). (**I**) Quantification of senescence-associated β-galactosidase–positive cells in HGPS AG11498 after 8 days of Remodelin treatment at population doubling 12 (PDL 12) and after several weeks of Remodelin treatment and 12 cell divisions (PDL 24) (means of two independent experiments with $n >$ 298 cells ± SD).

function (Fig. 2F). Thus, inactivating NAT10 KAT activity through mutation or with Remodelin restores normal nuclear morphology in siLMNA cells.

We next investigated the effects of Remodelin on cells derived from *LMNA*-mutated HGPS patients (AG11498 and AG06297). HGPS cells accumulate Progerin, a permanently farnesylated, truncated form of lamin A, leading to nuclear membrane folding and nuclear blebbing (Fig. 3A) that contribute to the premature-aging phenotypes of HGPS patients. Remodelin markedly reduced the prevalence of misshapen nuclei in HGPS cells (Fig. 3B) as well as in primary MRC5 fibroblasts aged in culture (fig. S7, A and B), which also accumulate Progerin upon extended passaging (*16*). In contrast, Remodelin had no effect on nonlaminopathic Werner syndrome cells (fig. S7, C and D). Farnesyltransferase inhibitors (FTIs) prevent accumulation of farnesylated Progerin at the nuclear membrane, thus reducing HGPS nuclear blebbing (*17*). Unlike FTIs, however, Remodelin did not trigger pre-lamin A accumulation (fig. S8A), indicating that

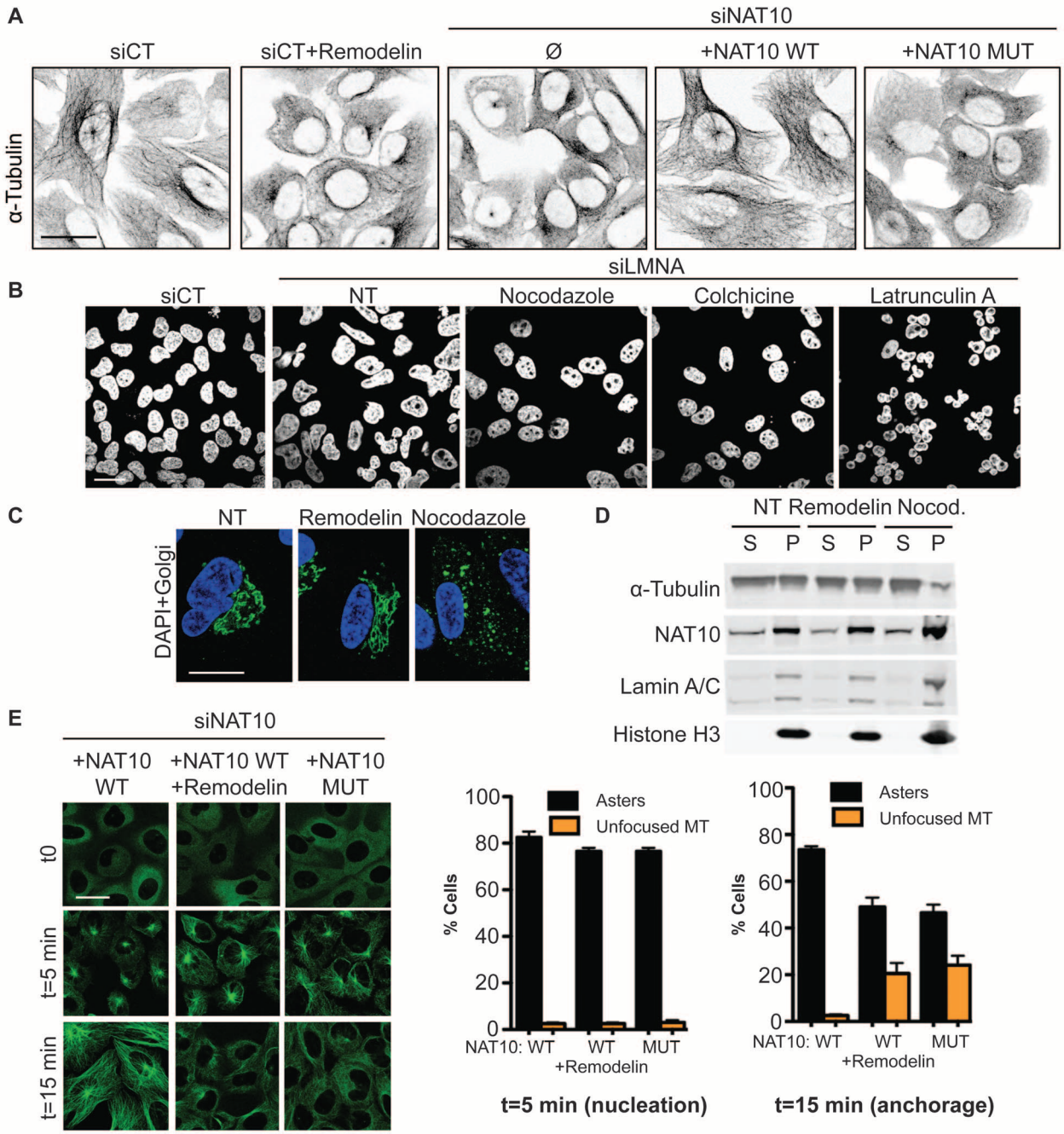


Fig. 4. Inhibiting NAT10 acetyltransferase activity modifies microtubule organization to rescue nuclear shape defects. (**A**) Microtubule network visualization by means of inverted IF pictures of α-tubulin. (**B**) Nuclear shape visualization after treating cells with microtubule or actin cytoskeleton disrupting agents. (**C**) Visualization of nuclear shape (DAPI, blue) and Golgi (anti-Giantin, green) integrity in siLMNA cells. (**D**) Fractionation of polymerized (P) and soluble (S) tubulin upon Remodelin or nocodazole (Nocod.) treatment. (**E**) Microtubule regrowth in cells transfected with siNAT10 and expressing the indicated siRNA-resistant constructs. α-tubulin IF staining (left) shows nucleation phase: $t = 5$ min and microtubule anchorage ($t = 15$ min). (Right) Quantification of cells with indicated patterns (means of three independent experiments with $n > 103$ cells ± SEM).

Remodelin is not an FTI. However, Remodelin and FTI did not act synergistically on nuclear shape improvement, suggesting that they affect a common pathway (fig. S8, B and C). Unlike Remodelin, FTI did not improve nuclear morphology in siLMNA cells. Furthermore, although FTI improves HGPS nuclear shape, it had the opposite effect on Progerin-negative cells (fig. S8, B and C), probably by causing accumulation of unprocessed lamin A and B and centrosome separation defects (*18*–*20*). In contrast, Remodelin prevented FTI-induced nuclear shape defects in normal fibroblasts and U2OS cells (fig. S8, B to D). The proportion of misshapen nuclei in HGPS cells was similarly decreased by Remodelin treatment or NAT10 depletion (Fig. 3C and fig. S9A), implying that NAT10 inhibition by Remodelin mediates nuclear shape normalization in HGPS cells.

Although nuclear shape improvement is not always associated with overall amelioration of HGPS cell phenotypes (*21*), Remodelin improved global HGPS-cell fitness as observed by decreased steady-state levels of the DNA double-strand break markers γH2AX and autophosphorylated ATM (ataxia telangiectasia mutated), decreased DNA damage signaling (Fig. 3D and fig. S9, B to D), improved chromatin and nucleolar organization (assessed with histone H3K9me3 and NAT10 staining), and decreased SUN1 accumulation at the nuclear envelope (fig. S9, E to G). Blocking DNA damage signaling by inhibiting the apical DNA-damage response kinases ATM and ATR (ataxia telangiectasia and Rad3–related) decreased γH2AX (Fig. 3, E and F). However, unlike Remodelin—which improved DNA replication (fig. S9H), enhanced cell proliferation capacity (Fig. 3G), and decreased senescence (Fig. 3H) [other KAT inhibitors did not decrease senescence (fig. S9I)]—inhibiting ATM and ATR decreased proliferation and induced senescence (Fig. 3, G and H). Similar effects were observed upon p53-pathway inhibition (fig. S9I). Thus, Remodelin appears to reduce the amount of DNA damage in HGPS cells, whereas damage is still present but no longer signaled properly upon ATM/ATR inhibition, leading to cell growth arrest and senescence. Moreover, Remodelin conferred long-term benefits to HGPS cells, as seen by it decreasing senescence even after several weeks of treatment (Fig. 3I).

NAT10 localizes mainly in the nucleolus, which has a known role in maintaining nuclear shape (*22*, *23*). For example, depleting the nucleolar protein NPM1 changes microtubule stability (*24*) and affects nuclear shape via connections between the cytoskeleton and nuclear envelope. Because tubulin is a known NAT10 substrate, we examined the microtubule network and observed network reorganization upon Remodelin treatment, NAT10 depletion, or mutational inactivation of NAT10 (Fig. 4A). In accord with there being a functional link between microtubule reorganization and nuclear shape rescue by NAT10 inhibition, the microtubule-destabilizing drugs nocodazole and colchicine also rescued the nuclear shape defects of siLMNA cells (Fig. 4B) and HGPS cells (fig. S10A), whereas latrunculin A, an actin polymerization inhibitor, increased nuclear distortion. Remodelin effects were not linked to Golgi apparatus fragmentation or tubulin depolymerization because in contrast to nocodazole or colchicine, Remodelin did not affect Golgi apparatus integrity or tubulin polymer assembly (Fig. 4, C and D) and did not cause cells to accumulate in mitosis.

To gain insight into how NAT10 modifies microtubule organization, we analyzed microtubule regrowth dynamics. Whereas initial microtubule regrowth (nucleation phase) appeared normal after NAT10 inhibition in siLMNA cells [Fig. 4E, time (t) = 5 min] and HGPS cells (fig. S10C), microtubule anchorage to centrosomes was affected by Remodelin in both siLMNA cells (Fig. 4E) and HGPS cells (fig. S10B) or by the NAT10 G641E mutation (Fig. 4E, t = 15 min), indicating that NAT10 KAT activity promotes microtubule anchorage. These results suggest that inhibiting NAT10 KAT activity in laminopathic cells reduces microtubule anchorage, releasing an external force on the nuclear envelope, thus contributing to nuclear shape rescue and global enhancement of cellular fitness (fig. S11). This is in line with studies showing that releasing microtubule forces on the nucleus by growing them on a "soft" substrate normalizes the nuclear shape of laminopathic cells (*25*) and helps explain why Remodelin, like other microtubule-reorganizing agents (*26*), corrects FTI-induced nuclear shape defects in nonprogeric cells (fig. S8).

Here, we have shown that the small molecule Remodelin improves nuclear shape and fitness of both progeric and lamin A/C–depleted cells via inhibiting NAT10. Although these effects appear to be connected to NAT10 organizing the microtubule network, we cannot rule out that inhibiting additional nuclear functions of NAT10, related to chromatin, might also contribute to global improvement of cellular fitness. Small-molecule inhibitors of NAT10 may thus provide additional ways to study laminopathy-associated processes with spatial and temporal resolution, as well as opportunities for alleviating dystrophic and premature-aging diseases.

References and Notes

1. H. J. Worman, G. Bonne, *Exp. Cell Res.* **313**, 2121–2133 (2007).
2. A. De Sandre-Giovannoli *et al.*, *Science* **300**, 2055 (2003).
3. M. Eriksson *et al.*, *Nature* **423**, 293–298 (2003).
4. J. L. Broers *et al.*, *Am. J. Pathol.* **143**, 211–220 (1993).
5. S. F. Moss *et al.*, *Gut* **45**, 723–729 (1999).
6. R. S. Venables *et al.*, *Br. J. Cancer* **84**, 512–519 (2001).
7. G. Galiová, E. Bártová, I. Raska, J. Krejcí, S. Kozubek, *Eur. J. Cell Biol.* **87**, 291–303 (2008).
8. C. Y. Chen *et al.*, *Cell* **149**, 565–577 (2012).
9. J. I. Toth *et al.*, *Proc. Natl. Acad. Sci. U.S.A.* **102**, 12873–12878 (2005).
10. F. Chimenti *et al.*, *J. Med. Chem.* **52**, 530–536 (2009).
11. Y. H. Chi, K. Haller, J. M. Peloponese Jr., K. T. Jeang, *J. Biol. Chem.* **282**, 27447–27458 (2007).
12. Q. Shen *et al.*, *Exp. Cell Res.* **315**, 1653–1667 (2009).
13. X. Li *et al.*, *J. Am. Chem. Soc.* **134**, 1982–1985 (2012).
14. R. Rodriguez *et al.*, *Nat. Chem. Biol.* **8**, 301–310 (2012).
15. S. Chimnaronk *et al.*, *EMBO J.* **28**, 1362–1373 (2009).
16. P. Scaffidi, T. Misteli, *Science* **312**, 1059–1063 (2006).
17. B. C. Capell *et al.*, *Proc. Natl. Acad. Sci. U.S.A.* **102**, 12879–12884 (2005).
18. V. L. Verstraeten *et al.*, *Proc. Natl. Acad. Sci. U.S.A.* **108**, 4997–5002 (2011).
19. M. W. Glynn, T. W. Glover, *Hum. Mol. Genet.* **14**, 2959–2969 (2005).
20. Y. Wang *et al.*, *Nucleus* **3**, 452–462 (2012).
21. M. X. Ibrahim *et al.*, *Science* **340**, 1330–1333 (2013).
22. M. A. Amin *et al.*, *Biochem. Biophys. Res. Commun.* **360**, 320–326 (2007).
23. M. A. Amin, S. Matsunaga, S. Uchiyama, K. Fukui, *Biochem. J.* **415**, 345–351 (2008).
24. G. Wang *et al.*, *J. Biol. Chem.* **285**, 19060–19067 (2010).
25. C. Tamiello *et al.*, *Nucleus* **4**, 61–73 (2013).
26. N. Suzuki, K. Del Villar, F. Tamanoi, *Proc. Natl. Acad. Sci. U.S.A.* **95**, 10499–10504 (1998).

Acknowledgments: We thank all members of the Jackson laboratory for help and support, J. Forment for discussions, and K. Dry and J. Travers for discussions and critical reading of the manuscript. We thank R. Belotserkovskaya for the GFP-H2B U2OS cell line and S. Heidorn and M. Garnett (Wellcome Trust Sanger Institute) for providing us with the cancer cells used in the lamin A/C expression screen. We thank Imagif and Institut de Chimie des Substances Naturelles, Centre National de la Recherche Scientifique (CNRS) de Gif-sur-Yvette, France, for proteomic analysis. Research in the Jackson laboratory is funded by Cancer Research UK program grant C6/A11224, the European Research Council, and the European Community Seventh Framework Programme grant agreement HEALTH-F2-2010-259893 (DDR). Core funding is provided by CRUK (C6946/A14492) and the Wellcome Trust (WT092096). S.P.J. receives his salary from the University of Cambridge, UK, supplemented by CRUK. D.L is funded by a European Molecular Biology Organization (EMBO) long-term fellowship ALTF 834-2011 and by a Project Grant from the Medical Research Council, UK MR/L019116/1. S.B. was funded by a EMBO long-term fellowship ALTF 93-2010 and CRUK. R.R. is supported by CNRS. M.D. is supported by the European Research Council grant DDREAM. A patent (application number 1405991.9) on the small molecule Remodelin and structural analogs for the treatment of disease has been filed by the University of Cambridge and CNRS. The data presented in this paper are included in the main paper and the supplementary materials. D.L. conceptualized the study and carried out all the experiments unless stated otherwise. S.B. cloned NAT10 expression constructs, performed the NAT10 structure analysis, produced high-resolution microscopy images, and contributed to live-cell imaging. R.R. designed and synthesized the small molecules and performed circular dichroism spectroscopy experiment. M.D. provided assistance with IF, fluorescence-activated cell sorting, and western blotting experiments. D.L. designed the experiments and analyzed the data. D.L. and S.P.J wrote the paper, with contributions from R.R., and S.B.

Supplementary Materials

www.sciencemag.org/content/344/6183/527/suppl/DC1
Materials and Methods
Figs S1 to S11
Movie S1

25 February 2014; accepted 4 April 2014
10.1126/science.1252651

Molecular-Level Functional Magnetic Resonance Imaging of Dopaminergic Signaling

Taekwan Lee,[1] Lili X. Cai,[1] Victor S. Lelyveld,[1] Aviad Hai,[1] Alan Jasanoff[1,2,3]*

We demonstrate a technique for mapping brain activity that combines molecular specificity and spatial coverage using a neurotransmitter sensor detectable by magnetic resonance imaging (MRI). This molecular functional MRI (fMRI) method yielded time-resolved volumetric measurements of dopamine release evoked by reward-related lateral hypothalamic brain stimulation of rats injected with the neurotransmitter sensor. Peak dopamine concentrations and release rates were observed in the anterior nucleus accumbens core. Substantial dopamine transients were also present in more caudal areas. Dopamine-release amplitudes correlated with the rostrocaudal stimulation coordinate, suggesting participation of hypothalamic circuitry in modulating dopamine responses. This work provides a foundation for development and application of quantitative molecular fMRI techniques targeted toward numerous components of neural physiology.

Despite development of magnetic resonance imaging (MRI) contrast agents sensitive to molecular aspects of brain function (*1*), neural activity mapping using such probes has not previously been demonstrated. Molecular imaging using contrast agents could provide a powerful method for determining topography and dynamics of neural activity components over brain volumes inaccessible to conventional electrophysiology or optical imaging. MRI-based molecular mapping would also substantially exceed the spatiotemporal resolution of positron emission tomography.

A prime target for molecular functional MRI (fMRI) is the ventral striatum, a brain region that integrates multiple neurochemically and anatomically defined neural populations involved in motivated behavior. Particular interest focuses on dopaminergic striatal afferents that project from the midbrain (*2*). These cells are phasically activated by rewards and reward-predictive cues (*3*) and are targets of drugs that boost striatal dopamine concentrations (*4*). Although neuroarchitecture of dopaminergic systems (*5*) and some regional differences in dopamine release have been studied (*6*), spatial aspects of signaling are generally less well understood. This complicates characterization of relationships among dopamine neuron firing, dopamine release, and broader neural activity.

Neurotransmitter-sensitive MRI contrast agents that we recently developed (*7*) could be used for mapping dopamine signaling in living brains. These probes are engineered forms of BM3h, a paramagnetic heme protein that alters T_1-weighted MRI signals. BM3h-based contrast agents can be injected intracranially to fill volumes of several cubic millimeters, comparable in size to the entire ventral striatum. A BM3h sensor variant called BM3h-9D7 displays optimal specificity for dopamine (dissociation constant K_d = 1.3 μM) versus norepinephrine (K_d = 37 μM) and serotonin (K_d = 70 μM) (*8*). Longitudinal relaxivity (r_1) of BM3h-9D7 at 37°C was measured to be 0.83 ± 0.01 and 0.10 ± 0.00 mM^{-1} s^{-1} in the absence and presence of saturating dopamine, respectively (fig. S1). These r_1 values imply that T_1-weighted MRI signal decreases are expected when dopamine is released in the presence of sensor.

We applied BM3h-9D7 in conjunction with electrical stimulation of the medial forebrain bundle (MFB) in lateral hypothalamus (LH); MFB microstimulation engages mesolimbic dopamine fibers (*9*) and is the basis for common addiction models. Rats were implanted with striatal injection cannulae and MFB-targeted electrodes (Fig. 1A) and assessed for operant performance in a self-stimulation task. Animals that learned the behavior were anesthetized and inserted into a 9.4-T MRI scanner. L-3,4-Dihydroxyphenylalanine (L-DOPA, 160 mg per kilogram of body weight) was injected to prevent dopamine depletion, and a relatively low dose of dopamine reuptake blocker, GBR-12909 (8 mg/kg), was administered to enhance synaptic overflow (*10*); these treatments promoted robust repeated measurements, but were not required for MRI signal changes (fig. S2). BM3h-9D7 (500 μM) was infused at 0.1 μl/min (Fig. 1B). After a 42-min preinjection period, periodic MFB stimuli were delivered in blocks of 16 s, separated by 5-min rest periods. T_1-weighted images were collected every 8 s throughout.

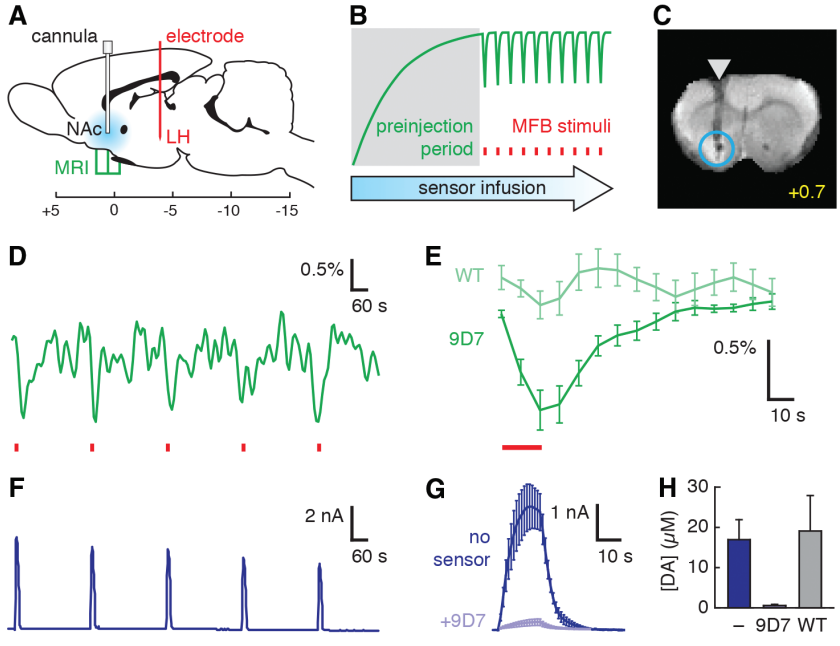


Fig. 1. Molecular fMRI detects dopamine signaling in ventral striatum. (**A**) Stimulation electrodes (red) were implanted in LH. Cannulae in NAc allowed dopamine sensor infusion (blue), and MRI data were acquired from surrounding slices. Scale shows coordinates relative to bregma. (**B**) Experimental design: Sensor preinjection (gray shading) is followed by functional imaging with MFB stimulation (red ticks). Green line represents expected MRI signal changes due to injection and stimulus-induced dopamine release. (**C**) Coronal slice (bregma + 0.7 mm) from a single rat brain after preinjection with BM3h-9D7. Arrowhead denotes cannula and circle defines an ROI. (**D**) ROI-averaged MRI signal over five stimuli (red ticks) in one animal, after preinjection of BM3h-9D7. (**E**) Average peristimulus IRF calculated within the ROI from animals injected with BM3h-9D7 (dark green, n = 7) or control BM3h-WT (light green, n = 7). Stimulation period indicated by red line. (**F**) Amperometric measurement of NAc dopamine release evoked by MFB stimuli (red ticks). (**G**) Average (n = 4) amperometry transients before (dark blue) or after (light blue) infusion of BM3h-9D7 (red line indicates stimulation period). (**H**) Calibrated dopamine amplitudes measured without sensor infusion (dark blue, n = 7), after infusion of BM3h-9D7 (light blue, n = 4), or after infusion of BM3h-WT (gray, n = 3). Error bars denote SEMs.

[1]Department of Biological Engineering, Massachusetts Institute of Technology (MIT), Cambridge, MA 02139, USA. [2]Department of Brain and Cognitive Sciences, MIT, Cambridge, MA 02139, USA. [3]Department of Nuclear Science and Engineering, MIT, 77 Massachusetts Avenue, Room 16-561, Cambridge, MA 02139, USA.

*Corresponding author. E-mail: jasanoff@mit.edu

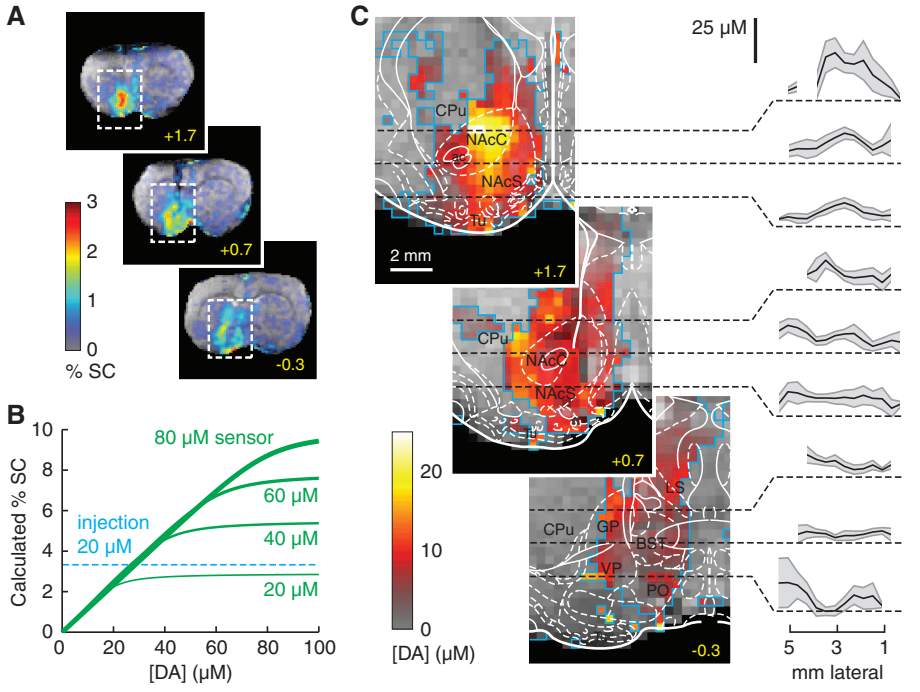


Fig. 2. Quantitative functional imaging of dopamine concentrations. (**A**) Raw maps of signal change averaged over seven animals injected with BM3h-9D7. Distribution of percent signal change (% SC) over three coronal sections; rostrocaudal coordinates in yellow. (**B**) Calculated % SC as a function of released dopamine concentration ([DA]) for four sensor concentrations, showing linearity of % SC versus [DA], except for saturation effects. In areas that received substantial contrast agent infusion, a ratio of 8 μM dopamine per % SC can be used to estimate dopamine concentrations. (**C**) Quantitative mapping of average peak dopamine concentrations over regions outlined in (A). Blue outlines indicate voxels included in the analysis, each incorporating data from two to seven animals (compare fig. S3). Rat brain atlas (*20*) is overlaid with labels in black; regions defined in text, plus anterior commissure (ac), bed nucleus of the stria terminalis (BST), globus pallidus (GP), lateral septum (LS), olfactory tubercle (Tu), and ventral pallidum (VP). Plots show means (black lines) and SEMs (shading) of dopamine concentrations along dashed lines in respective images.

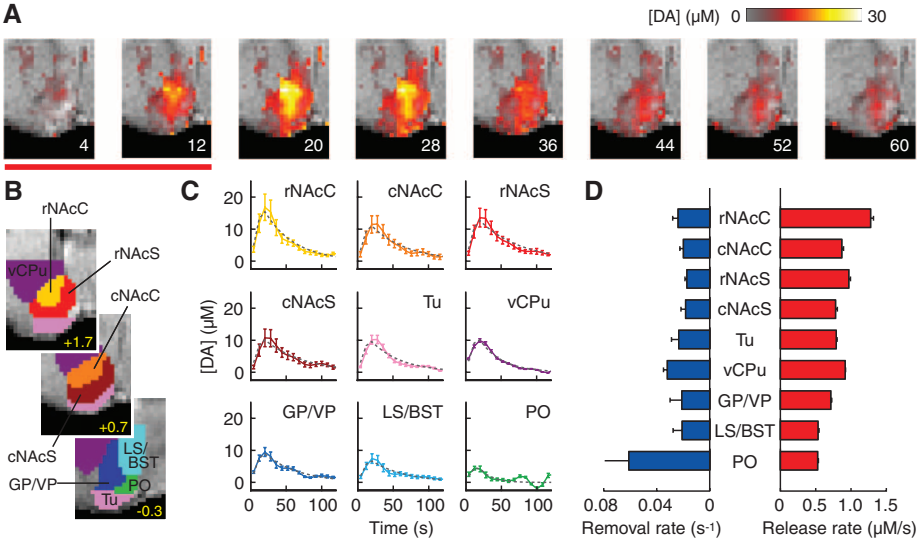


Fig. 3. Dynamics of dopamine-dependent MRI responses to MFB stimulation. (**A**) Image frames from the first eight time points of the IRF. Color bar indicates dopamine concentrations during and after an MFB stimulus (red line). (**B**) ROIs defined by brain atlas alignment to MRI data. (**C**) IRFs calculated for each ROI. Data points indicate mean [DA] at each time. Gray dashed lines show best-fit simulated time courses using a single compartment model. (**D**) Dopamine release (red) and removal (blue) rates estimated from model fitting. SEMs computed by jackknife resampling over seven animals.

MRI signal was examined in a region of interest (ROI) around the cannula tip (Fig. 1C). Transient signal decreases were observed with each stimulus (Fig. 1D). A peristimulus impulse response function (IRF) was calculated from each data set and averaged over seven animals (Fig. 1E). An average maximum signal decrease of 1.1 ± 0.2% was observed, peaking around the stimulus offset time; this change was statistically significant (Student's *t* test, $P = 0.0008$). Control experiments were performed with BM3h-WT (*7*), a dopamine-insensitive protein that differs from BM3h-9D7 by only four residues and exhibits similar r_1 at 25°C (*8*). No significant signal changes were observed with BM3h-WT ($P = 0.25$, $n = 7$), indicating that the dopamine-binding property of BM3h-9D7 is necessary for MRI-detectable responses near the contrast agent injection site.

Fixed-potential amperometric recordings from separate animals ($n = 7$) treated identically to the MRI subjects confirmed that substantial dopamine release takes place in the area where MRI signal changes were recorded (Fig. 1, F and G); maximal concentrations of 17 ± 5 μM were detected. Electrochemical and MRI-based measurements showed similar temporal properties, with little adaptation of responses over multiple stimuli and similar onset kinetics after each stimulus. MRI recordings showed slower return to baseline, however. Amperometry after infusion of BM3h-9D7 ($n = 4$) showed stimulus-evoked dopamine release of only 0.59 ± 0.27 μM, significantly lower than measurements obtained in the absence of sensor (Student's *t* test, $P = 0.0092$) (Fig. 1H). By contrast, recordings after injection of BM3h-WT ($n = 3$) were indistinguishable from recordings without contrast agent ($P = 0.84$). BM3h-9D7 thus binds to stimulus-evoked dopamine in vivo, explaining the observed MRI contrast changes. Although dopamine buffering is a consequence of this interaction, buffering is unlikely to be severe near synapses, where dopamine transients probably exceed 1 mM (*11*).

Imaging data from the seven animals of Fig. 1E were coregistered, and a map of peak MRI changes was assembled (Fig. 2A). Signal changes were concentrated near the area of contrast agent injection. To distinguish regions that experienced little dopamine release from those that did not receive contrast agent, we used experimental parameters to model the expected MRI signal change as a function of sensor and dopamine concentration (Fig. 2B) (see materials and methods). The percentage of MRI signal change was a pseudolinear function of dopamine concentration up to a saturation point dependent on the voxel concentration of BM3h-9D7. By considering only those voxels (fig. S3) that experienced statistically significant ≥3.4% signal change during contrast agent injection, equivalent to ≥20 μM BM3h-9D7, we could obtain quantitative maps of released dopamine concentrations from individual fMRI data sets and averaged across animals.

We constructed a map of peristimulus dopamine concentration maxima across ventral striatum

and surrounding regions (Fig. 2C). Line profiles in Fig. 2C indicate error margins around the measured dopamine values and validate prominent features of the spatial map. Peak concentrations measured by molecular fMRI corresponded fairly closely to the electrochemical measurements of Fig. 1H. The most pronounced focus of MRI-detectable neurotransmitter release was found in the nucleus accumbens (NAc) core (NAcC), where dopamine concentrations reached 27 μM. Some areas that received substantial contrast agent doses showed little dopamine release.

Molecular fMRI allowed dynamic dopamine mapping over each MFB stimulus cycle (Fig. 3A). Average time courses for nine anatomically defined ROIs (Fig. 3B) were determined and fit to a simple model in which dopamine is released at a fixed rate during stimulation and removed according to a first-order rate constant. This model accounted well (squared correlation coefficent $R^2 \geq 0.9$) for data from eight regions (Fig. 3, C and D). Significant dopamine release rates (Student's t test, $P < 10^{-7}$) were found in all ROIs, though the quality of the fit to one region, the preoptic area (PO), was poor ($R^2 = 0.40$). The highest dopamine release rate (1.28 ± 0.04 μM/s) was observed in rostral NAcC (rNAcC), where peak dopamine amplitudes were highest (compare to Fig. 2C). Release rates in neighboring structures were ~30% lower, and differences in estimated release between rNAcC and all other ROIs were statistically significant (Student's t test, $P < 10^{-4}$). Apparent dopamine removal rates averaged 0.026 s^{-1}. Most pairwise differences among ROIs were insignificant ($P > 0.13$). Only ventral caudate putamen (vCPu) showed significantly higher removal than rostral and caudal NAc shell (rNAcS and cNAcS) and caudal NAcC (cNAcC). Dopamine removal and release rates were uncorrelated ($r = –0.39$, $P = 0.3$). Transport parameters were probably affected by binding kinetics of dopamine to BM3h-9D7 itself ($k_{obs} \sim 0.3$ s^{-1} for 20 μM sensor; fig. S4). Results nevertheless indicate that the profile of phasic dopamine amplitudes observed here can be explained by single compartment dynamics arising primarily from differences in stimulus-associated dopamine release, as opposed to dopamine elimination or catabolism.

We addressed the possibility that the electrode position in LH, which varied slightly in our experiments, influenced the spatial profile of dopamine responses measured by MRI. Response centroids were clustered within a sphere of ~1 mm diameter in NAc and showed no systematic relation to electrode positions (fig. S5A). This suggests that dopamine profiles do not purely reflect architecture of projections from the stimulation sites in LH (*12*). We also examined the relation between dopamine response amplitudes and stimulation coordinates (fig. S5B). Significant correlation between rostrocaudal electrode position and response magnitude was observed ($r = –0.97$, $P = 0.001$); mediolateral and dorsoventral electrode coordinates were uncorrelated ($P > 0.3$). Apparent dependence of dopamine release on rostrocaudal positioning of the stimulation site within a narrow spatial range (0.9 mm) suggests that ventral striatal dopamine release is modulated by distinct neural populations that were stimulated to varying extents.

Our molecular fMRI results offer insights related to dopaminergic signaling: First, among brain regions analyzed, rNAcC displayed maximal dopamine transients evoked by MFB stimulation. The observation of peak release in rNAcC is consistent with point measurements obtained with similar stimuli (*13*–*15*), but could not be predicted from immunohistological (*16*, *17*) or connectivity data (*18*). Second, the relation between stimulation coordinates and responses suggests that local circuitry near the stimulation site can modulate the amplitude of striatal dopamine release. The spatial profile of dopamine signaling did not vary strongly with stimulus location, but might relate to operant behavior. Third, the reward-related stimulation that we used promotes substantial phasic dopamine release outside NAc, where dopamine is less studied. Examination of an extended field of view even showed evidence of extrastriatal dopamine release in the thalamic reticular nucleus (fig. S6). Fourth, molecular fMRI data presented here provide an unprecedented microscopically averaged measure of phasic dopamine, including contributions from multiple extracellular environments. Approximate quantitative agreement between imaging and electrochemical measurements argues for functional equivalence of these techniques and corroborates validity of interstitial dopamine as a surrogate indicator of synaptic neurotransmitter release (*19*).

This work establishes a foundation for extension of molecular fMRI techniques along multiple trajectories. Relationships between dopamine signaling and other components of neural activity could be analyzed by combining our dopamine imaging method with conventional hemodynamic fMRI or additional molecular fMRI approaches. Higher-resolution imaging could be performed to characterize signaling at spatial scales below 100 μm. Sensitivity would be enhanced beyond concentrations of 2 to 5 μM dopamine achieved here by using better contrast agents or different imaging parameters, and improved probe delivery strategies could enable completely noninvasive experiments. These steps will facilitate application of molecular fMRI to numerous problems in neuroscience.

References and Notes

1. A. Jasanoff, *Curr. Opin. Neurobiol.* **17**, 593–600 (2007).
2. J. D. Salamone, M. Correa, *Neuron* **76**, 470–485 (2012).
3. W. Schultz, *Trends Neurosci.* **30**, 203–210 (2007).
4. D. Sulzer, *Neuron* **69**, 628–649 (2011).
5. S. Ikemoto, *Brain Res. Brain Res. Rev.* **56**, 27–78 (2007).
6. M. P. Saddoris, J. A. Sugam, F. Cacciapaglia, R. M. Carelli, *Front. Biosci.* **E5**, 273 (2013).
7. M. G. Shapiro *et al.*, *Nat. Biotechnol.* **28**, 264–270 (2010).
8. E. M. Brustad *et al.*, *J. Mol. Biol.* **422**, 245–262 (2012).
9. A. G. Ewing, J. C. Bigelow, R. M. Wightman, *Science* **221**, 169–171 (1983).
10. L. J. May, W. G. Kuhr, R. M. Wightman, *J. Neurochem.* **51**, 1060–1069 (1988).
11. P. A. Garris, E. L. Ciolkowski, P. Pastore, R. M. Wightman, *J. Neurosci.* **14**, 6084–6093 (1994).
12. R. Nieuwenhuys, L. M. Geeraedts, J. G. Veening, *J. Comp. Neurol.* **206**, 49–81 (1982).
13. S. R. Jones, S. J. O'Dell, J. F. Marshall, R. M. Wightman, *Synapse* **23**, 224–231 (1996).
14. N. A. Addy, D. P. Daberkow, J. N. Ford, P. A. Garris, R. M. Wightman, *J. Neurophysiol.* **104**, 922–931 (2010).
15. J. Park, B. J. Aragona, B. M. Kile, R. M. Carelli, R. M. Wightman, *Neuroscience* **169**, 132–142 (2010).
16. B. J. Ciliax *et al.*, *J. Neurosci.* **15**, 1714–1723 (1995).
17. C. Freed *et al.*, *J. Comp. Neurol.* **359**, 340–349 (1995).
18. D. S. Zahm, *Ann. N.Y. Acad. Sci.* **877**, 113–128 (1999).
19. S. J. Cragg, M. E. Rice, *Trends Neurosci.* **27**, 270–277 (2004).
20. G. Paxinos, C. Watson, *The Rat Brain in Stereotaxic Coordinates* (Academic Press, San Diego, CA, ed. 3, 1997).

Acknowledgments: This work was supported by NIH grants R01-DA02899, R01-NS076462 and DP2-OD002114, and Defense Advanced Research Projects Agency grant W911NF-10-0059 to A.J. We thank G. Westmeyer for technical guidance and A. Graybiel for comments on the manuscript. We also thank C. Blaha, A. Graybiel, M. Howe, T. Rogers, and T. Schneider for assistance with electrochemistry; E. Brustad and F. Arnold for collaboration on sensor development; and A. Liang and S. Lippard for help with stopped-flow measurements. U.S. patent application 12/675,256 pertains to BM3h-9D7.

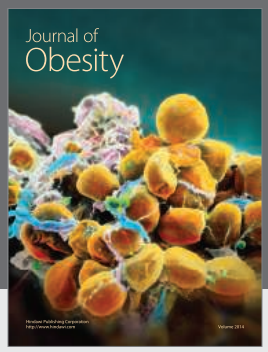
Supplementary Materials

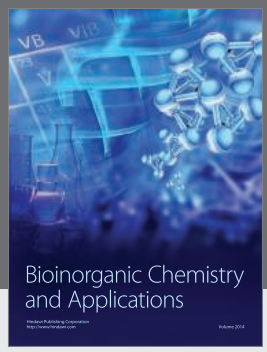
www.sciencemag.org/content/344/6183/533/suppl/DC1
Materials and Methods
Figs. S1 to S6
Reference (*21*)

5 December 2013; accepted 3 April 2014
10.1126/science.1249380

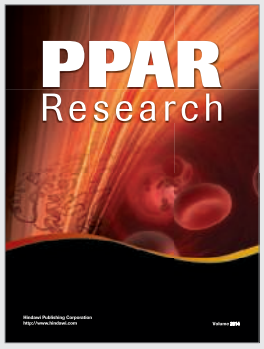












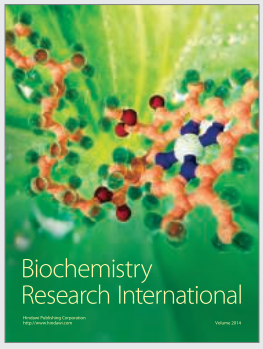


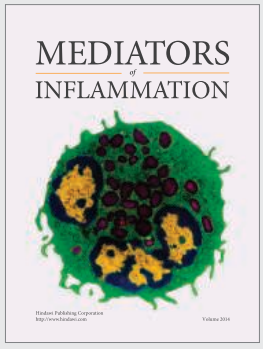




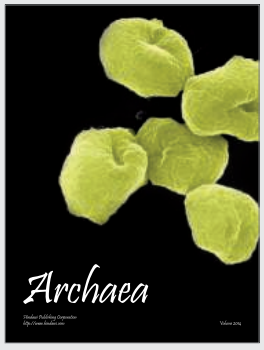


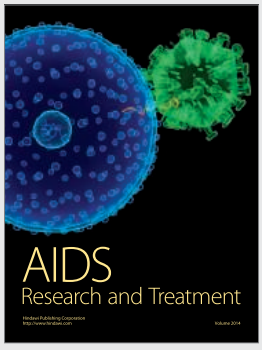


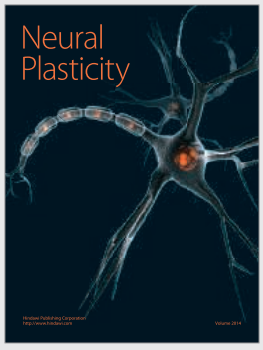


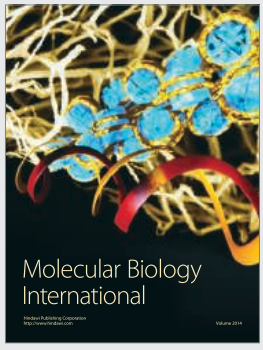


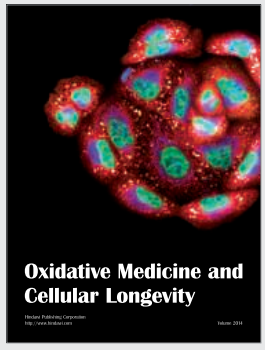












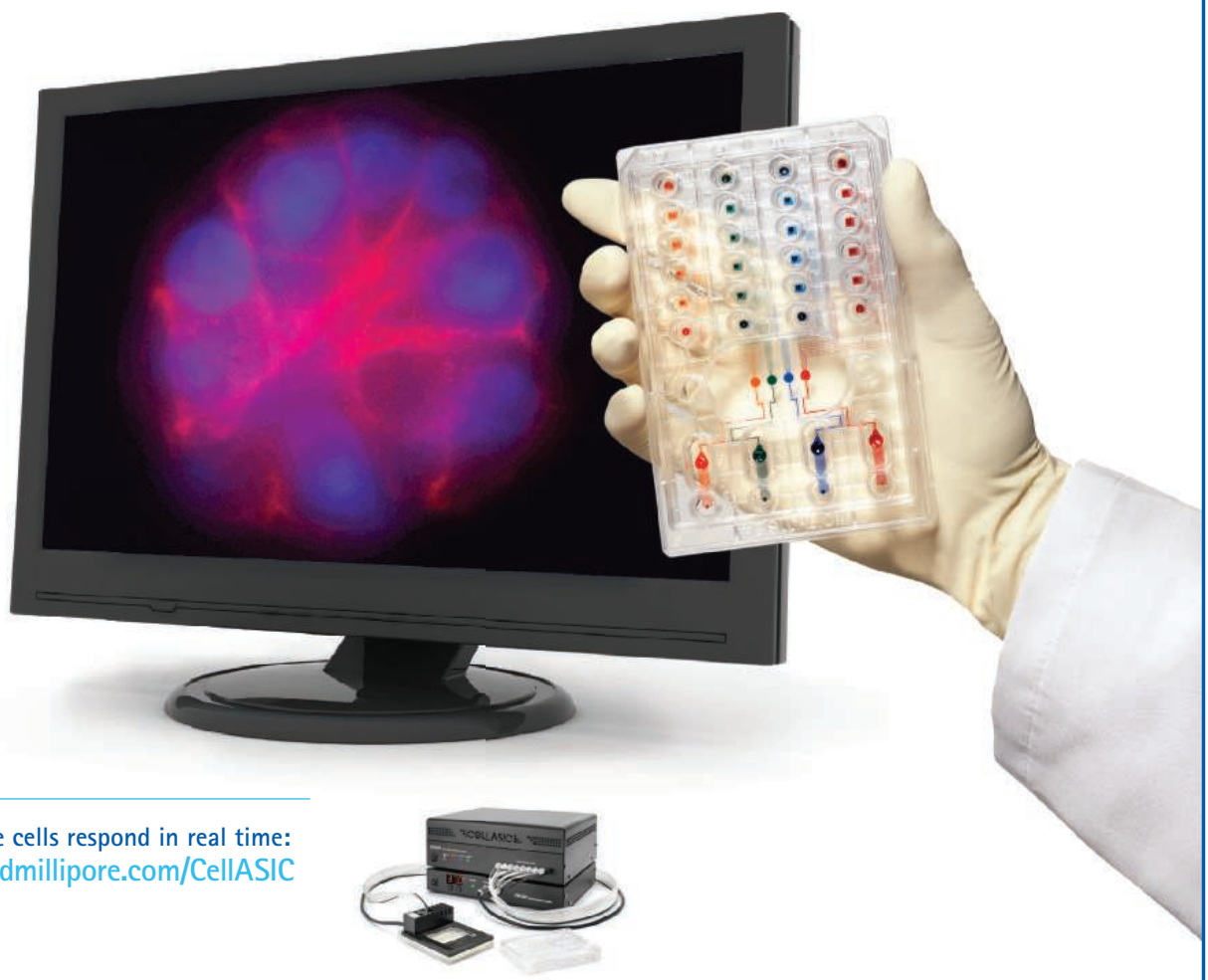
Hindawi

Submit your manuscripts at
http://www.hindawi.com

EMD MILLIPORE

Take Control
with dynamic cell culture.

Biology is so much more than DMEM/FBS, 37 °C, 5% CO_2.
It's easy to program automated changes to culture media, gas and temperature, while tracking cell responses, with the flexible, intuitive CellASIC® ONIX Microfluidic Platform. By taking control of this truly *in vivo*-like environment, you'll be able to perform dynamic, time-lapse experiments never before possible.



Watch live cells respond in real time:
www.emdmillipore.com/CellASIC

EMD Millipore is a division of Merck KGaA, Darmstadt, Germany

EMD Millipore and the M logo are trademarks and CellASIC is a registered trademark of Merck KGaA, Darmstadt, Germany.
© 2014 EMD Millipore Corporation, Billerica, MA, USA. All rights reserved. BS GEN-14-09917 03/2014

eppendorf & Science

PRIZE FOR NEURO BIOLOGY



2013 Winner
Dr. Michael Yartsev
CV Starr Research Fellow
Princeton Neuroscience Institute

Application Deadline
June 15, 2014

Call for Entries

Eppendorf & Science Prize for Neurobiology
The annual Eppendorf & Science Prize for Neurobiology, an international award, honors young scientists for their outstanding contributions to neurobiological research based on methods of molecular and cell biology.
The winner and finalists are selected by a committee of independent scientists, chaired by Science's Senior Editor, Dr. Peter Stern. To be eligible, you must be 35 years of age or younger.

You could be next to win this prize and to receive
> Prize money of US$25,000
> Publication of your work in Science
> Full support to attend the Prize Ceremony held in conjunction with the Annual Meeting of the Society for Neuroscience in the USA
> An invitation to visit Eppendorf in Hamburg, Germany

It's easy to apply!

Learn more at: www.eppendorf.com/prize

eppendorf

Science AAAS

AAAS® and Science® are registered trademarks of the American Society for the Advancement of Science, USA. Eppendorf® and the Eppendorf logo are registered trademarks of Eppendorf AG.
All rights reserved, including graphics and images. Copyright © 2014 by Eppendorf AG. Kurstin Roe Photography.

Accurate, Fast, Apoptosis Studies

Made easy using the BD Accuri™ C6 Personal Flow Cytometer.



Arguably, as easy as Apoptosis is going to get.

The BD Accuri C6 is making it even easier to apply the power of flow cytometry to your research with free software templates and ready-to-go reagent kits for apoptosis studies involving Annexin V, JC-1, and active caspase-3. You get more insight and easier workflow, whether you're a flow expert or have never used flow cytometry before.

These templates feature predefined workspace that speeds setup and analysis. Applying the power of flow cytometry, the BD Accuri C6 uses less samples and delivers greater accuracy.

Several kits are available including BD Pharmingen™ Annexin V Apoptosis Detection Kits that detect externalization of phosphatidylserine (PS) molecules on the plasma membrane, BD™ MitoScreen Kit that detects apoptosis from changes in mitochondrial membrane potential, and BD Pharmingen™ Caspase-3 Assay Kit that detects apoptosis from the presence of cleaved (activated) caspase-3.

Find out more about how the BD Accuri C6 puts the power of 4-color cell analysis within reach by being easy to use, simple to set up and maintain, transportable, and affordable.

bdbiosciences.com/go/templates

BD

Helping all people live healthy lives

Class 1 Laser Product.
For Research Use Only. Not for use in diagnostic or therapeutic procedures.
BD, BD Logo and all other trademarks are property of Becton, Dickinson and Company. © 2013 BD
23-15942-00

BD Biosciences
2350 Qume Drive
San Jose, CA 95131
bdbiosciences.com



Join the Conversation!

Twitter is a great way to connect with AAAS members and staff about the issues that matter to you most. Be a part of the discussion while staying up-to-date on the latest news and information about your personal member benefits.

Follow us @AAASmember and join the conversation with #AAAS

AAAS MemberCentral
MemberCentral.aaas.org

Lambda TLED™
Transmitted Light Source



High-output white light LED!

NEW!

FEATURES

- >10,000 hour lifetime
- <25µsecs on-off time
- TTL control (with polarity switch)
- Very stable output
- Compact stand-alone design
- Easy installation

SUTTER INSTRUMENT

PHONE: 415.883.0128 | FAX: 415.883.0572
EMAIL: INFO@SUTTER.COM | WWW.SUTTER.COM

AAAS Travels



Discover BURMA!
January 4-17, 2015
Angkor Wat Ext., January 17-20!

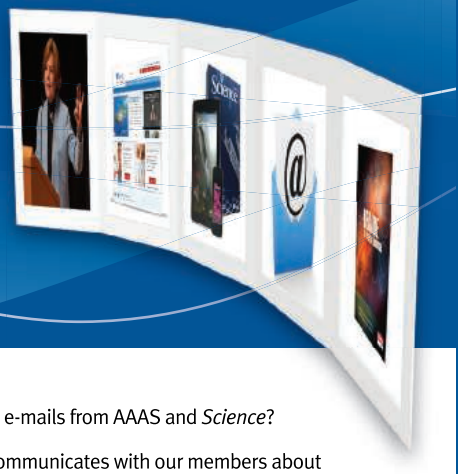
Burma is one of the least globalized lands in the world and one of Asia's most fascinating locations. Explore from Inle Lake and the fabled city of Mandalay to the stunning Bagan plain where thousands of temples dot the lush savanna. $4,595 + air
Angkor Wat extension $1,495 + air

For a detailed brochure, please call (800) 252-4910
All prices are per person twin share + air

Betchart Expeditions Inc.
17050 Montebello Rd, Cupertino, CA 95014
Email: AAASInfo@betchartexpeditions.com
www.betchartexpeditions.com

STAY INFORMED!
STAY CONNECTED!

Get more from your AAAS membership



Are you currently registered to receive e-mails from AAAS and *Science*?

E-mail is the primary way that AAAS communicates with our members about AAAS programs, new member benefits, invitations to special events, and, of course, the latest news and research being published in *Science*.

Sign up today to receive e-mails from AAAS and ensure that you are getting the most out of your membership and *Science* subscription.*

To get started visit: **promo.aaas.org/stayconnected** You'll need your AAAS Member number. Find it above your name on your *Science* mailing label.

Don't miss a thing. Sign up for e-mail communications from AAAS today!

Science AAAS

*AAAS follows CAN-SPAM and European Safe Harbor guidelines for protecting your privacy. We will never sell your e-mail address and you can opt-out of receiving e-mails at any time.

Bat man wins young scientist prize in Stockholm. Are you next?

Science & SciLifeLab PRIZE FOR YOUNG SCIENTISTS



Photo: Nancy Evelyn - UGA

The 2014 *Science* and SciLifeLab Prize is now open and we are looking for new bright ideas. Are you like Daniel Streicker? Are you a recent PhD graduate eager to win a prize? Daniel is a true "bat man" having spent many hours in dark caves studying bats, to better understand how infectious diseases emerge and establish in new host species. It is for this work that Daniel was published in the journal *Science*, December 6, 2013, as the Grand Prize winner of the 2013 *Science* & SciLifeLab Prize for Young Scientists.

The journal *Science* and SciLifeLab have come together to recognize and celebrate excellence in PhD Research. The *Science* & SciLifeLab Prize has been established to support young scientists at the start of their career.

The four categories for the 2014 prize are: Cell and Developmental Biology; Genomics and Proteomics; Environment; and Translational Medicine. The Grand Prize winner will receive 25,000USD and the other three Category Prize winners will receive 3,000USD each. The Grand Prize winning essay will be published in *Science* and the Category Prize winners will be published in *Science* online.

The deadline for submissions is August 1, 2014.
For further details and to enter, please visit: www.sciencemag.org/scilifelabprize

For over 130 years the journal Science has been the world's leading journal of original scientific research, global news and commentary.

SciLifeLab is a collaboration among four universities in Stockholm and Uppsala, Sweden, and is a national center for molecular biosciences with focus on health and environmental research.

This prize is made possible with the kind support of the Knut and Alice Wallenberg Foundation.

Science AAAS

SciLifeLab

Knut och Alice Wallenbergs Stiftelse

Souping Up Your 'Scope



The diversity of options for today's microscopes—objectives and cameras, advanced stages and software, sources of illumination, and more—challenge even the experts when designing a new system. The process gets even more complex when faced with constraints, such as a budget or a specific set of necessary applications. Consequently, life scientists need to know where to spend and when to save. The experts interviewed here provide some pointers and give us insight into some of the newest components in the fast-changing field of microscopy. **By Mike May**

How you build your microscope depends entirely on how you plan to use it.

A scientist's ability to visualize the intricate details of their experimental model depends upon their microscope's capabilities. "An old adage is that a microscope is only as good as the sum of its parts," says Douglas Richardson, director of imaging at the **Harvard Center for Biological Imaging** in Cambridge, Massachusetts. "If one component—lens, detector, or anything else—is of lower quality than the rest, it affects the image in the end." He adds, "You need all of the parts to function at their highest levels."

A scientist can easily dream of their ideal microscope system, but building one takes more work. As Richardson says, "It's a lengthy process to select which components to put on your system. It needs to be customized for your own applications."

With so many components available today, every scientist needs to make some choices, often based on price, about which ones are must-haves. When asked if any particular pieces matter more than others, Richardson says, "With any system, the most important component is the objective." He adds, "When we look at a system, one of the first things that I consider is: What objectives are available and which ones will work for the applications that we have in mind for the microscope?" So Richardson would put more money in an objective first. Next, he'd invest in a good detector.

How you build your microscope depends entirely on how you plan to use it. For example, certain types of cameras work better in different lighting situations than others. Likewise, microscope stages can address specific needs, such as mobility or environmental constraints. To get the optimum results, you need to combine the parts that work well together to meet the specifications that your experiments demand.

CONNECTING THE RIGHT CAMERA

Many life scientists attach a camera to their microscopes to both document and analyze images. In today's microscope cameras, an electronic sensor takes the place of film. One of the oldest sensors is a charge-coupled device (CCD), in which an array of pixels captures light and turns it into an electrical signal. Many manufacturers continue to use this type of sensor, which is extremely reliable.

A less expensive technology, complementary metal-oxide semiconductor (CMOS) sensors, came from the integrated-circuit industry. This kind of sensor also turns light into an electrical signal, but it requires more circuitry on the sensor, which takes up space for sensing, thereby making this technology less sensitive to light, on average, than a CCD. Nonetheless, CMOS sensors enable faster frame rates (images per second) than CCD sensors since pixels are detected in groups rather than individually. A new version of CMOS, called scientific CMOS (sCMOS), addresses the technology's limitations by providing increased sensitivity while maintaining the speed.

Different applications, however, often determine which unique camera features are necessary. "If you're building a simple microscope to snap a picture of a sample stained with H&E—hematoxylin and eosin—your camera does not need to be overly extravagant." If you need higher imaging rates or the ability to detect weak fluorescent signals, says Richardson, "you could be going from a $2,000 camera to a $20,000 or $30,000 one." The former could be a high-end consumer CCD camera, and the latter might be an sCMOS camera.

Manufacturers continue to make advances in microscope cameras using a variety of sensors. As an example, Scott Olenych, product

Upcoming Features

Big Data—June 13

Digital Lab Management—July 25

Metabolomics—September 19

CREDIT: © ANYAIVANOVA/SHUTTERSTOCK.COM

marketing manager of imaging products at **Carl Zeiss Microscopy** in Oberkochen, Germany, points out his company's new Axiocam 506, which uses a CCD sensor with a 16 mm diagonal dimension. Compared to cameras that use a sensor with an 11 mm diagonal or less, the Axiocam 506 can grab a larger area of view. In addition, this camera comes in color and monochromatic versions with software that controls image acquisition and provides other tools, including the ability to add labels or scale bars to an image. In describing this software, Olenych says, "People generally agree that it's fairly simple to use." That really matters, because, as Olenych says, "You interact with the microscope at the computer, and the software determines the overall experience."

When outfitting a microscope with a camera, scientists can choose from other options with a 16 mm diagonal CCD. An example is the Retiga 6000, which is made by **QImaging** in Surrey, British Columbia, Canada. This camera, says Chris Ryan, product manager at QImaging, "is for customers who want to scan a whole slide or simultaneously monitor large populations of cells, say for high-content screening."

In fluorescent imaging, for example, scientists look for sensitivity and resolution, says Ryan. Sensitivity determines the weakest fluorescent signal that can be detected, and resolution reveals the smallest features that can be distinguished in an image. "Those features are a combination of the camera and the objective," says Ryan.

In some cases, a life scientist might prefer a camera with a range of features. For that, they might select an sCMOS camera. As an example, Orla Hanrahan, a life science application specialist at **Andor Technology** in Belfast, Ireland, mentions Andor's Zyla 4.2. "This can provide sensitivity, speed, and a large field of view, sort of an everything-in-one camera," says Hanrahan.

In low-light imaging, though, a researcher might prefer an electron-multiplying charge-coupled device (EMCCD) camera. An EMCCD includes an electronic device that multiplies the output from a conventional CCD. As a result, an EMCCD can detect weaker signals. For example, the Evolve 512 Delta from **Photometrics** in Tucson, Arizona, uses an EMCCD sensor. Rachit Mohindra, product manager at Photometrics, points out a downside, however: "To work at such low-light levels, EMCCD cameras use sensors with much larger pixels, which collect more light in a given amount of area, so you can't see the finer details."

KEEPING SAMPLES ALIVE

Today's life scientists often image live cells. Traditionally, scientists mostly looked at dead cells, which were prepared using a process that makes the samples robust and able to survive storage for years without any special care. Live cells, by contrast, must be nurtured—kept in the right surroundings and temperature—to keep them alive. As Michael O'Grady, senior R&D manager at **Life Technologies** in Carlsbad, California, says, "To get crisp images, you need to keep the cells healthy."

To do that, scientists must maintain specific environmental conditions when viewing live cells. To decide what devices provide the best conditions for a specific application, a scientist can ask an expert, such as Jeffrey D. McGinn, president and director of instrument sales, **McCrone Microscopes & Accessories** in Westmont, Illinois. He says, "When someone contacts us, we go through some needs-assessment questions, like asking about the types of samples the customer wants to look at and if the samples need to be in some particular environment." As a result, he might suggest outfitting a system with a temperature-controlled stage like that available from **Linkam Scientific Instruments** in Surrey, United Kingdom. These stages can maintain a sample at temperatures of -196°C to 1,500°C. As an example of an application that requires heating, McGinn points to the pharmaceutical industry. He says, "When you heat a drug product, it may go through polymorphic transformations. Some of these may react differently." So a pharmaceutical scientist might expose a sample to a range of temperatures to find the transformation points. In other cases, a researcher may simply want to keep a cellular sample at body temperature during an imaging experiment.

Each part matters, as does the interaction between them, and these must all merge into a system that meets the individual scientist's needs.

Some applications require even greater environmental control, which scientists can obtain with an on-stage incubator from the Advanced Microscopy Group (recently acquired by Life Technologies, which has in turn been acquired by Thermo Scientific), which includes an environmentally controlled chamber. "The device is essentially a plug-in for the EVOS fluorescent microscope," adds Hans Beernink, product management leader at Life Technologies. "It integrates into the microscope and is controlled by software." It can be controlled for temperature, humidity, and even gases, such as oxygen. continued>

Featured Participants

Andor
www.andor.com

Carl Zeiss
www.zeiss.com/microscopy

Femtolasers Produktions
www.femtolasers.com

Life Technologies
www.lifetechnologies.com

Linkam Scientific Instruments
www.linkam.co.uk

Harvard Center for Biological Imaging
labs.mcb.harvard.edu/hcbi/

MBF Bioscience
www.mbfbioscience.com

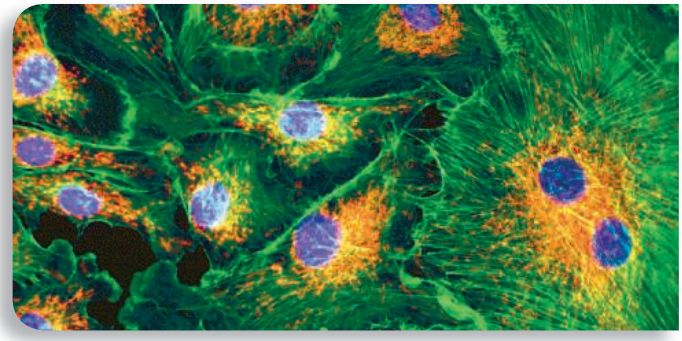
McCrone Microscopes & Accessories
www.mccronemicroscopes.com

Nikon Instruments
www.nikoninstruments.com

Olympus Canada
www.olympuscanada.com

Photometrics
www.photometrics.com

QImaging
www.qimaging.com



Sensitivity determines the weakest fluorescent signal that can be detected, and resolution reveals the smallest features that can be distinguished in an image.

STAYING IN FOCUS

Beyond keeping cells in good health, live-cell imaging creates other unique challenges. Some of the obstacles scientists must overcome are optical, and others are more mechanical.

Distinctive optical factors come into play with live-cell imaging. This creates a need for new microscopy solutions since objectives were originally designed for fixed samples, which have different optical properties than live cells. As Andrew Millar, marketing manager for the scientific equipment group at **Olympus Canada** in Richmond Hill, Ontario, says, "Our silicone immersion objectives were designed for imaging live cells." He adds, "Images collected from live cells are brighter and more highly resolved when using silicone immersion optics." These objectives come in 30x, 40x, and 60x, and work on any Olympus microscope. They improve the quality of an image because the refractive index of the silicone immersion media is very similar to that of live cells.

Live-cell imaging technologies cover a wide range of applications, and some can be extremely specific. In electrophysiology, for example, once you insert a glass electrode into the desired neuron, you don't want anything bumping it, which can abruptly end your recording. But what if you want to look at something nearby, maybe to even place a second electrode? You can't move the microscope stage, but some technologies allow you to reposition the objective. That's just what you can do with the Radially Moving Objective, or RMO, from **MBF Bioscience** in Williston, Vermont. "It moves the objective lens in the *x* and *y* direction," says Jack Glaser, the company's president. "The specimen stays stationary, and the objective lens moves to scan different points." Glaser adds that the RMO works with most microscopes and objective lenses. "You just remove the objective turret, slide on the RMO, tighten a setscrew, and you're ready to go," Glaser explains. The RMO comes with a control box that allows a computer to move the objective.

FEATURES FOR FLUORESCENCE

Whether a scientist is imaging live cells or fixed ones, controlling the illumination is an important tool for microscopy experiments. This is particularly true for today's imaging techniques that involve multiple lasers to light up different fluorescent labels in a sample. "People have their own preferences and needs for their experiments," says Stephen T. Ross, general manager of products and marketing for North and South America at **Nikon Instruments**, which is headquartered in Melville, New York.

To help with that, Nikon developed some new components for its Ti inverted microscopes. For instance, the Nikon LU-N laser unit can be equipped with up to eight lasers, ranging from 356–756 nm. "This laser unit also provides up to seven different outputs that can connect to various devices, like a photo-activation system for fluorescence imaging," Ross says. "Plus, it's a solid-state laser system, and there are no mirrors or adjustments needed when it comes out of the box."

Released in conjunction with the LU-N, Nikon developed its L-Apps system components. "These application components and the LU-N work synergistically through our software," says Ross. "This can take complicated experiments and make them accessible to people at all different levels of expertise." When illuminating live cells, laser light can damage the sample. So having more control over the illumination comes in handy.

To really lessen the potential damage from laser illumination in fluorescence imaging, a scientist can use two-photon microscopy. It decreases the impact of light on a sample by exciting the fluorescent molecule with two photons at once, with each carrying only about half the energy required with just one photon. To further prevent tissue damage, a scientist can use a laser that creates very short pulses, which also applies less energy to the sample. Today's fastest lasers for this kind of imaging produce pulses in the range of femtoseconds—just millionths of a billionth of a second.

When asked about the key challenges to making femtosecond lasers that can be used in most life science laboratories, Andreas Stingl, president of **Femtolasers Produktions** in Vienna, Austria, points out three things: ease of use, a lifetime of 10,000 hours, and robust construction. He says, "Currently, tunable titanium-sapphire–based oscillators operating at repetition rates of 80 megahertz and delivering pulses in the 100 femtosecond range are standard sources used in two-photon microscopy." Beyond causing less damage, a femtosecond pulse can penetrate deeper into tissues than longer pulses. For instance, Stingl says, "Sub-20 femtosecond pulses show 160% increased penetration depth compared to 120 femtosecond pulses at the same average power."

The power to transform images with such minute—femtosecond—changes reveals the precision involved in today's microscopes. But focusing on such tiny parameters should not overshadow the need to blend together the right microscope components overall. Each part matters, as does the interaction between them, and these must all merge into a system that meets the individual scientist's needs.

Mike May is a publishing consultant for science and technology.

DOI: 10.1126/science.opms.p1400085

CREDIT: IIMAGE COURTESY OF QIMAGING.

CORRELATIVE RAMAN-SEM IMAGING SYSTEM

RISE Microscopy is a novel correlative microscopy technique which combines confocal Raman Imaging and Scanning Electron (RISE) Microscopy within one integrated microscope system. This unique combination provides clear advantages for the microscope user with regard to comprehensive sample characterization: electron microscopy is an excellent technique for visualizing the sample surface structures in the nanometer range, and confocal Raman imaging is an established spectroscopic method used for the detection of the chemical and molecular components of a sample. It can also generate 2-D and 3-D images and depth profiles to visualize the distribution of the molecular compounds within a sample. The RISE Microscope enables the acquisition of SEM and Raman images from the same sample area and the correlation of ultrastructural and chemical information. Between the different measurements, an extremely precise scan stage automatically transfers the sample inside the microscope's vacuum chamber and repositions it. The integrated RISE software carries out the required parameter adjustments and instrument alignments. The acquired results can then be correlated and the Raman and SEM images overlaid.

WITec

For info: +49-731-140-700 | www.witec.de



CORRELATIVE IMAGING SOLUTION

JEOL and Nikon have integrated optical microscopy and field emission scanning electron microscopy in a way that enables seamless observation of the same region of interest on a sample with fast, accurate navigation. The technique, MiXcroscopy, employs the same specimen holder for both the optical microscope (OM) and the scanning electron microscope (SEM). The specimen stage registration is fully controlled by dedicated software that allows the OM and SEM to share, recall, and observe exact locations of specific areas on the specimens. The Nikon ECLIPSE LV-N series optical microscope and any of the JEOL JSM-7000 series Field Emission SEMs work concurrently as the optical image taken on the OM, along with specimen stage coordinates, are transferred to the SEM for navigation and correlation via Nikon's Elements software. When the sample holder is moved to the SEM, the researcher can observe detailed structures at higher magnifications and easily compare to the optical image on screen.

JEOL

For info: 978-535-5900 | www.jeolusa.com

INFRARED MICROSCOPY PLATFORM

Spero is a laser-based infrared microscopy platform that opens up a new world of research possibilities with breakthrough chemical imaging and analysis on a real-time basis. Spero offers a unique combination of unparalleled visibility, instantaneous results in "live mode," and a small resource footprint to easily fit into any lab setting. By seamlessly incorporating a high-brightness, broadly tunable mid-infrared laser source, Spero provides unprecedented image resolution with an ultrawide field of view. This unique combination enables researchers to observe micron-scale features while also covering large areas very quickly for high throughput applications. The instrument operates in the feature-rich mid-infrared region and provides high-fidelity spectral data for the accurate identification of molecular and chemical components of complex, heterogeneous samples. Spero is powered by an elegant and easy-to-use spectral imaging software platform that enables both novice and expert users to quickly generate high-quality images and accurate spectral information.

Daylight Solutions

For info: 858-432-7500 | www.daylightsolutions.com/spero

RAMAN SPECTROSCOPY SYSTEM

The XploRAPLUS is a fully confocal and high-performance Raman microscope, offering an unmatched and enhanced range of options such as multiple laser wavelengths, complete automation, EMCCD detection, Raman polarization, and even AFM coupling. Our SWIFT Fast Raman imaging offers the best and most detailed Raman images, typically 10x faster than conventional mapping methods. The new LabSpec 6.3 software offers features ideally suited to multiple user environments, such as HORIBA's "One-Click" Raman. Ensuring easy and reliable Raman measurements, HORIBA One-Click will automatically adapt and optimize data acquisition parameters, producing quality Raman spectra time after time. Security of the system and hardware is assured by user-specific LabSpec software login accounts, while LabSpec sample "methods" provide an ideal way to standardize or automate Raman analysis at the touch of a button. The XploRA PLUS is the full Raman microscope package.

HORIBA Scientific

For info: 732-494-8660 | www.horiba.com/raman

X-RAY MICROSCOPE

The nano3DX is a true X-ray microscope with the ability to measure relatively large samples at high resolution. The nano3DX images the entire sample from multiple angles and can reconstruct a 3-D image at 0.27 µm resolution. The computer model allows the user to view sections at any point on any plane, providing valuable insights into the structure of the sample. The secret behind the nano3DX is the high-power rotating anode and high-resolution optics coupled with submicron charge-coupled device technology. This combination is capable of fast data collection and has the ability to switch anode materials rapidly to optimize data acquisition. Furthermore, the magnification occurs in the detector using true microscope elements. The geometry of the system allows the sample to be located very close to the high-resolution detector, which provides near-parallel beam optics. This design results in improved instrument stability, which prevents smearing and allows for faster data collection times.

Rigaku

For info: 888-362-2324 | www.rigaku.com

Electronically submit your new product description or product literature information! Go to **www.sciencemag.org/products/newproducts.dtl** for more information.

Newly offered instrumentation, apparatus, and laboratory materials of interest to researchers in all disciplines in academic, industrial, and governmental organizations are featured in this space. Emphasis is given to purpose, chief characteristics, and availability of products and materials. Endorsement by *Science* or AAAS of any products or materials mentioned is not implied. Additional information may be obtained from the manufacturer or supplier.

immunogenomics 2014

September 29 - October 1, 2014

HudsonAlpha Biotechnology Campus
Huntsville, Alabama, USA

Bringing together preeminent leaders and thinkers at the intersection of genomics and immunology

Our Keynote Speakers:

Christophe Benoiste
Professor, Department of Microbiology and Immunobiology, *Harvard Medical School*

Mary Ellen Conley
Federal Express Chair of Excellence and Professor, Department of Pediatrics, *University of Tennessee, College of Medicine, Memphis*

Mark Davis
Investigator, Howard Hughes Medical Institute; Professor, Department of Microbiology and Immunology; Director, Institute for Immunity, Transplantation, and Infections, *Stanford University School of Medicine*

Sponsored by

Platinum Sponsors

iRepertoire, Inc.

Gold Sponsors

UAB COMPREHENSIVE ARTHRITIS, MUSCULOSKELETAL, AND AUTOIMMUNITY CENTER

Silver Sponsors

GenapSys

illumina

Interested in sponsoring Immunogenomics 2014? Visit our website for more information.

Register today at

haig.aaas.org

follow @immunogenomics on twitter

presented by

HUDSONALPHA INSTITUTE FOR BIOTECHNOLOGY

Science AAAS

NEW ENGLAND BioLabs® Inc.
enabling technologies in the life sciences

Make ends meet.

Gibson Assembly® Cloning Kit

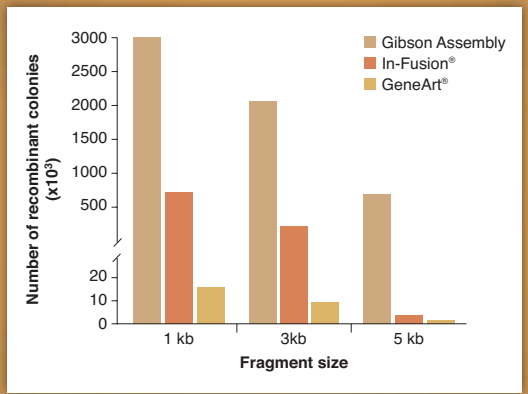
New England Biolabs has revolutionized your laboratory's standard cloning methodology. The Gibson Assembly Cloning Kit combines the power of the Gibson Assembly Master Mix with NEB 5-alpha Competent *E. coli*, enabling fragment assembly and transformation in just under two hours. Save time, without sacrificing efficiency.

Making ends meet is now quicker and easier than ever before, with the Gibson Assembly Cloning Kit from NEB.

NEBuilder™ for Gibson Assembly

Visit **NEBGibson.com** to view the latest tutorials and to try our primer design tool.

Gibson Assembly Cloning Kit provides robust transformation efficiencies



Assembly reactions containing 25 ng of linear pUC19 vector and 0.04 pmol of each fragment were performed following individual suppliers' recommended protocols and using the competent cells provided with the kit. The total number of recombinant colonies was calculated per 25 ng of linear pUC19 vector added to the assembly reaction.

IN-FUSION® is a registered trademark of Clontech Laboratories, Inc.
GENEART® is a registered trademark of Life Technologies, Inc.
GIBSON ASSEMBLY® is a registered trademark of Synthetic Genomics, Inc.

SGI-DNA

Some components of this product are manufactured by New England Biolabs, Inc. under license from Synthetic Genomics, Inc.



Science Careers Advertising

For full advertising details, go to ScienceCareers.org and click For Employers, or call one of our representatives.

Tracy Holmes
Worldwide Associate Director
Science Careers
Phone: +44 (0) 1223 326525

THE AMERICAS

E-mail: advertise@sciencecareers.org
Fax: 202-289-6742

Tina Burks
Phone: 202-326-6577

Nancy Toema
Phone: 202-326-6578

Marci Gallun
Sales Administrator
Phone: 202-326-6582

Online Job Posting Questions
Phone: 202-312-6375

EUROPE / INDIA / AUSTRALIA / NEW ZEALAND / REST OF WORLD

E-mail: ads@science-int.co.uk
Fax: +44 (0) 1223 326532

Axel Gesatzki
Phone: +44 (0)1223 326529

Sarah Lelarge
Phone: +44 (0) 1223 326527

Kelly Grace
Phone: +44 (0) 1223 326528

JAPAN

Yuri Kobayashi
Phone: +81-(0)90-9110-1719
E-mail: ykobayas@aaas.org

CHINA / KOREA / SINGAPORE / TAIWAN / THAILAND

Ruolei Wu
Phone: +86-1367-1015-294
E-mail: rwu@aaas.org

All ads submitted for publication must comply with applicable U.S. and non-U.S. laws. *Science* reserves the right to refuse any advertisement at its sole discretion for any reason, including without limitation for offensive language or inappropriate content, and all advertising is subject to publisher approval. *Science* encourages our readers to alert us to any ads that they feel may be discriminatory or offensive.

Science Careers
From the journal *Science* AAAS

ScienceCareers.org

MUSC
MEDICAL UNIVERSITY of SOUTH CAROLINA

Medical University of South Carolina
Dean, College of Graduate Studies

The Medical University of South Carolina (MUSC) invites nominations and applications for the position of Dean, College of Graduate Studies. Located in historic downtown Charleston, MUSC is home to approximately 1,200 faculty and provides state-of-the-art laboratories and interdisciplinary centers for basic, clinical, translational, and public health researchers. MUSC ranks in the top quartile of domestic educational institutions with research funding exceeding $230 million annually and is home to the South Carolina Clinical and Translational Research Institute (funded by an NIH Clinical and Translational Science Award) and the Hollings Cancer Center, South Carolina's only National Cancer Institute-designated cancer center.

The College of Graduate Studies offers Ph.D. programs in Biomedical Sciences and combined Ph.D. programs with medicine (MSTP), dental medicine (DMSTP), and pharmacy (PharmD/PhD), and Master of Science programs in Clinical Research and Biomedical Sciences. The College also houses the Clemson University-MUSC Bioengineering Alliance, which offers a Ph.D. in Bioengineering. Additional certificate and M.S. programs are in the planning stages. The College conducts several research training programs with South Carolina's historically black colleges and universities.

The Dean reports to the Vice President for Academic Affairs and Provost. As the chief academic and administrative officer of the College of Graduate Studies, this individual is responsible for the educational, research and service missions of the College. As a member of the Provost's leadership team, the Dean will be expected to engage in all aspects of MUSC's vision and mission, advocate for graduate education, work collaboratively with the deans of the five other Colleges (Dental Medicine, Health Professions, Medicine, Nursing and Pharmacy) and promote an academic enterprise that is innovative, entrepreneurial, diverse and global in its reach.

Applicants or nominees will hold an earned Ph.D. degree in one of the biomedical sciences and will have academic credentials commensurate with appointment as a full professor with tenure to include a distinguished record of research productivity, teaching excellence, and administrative experience. Successful candidates will also have an ongoing federally funded research program in the biomedical sciences, excellent interpersonal and communication skills, strong potential to attract financial support for the college, and the ability to foster interprofessional collaboration.

Review of applications will begin **May 15, 2014** and will continue until the position is filled. All applications and nominations will be submitted electronically at **https://www.jobs.musc.edu/postings/24100** and should include a letter of application, a comprehensive resume, and a list of five references. For more information or nominations contact Dr. Craig E. Crosson, Chair, College of Graduate Studies Search Committee, in care of Mary McConnell at **mcconnem@musc.edu**.

MUSC is an EEO/AA Employer.



AAAS is here – helping scientists achieve career success.

Every month, over 400,000 students and scientists visit ScienceCareers.org in search of the information, advice, and opportunities they need to take the next step in their careers.

A complete career resource, free to the public, *Science* Careers offers a suite of tools and services developed specifically for scientists. With hundreds of career development articles, webinars and downloadable booklets filled with practical advice, a community forum providing answers to career questions, and thousands of job listings in academia, government, and industry, *Science* Careers has helped countless individuals prepare themselves for successful careers.

As a AAAS member, your dues help AAAS make this service freely available to the scientific community. If you're not a member, join us. Together we can make a difference.

To learn more, visit
aaas.org/plusyou/sciencecareers

AAAS + U = Δ



With a boom in research at QU, the institution with the highest growth rate in research in the region, Qatar University is poised to become a

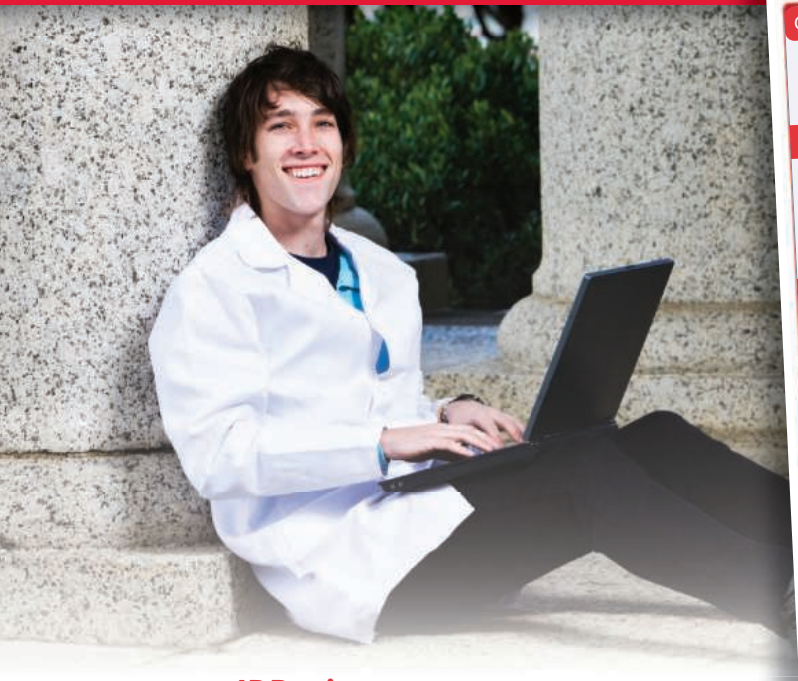
regional leader of thought

www.qu.edu.qa

جامعة قطر
QATAR UNIVERSITY

For your career in science, there's only one **Science**

A career plan customized *for* you, *by* you.



myIDP.sciencecareers.org



Recommended by leading professional societies and endorsed by the National Institutes of Health, an individual development plan will help you prepare for a successful and satisfying scientific career.

my IDP Science Careers

In collaboration with FASEB, UCSF, and the Medical College of Wisconsin and with support from the Burroughs Wellcome Fund, AAAS and *Science* Careers present the first and only online app that helps scientists prepare their very own individual development plan.

Visit the website and start planning today!
myIDP.sciencecareers.org

In partnership with:

advancing the life sciences 1912-2012 FASEB Federation of American Societies for Experimental Biology

UCSF University of California San Francisco

Medical College of Wisconsin

Burroughs Wellcome Fund



TOGETHER, LET'S SAVE THE PLANET...
...FROM THE FOOD CRISIS, PLANT AND ANIMAL DISEASES, GLOBAL WARMING

INRA, ACCESSIBLE TO ALL AMBITION

As part of its Human Resources policy, INRA recruits research scientists and engineers with disabilities: these positions are within strategic areas of the institute. You are invited to join our research units focused in the scientific challenges of tomorrow.
To apply, please download the application form available on our website jobs.inra.fr/en

APPLICATIONS UNTIL JUNE 16TH 2014
ON **JOBS.INRA.FR/EN**

INRA SCIENCE & IMPACT

HR EXCELLENCE IN RESEARCH

PUBLICODE

Join the Minds of Janelia Graduate Fellowship

Janelia Farm Research Campus



A Unique Fellowship Program

Janelia Farm Research Campus, near Washington, DC, invites graduate students from the U.S. and abroad who are interested in doing doctoral research at Janelia to apply for the Visitor Graduate Fellowship.

The fellowship is designed for highly committed students from diverse research disciplines who want to understand neural circuits and develop novel bioimaging technologies.

Highlights
- Collaborative culture
- Vibrant student community
- Unparalleled scientific facilities
- World-class conferences

Application deadline:
2PM ET/7PM GMT
July 15, 2014

www.janelia.org/gf14/sci

HHMI janelia farm research campus

THE UNIVERSITY OF TEXAS MD Anderson Cancer Center
Making Cancer History®

Molecular Carcinogenesis
Assistant Professor, Term Tenure Track

Department of Molecular Carcinogenesis
The University of Texas
MD Anderson Cancer Center
1808 Park Road 1C, P.O. Box 389
Smithville, TX 78957

The Department of Molecular Carcinogenesis at The University of Texas MD Anderson Cancer Center, Science Park, seeks applicants for a term tenure track position at the rank of assistant professor. Research in the department focuses on cellular, molecular and genetic mechanisms of carcinogenesis and cancer prevention. We seek individuals working in the areas of genetic susceptibility, epigenetic reprogramming, genomic instability and cancer stem cells. Candidates must be committed to working in a highly collaborative, interdisciplinary environment. The successful candidate will be expected to develop and maintain an internationally recognized and competitively funded research program, and to participate in graduate training. The department is well funded with many outstanding core support services, including facilities for analysis of genetically engineered mouse models and next-generation sequencing. Our department is located in a pine-oak forest near the city of Austin, TX. MD Anderson offers outstanding research facilities, startup packages, and faculty benefits.

Required qualifications include a Ph.D. or equivalent, postdoctoral or independent scholarly research experience, and a strong publication record. Interested applicants should submit a statement of research interest and a curriculum vitae, and three letters of recommendation to the email address below by July 1, 2014.

Email: sciencepark@mdanderson.org

Mark Bedford, Ph.D., Professor
Search Committee Chair
Department of Molecular Carcinogenesis
The University of Texas MD Anderson Cancer Center
1808 Park Road 1C, P.O. Box 389, Smithville, TX 78957
http://sciencepark.mdanderson.org

MD Anderson is an equal opportunity employer and does not discriminate on the basis of race, color, national origin, gender, sexual orientation, age, religion, disability or veteran status except where such distinction is required by law. All positions are security sensitive and subject to examination of criminal history record information. The University of Texas MD Anderson Cancer Center is a smoke-free and drug-free environment.

FACULTY POSITIONS IN DEVELOPMENTAL AND PEDIATRIC SYSTEMS BIOLOGY

The Division of Developmental Biology (DB) at Cincinnati Children's Hospital Medical Center is launching a major new initiative to recruit 3-5 world-class junior investigators focused on Quantitative Systems-level analysis of Developmental Biology or Pediatric Disease. We are seeking individuals who tackle fundamental cutting-edge questions by combining quantitative and/or theoretical approaches with wet bench experiments. Candidates must have completed a postdoctoral training period, published high-quality and original work, and hold an MD, PhD, or MD/PhD degree. We envision this faculty will bridge basic research with bioinformatics and translational medicine activities at Cincinnati Children's.

The DB division at Cincinnati Children's represents one of the largest assemblies of basic scientists investigating model organism development and pediatric disease in the world. DB is embedded within a top-three ranked pediatric hospital specializing in providing cutting-edge care for some of the most in need young patients on the planet. Our vision is to leverage our rich patient database and robust mechanism-based research to develop innovative systems level analyses of development and/or disease.

Interested candidates should submit curriculum vitae, contact information for three references, a summary of past research accomplishments and future research plan to: db_systembiologists@cchmc.org.

Please visit our website at: http://www.cincinnatichildrens.org/research/divisions/d/dev-biology/default/

UNIVERSITY OF Cincinnati

Cincinnati Children's
change the outcome®

The Cincinnati Children's Hospital Medical Center and the University of Cincinnati are Affirmative Action/Equal Opportunity Employers. Qualified women and minority candidates are encouraged to apply.

Science | Careers



There's only one

Dr. Shirley Malcom

To Dr. Shirley Malcom, born and raised in the segregated South more than 65 years ago, a career based on her studies in science seemed even less likely than the launch of the Soviet's Sputnik. But with Sputnik's success, the Space Race officially started and, in an instant, brought a laser-like focus to science education and ways to deliver a proper response. Not long after, Dr. Malcom entered the picture.

Although black schools at the time received fewer dollars per student and did not have sufficient resources to maintain their labs at a level equivalent to the white schools, Dr. Malcom found her way to the University of Washington where she succeeded in obtaining a B.S. in spite of the difficulties of being an African American woman in the field of science. From there she went on to earn a Ph.D. in ecology from Penn State and held a faculty position at the University of North Carolina, Wilmington.

Dr. Malcom has served at the AAAS in multiple capacities, and is presently Head of the Directorate for Education and Human Resources Programs. Nominated by President Clinton to the National Science Board, she also held a position on his Committee of Advisors on Science and Technology. She is currently a member of the Caltech Board of Trustees, a Regent of Morgan State University, and co-chair of the Gender Advisory Board of the UN Commission on Science and Technology for Development. She has held numerous other positions of distinction and is the principal author of *The Double Bind: The Price of Being a Minority Woman in Science*.

Of her active career in science, Dr. Malcom says, "I guess I have become a poster child for taking one's science background and using that in many other ways: we ask questions; we try to understand what we find; we consider what evidence we would need to confirm or refute hypotheses. And that happens in whatever setting one finds oneself."

At *Science* we are here to help you in your own scientific career with expert career advice, forums, job postings, and more — all for free. Visit *Science* today at **ScienceCareers.org**.



For your career in science, there's only one Science

AAAS

ScienceCareers.org

Career advice | Job postings | Job Alerts | Career Forum | Crafting resumes/CVs | Preparing for interviews

PENNSTATE
University Park

FACULTY POSITION IN PLANT BIOLOGY

The Biology Department at The Pennsylvania State University (Penn State) seeks candidates for a tenured or tenure-track faculty position in the area of plant biology. Candidates using genetics, genome-wide association studies (GWAS) or other big data approaches, functional genomics, or phenomics to study fundamental questions in plant biology are encouraged to apply. Candidates for the ranks of Associate Professor or Professor should have well-established research programs as well as strong records of teaching and service, and be widely recognized as leaders in their field. Candidates for the rank of Assistant Professor should have a strong record of research accomplishments.

Penn State has one of the top US graduate programs in the plant sciences, and a large, vibrant, and collaborative group of faculty in plant biology and the wider life sciences. Penn State`s flagship University Park campus is situated in a community consistently rated as among the most livable small cities in the US.

Applicants should prepare a cover letter, CV, and a third document containing a statement of research interests and a statement of teaching philosophy. Candidates for the rank of Assistant Professor should also include a fourth document with names and contact information for three professional references. Apply by submitting the requested documents at the Penn State employment website **www.psu.jobs** for **job #42967**. Review of applications will begin immediately and continue until a suitable candidate is found.

CAMPUS SECURITY CRIME STATISTICS: For more about safety at Penn State, and to review the Annual Security Report which contains information about crime statistics and other safety and security matters, please go to **http://www.police.psu.edu/clery/** , which will also provide you with detail on how to request a hard copy of the Annual Security Report.

Penn State is an Equal Opportunity, Affirmative Action Employer, and is committed to providing employment opportunities to minorities, women, veterans, disabled individuals, and other protected groups.

UNIVERSITY of MARYLAND
SCHOOL OF MEDICINE

Neurobiology Faculty Position

University of Maryland
School of Medicine
Baltimore, Maryland

The Department of Anatomy and Neurobiology (**http://neurobiology.umaryland.edu**) is recruiting for tenured/tenure-track faculty positions in Neuroscience. We are particularly interested in candidates whose research will complement existing strengths in the Department. Although we will consider all relevant research areas, we are particularly interested in candidates whose research focuses on neural circuits of motivated behaviors and addiction, sensory perception, and pain. Candidates should have a strong record of scholarly activity and an independent funded research program that can catalyze multi-PI initiatives within the department or across the institution.

We offer an outstanding intellectual and collaborative environment with highly competitive salary and recruitment packages. All department faculty are members of the Graduate Program in Life Sciences (**http://bit.ly/PVsKZL**) and the interdisciplinary Program in Neuroscience (**http://bit.ly/1su2aGq**).

Candidates should submit the following as a single PDF to the email address **facsearch@umaryland.edu**: curriculum vitae, brief statement of research interests and goals, and contact information for three references. For best consideration candidates should submit their application by **July 1, 2014** and should be addressed to the attention of: **Dr. Joseph Cheer, Chair of Faculty Search Committee**.

University of Maryland is an Equal Opportunity, Affirmative Action Employer. Minorities, women, veterans, and individuals with disabilities are encouraged to apply.

2014 Yamada Research Grant (Japan)

The Yamada Research Grant aims to promote creative researches on preventive medicine with bee products and natural products.

1. Theme of the Application:
I. General Research Program
1) New Research Grant (Grant amount: Up to 2,000,000 Japanese Yen per theme)
For researchers or beekeepers who have never received a research grant from the Yamada Research Grant.
(1) Preventive medical research, (2) Research on environmental protection, (3) Research on utility of preventive medicine

2) Continuing Research Grant (Grant amount: Up to 10,000,000 Japanese Yen per theme)
For researchers or co-researchers who have previously received a research grant from the Yamada Research Grant.

II. Specified Research Program (Grant amount: Up to 30,000,000 Japanese Yen per theme)
Research topics must be focused on clinical trials in this program as described below.
1) Research on royal jelly
(1) Health maintenance and improvement of muscle or bone, (2) Improvement of blood pressure or flow, (3) Maintenance and improvement of brain function, (4) Immunostimulating effect, (5) Health maintenance of skin

2) Research on propolis
(1) Immunostimulating effect, (2) Anti-allergy, (3) Maintenance and improvement of brain function, (4) Improvement of insulin resistance

2. Language: English or Japanese

3. How to apply: Applications should be filled out the specified format on the following website according to application guideline for this grant.
http://www.bee-lab.jp/grant/grant/grant_2014/guideline_eng.html

4. Application period: From May 1st, 2014 until exactly 17:00, Japan time, May 29th, 2014

How to inquire: Please contact the secretariat of this grant by e-mail.
E-mail address: research-grant@yamada-bee.com

FUNDING OPPORTUNITIES

U.S. Department of Defense
Defense Medical Research and Development Program

Peer Reviewed Medical Research Program

The Peer Reviewed Medical Research Program (PRMRP) funds exceptional research with the goal to improve the health and well-being of all military service members, Veterans, and beneficiaries. The PRMRP received ***$200 million*** in fiscal year 2014 (FY14), and seeks grant applications in the following ***topic areas***:

Acupuncture
Arthritis (other than post-traumatic osteoarthritis and rheumatoid arthritis)
Chronic Migraine and Post-Traumatic Headaches
Congenital Heart Disease
DNA Vaccine Technology for Post-Exposure Prophylaxis
Dystonia
Epilepsy
Food Allergies
Fragile X Syndrome
Hereditary Angioedema
Illnesses Related to Radiation Exposure (excludes cancer)
Inflammatory Bowel Disease
Interstitial Cystitis
Lupus
Malaria
Metabolic Disease
Neuroprosthetics
Pancreatitis
Polycystic Kidney Disease
Post-Traumatic Osteoarthritis
Psychotropic Medications
Respiratory Health (excludes lung cancer and mesothelioma)
Rheumatoid Arthritis
Segmental Bone Defects
Tinnitus

The FY14 PRMRP Program Announcements and General Application Instructions are anticipated to be posted on Grants.gov by ***May 1, 2014:***

- Clinical Trial Award
- Discovery Award
- Focused Program Award
- Investigator-Initiated Research Award
- Technology/Therapeutic Development Award

All applications must conform to the Program Announcements and General Application Instructions that will be available for electronic downloading from the Grants.gov website (all viewable under CFDA number 12.420). Execution management support will be provided by the Congressionally Directed Medical Research Programs.

http://cdmrp.army.mil
http://cdmrp.army.mil/funding/prmrp.shtml

POSITIONS OPEN

RESEARCH ASSOCIATE
Biological Mass Spectrometry
Indiana University, Bloomington

The Laboratory for Biological Mass Spectrometry at Indiana University (**website: http://www.chem.indiana.edu/bms/**), directed by **Dr. Jonathan Trinidad,** is seeking a Ph.D. to fill a Research Associate position. The Laboratory specializes in the development of novel mass spectrometry methodology, with an emphasis on posttranslational modifications, and provides service for researchers both within and external to IU. This position involves working on a mix of collaborator-driven projects as well as one's own independent research. The ideal candidate will possess a creative, analytical approach to problem solving, the ability to work independently, and the willingness to lead interdisciplinary collaborations and have 0–3 years of postdoctoral experience. Proficiency with mass spectrometry/proteomics is desirable, however candidates with a Ph.D. in biochemistry or cell biology will also be considered. Annual salary is $40,000 to $46,000, commensurate with qualifications and experience. Interested applicants should provide a cover .letter indicating research interests, career goals, and experience as well as curriculum vitae and arrange to have two letters of reference sent to **website: https://indiana.peopleadmin.com.** Questions regarding the position or application process can be directed to: **Dr. Jonathan Trinidad, Director of Biological Mass Spectrometry, Department of Chemistry, Indiana University, Bloomington, IN 47405-7102** (**e-mail: trinidad@indiana.edu**). *Indiana University is an Affirmative Action/Equal Opportunity/Employer and especially encourages applications from women and members of minority groups.*

TENURE-TRACK ASSISTANT/ASSOCIATE PROFESSOR

The Department of Physiology at Wayne State University (WSU) School of Medicine invites applications for a tenure-track Assistant/Associate Professor position. Major areas of interest include cellular, molecular, and systems approaches to investigations related to contemporary physiology and pathophysiology. Special consideration will be given to investigators who complement existing strengths of the Department (**website: http://physiology.med.wayne.edu**).

Candidates are expected to establish and maintain active extramurally funded research programs and participate in teaching medical and graduate students. Startup packages and salaries are highly competitive. Candidates must hold Ph.D., M.D., or equivalent and apply with curriculum vitae, detailed research plan, and names/contact information of three references to **e-mail: wsuphysiologyfacultysearch@med.wayne.edu.** Review of applications will begin after July 1, 2014 and continue until position is filled.

WSU offers 350 academic programs through 14 schools and colleges to over 30,000 students in the Detroit Midtown area. WSU School of Medicine is a state-of-the-art research environment, and rated by the Carnegie Foundation in the top third of all U.S. Research Institutions. The Detroit Metro area is home to four million people and a hub to many of the nation's high-tech industries. *WSU is an Equal Opportunity/Affirmative Action Employer.*

ASSISTANT/ASSOCIATE/PROFESSOR

The new Center for Research on Environmental Disease, College of Medicine, University of Kentucky is seeking candidates for several faculty positions at the Assistant/Associate/Professor (tenure-track and tenured) levels with 12-month appointment. Applicants are sought in the broad area of environmental disease. Applicants should submit their curriculum vitae to **Dr. Xianglin Shi,** Professor and Director, Center for Research on Environmental Disease by **e-mail: xianglin.shi@uky.edu.** Review of applications will begin immediately and continue until the positions are filled.

POSITIONS OPEN

FACULTY POSITION

The Department of Molecular Physiology and Biophysics at Baylor College of Medicine is seeking scientists using vertebrate models of human disease in one or more of the following areas: metabolism, skeletal muscle, or cardiovascular system. We are recruiting for an **ASSOCIATE PROFESSOR** (tenure) with a strong independent research program with current NIH funding and a commitment to excellence in graduate and medical student education. The department currently has strong research programs in both basic and translational biomedical research and has state-of-the-art facilities for confocal and multiphoton imaging, mouse MRI, computed tomography, and cores for the creation and phenotypic analysis of new mouse models. Baylor College of Medicine is a world-renowned research institution with ample opportunities for scientific interaction and collaborations within the department, throughout the College, and with the other world class institutions of the Texas Medical Center (**website: http://www.bcm.edu/departments/molecular-physiology-and-biophysics**).

Applications must be received by June 30, 2014. Please e-mail your application materials to **e-mail: molphys@bcm.edu** and include a curriculum vitae and a description of your current and future research program. Additionally, have three letters of references sent separately to the same e-mail address.

Your career is our cause.

Get help from the experts.

www.sciencecareers.org

- Job Postings
- Job Alerts
- Resume/CV Database
- Career Advice
- Career Forum

Science Careers
From the journal *Science* AAAS

Find your future here.
www.ScienceCareers.org



Nontraditional Careers: Opportunities Away From the Bench

Webinar

Want to learn more about exciting and rewarding careers outside of academic/industrial research? View a roundtable discussion that looks at the various career options open to scientists and strategies you can use to pursue a nonresearch career.

Now Available On Demand
www.sciencecareers.org/webinar

Produced by the *Science*/AAAS Business Office.

Science Careers
From the journal *Science* AAAS